Pontifícia Universidade Católica
do Rio de Janeiro

Clara Elizabeth Verdugo Muñoz

Fog and rain attenuation models for the design of FSO links in 5G+

Tese de Doutorado

Thesis presented to the Programa de Pós–graduação em Engenharia Elétrica, do Departamento de Engenharia Elétrica da PUC-Rio in partial fulfillment of the requirements for the degree of Doutor em Engenharia Elétrica.

Advisor : Prof. Luiz Alencar Reis da Silva Mello
Co-advisor: Dr. Roberto Nebuloni

Rio de Janeiro
July 2022

Pontifícia Universidade Católica
do Rio de Janeiro

Clara Elizabeth Verdugo Muñoz

Fog and rain attenuation models for the design of FSO links in 5G+

Thesis presented to the Programa de Pós–graduação em Engenharia Elétrica da PUC-Rio in partial fulfillment of the requirements for the degree of Doutor em Engenharia Elétrica. Approved by the Examination Committee:

Prof. Luiz Alencar Reis da Silva Mello
Advisor
Centro de Estudos em Telecomunicações – PUC-Rio

Dr. Roberto Nebuloni
IEIIT/CNR-IT

Prof. Carlo Giuseppe Riva
POLIMI

Prof. Lorenzo Luini
POLIMI

Dr. Laura Resteghini
Huawei-IT

Prof. Claiton Pereira Colvero
UFSM

Prof. Jean Pierre von der Weid
Centro de Estudos em Telecomunicações – PUC-Rio

Rio de Janeiro, July the 25th, 2022

Clara Elizabeth Verdugo Muñoz

She majored in Electronic Engineering at the University of Nariño (Pasto, Colombia). She was awarded a Master's degree in Electrical Engineering in the research area of Communications Systems at Pontifical Catholic University of Rio de Janeiro (Rio de Janeiro, Brazil). As part of her doctoral work, she spent a year as a visiting Ph.D. student at the Politecnico di Milano (Milan, Italy). In addition to her research interests, she likes to highlight her passion for learning new languages and interacting with people from different cultures.

Bibliographic data

Verdugo Muñoz, Clara Elizabeth

Fog and rain attenuation models for the design of FSO links in 5G+ / Clara Elizabeth Verdugo Muñoz; advisor: Luiz Alencar Reis da Silva Mello; co-advisor: Roberto Nebuloni. – 2022.

200 f: il. color. ; 30 cm

Tese (doutorado) - Pontifícia Universidade Católica do Rio de Janeiro, Departamento de Engenharia Elétrica, 2022.

Inclui bibliografia

1. Engenharia Elétrica – Teses. 2. Atenuação. 3. Efeitos do clima. 4. Ópticas do espaço livre. 5. Perda de percurso. 6. Visibilidade.
I. Mello, Luiz Alencar Reis da Silva. II. Nebuloni, Roberto. III. Pontifícia Universidade Católica do Rio de Janeiro. Departamento de Engenharia Elétrica. IV. Título.

CDD: 621.3

To my parents, siblings, and niece for their support and encouragement.

To myself, for not giving up even when everything seemed to fall apart.

Acknowledgments

I would like to say a special thank you to my advisor, Luiz Alencar da Silva Mello, who trusted in my potential even when I doubted it. His guidance, patience, and overall support made this an inspiring experience for me.

I wish to thank Roberto Nebuloni, from the Consiglio Nazionale Delle Ricerche, for the innovative ideas for developing this work, the interesting conversations, and his support during the challenging times in Milan.

I am grateful to the Pontificia Universidade Catolica do Rio de Janeiro for challenging me to grow as a researcher and supporting me to obtain the one-year grant as a visiting Ph.D. student at Politecnico di Milano.

I am also grateful to the Politecnico di Milano, to the Dipartimento di Elettronica, Informazione e Bioingengeria and, specially to Carlo Riva and Lorenzo Luini, who trusted in my work and welcomed me in their research group.

I would like to thank Mr. Sergey Kuznetsov of MOSTCOM for assistance during the calibration and maintenance of the FSO link, Mr. Daniel Toribio and Lorenzo Luini for processing the Huawei mmWave data set, and NASA for providing the disdrometer data.

I would like to thank the Coordenação de Aperfeiçoamento de Pessoal de Nível Superior – Brasil (CAPES) for awarding me a mobility scholarship as part of the Ph.D. for a one-year visit at Politecnico di Milano, Italy.

To CNPq for the financial support during the time of the Ph.D. studies in Brazil.

This study was financed in part by the Coordenação de Aperfeiçoamento de Pessoal de Nível Superior - Brasil (CAPES) - Finance Code 001.

Abstract

Verdugo Muñoz, Clara Elizabeth; Mello, Luiz Alencar Reis da Silva (Advisor); Nebuloni, Roberto (Co-Advisor). **Fog and rain attenuation models for the design of FSO links in 5G+**. Rio de Janeiro, 2022. 200p. Tese de Doutorado – Departamento de Engenharia Elétrica, Pontifícia Universidade Católica do Rio de Janeiro.

Free-space optics (FSO), initially studied in the 60s, is attracting attention in the frame of 5G+ systems, which demands wireless back-hauling technologies with extremely high data rates over distances up to a few kilometers. The current lack of a global path loss model for FSO motivates studying the optical link's behavior under different atmospheric conditions. This thesis deals with the development of models for predicting the attenuation due to fog and rain for designing FSO links in 5G and beyond technologies. We study extensive surface measurement databases worldwide as a benchmark for analyzing FSO responses considering available long-term data. We find that the highest impact on visibility worldwide is caused by fog, snow, and rain. Thus, we select fog and rain as the focus of this study. Several path loss models based on visibility are assessed. We propose lower and upper-bound models to estimate the specific attenuation, γ, due to fog which considers uncertainties as the sensitivity of γ to the visibility at 1.550 μm and a micro-physical model of fog. Regarding attenuation caused by rain, we study models available in the literature for microwave links and modify them for application to FSO. When the multiple scattering effects are considered, a significant reduction in the rain attenuation has been found. From the findings, we build a method to statistically combine the attenuation effects on FSO caused by different weather conditions. The performance of FSO links is assessed in terms of the maximum link range against availability under four weather conditions: (i) rain only, (ii) fog only, (iii) rain and fog, and (iv) all conditions. Finally, experimental events for FSO and mmWave links implemented at Leonardo Campus of Politecnico di Milano are classified and analyzed depending on the studied atmospheric effects: stratiform rain, convective rain, light rain, wind, heavy fog, snow, and others.

Keywords

Attenuation; Free-space optics; Path loss; Visibility; Weather effect.

Resumo

Verdugo Muñoz, Clara Elizabeth; Mello, Luiz Alencar Reis da Silva; Nebuloni, Roberto. **Modelos de atenuação de neblina e chuva para o projeto de enlaces FSO em 5G+**. Rio de Janeiro, 2022. 200p. Tese de Doutorado – Departamento de Engenharia Elétrica, Pontifícia Universidade Católica do Rio de Janeiro.

A óptica de espaço livre (FSO), inicialmente estudada na década de 60, está atraindo atenção no contexto dos sistemas 5G+, que exige tecnologias de back-hauling sem fio com taxas de dados extremamente altas em distâncias de poucos quilômetros. A atual falta de um modelo global de perda de percurso para FSO motiva o estudo do comportamento do enlace óptico sob diferentes condições atmosféricas. Esta tese trata do desenvolvimento de modelos para prever a atenuação devido a neblina e chuva para projetar enlaces FSO em tecnologias 5G e além. Estudamos os bancos de dados de medições de superfície disponíveis em todo o mundo como referência para analisar as respostas do FSO considerando os dados disponíveis de longo prazo e descobrimos que o maior impacto na visibilidade em todo o mundo é causado por neblina, neve e chuva. Assim, selecionamos neblina e chuva como o foco deste estudo. Vários modelos de perda de percurso, baseados na visibilidade, são avaliados através de uma abordagem analítica. Propomos modelos de limite inferior e superior para estimar a atenuação específica devido ao nevoeiro considerando incertezas quanto à sensibilidade da atenuação específica, γ, em função da visibilidade em 1.550 μm e o melhor ajuste aos resultados do modelo microfísico. Com relação à atenuação causada pela chuva, estudamos modelos disponíveis na literatura para enlaces de micro-ondas e os modificamos para aplicação em enlaces FSO. Quando os efeitos de espalhamento múltiplo são considerados, foi encontrada uma redução significativa na atenuação da chuva. Construímos a partir dos modelos, um método para combinar estatisticamente a atenuação em enlaces FSO causada por diferentes condições climáticas. O desempenho dos enlaces ópticos é avaliado em termos do máximo comprimento do enlace em relação à disponibilidade sob quatro condições climáticas: (i) somente chuva, (ii) somente neblina, (iii) chuva e neblina, e (iv) e todas as condições. Finalmente, eventos experimentais para os enlaces FSO e mmWave implementados no campus Leonardo do Politecnico di Milano são classificados e analisados dependendo do efeito atmosférico estudado: chuva estratiforme, chuva convectiva, chuva leve, vento, neblina pesada, neve e outros.

Palavras-chave

Atenuação; Efeitos do clima; Ópticas do espaço livre; Perda de percurso; Visibilidade.

Table of contents

List of figures

List of tables

List of Abreviations

BER – Bit Error Rate

CCD – Charge-coupled device

CCDF – Complementary Cumulative Distribution Function

CDF – Cumulative Distribution Function

CAGR – Compound Annual Growth Rate

DSD – Drop Size Distribution

FOV – Field Of View

FSO – Free-Space Optics

IC – Interface Cable (Artolink FSO)

ICT – Information Communication Technology

IoT – Internet of Things

IU – Interface Unit (Artolink FSO)

LDC – Least Developed Country

mmWave – Milimeter Wave

MODCOD – Modulation Code

MOR – Meteorological Optical Range

M2M – Machine to machine

OOK – On–off keying

OU – Optical Unit (Artolink FSO)

OWC – Optical Wireless Communications

PSD – Particles Size Distribution

QCL – Quantum Cascade Laser

RF – Radio Frequency

RMSE – Root Mean Square Error

SNR – Signal-to-Noise Ratio

UAV – Unmanned Aerial Vehicle

WPP – World Population Prospects

1
Introduction

1.1
Context and motivation

In the World Population Prospects (WPP) revision developed in 2019, the United Nations projected that the world's population would grow from 7.7 billion in 2019 to 8.5 billion in 2030, 9.7 billion in 2050, and 10.9 billion in 2100 [1]. With a probability of 95%, the size of the global population will stand between 8.5 and 8.6 billion in 2030, between 9.4 and 10.1 billion in 2050, and between 9.4 and 12.7 billion in 2100, as presented in Figure 1.1.

Regarding the current demographic profiles and regions, only 17% of the population inhabits countries belonging to the "more developed region" (i.e., Europe and Northern America, Australia, New Zealand, and Japan, according to United Nations in [1]). At the same time, 70% of the current population inhabits "less developed regions" (i.e., lower-middle-income countries [1]). Finally, around 13% of people inhabit the "least developed region". As defined by the United Nations, least developed countries (LDCs) are low-income countries

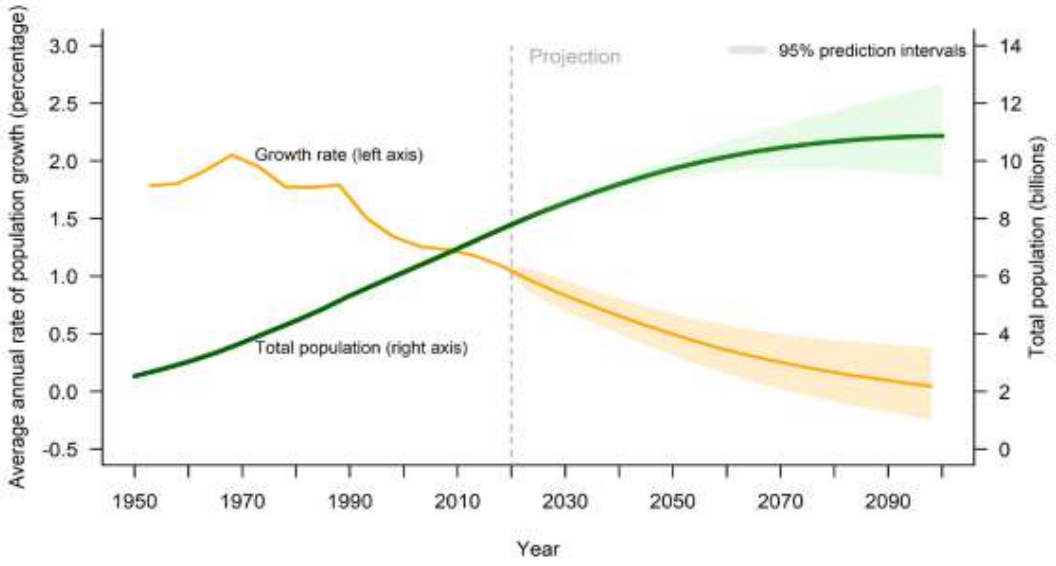

Figure 1.1: Population size and annual growth rate for the world: estimates 1950-2020, and medium-variant projection with 95% prediction intervals, 2020-2100. Source: [1].

that face significant challenges in creating a sustainable and self-supporting economy. There are currently 46 LDC countries, most of which are located in Africa and, to a lesser extent, South America and Asia/Oceania. As an example of an LDC country, Nigeria is afflicted with widespread malnutrition, and 44.1% of its people live below the poverty line. Additionally, Nigeria's population continues to grow, which increases demand on the country's struggling economy and infrastructure and contributes further to widespread poverty [1].

Transportation systems; sewage, water, and electric systems; good quality healthcare system, and communication networks are the infrastructure challenges in the least developed countries [2]. As proof of this situation, the novel coronavirus, COVID-19, has exposed the health system's fragility revealing persistent and deep inequities. In this context, information communication technology (ICT) and digital health figure prominently in this process. Multiple factors contribute to the promotion of ICT and digital health as supporters of service delivery innovation. These include, among others, the expansion of mobile phone availability and internet access in remote areas [3].

The connectivity challenges in remote areas are low return on investment, inaccessibility that obstructs deployment and regular maintenance of network infrastructures, and lack of favorable spectrum and critical infrastructure such as backhaul and power grid, respectively. Within this framework, beyond 5G technologies appear as a solution for wireless communication in remote areas offering massive connectivity in low-income countries [4]. Figure 1.2 presents a summary of the specific challenges and their possible solutions. More specifically, service accessibility in rural areas involves prohibitive deployment expenditures for network operators and requires high-capacity backhaul connections for several different use cases. Thus, high availability (from 99.9% to 99.999% of the time), increased data rate, cost-efficiency, easy-to-deploy, and scalability are essential in the upcoming 5G and beyond wireless networks in the backhaul framework [5].

Besides the current challenges in remote areas and the population growth, the increased use of new technologies such as the Internet of Things (IoT) and the introduction of new concepts as smart-cities areas leads to the increase of density in urban areas congesting the spectrum. Therefore, the need for technologies for backhaul and fronthaul in 5G and beyond systems arises to overcome the spectrum limitations, support many users, and deliver fast speeds. We can see this effect on the yearly increase in smart device use and, at the same time, the exponential increase in data traffic. Figure 1.3 estimates how the wireless data rates may increase in the next eight years. It shows that mobile traffic, with and without machine-to-machine (M2M) traffic, is

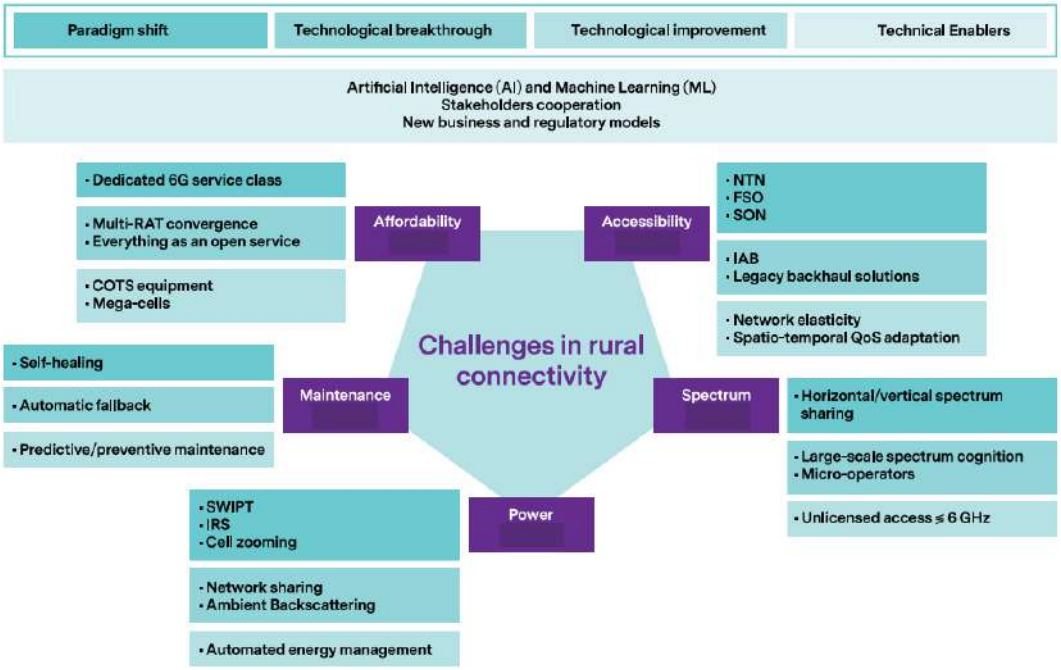

Figure 1.2: A summary of the challenges for providing wireless connectivity to remote areas with proposed solutions, source: [4].

expected to grow at an annual rate of around 50% in the next ten years. Since the current technologies are insufficient to satisfy such traffic and users, a significant improvement is necessary to meet such traffic requirements for urban areas, including high throughput, high availability and reliability, and very low latency [6].

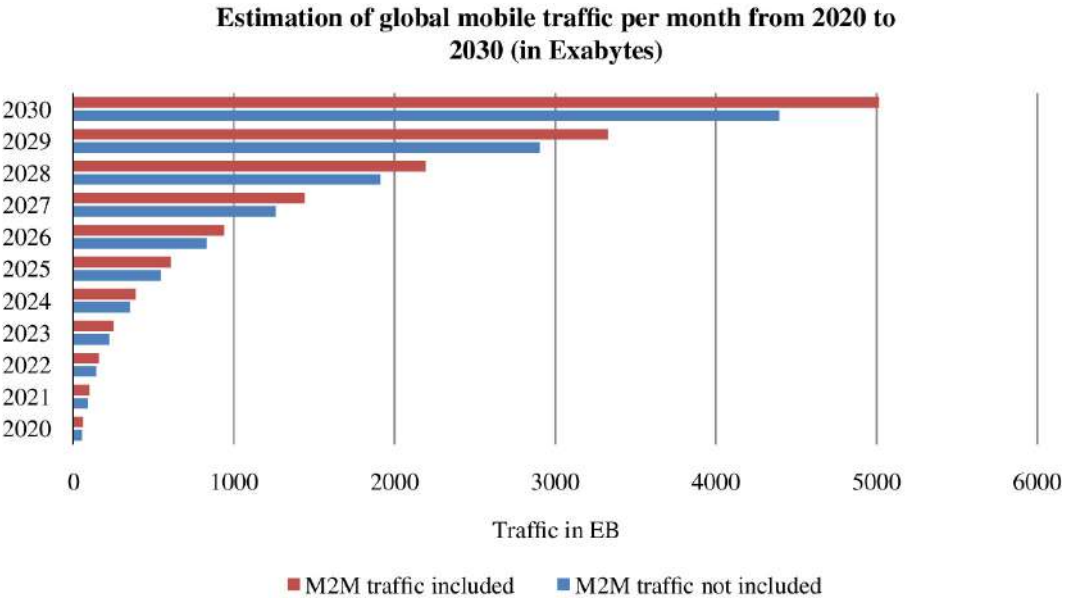

Figure 1.3: Estimation of global mobile traffic from 2020 to 2030, source: [6].

Therefore, in the next section, we discuss the technologies that can provide high data rate connectivity in outdoor environments.

1.2 Wireless system offering high data rate connectivity

There is now a wide variety of wireless connectivity systems, such as mobile cellular networks, wireless LAN, Bluetooth, ZigBee, ultra-wideband networks, Wi-Fi, satellite networks, and optical wireless communications. Specifically, for outdoor environments and high data rate connectivity, mmWave communications and Free-Space Optics (FSO), which refers to optical wireless terrestrial links, are the next-generation wireless technology options, reaching tens of Gpbs for paths up to a few kilometers [7]. This section describes both technologies, as well as their advantages and challenges. Since FSO and mmWave can be considered alternative or complementary, hybrid links using both technologies are also discussed.

1.2.1 FSO links

A current alternative to increase connectivity in isolated regions and overcome high-density urban areas, offering a high data rate, is the implementation of Optical Wireless Communications (OWC). OWC can be used either in terrestrial deployments (FSO), by placing optical wireless equipment on transmission towers as in the case of microwave links [6], or in satellite-to-ground communication [8][9][10]. FSO offers high throughput (i.e., up to 40 Gbps over a 4 km path under clear-air conditions [7]), fast deployment, low implementation cost, and maintenance compared to microwave equipment [8], besides the unlicensed operational frequency.

Although FSO technology is not new and has been studied since the 60s, there are still some gaps in the research of FSO, such as the prediction of the performance of the terrestrial FSO path under specific weather conditions, the lack of a global path loss model to use in the design stage, and the required characteristics of the equipment to deploy a particular link in a selected place.

FSO presents applications in multiple scenarios. For instance, Figure 1.4 exhibits the possible applications of FSO in mobile backhaul, connecting homes through fixed wireless links and bridging a base station to a small cell [11]. The latest, in turn, may use radio frequency (RF) with the Internet of Things (IoT) connectivity such as emergency response devices, smart agriculture, e-health services, unmanned aerial vehicles (UAVs) communications, communication to sensors, and industry in general. Another important application is Enterprise or Campus connectivity; as in Figure 1.5, FSO offers high security since laser transmissions travel alongside a line of sight path and, therefore, cannot be intercepted [12].

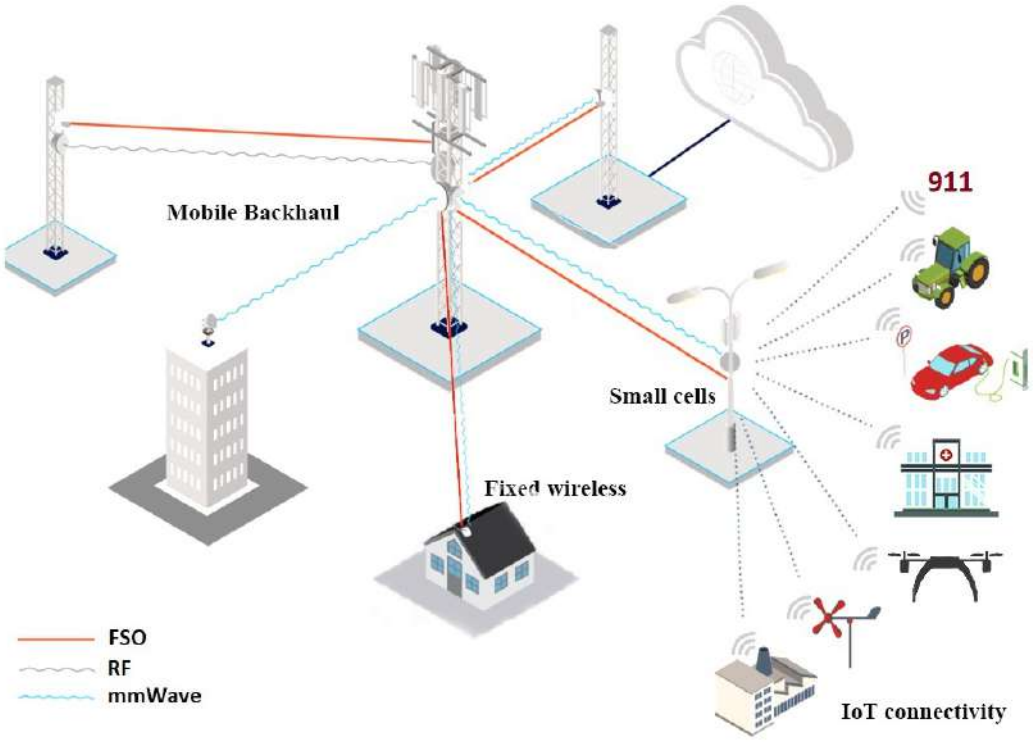

Figure 1.4: Possible applications of terrestrial FSO in the framework of 5G and beyond networks, part 1.

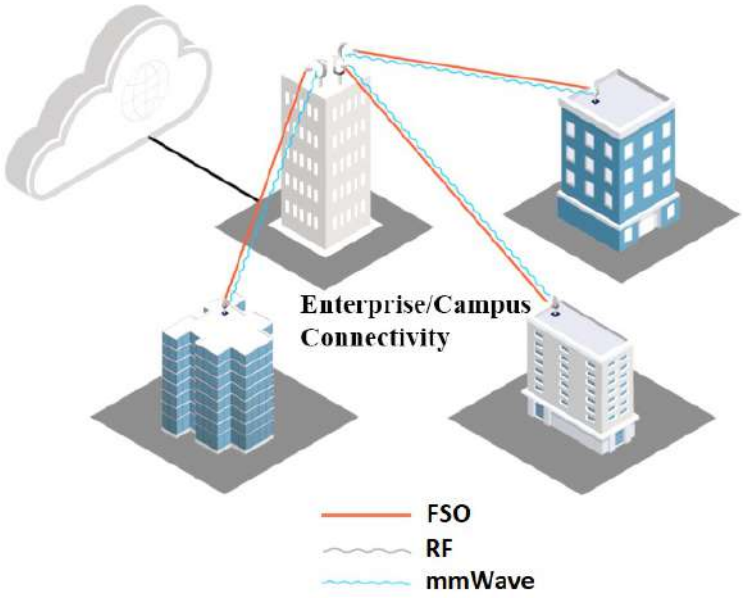

Figure 1.5: Possible applications of terrestrial FSO in the framework of 5G and beyond networks, part 2.

Although FSO has substantial advantages compared to RF links, it also presents some weak points that affect its performance. Environmental factors, atmospheric effects, and equipment instability impair the proper functioning of the terrestrial links [13]. We distinguish three classes: i) The propagation medium, i.e., the atmosphere; atmospheric effects include particle

scattering, gas absorption, clear-air turbulence causing scintillation; rain or snow occurrence can disturb the signal level at the receiver, and since FSO uses a laser to communicate between the transceivers, the impact of fog on visibility strongly affects the communication availability. ii) Equipment, as possible issues with the equipment instability can also cause a reduction in availability. iii) Environmental factors, all factors not directly related to i) and ii) but with an impact either on the atmosphere or on the equipment operation or both, e.g., solar radiation into the receiver, obstruction caused by machinery and trees and some other interfering objects as birds, misalignment due to wind loading, and, thermal effects on buildings.

One example of an FSO link is the link at 1.55 μm deployed at Leonardo Campus of Politecnico di Milano in Milan, Italy, operational from late 2018 to 2021. It uses commercial equipment modified to conduct scientific experiments over a path length of around 300 m. We study the behavior of this link later in Chapter 7, where we analyze actual experimental data from events of rain and fog occurrence under the presence of environmental effects such as solar radiation and beam misalignment due to wind. It has been found experimentally that the most relevant impairments causing signal fading are the fog occurrence and presence of isolated heavy rain events that cannot be countered by the link margin provided by the current equipment, significantly reducing the availability of the FSO path.

Regarding the demand for FSO in the global market, the global FSO communication market was valued at USD 940.89 million in 2021 and is expected to reach USD 14.3 billion by the end of 2031 [14]. The growing demand for FSO communication technology in the military and defense sectors and the increasing demand for high broadband connectivity are driving this growth of the FSO communication market. The bandwidth and security quality of FSO technology makes it an attractive communication network for the military sector. Besides, the Europe FSO communication market might witness a compound annual growth rate (CAGR) higher than 35% from 2021 to 2027 due to growing demand for high-speed internet and technological advancements across telecom and military sectors. The principal companies operating in the FSO communication market are AVDA Optical Networking SE, Airlinx Communications Inc, Collinear Networks, Excellence Networks, FSOna Networks, and Mostcom JSC.

On the other hand, using complementary technologies as a backup of FSO links is key to reaching high availability values comparable with those required in 5G and beyond networks [15]. Due to the relation between fog particles and the wavelength of mmWave technologies, the impact of low visibility caused by

fog on mmWave terrestrial links is negligible. However, rain droplets negatively impact the transmitted signal at mmWave frequencies because of the proximity between the wavelength and the drop size causing scattering and absorption of the signal. Thus, a mmWave terrestrial link parallel to the FSO one that backs it up may provide higher availability values than the FSO link alone. In this context, the following subsection presents a brief overview of mmWave terrestrial links as a solution for backhauling.

1.2.2 mmWave terrestrial links

It is expected that mmWave technology supports a very high data rate, up to multi-gigabits per second, benefiting from its large bandwidth [16]. MmWave provides low latency (i.e., milli-second), a considerable traffic density, and improved energy and cost efficiency [17]. MmWave cellular systems are expected to have highly directional antenna arrays to overcome high propagation loss. Besides, mmWave mesh networks can be used as a wireless backhaul for 5G to provide rapid deployment and mesh-like connectivity [18][6]. However, considerable path-loss and absorption due to air and rain and increased susceptibility to blockage compared to microwave are the highest challenges in the mmWave channel [19]. The Politecnico di Milano is currently studying the behavior of terrestrial links deployed at mmWave frequencies [20][21][22]. So far, the primary impairment to the proper functioning of the link has been the occurrence of rain episodes and its consequences as the wet antenna effect [22]. Although the propagating medium is also the free space, mmWave technologies do not use direct light to communicate between the terminals; then, low visibility occurrence is not an essential condition to deflect the signal and, in turn, reduce availability.

Therefore, a hybrid terrestrial link composed of an FSO path parallel to a mmWave one that backs each other depending on the occurrence of fog or rain is a promising proposal to keep the availability at the required figures for backhauling in the 5G and beyond systems [23].

1.2.3 Hybrid FSO/RF link

The objective of a hybrid FSO/RF or FSO/mmWave link might be to reach higher values of availability than using each of them as individuals by enabling one of the links as backup depending on the occurrence of a given atmospheric effect. For instance, assuming FSO as the principal link, there are two main cases: 1) rain occurrence and 2) fog occurrence. In the

former case, as the primary impairment against availability in mmWave and RF links is the rain, due to the relation between the size of the raindrops and the operational wavelength, the FSO link will work, providing the highest availability. In the former case, fog reduces visibility, and in turn, it causes a reduction in the optical received signal. Thus, enabling the mmWave path under these conditions might overcome the decrease in availability under severe weather conditions. Several studies have been developed concerning hybrid FSO/RF links in recent years; thus, we present some publications available in the literature.

In 2003, Akbulut, Ahmet, et al. [24] set up an experimental hybrid FSO/RF communication system in Ankara, Turkey, which was in operation for four months. During that period, the region suffered from severe snowstorms and fog, reducing the visibility and forcing the FSO link to stop transmission and switch to the RF. The links operated at 1.55 μm and 2.4 GHz for FSO and RF, respectively. The data indicated that the experimental link has been up to 99.986% of the operation time.

Three years later, in Greece, Kamalakis, Thomas, et al. [25] proposed a hybrid FSO/MMW outdoor link as a solution for broadband wireless access networks. They presented the hybrid system architecture for future systems and a brief overview of the planned trials. This paper highlighted the state-of-the-art of FSO at the time, and certain key design aspects, including the link budget. In [26], a hybrid FSO/RF link established in Austria was analyzed under weather phenomenons such as fog, rain, and snow. The link operated at 0.850μm and 40 GHz using the FSO path as the main link and the RF system as a backup. The range was 79.8 m. Based on their results on the availability of the FSO link, the 40 GHz link, and the hybrid system, they concluded that combining an FSO main link and an RF backup link is a viable solution to overcome the atmospheric attenuation.

Some designs and simulations related to the performance analysis of the hybrid link have also been researched. In [27], Zhang, Yang, et al. proposed, based on simulations, an RF link at 60 GHz as a backup, assuming a 500 m path. They suggest low threshold values depending on the atmospheric conditions (fog and rain attenuation) to switch from one link to the other. Kolka, Zdeněk, et al. in [28] designed an experimental hybrid system working at 0.850 μm, 1.55 μm in FSO, and 122 GHz in RF, with an 800-m link using an ON/OFF Keying (OOK) modulation. Based on the conclusions obtained in [28], Touati, Abir, et al. [29] explored the effects of combined atmospheric fading and misalignment on the behavior of an FSO link using OOK modulation. Their results showed that the degradation of the FSO link

under combined fading affects the behavior of the hybrid FSO/RF link. For low SNR, the hybrid FSO/RF system performs better than FSO alone and may be more resistant to such conditions ensuring good performance [29].

Although some studies related to the performance of hybrid FSO/RF links affected by weather events have been documented in the literature review, few considering the atmospheric turbulence were founded. For example, in [30], when the primary link (FSO) is under atmospheric turbulence, the secondary one maintains connectivity. The authors also derived analytical expressions for outage probability and average BER by modeling the RF fading with Rayleigh statistics and the atmospheric turbulence-induced FSO fading with gamma-gamma statistics. In this work, the hybrid FSO/RF-FSO system achieved improved outage and BER performances compared to the FSO-only system in all weather conditions.

Therefore, the idea of a hybrid FSO/RF should be studied in the future since the availability might increase up to around 99.986% [24], which is one of this link's advantages. The combination of an FSO as the main link and an RF as a backup link provides a viable solution to overcome the atmospheric attenuation [26]. Furthermore, for low SNR, the hybrid FSO/RF system performs better than FSO alone and may be more resistant to severe weather conditions ensuring good performance [29]. Finally, the hybrid RF/FSO is a cost-efficient solution and a good candidate for upgrading existing backhaul networks [23].

1.3 Structure of the work

After this introduction, an analysis of global surface meteorological data is carried out in Chapter 2, considering four sources of measurements around the world. We find that the Wyoming University repository gives the framework to build the models of fog and rain attenuation on FSO after comparing visibility measurements in places with more than one data source. Moreover, the analysis provides worldwide information about the relative frequency of the significant propagation impairments such as fog, rain, snow, and sand. At the end of this chapter, we present in maps the total percentage of time that fog, rain, and snow reduce visibility lower than 1 km in Europe; and the total percentage of time that fog reduces visibility less than a given threshold in South America. We conclude that fog and rain are the main effects we should consider in our attenuation study on FSO links.

The attenuation due to fog on FSO links is studied in Chapter 3, considering the wavelength dependence of the models and transmission measurements

found in the literature. The model based on fog micro-physics is studied at different wavelengths to provide a theoretical validation of the γ-V models using an extensive database of 54 PSDs of fog and haze, including recent measurements. After that, we estimate the link range considering fog microphysics at mid-IR (10.6 μm) and near-IR (1.55 μm), relying on data from state-of-the-art particle sensors collected during radiation fog at mid-latitude continental climate. Moreover, we propose a new version of the well-known Kim model to obtain the extinction coefficient of fog as a function of visibility, named a *lower bound model*. In contrast, an *upper bound model* is identified considering visibility thresholds to fit better the outcomes of micro-physics of fog. Finally, we present the analysis of the uncertainties in the conversion from visibility measurements into the extinction coefficient of fog.

The study of attenuation caused by rain is relevant for the FSO availability in locations where the occurrence of rain is statistically relevant. Thus, this effect on FSO is analyzed in Chapter 4. First, we present and apply the rainfall rate estimation proposed by the ITU recommendation for a few locations. Then, we study the rain attenuation models available in the literature for microwave frequencies considering modifications for FSO frequencies. After that, we put side-by-side the attenuation obtained using models based on micro-physics of rain droplets and the attenuation due to rain estimated by the available visibility measurements. At the end of this chapter, we study the gain in attenuation when the multiple scattering effects caused by rain droplets are considered.

Since the occurrence of different weather conditions causes a reduction in visibility, then additional losses are perceived by the optical receiver. Thus, Chapter 5 presents a method to combine the attenuation statistically on FSO caused by different conditions using as input the Wyoming university repository studied in Chapter 2, and the rainfall rate estimation presented in Chapter 4. The proposed method is illustrated using flux diagrams, and each step is explained afterward. Specifically, we take into account four weather conditions: (i) rain, (ii) fog, (iii) other weather conditions different from fog or rain, and (iv) non-tagged conditions (corresponding to samples without an available label). We use the power-law model with the multiple scattering effects to estimate the attenuation due to rain. In contrast, we apply the lower bound model of the γ-V conversion proposed in Chapter 3 for the other conditions.

The performance of FSO links is studied in terms of the maximum link distance in Chapter 6. First, we use the power budget equation to relate the atmospheric attenuation with the attenuation caused by geometric beam-

spreading and the system losses caused by the equipment parameters. After that, we find the link range as a function of availability by solving the power budget expression. We take into account four conditions: (i) rain only, (ii) fog only, (iii) fog and rain, and (iv) fog, rain, neither fog nor rain, and non-tagged conditions. For the case of fog, we apply the lower bound model proposed in Chapter 3 to calculate the attenuation. In contrast, we consider the power-law model with the multiple scattering effects to estimate the rain attenuation as presented in Chapter 4. Finally, the method shown in Chapter 5 is applied here to calculate the attenuation for combined conditions: (iii) and (iv).

As an example of an implemented FSO link, we present the link available at Leonardo Campus of Politecnico di Milano in Milan, Italy, in Chapter 7. The 300-m link has two channels: the information channel at 1.55 μm and the service channel at 0.785 μm. Moreover, parallel to the FSO link, there is a mmWave link designed in the Huawei Microwave Centre of Milan operating at D-Band and E-band frequencies (i.e., 148 and 73 GHz). Thus, before presenting side-by-side the measurements carried out by the available equipment, we also describe the characteristics of the mmWave link. After that, available measurements of the received signals and experimental data of ancillary equipment (i.e., sonic anemometer and disdrometer) have been processed. Finally, we select atmospheric events detected by the links, as multiple case studies, from March 2019 to December 2020. We also classify them according to the studied atmospheric effect: stratiform rain, convective rain, light rain, wind, heavy fog, snow, and others.

The conclusions section and the future work are withdrawn in the last chapter, Chapter 8, followed by the references and the appendixes cited in the text.

1.4 Original contributions

The contributions of this thesis can be summarized as follows:

1. Analysis of global surface meteorological data.

2. Setting up an empirical model for path loss of FSO due to fog valid on a global scale.

3. Extension of the rain attenuation models for microwave frequencies considering modifications for FSO frequencies.

4. Setting up a method, valid on a global scale, to statistically combine the attenuation effects on FSO links caused by different weather conditions.

5. Assessment of the performance of FSO links in terms of the maximum link distance against availability under four weather conditions: (i) rain only, (ii) fog only, (iii) rain and fog, and (iv) rain, fog, and conditions different from rain and fog.

6. Analysis of experimental events for the FSO and mmWave links implemented at Leonardo Campus of Politecnico di Milano, classified depending on the studied atmospheric effect: stratiform rain, convective rain, light rain, wind, heavy fog, snow, and, others.

2
Analysis of Global Surface Meteorological Data

The current lack of a global path loss model for designing FSO links motivates the study of the optical link's behavior under different atmospheric conditions. This chapter considers available databases of surface meteorological parameters that will be the basis for predicting attenuation statistics in FSO links. First, we describe and evaluate the available long-term data, particularly visibility data, since the reduction in visibility in the propagation path is one of the major causes of attenuation in optical links. Then, we compare visibility measurements in places with more than one data source. Finally, we analyze the occurrence worldwide of fog, rain, snow, smoke, and sand and conclude that fog and rain are the main effects we should consider in our study.

2.1
Available databases

We consider surface meteorological data measurements in different locations to be able to predict the FSO link behavior under various atmospheric conditions. Low visibility is particularly interesting since it strongly affects the optical signal strength when fog occurs. The measured meteorological data have been obtained from four sources: the University of Wyoming repository and the National Oceanic and Atmospheric Administration (NOAA) in the U.S.; the Centre for Environmental Data Analysis (CEDA) in the U.K.; and the Brazilian Airspace Control Department (DECEA).

Although the method used to acquire the visibility data at each location is not specified in the databases, we assume that for the U.S. and U.K. databases, the visibility was measured using a forward scatter detector, including an emitter and a receiver. The transmitter emits an infrared light beam at an offset angle from the receiver. The visibility range is calculated from the extinction coefficient, determined by the amount of light scattered by particles in the air and detected by the receiver. In the case of the Brazilian data (i.e., DECEA), the visibility was estimated by human observations [31] [32]. Table 2.1 lists the relevant characteristics of the sources. The following subsections present brief descriptions of each database.

Table 2.1: Databases characteristics.

Database	Wyoming	NOAA	CEDA	DECEA
Location	Around the world	The U.S.	The U.K.	Brazil
Processed sites	>730	2	1	5
Data records	Visibility (km) Temp. (°C) Pressure (hPa) Dew point (°C) Rel. hum. (%) W. dir. (°) W. sp. (m/s) Clouds tag Weather tag	Ex. Coef W. dir. (°) W. sp. (m/s)	Visibility (km) Temp. (°C) Pressure (hPa) Rel. hum. (%)	Visibility (km) Precipitation (mm/h) Pressure (hPa) Temp. (°C) Rel. hum. (%) W. sp. (m/s)
Sampling rate (aprox.)	30 min - 1 h	1 min	1 min	30 min - 1 h
Period	1997 - 2021	1997 - 2020	2010 - 2017	1997 - 2020

2.1.1 University of Wyoming repository

Surface data are acquired in airports worldwide with a sampling time of 30 or 60 minutes. For some locations, the data are available from 1997 until the present. The database provides relative humidity, atmospheric pressure, temperature, visibility, and cloud-type measurements. The range of visibility data is from 0.0 km to 10 km [33].

2.1.2 National Oceanic and Atmospheric Administration (NOAA)

The data are acquired in multiple stations in the U.S. by the Automated Surface Observing System (ASOS). ASOS program is a joint effort of the National Weather Service (NWS), the Federal Aviation Administration (FAA), and the Department of Defense (DOD). The ASOS systems serve as the nation's primary surface weather observing network [34]. It is designed to support weather forecast activities and aviation operations while supporting the needs of the meteorological, hydrological, and climatological research communities. Data are available from 2000 to 2020, providing extinction coefficient measurements, wind velocity, and direction with a sampling time of 1 min. The visibility V(km) can be obtained from the measured extinction coefficient c. The range of visibility data is from 0.05 to 100 km [34].

2.1.3
Centre for Environmental Data Analysis (CEDA)

The CEDA Archive is the national data center for atmospheric and earth observation research in the U.K. It hosts over 15 Petabytes of surface data [35]. Sources include aircraft campaigns, satellites, automatic weather stations, and climate models. Experimental data are acquired in the countryside of the U.K., specifically in Cardington, with a sampling time of 1 minute. The data are available from 2006 to 2017. It includes visibility, wind velocity and direction, and relative humidity measurements. The range of visibility data is from 0.0 to 100 km [35].

2.1.4
Brazilian Airspace Control Department (DECEA)

The Department of Airspace Control (DECEA) is responsible for managing all the activities related to the safety and efficiency of Brazilian airspace control. Its mission is to manage and control the air traffic in the Brazilian sovereign airspace and guarantee its defense [32]. They provide surface measurements acquired in Brazilian airports. Data are available for Brasilia, Manaus, Rio de Janeiro, São Paulo, and Porto Alegre with a 1-hour sampling time from 1990 to 2020. The database includes visibility, wind velocity, temperature, relative humidity, pressure, and precipitation measurements. The range of visibility data is from 0.1 to 20 km [32].

2.2
Data reduction

This section explains how the raw data provided by each database have been processed to obtain the statistics of interest. We use the Matlab software since it contains predefined functions that offer tested and prepackaged solutions to primary technical tasks, such as statistics subroutines. It is essential to keep in mind that the structure of the files is different depending on the sources. Thus, the information delivered by each of them has been processed individually. However, we follow a general procedure to obtain CCDFs of visibility in every desired location.

1. **Step 1:** The raw data of the desired or available location are downloaded from the respective source and imported in Matlab, one file at a time. In the case of NOAA, a monthly file is downloaded. For CEDA and Wyoming databases, it is obtained as a daily file; finally, in the case of the Brazilian database, DECEA, a single file is provided containing all the information required.

2. **Step 2:** We define a magnitude range of each measured quantity to be considered *valid* for our purposes. These ranges are based on the information gathered from the source sites and direct communication to the database's responsible staff.

3. **Step 3:** Based on the previous step, we identify outliers in the measurement data, and those figures are classified as *invalid*.

4. **Step 4:** We create and save daily metadata files containing a preprocessing version of the valid raw data.

5. **Step 5:** Once the data is validated in terms of outliers and the metadata files have been produced. We continue processing the valid samples, grouping the data into three different types of .mat files to facilitate processing in the following stages. These are the types of .mat files:

   – annual files.
   – monthly files.
   – all available samples in one file.

6. **Step 6:** After that, the CCDF of visibility of each type of classification is calculated and saved in a corresponding file with the metadata files.

7. **Step 7:** For the data from the Wyoming University repository, an additional step has been considered before calculating the CCDF, it is a *timestamp classification* depending on the presence of a given weather occurrence tag (e.g., fog, rain, snow, haze, sand among others) , as we will explain deeply later in Section 2.5.

8. **Step 8:** Finally, an evaluation of all the data is carried out as we describe in the next section.

2.3 Databases Evaluation

This section analyzes data quality from each source regarding the expected number of samples, valid years, and percentage of valid samples to define criteria to exclude unreliable data.

2.3.1 University of Wyoming repository

As shown in Table 2.1 in the previous section, the Wyoming University repository provides data from 730 locations, the highest quantity of sites to be processed in this work. We define the conditions to discard (and keep) a given station and assess the available data for this database in Appendix A. After the evaluation of 731 locations based on these criteria, we keep 593 (81%) stations from the Wyoming University repository. Thus, 137 (18.7%) stations need to be discarded: 70 sites (9.6%) present lower than 100.000 samples, and 67 locations (9.1%) present seven or fewer years classified as valid. We also find that 90% of the years are valid (i.e., 23 years) in 430 (59%) stations. In 657 (90%) places, at least 20% of the years (i.e., 5 years) have been considered valid.

2.3.2 NOAA database

Regarding the NOAA database, the percentage of valid visibility data is between 87% (for New York City) and 93% (for Sacramento). The quantity of valid samples per year is higher than 400.000, except for 2013 in NYC, which is around 200.000. There are more than 100.000 samples for both locations. That is, the minimum quantity of samples to find a statistically valid value for the visibility exceeded 99.99% of the time, and more than 85% of the samples were valid. Thus, we decide to keep both locations.

2.3.3 CEDA database

The percentage of valid visibility data for Cardington in the U.K. is 98.7%, and the quantity of valid samples per year is higher than 500.000. Thus, we decide to keep the database of this location.

2.3.4 DECEA database

The percentage of valid visibility data for the locations in Brazil ranges between 98% and 99.9% of valid samples. In Brasilia's database, more than 35% of samples for 2005 and 2006 are invalid. For the other locations, the quantity of valid samples per year is higher than 300.000, which is around 99% of valid samples. Therefore, we decide to keep all the databases but pay special attention to the case of Brasilia.

2.4 Multiple sources evaluation

To evaluate the consistency of data for the locations where we have information from multiple sources, we set the CCDFs of visibility obtained from the Wyoming University repository and another source (referred to as *the principal station*). For cases where experimental measurements are unavailable in the Wyoming database for the exact same location, the comparison is made with the Wyoming data at the nearest location. Before calculating the CCDFs, we selected the visibility samples corresponding to the identical timestamps in both sources.

2.4.1 NOAA database and Wyoming University repository

In New York City, the principal station is located in Central Park (designated as NYC). Since there is no available data for the same site from the Wyoming source, three additional places have been considered: John F. Kennedy International Airport (JFK), LaGuardia Airport (LGA), and Newark Liberty International Airport (EWR), as presented in Figure 2.1. We take the timestamps without outliers so that the same quantity of samples at the same timestamp are considered when the CCDF is calculated. The closest Wyoming station to NYC is LaGuardia Airport, at a distance of approximately 9 km. Figure 2.2 shows the respective CCDFs of visibility for the four sites of interest.

We obtain the visibility value at a given percentage of time for each CCDF to have a quantitative reference of the difference among them. The results are listed in Table 2.2. The closest location (LaGuardia Airport) presents the lowest difference to the main station in Central Park, whereas we find the highest distinction in JFK Airport. That may be due to the long distance between the measurement locations and JFK airport's surrounding environment, as it is located in a coastal area.

Table 2.2: Visibility (km) at a given percentage of time from the CCDFs obtained using data from two databases: NOAA database and Wyoming university repository, New York City.

Location - Source	**99%**	**99.9%**	**99.95%**
Central Park (NYC) - NOAA	1.93	0.45	0.31
John F. Kennedy (JFK) - Wyoming	0.48	<0.10	<0.10
La Guardia (LGA) - Wyoming	1.53	0.39	0.22
Newark Liberty (EWR) - Wyoming	1.50	0.38	0.10

There are available measurements from both sources for Sacramento airport, and we also consider Wyoming data recorded in Sacramento Metropolitan

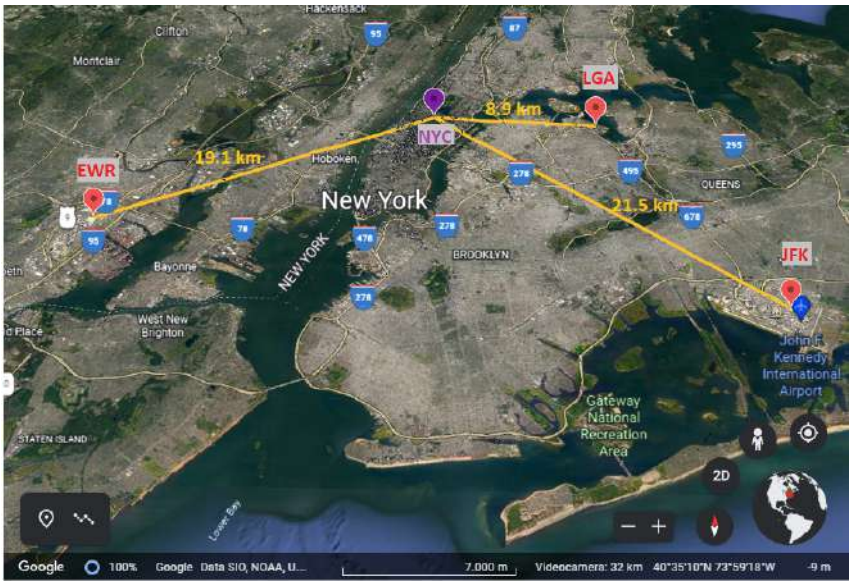

Figure 2.1: Locations of the stations considered in New York.

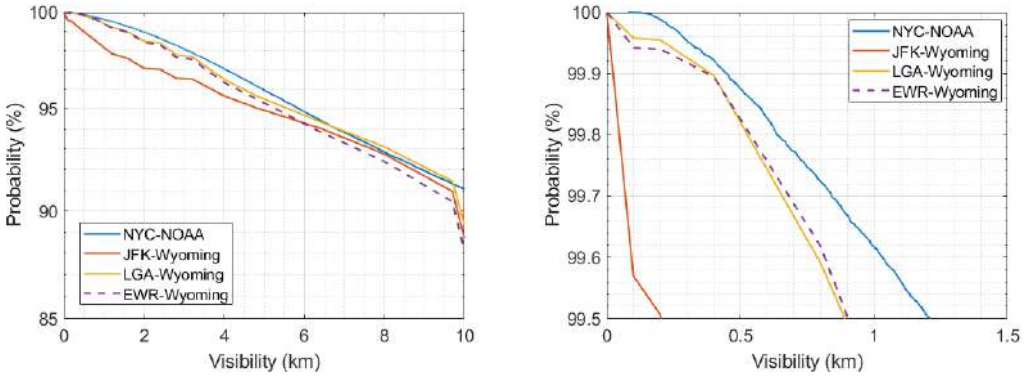

Figure 2.2: Comparison of CCDF calculated with visibility data from two sources: NOAA database and Wyoming University repository considering three locations near the main station in Central Park.

Field (SMF) as presented in Figure 2.3. It is essential to keep in mind that the precision of the location indicated on the map is around 1 km since the coordinates are given in decimals with a precision of 0.01; thus, we lack more precise information about the stations' location. Table 2.3 lists the visibility in km at a specified percentage of time for the sites near Sacramento Airport. Although the location precision explains the difference in distance between the stations of NOAA and Wyoming, we assume both sources are located in the same airport. However, the visibility discrepancy at a given time may be due to the sensors employed to carry out the measurements, as the information about the measurement procedure and the used sensors are unavailable.

Table 2.3: Visibility (km) at a given percentage of time from the CCDFs obtained using data from two databases: NOAA database and Wyoming university repository, Sacramento.

Location - Source	**99%**	**99.9%**	**99.95%**
Sacramento Airport (SAC) - NOAA	0.37	0.12	0.10
Sacramento Airport (SAC-W) - Wyoming	0.75	<0.10	<0.10
Sacramento Metropolitan Field (SMF) - Wyoming	0.67	0.21	0.13

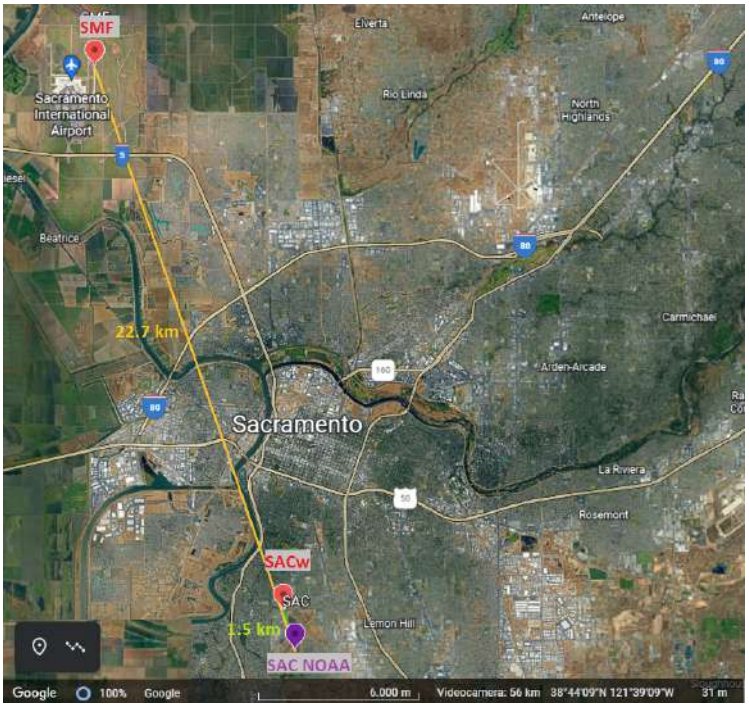

Figure 2.3: Locations of the stations considered in Sacramento.

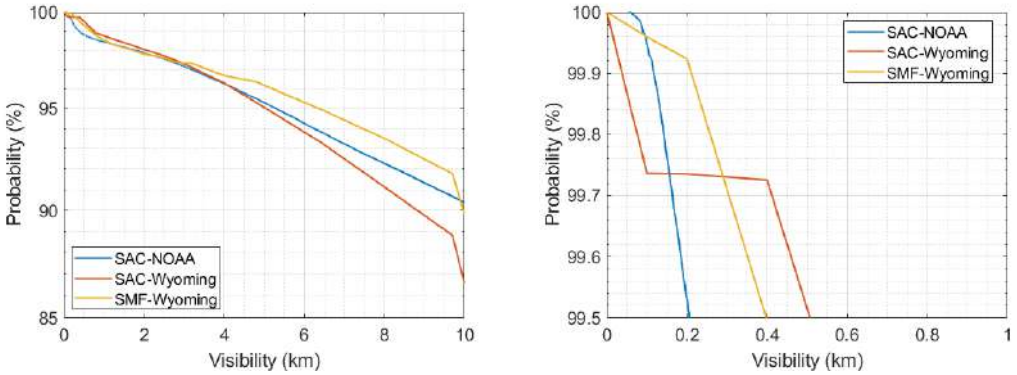

Figure 2.4: Comparison of CCDF calculated with visibility data from two sources: NOAA database and Wyoming University repository considering two locations near the main station in Sacramento.

2.4.2 DECEA database and Wyoming University repository

Surface data from the Wyoming repository are available in the same five locations provided by the Brazilian source, DECEA; these places are Galeão Airport in Rio de Janeiro, Guarulhos Airport in São Paulo, International Airport of Brasilia, Salgado Filho Airport in Porto Alegre, and Eduardo Gomes International Airport in Manaus. A pair of CCDF functions of visibility is obtained for each airport; one is obtained from the Wyoming data and the other from DECEA data for the same measurement period: 1997 - 2020 and the identical timestamps.

Figures 2.5, 2.6, 2.7, 2.8 and 2.9 present CCDF curves of visibility from both sources for airports in São Paulo, Rio de Janeiro, Brasilia, Manaus, and Porto Alegre, respectively. Visibility values are also obtained for each couple of curves, assuming three figures of percentage of the time; the results are listed in Table 2.4. The values obtained from the calculation using the Wyoming data agree with their respective value estimated from DECEA data. An exception occurs in the Brasilia airport. In this case, the visibility values obtained from the Wyoming source could double the ones from DECEA at very high values of percentage of the time. It may be due to an error in the timestamps record, specifically, the lack of samples compared to the Wyoming database, as reported in Section 2.3.4, or the measurements are taken from two different sensors located in the same airport.

Table 2.4: Visibility (km) at a given percentage of time from the CCDFs obtained using data from two databases: DECEA database and Wyoming university repository.

Location - Source	**99%**	**99.9%**	**99.95%**
São Paulo - DECEA	0.80	0.12	0.09
São Paulo - Wyoming	0.81	0.13	0.10
Rio de Janeiro - DECEA	3.01	0.55	0.21
Rio de Janeiro - Wyoming	3.00	0.58	0.25
Brasilia - DECEA	3.01	0.55	0.22
Brasilia - Wyoming	4.08	0.90	0.51
Manaus - DECEA	1.51	0.33	0.23
Manaus - Wyoming	1.53	0.36	0.26
Porto Alegre - DECEA	0.85	0.13	0.11
Porto Alegre - Wyoming	0.86	0.15	0.12

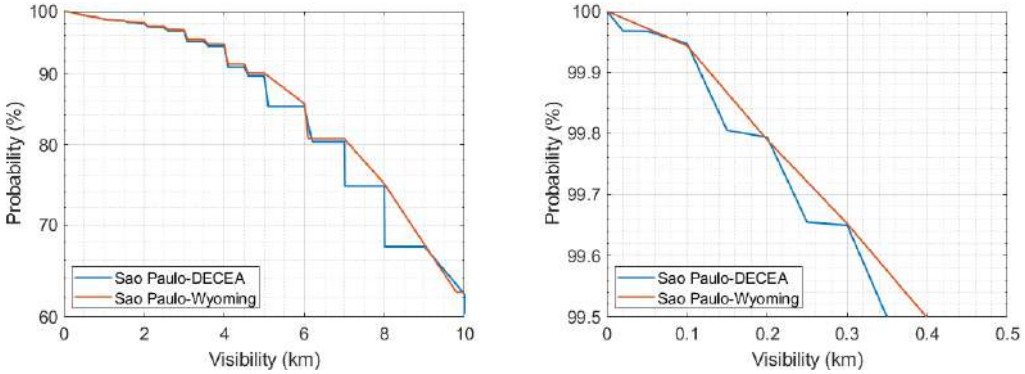

Figure 2.5: Comparison of CCDF calculated with visibility data from the DECEA database and the Wyoming University repository for Guarulhos Airport in São Paulo.

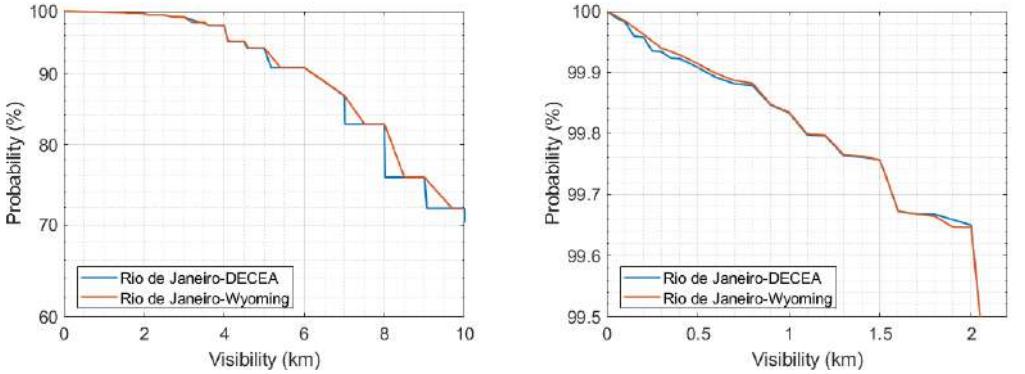

Figure 2.6: CCDF calculated with data from the DECEA database and the Wyoming University repository for Galeão Airport in Rio de Janeiro.

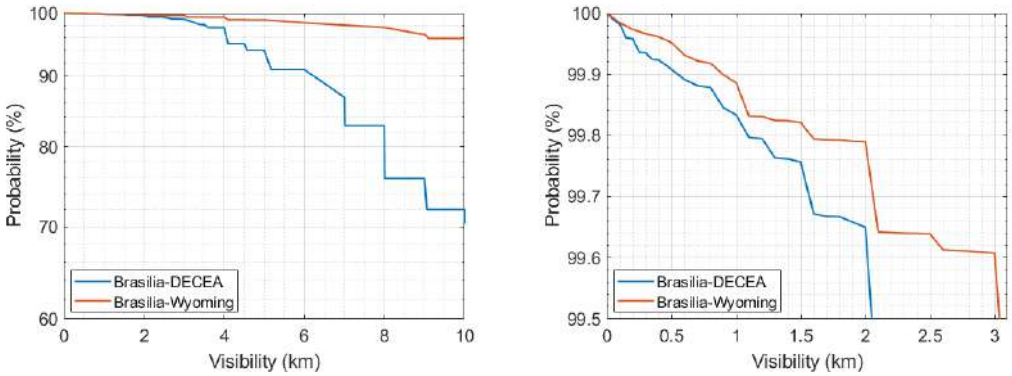

Figure 2.7: CCDF calculated with data from the DECEA database and the Wyoming University repository for the International Airport of Brasilia.

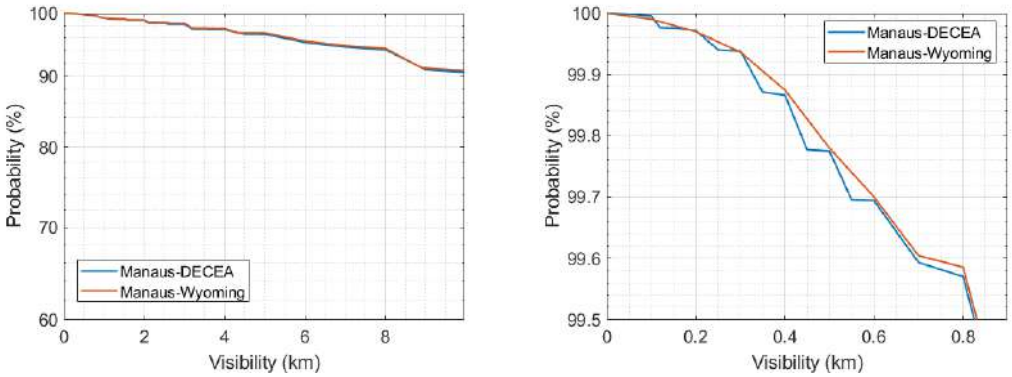

Figure 2.8: CCDF calculated with data from the DECEA database and the Wyoming University repository for Eduardo Gomes International Airport in Manaus.

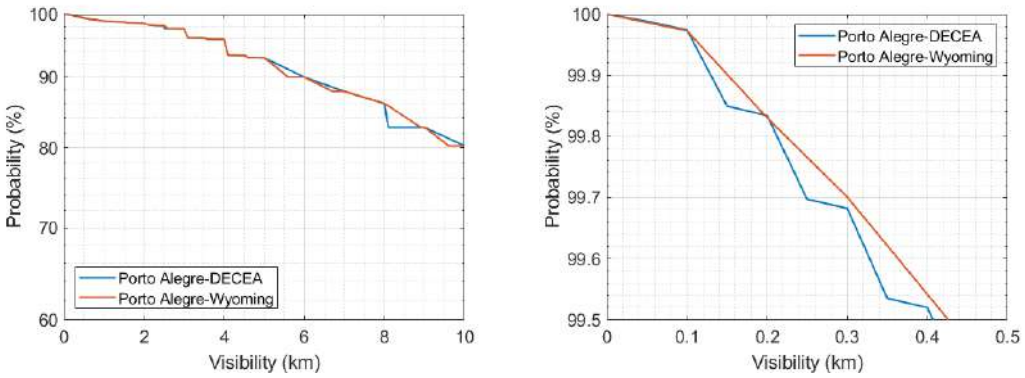

Figure 2.9: CCDF calculated with data from the DECEA database and the Wyoming University repository for Salgado Filho Airport in Porto Alegre.

2.5 Weather occurrences

We use the information on weather conditions to identify the critical atmospheric variables we should consider to build propagation models. Specifically, we use the METAR Decoder Key [36] to relate the weather tag in the Wyoming University data to one of the defined data classes of weather occurrence. Each daily file of the Wyoming repository contains, at each timestamp, a label related to weather conditions. We define 13 *cases* or *filter classifications* as presented in Table 2.5.

The filter classification is described as follows. On the one hand, the four first cases in Table 2.5 correspond to the occurrence of fog. Case 2 includes fog or mist occurrence and rain presence, whereas Case 3 refers to fog or mist occurrence under the presence of snow. Suspended water particles reducing visibility belong to Case 4, which means fog or mist without rain or snow. Finally, Case 1 includes all tags referred to as fog with and without precipitation; (it is the occurrence of a label included in Cases 2 or 3, or 4). On the other hand, Cases 5, 6, and 7 consider rain occurrences. Specifically, Case 5 includes only rain (considering the labels for different intensities, i.e., drizzle and thunderstorm) without considering another atmospheric effect. Case 6 includes rain and another atmospheric effect different from fog or mist (because those cases are already in Case 2). Finally, Case 7 refers to all tags of rain: Cases 5 or 6. Cases of snow occurrence, considering different intensities, are included in Case 8. It is important to highlight that snow and rain occurrences together are classified as Case 6, whereas Case 3 consists of the occurrence of snow and fog or mist. Case 9, 10, and 11 classify the occurrence of more specific atmospheric conditions, such as hail, smoke or haze, and sand, respectively.

Table 2.5: Filter classifications for different atmospheric effects.

Case ID	Atmospheric effect filter	Tag
1	Fog or mist (It includes Case 2, Case 3 and Case 4)	'FOG'
2	(Fog or Mist) + Rain	'FGRN'
3	(Fog or Mist) + Snow	'FGSN'
4	Suspended particles that are water	'SW'
5	Only rain or drizzle or thunderstorm	'RAIN'
6	Rain or drizzle or thunderstorm with all mixed situations involving rain (hail, snow)	'RNAll'
7	Rain or drizzle or thunderstorm and also, all possible mixed situations (It includes Case 5 and Case 6)	'RNMix'
8	Only snow	'SNOW'
9	Hail	'HAIL'
10	Smoke and haze	'HAZE'
11	Sand	'SA'
12	Other	'OTHER'
13	All conditions not tagged before	'UC'

Lastly, we recognized exceptional events of atmospheric conditions as different from previous cases in Case 12, for instance, volcanic ashes presence. Finally, Case 13 includes conditions not specified in any case before. The weather occurrence classification is developed to identify the dominant or prevailing factors (in statistical terms) that affect FSO path loss. Then, using the Wyoming database, the studied locations worldwide are sorted based on the percentage of occurrence of the following main weather conditions: fog, rain, and snow.

Fog occurrence

The top panel in Figure 2.10 presents the top 30 stations with the highest percentages of fog occurrence out of the almost 600 locations considered in this study. Fog is considered in Case 1 of the filter classification explained, i.e., all suspended particles that are water or simultaneous occurrence of fog (or mist) and rain or simultaneous event of fog and snow (see Table 2.5). The percentage of fog occurrence is calculated as the ratio between the number of samples classified as Case 1 and the total samples available for a given station.

An interesting point is that the three airports close to Milan city are in the top 30. The bottom panel in Figure 2.10 indicates the distribution of fog occurrence (in percentage), considering all the valid stations. Almost 50% of the stations present up to 6% of fog occurrence, whereas more than 10% of the

studied locations can reach more than 15% of fog occurrence labels. Moreover, almost 70% of the studied stations present at least 3% of fog occurrence, that is about ten days in a year; therefore, considering the large values of optical attenuation produced by fog, we can conclude that fog is a key factor in most locations around the world that we must consider during the design stage of terrestrial links.

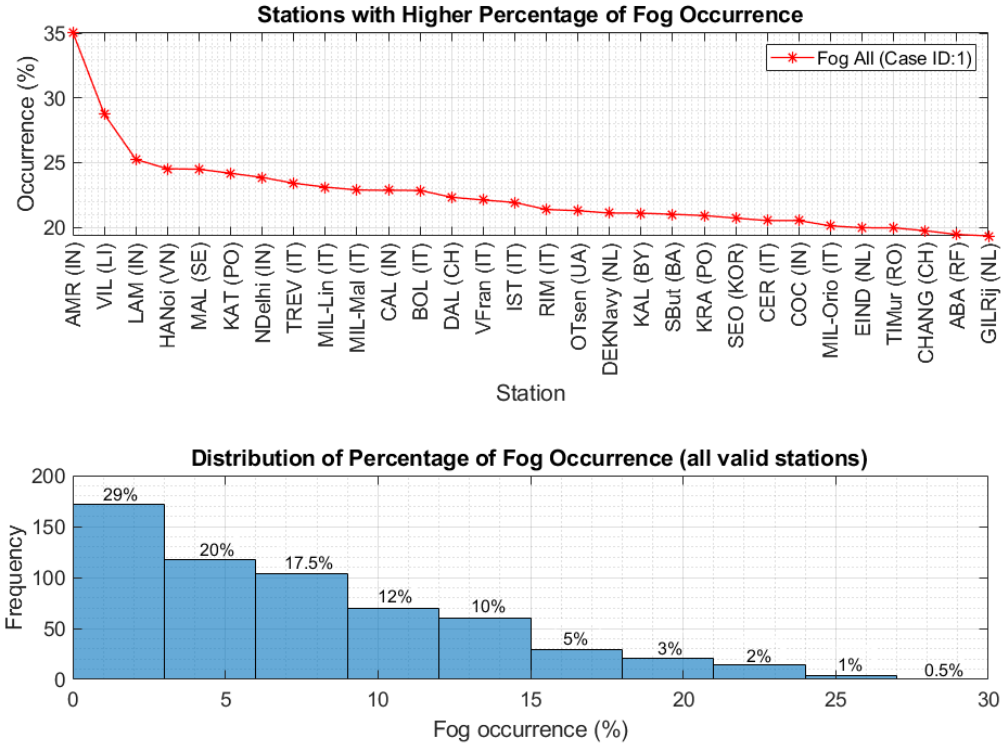

Figure 2.10: Percentage of fog occurrence figures, top: the top 30 stations with the highest rates of fog occurrence, bottom: distribution of the percentages of fog occurrence.

Rain occurrence

A similar analysis was carried out for rain. The top panel in Figure 2.11 shows the top 30 locations worldwide, among the 600 studied, with the highest percentages of rain occurrence. The bottom panel in Figure 2.11 presents the distribution of the percentages of rain occurrence when all stations are considered. 50% of the studied stations show at least 6% of rain occurrence labels (20 days per year). In other words, 50% of the locations have less than 6% rain occurrence. In comparison, more than 10% of the studied sites can reach more than 10% of rain occurrence labels. Moreover, almost 70% of the studied stations presents at least 3.3% of rain occurrence, about twelve days a year. Thus, given the frequency of rain occurrence worldwide, we conclude that

rain is more frequent than fog worldwide, but it is not as challenging in terms of attenuation. The relative impact in statistical terms must be quantified by comparing the corresponding CCDFs of attenuation.

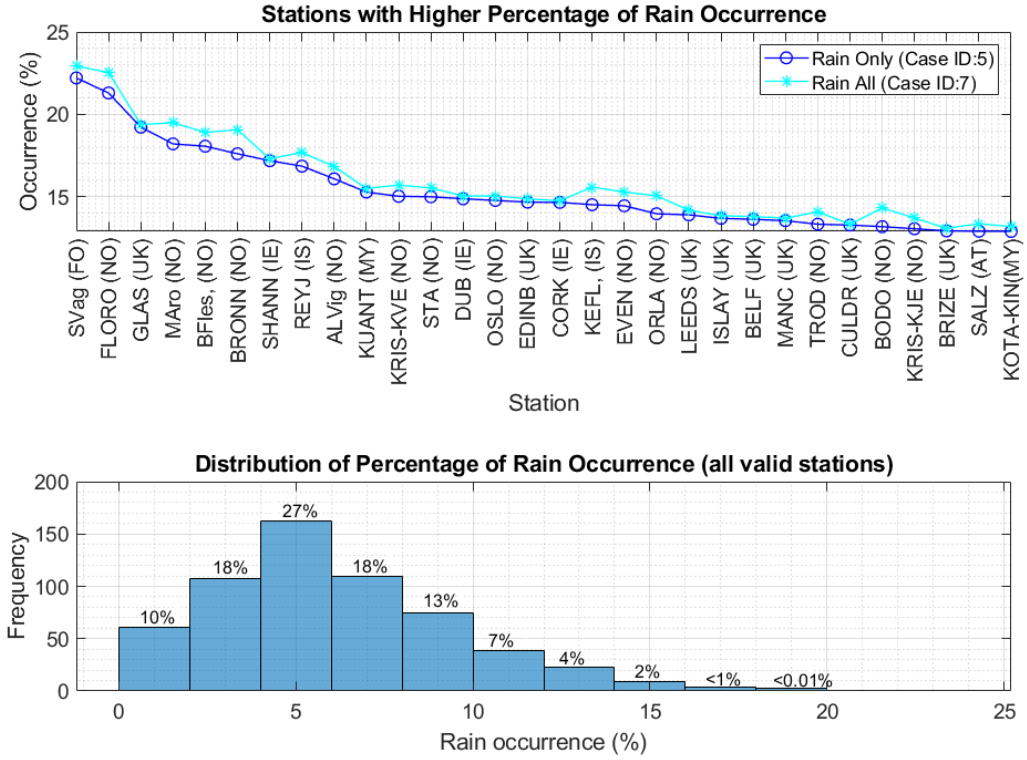

Figure 2.11: Percentage of rain occurrence figures, top: the top 30 stations with the highest percentages of rain occurrence, bottom: distribution of the percentages of rain occurrence.

Snow occurrence

The top panel in Figure 2.12 shows the top 30 locations worldwide, among the 600 studied, with the highest percentages of snow occurrence. Opposite to fog occurrence, only 30% of the studied locations showed a rate of snow occurrence higher than 2% of the time, about seven days a year (see the bottom panel in Figure 2.12). Anyway, it is also essential to study the snow effect on visibility reduction because there are many places where snow is the main atmospheric effect, as presented in Figure 2.12. Besides, areas near the poles, in northern Europe, such as Oulu, Finland, locations with a mid-latitude climate, such as Paris or Milan, or even high-latitude sites such as La Paz, Bolivia (see Figure 2.13), have also an impact on visibility reduction caused by snow presence. However, the snow effect on FSO is challenging due to the random nature of the particle parameters [37].

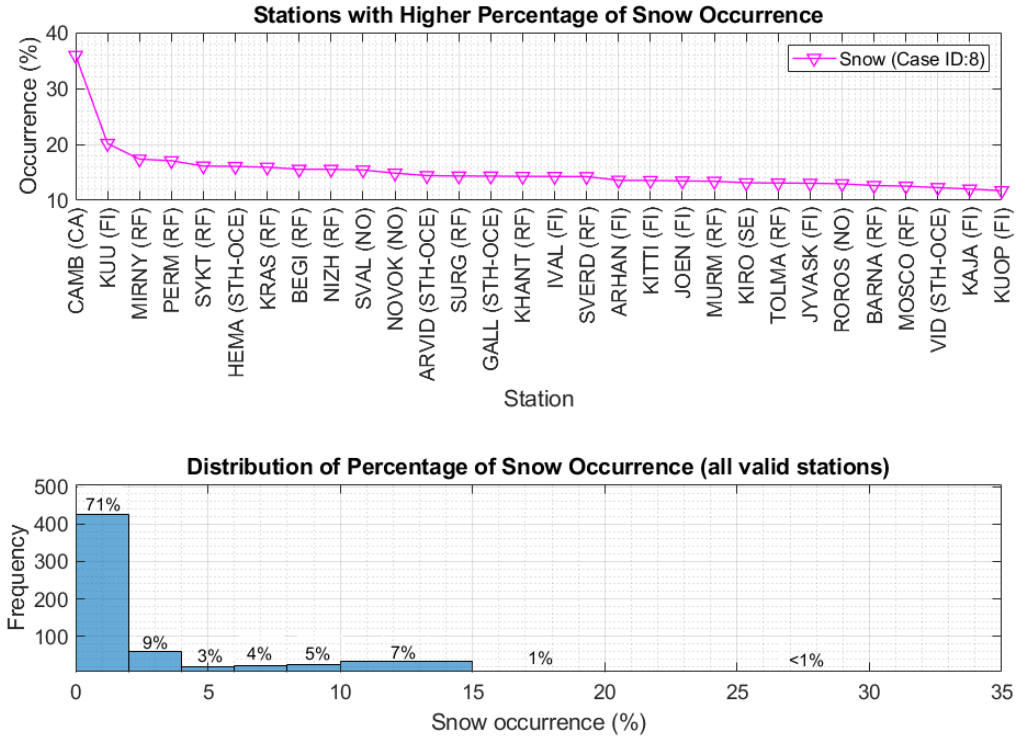

Figure 2.12: Percentage of snow occurrence figures, top: the top 30 stations with the highest percentages of snow occurrence, bottom: distribution of the percentages of snow occurrence.

Overall, the impact of a given weather condition on FSO depends on its effect on visibility reduction. Figure 2.13 presents the occurrence in terms of the percentage of a given event among fog, rain, snow, smoke or haze, sand, and others. It considers the measurements when visibility is lower or equal to 1 km. We select nine locations with different climate conditions to consider different environments. The corresponding figure next to the place's name refers to the percentage of low visibility (i.e., $V \leq 1$ km) in all available data. We find that fog or rain generates the highest impact on visibility reduction in all nine locations. Fog drives visibility reduction in seven sites out of nine, as presented in blue bars in Figure 2.13. Rain is the driver in the remaining two sites, orange bars in Figure 2.13.

Smoke (or haze) is significant in visibility in very polluted sites, e.g., in Mumbai, India, it causes a 30% reduction. In comparison, sand presence is important to the visibility reduction in some locations. For example, sand contributes around 20% to visibility reduction in Cairo, Egypt. However, rain and fog generate the highest impact on the visibility reduction in those places. Rain causes approximately 50% of the visibility reduction in Mumbai, whereas fog generates 75% of the low visibility samples in Cairo.

To have a more general view of the impact of specific weather effects

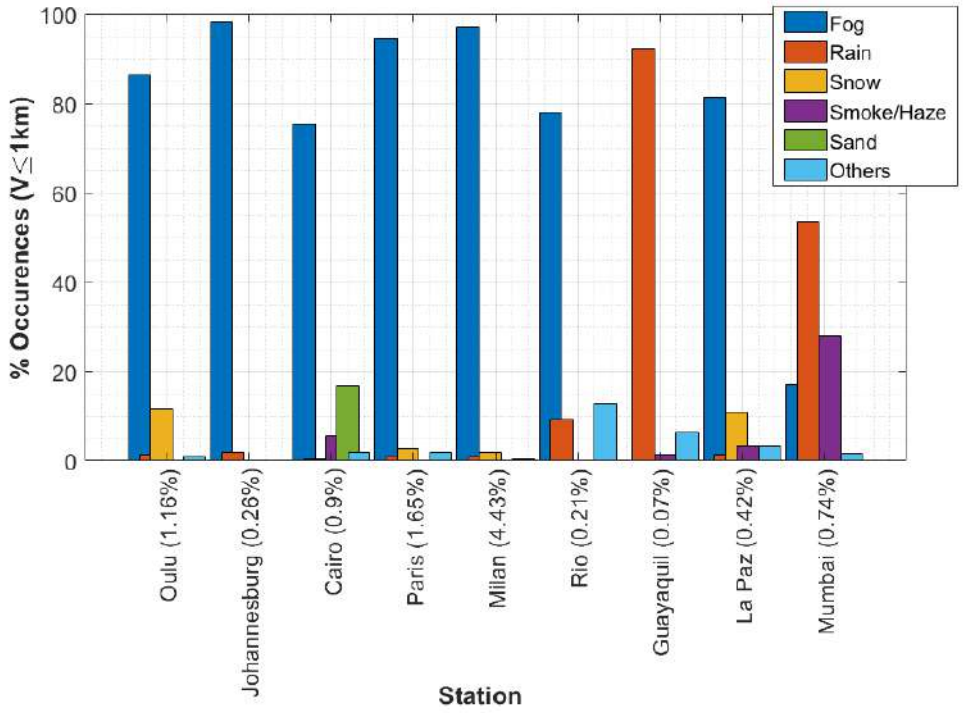

Figure 2.13: Distribution of atmospheric effects causing visibility reduction in the threshold $V \leq 1$ km.

on FSO as seen through visibility reduction, we generate maps with the distribution of the total percentage of the time each condition reduces visibility lower than a given threshold. Figure 2.14 presents bubbles indicating the total percentage of the time each effect (i.e., fog, rain, and snow) reduces V<1 km in Europe (results considering 347 valid stations). The percentages are divided into five ranges:

1. 0.1% - 0.5%
2. 0.5% - 0.8%
3. 0.8% - 1%
4. 1% - 2%
5. > 2%

Comparing the different weather conditions, fog is the dominant event of the visibility decrease in central and Southern Europe (see panel (a) in Figure 2.14). In contrast, snow is the main cause of visibility reduction in Northern Europe (see panel (c) in Figure 2.14). At some sites in mid-latitude climates, rain may generate a significant reduction in visibility, as seen in panel

(b) in Figure 2.14. Moreover, Figure 2.15 presents bubbles corresponding to the total percentage of time that fog reduces visibility lower than 0.5 and 0.1 km in panels (a) and (b).

Figure 2.17 presents histograms of the total percentage of time fog reduces visibility for the five ranges of percentages defined in the bubbles. We find that in around 49% of the studied locations in Europe (i.e., 170 places), at least 1% of the time, fog reduces the visibility lower than 1 km (last two columns of histogram in panel (a) in Figure 2.17). On the contrary, for 25% of the studied locations (i.e., 86 places), the time that fog reduces $V \leq 1$ km is lower than 0.1%.

In the case of $V \leq 0.5$ km, the histogram is in panel (b) in Figure 2.17. For 19.5% of the studied locations (i.e., 70 places), fog is present less than 0.1% of the time. And, in 37.8% of the valid stations (i.e., 131 locations), at least 1% of the time, fog reduces $V \leq 0.5$ km, as seen in panel (a) in Figure 2.15 and the histogram.

Finally, the histogram relating the reduction of $V \leq 0.1$ km due to fog is in panel (c) in Figure 2.17. For 56% of the studied locations (i.e., 195 places), fog occurs less than 0.1% of the time. And, in 5.8% of the valid stations (i.e., 20 locations), at least 1% of the time fog reduces $V \leq 0.1$ km, as seen in panel (b) in Figure 2.15 and the histogram.

Additionally, we find a limitation of the considered database for the European locations when non-specific weather tags cause a reduction of visibility lower than 1 km, here named *others*, as exhibited in Figure 2.16, this classification includes Cases 9, 12, and 13 presented in Table 2.5.

Maps of the total percentage of the time that fog reduces $V \leq 1$ km in South America are in Figure 2.18 (results considering 30 valid stations). In 50% of the locations, fog reduces $V \leq 1$ km less than 0.1% of the time. Whereas in 20% the percentage of time is higher than 1%, similar results have been found for $V \leq 0.5$ km. On the contrary, in 83% of the stations, fog reduces $V \leq 0.1$ km in less than 0.1% of the time and, only in one station the percentage of time that fog reduces $V \leq 0.1$ km is higher than 1%. Conditions such as rain, snow, and others for the studied locations in South America are not presented here since the percentages are low (lower than 0.1%). It is also necessary to study more sites to exhibit reliable results.

Therefore, considering the highest impact on visibility in the studied locations is caused by fog, snow, and rain; and avoiding snow effects on FSO due to both the lack of experimental data and the complexity in the study of the drops attenuation, we select fog and rain to be the focus of this study.

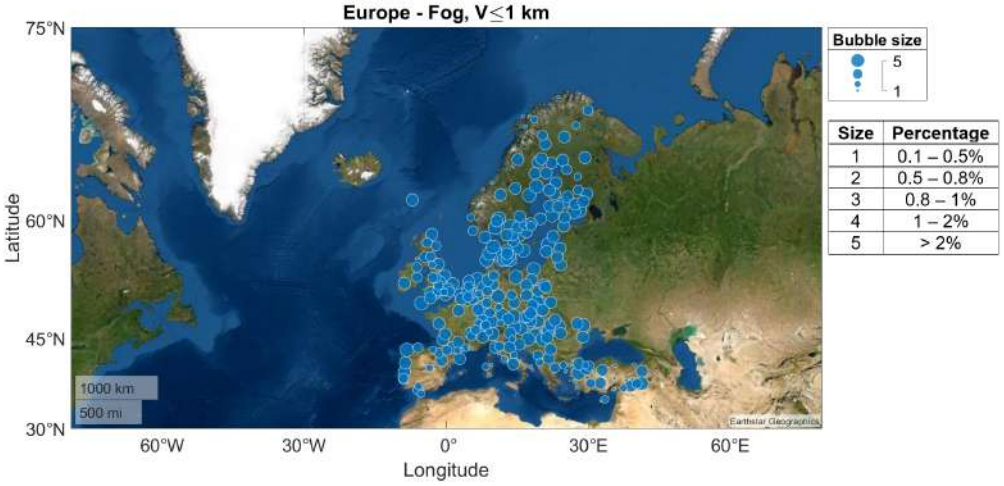

(a)

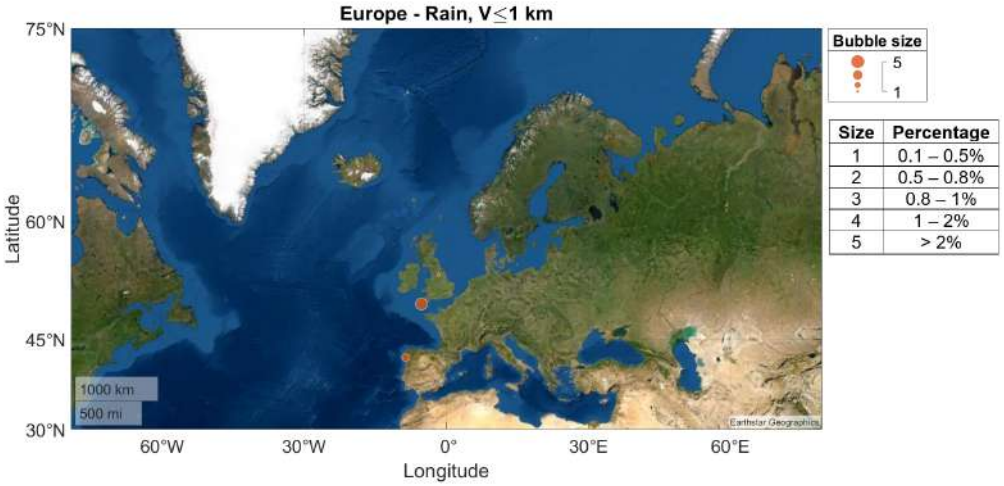

(b)

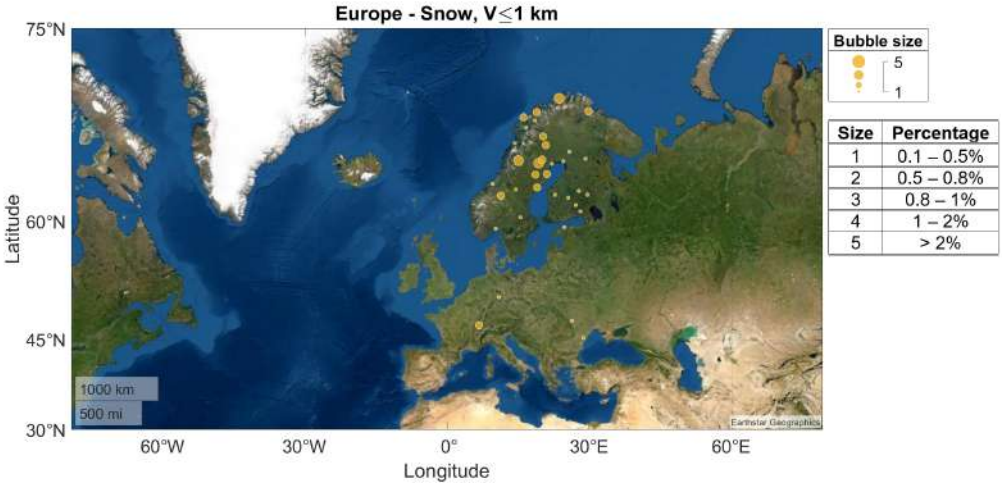

(c)

Figure 2.14: Total percentage of time that (a) fog, (b) rain, and (c) snow reduce visibility to less than 1 km for the valid stations in Europe.

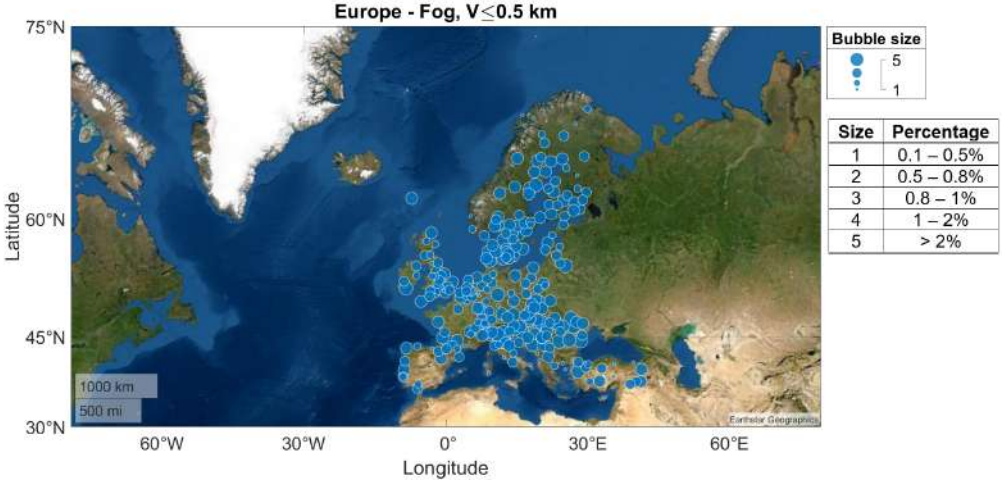

(a)

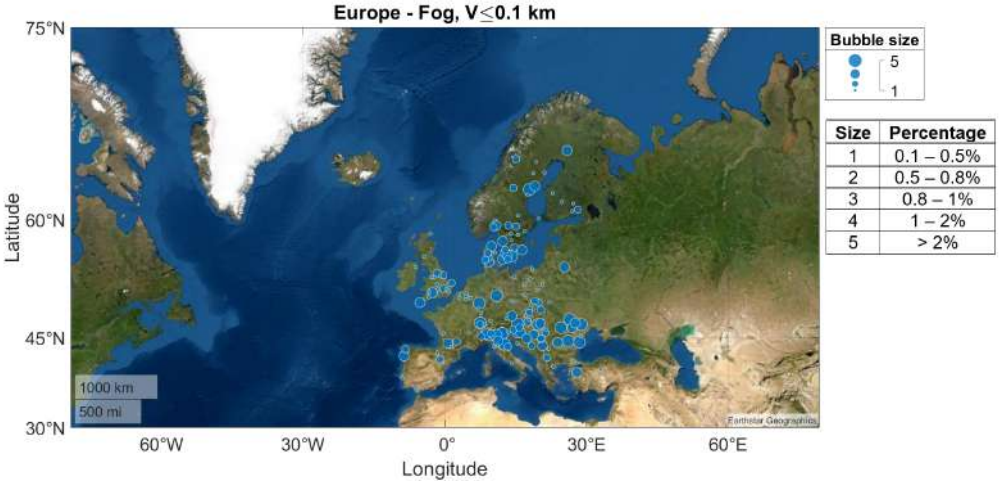

(b)

Figure 2.15: Total percentage of time that fog reduces visibility to less than (a) 0.5 km and (b) 0.1 km for the valid stations in Europe.

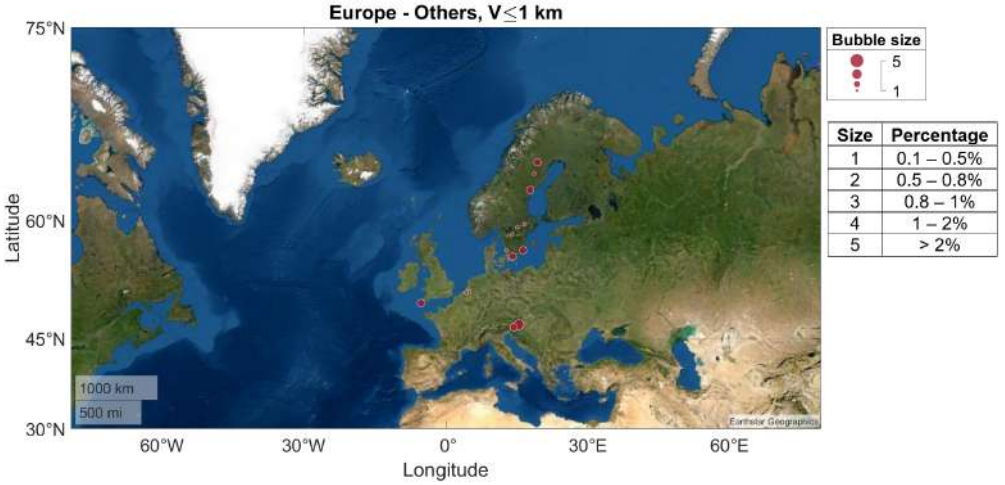

Figure 2.16: Total percentage of time that *others* reduces visibility less than 1km for the valid stations in Europe.

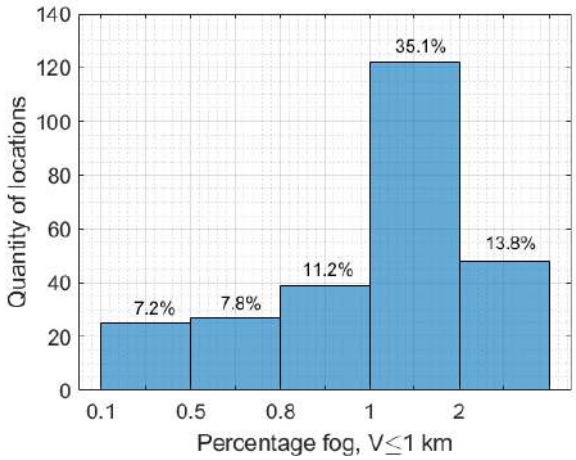

(a)

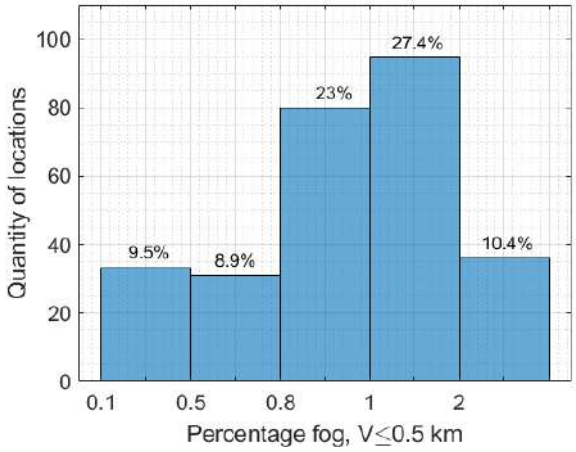

(b)

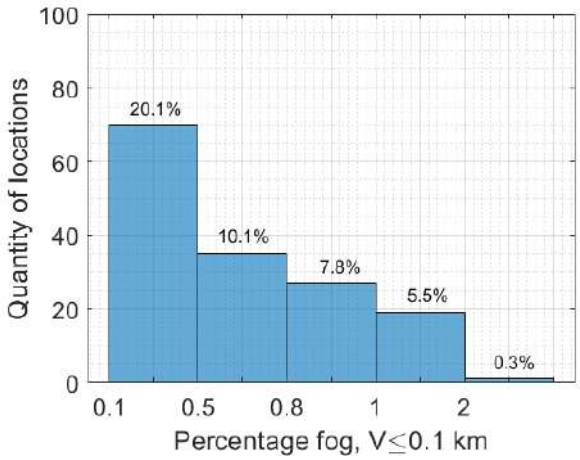

(c)

Figure 2.17: Distribution of total percentage of time that fog reduces visibility to less than (a) 1 km, (b) 0.5 km, and (c) 0.1 km for the valid stations in Europe.

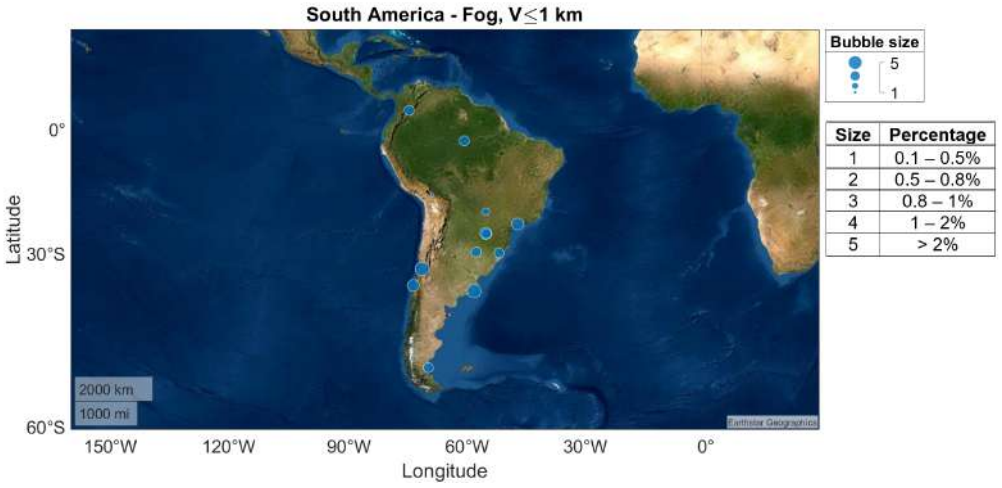

(a)

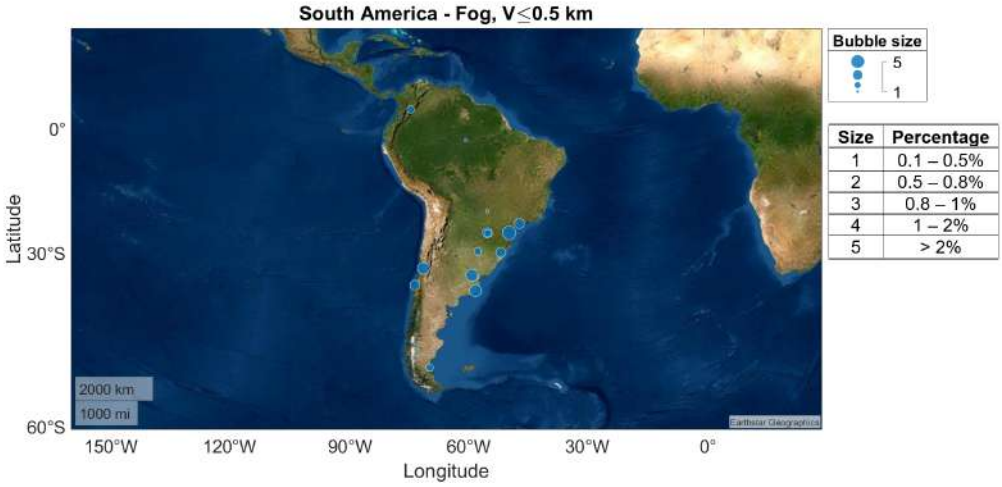

(b)

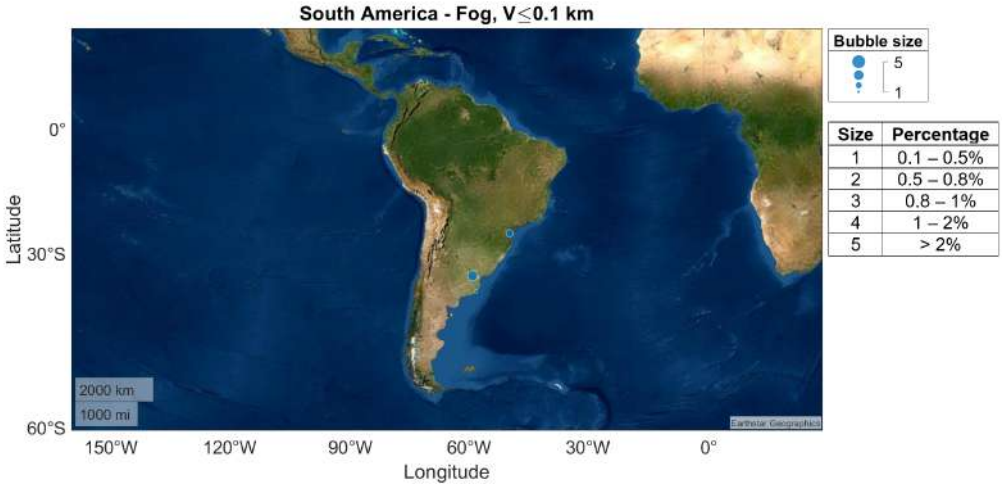

(c)

Figure 2.18: Total percentage of time that fog reduces visibility less than (a) 1 km, (b) 0.5 km, and (c) 0.1 km for the valid stations in South America.

3
Fog Attenuation on FSO

Propagation impairments are the biggest challenge for FSO. It is well known that fog, rain, snow, and turbulence produce significant signal fades across short terrestrial FSO links [37][38][39][40][41]. Specifically, the severe propagation loss caused by fog reduces the availability of terrestrial optical links where fog occurrence is statistically relevant. Hence, propagation limits the maximum path length if high-availability standards are required. The optical channel is wavelength sensitive; most current FSO systems work in the 1.550 μm window due to its compliance with eye-safety regulations [42] and the relatively low cost of the hardware. However, following the development of quantum cascade laser sources and detectors [43], [44] in the 10 μm band, there is a growing interest in the longer wavelengths [45], where fog attenuation is, in principle, less challenging. Given a possible deployment of FSO in mobile networks, there is a demand for simple and global channel models. Different from the well-settled ITU-R recommendations containing methods for predicting propagation impairments at microwaves and mmWaves [46], there is a lack of standardization in the frame of FSO. ITU-R P.1817.1, entitled "Propagation data required for the design of terrestrial free-space optical links", includes general guidelines and has not been updated for a while [47].

This chapter aims to fill gaps in the modeling and quantification of the path loss component due to fog, considering the wavelength dependence of the models and transmission measurements found in the literature. The model based on fog micro-physics is studied at different wavelengths to provide a theoretical validation of the extinction coefficient (γ), from visibility (V) models (named γ-V) using an extensive database of 54 PSDs of fog and haze, including recent measurements. After that, we estimate the link range considering fog micro-physics at mid-IR (10.6 μm) and near-IR (1.55 μm), relying on data from state-of-the-art particle sensors collected during radiation fog at mid-latitude continental climate. Moreover, we propose a new version of the well-known Kim model to obtain the extinction coefficient of fog as a function of visibility, named a *lower bound model*. In contrast, an *upper bound model* is identified considering visibility thresholds to fit better the outcomes of micro-physics of fog. Finally, we present the analysis of the uncertainties in

the conversion from visibility measurements into the extinction coefficient of fog.

3.1 Models for propagation through fog

Based on the extensive analysis of the surface observations data set from Wyoming University [33], developed in Chapter 2, we concluded that the visibility value exceeded 99.9% of the time in most European cities is in the range from less than 100 m to about 2 km. This effect is primarily due to fog as rain only reduces the visibility below a few km during a much smaller percentage of the time. On the other side, heavy rain may significantly impact the statistical distribution of optical attenuation in climates where fog is relatively infrequent. Then, a propagation model based on the rainfall rate statistics also shall be adopted, as we will study in Chapter 4. When FSO availability is driven by fog occurrence, we suppose that the actual attenuation across a path L is given by $\gamma \times L$ and that multiple scattering effects are negligible. These assumptions will be discussed later in this chapter.

The γ-V models proposed in the literature are applicable under these assumptions and rely mainly on two approaches:

1. Electromagnetic theory and the micro-physics of fog;
2. Empirical derivation of parameters from joint optical attenuation and visibility measurements.

In principle, the extinction coefficient of an optical wave traveling through any atmospheric particulate (fog, haze, rain, snow, etc.) can be accurately calculated from the particle size distribution (PSD), i.e., the number of fog droplets per unit volume falling within a size bin, and the extinction cross-section of a particle of given size [48]. The micro-physical model highlights the sensitivity of wave attenuation to the radiation wavelength and the PSD shape. However, this approach is unsuitable for assessing the climatology (i.e., long-term) attenuation distribution required by link budget calculations. Micro-physical data are seldom known and variable over different space and time scales (e.g., environment, climatic area, event life cycle, season). Thus, empirical models based on other atmospheric parameters have been developed to predict optical attenuation [49][50][51][52][53][54][55]. We consider simple models using visibility as the only input in this work. Visibility is routinely collected at many airports throughout the world. Hence this approach may help set up a global model to predict the contribution of fog to optical attenuation, considering the Wyoming university repository presented in Chapter 2 as input.

3.1.1 The γ-V Relationship

The literature highlights variations among different γ-V models [49][50][51][52][53][54][55], depending on the followed methodology, the derivation, and the definition of visibility [31]. First, visibility must be defined according to an objective rule. Following WMO recommendations [31], the visibility is equivalent to the meteorological optical range (MOR), defined as the atmospheric path length required to reduce the irradiance (i.e., the optical power per unit area) of a perfectly collimated beam emitted by an incandescent lamp at a color temperature of 2700 K to 0.05 of its value at the transmitter aperture. Using the Bouguer-Lambert law [56][57], which predicts an exponential decay of the irradiance for propagation through a uniform layer of particles, it is straightforward to retrieve the following relationship between γ (in dB/km) and V (in km)

$$\gamma = 13/V \tag{3-1}$$

Instrumental methods often use (3-1) to derive V from measurements of γ within a sample volume of the atmosphere. Sometimes, a different threshold value T for the irradiance is used. Hence, for convenience, let us write (3-1) in a more general way as

$$\gamma = K/V \tag{3-2}$$

where

$$K = -4.34ln(T) \tag{3-3}$$

Even though actual visibility sensors generally follow WMO recommendations and return the MOR, the majority of γ -V models used in FSO applications adopt $T = 0.02$ (for the reasons detailed below), hence $K = 17$. Please note that (3-2) is just a definition that holds on the visible part of the optical spectrum (0.400-0.700 μm) and results from the concept of MOR, which, in turn, quantifies the power loss of a collimated beam of given characteristics as it travels through the atmosphere. Therefore, if the atmosphere is homogeneous across a path L and multiple scattering is negligible, V is inversely proportional to the extinction coefficient of the visible radiation.

3.1.2 Visibility measurements

As human observers usually measure visibility, the MOR should be linked to the intuitive definition of visibility: the maximum distance an object can be seen and recognized (in the daytime) against the background. It can be quantified using the concept of irradiance contrast. This concept refers to the

ratio of the difference between an object's irradiance and its background to the irradiance of the background itself. Hence, if the visibility (strictly speaking, the visual range) is defined as the distance at which the contrast of the observed object equals the contrast threshold of the observer, then the γ -V formula can be written as in (3-2), with T being the contrast threshold value [31]. The derivation of (3-2) from the contrast is due to Koschmieder [58], who proposed T=0.02 corresponding to $K = 17$. It is often used instead of (3-1). Indeed, (3-2) with $K = 17$ has been incorporated by several γ -V models, as the relationship at $\lambda = 0.550$ μm. Pierce et al. [59] reviewed the assumptions behind Koschmieder derivation. They defined the contrast in a foggy and hazy atmosphere that accounts for light scattering from the suspended particles and the effect of other light sources. Both atmospheric effects concur in reducing the contrast. Hence, visibility measurements contaminated by scattering and background radiation may overestimate optical attenuation if the Koschmieder formula is used. The authors came up with the main conclusion that optical attenuation can still be estimated by (3-2) and provided an interval of values for the coefficient K ($8.5 \leq K \leq 17$) rather than an optimum value. They indicated Koschmieder's' values as a reasonable upper bound and concluded that the actual value of K should be determined experimentally.

Visibility measurements based on the contrast of a distant object are carried out by the naked eye in many cases or, sometimes, by a CCD camera [60][61][62]. In the former case, the contrast threshold is subjective, generating further uncertainty in linking visibility measurements to the MOR and the extinction coefficient. [31], visual estimations of visibility during daylight are about 15% higher than instrumental measurements of MOR (i.e., $K = 11.3$) with a 22% standard deviation, assuming a Gaussian distribution of the uncertainty. Visual observations are even more problematic at night, as they require a light source of known intensity and depend on factors like background illumination. Human observers' estimations of night-time visibility are 30% higher than MOR ($K = 9.6$), with uncertainty up to 40%. On the other side, the manufacturer usually provides the accuracy of visibility sensors in datasheets, typically between 5 and 20% [63]. Another source of uncertainty is how visibility data are stored in the public domain databases. Sometimes the meteorological reports make available numerical codes instead of visibility values. For instance, SYNOP VV codes for horizontal visibility at the surface are integer values ranging from 00 to 99 [64] and have an accuracy within 100 m for visibility up to 5 km. A 500 m visibility value is affected by a 20% quantization error. Visibility data encoding is even coarser at times. Due to (3-2), the percent uncertainty over γ equals the one over V. Table 3.1

Table 3.1: Recommended value of the coefficient K of (3-2).

K	Measured method	Inaccuracy
9.6	Visual observation of a light source at night	40%
11.3	Visual observation of a black object against the sky horizon during day	22%
13.0	Instrumental measurement of the MOR defined as in Section 3.1.1	5-20%
$-4.34ln(T)$	Instrumental measurement of the visibility defined as the distance where the irradiance of a light source reduces to a fraction T of its value close to the source.	

summarizes the recommended relationships to turn visibility into extinction coefficient in the visible window and the associated uncertainties.

3.1.3 Wavelength dependence

Equation (3-2) strictly holds on the visible region of the spectrum. Existing FSO systems work in the near–IR spectral windows where the atmosphere is transparent, i.e., 0.780–0.950 μm, or, more often, around 1.550 μm, taking advantage of low-cost and well-consolidated optical fiber technology. Nowadays, mid-IR systems operating around 10.6 μm are attracting some interest due to developing and improving the performance of quantum cascade laser (QCL) sources and detectors [43]. The wavelength dependence of the γ-V relationship can be accounted for by a power-law function, which also fits the asymptotic regime of Rayleigh scattering. We then move from the following formulation that is common to several models: [49][50][52]

$$\gamma = \frac{K}{V}\left(\frac{0.550}{\lambda}\right)^q \tag{3-4}$$

λ is in μm and q depends on V. A few expressions have been proposed for q [49][50][51]. Table B.1 in Appendix B lists several models available in the open literature. Some are the best fits of optical propagation data collected through fog and haze, whereas others result from scattering calculations using known analytical expressions for the PSD. One of the most recurrent models is the one in the Kruse textbook [50], sometimes referred to as the Kruse model, even though it is largely based on earlier works. Several authors pointed out that this model is not appropriate for fog, so the expression of q for $V < 6$ km in Table B.1 should not be used for propagation through fog. Kim et al. in [49] proposed different values for q based on existing literature even though they did not provide any evidence of their findings. They just stated that *"in haze*

conditions, there is a wavelength dependence to the atmospheric attenuation. However, it has been shown through an extensive literature search of past experimental observations and some full Mie theory scattering calculations that this is not the case in fog". Specifically, they broke the 0 - 6 km visibility interval into three segments and suggested taking $q = 0$, if $V < 500$ m. This fact has deep implications as it means that in dense fog, optical attenuation is independent of the wavelength at least up to 1.550 μm, as the authors limited their analysis to the visible and near-IR domains. On the other hand, if $V > 500$ m [49] predicts a significant improvement of optical transmission in the 1.550 μm window over shorter wavelengths with increasing visibility. For instance, $\gamma_{1.550}$ (in dB/km) reduces by 40% if $V = 1$ km with respect to γ_{vis} and by 30% with respect to $\gamma_{0.785}$, respectively.

Two relationships based on Mie scattering theory and analytical models of the PSD of fog are also reported in Table B.1. Grabner and Kvicera [52] used a three-parameter gamma function to describe the PSD of fog, introducing constraints to reduce the number of free parameters. Their γ-V formulation is as in (3-4). However, the expression for q is rather complicated and wavelength-dependent because γ does not exhibit a monotonic decrease with increasing λ in the interval considered by the authors (0.2-2 μm).

Their γ-V curve is convex on log-log axes. On the contrary [49], it predicts larger γ values than (3-2) in the near-IR rather than in the visible range. Similar at 1.550, predicting larger values than at 0.785 μm. The increase of γ above the value at 0.550 μm is within 10% at 0.785 μm if $V \geq 2$ km, while it is a remarkable 35% at 1.550 μm in the interval 1 - 2 km. Al Naboulsi et al. [53] calculated best-fit expressions for γ of radiation fog and heavy advection fog models tabulated [65] in the wavelength interval 0.69 - 1.55 μm. Wavelength dependence is rather weak because the dominant particle size of the chosen PSDs (two modified gamma functions) is larger than the maximum wavelength in both cases (mode radius equal to 2 μm and 10 μm, respectively). Therefore, the departure of their γ-V formula from (3-2) is modest. Figure 3.1 highlights the pattern of the predicted extinction coefficient at 0.785 and 1550 μm against the visibility according to the models discussed here. For convenience, we used $K = 17$ as this value has been usually adopted in the models. Please note that when a different value of K is used instead (for instance, $K = 13$) if the visibility sensor measures the MOR, the corresponding threshold values on V in the Table must be scaled accordingly. The important limit of 500 m in [49] changes to 650 m when expressed in terms of the MOR. In the next section, an extensive database of PSDs will be considered to assess the above models considering fog variability.

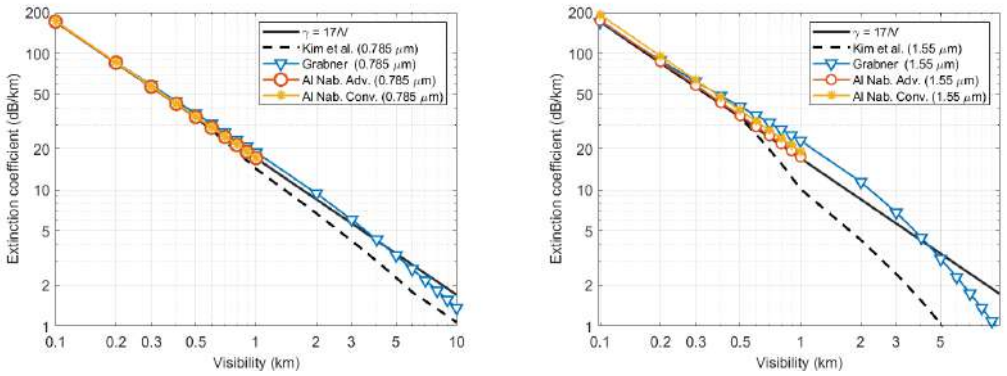

(a) (b)

Figure 3.1: Extinction coefficient against visibility according to different models at (a) 0.785μm and (b) 1.55 μm.

3.2 The micro-physical model

The micro-physical model relies on the knowledge of the PSD. Measured particles are binned into size intervals and usually fitted with analytical curves. Finally, γ is calculated through the classical single-scattering integral. The extinction cross-section σ_{ext} of fog droplets must be computed by Mie theory (assuming homogeneous and spherical water particles) as the droplet radius r is comparable with FSO wavelengths. The integral expression for the extinction coefficient is

$$\gamma(\lambda) = 4.34 \times 10^{-3} \int_{r_1}^{r_2} \sigma_{ext}(r, \lambda) N(r) dr \tag{3-5}$$

N(r) is the PSD expressed in $cm^{-3}\mu m^{-1}$, σ_{ext} is in μm^2 and γ is in dB/km.

The two microphysical models discussed in the previous section highlight somewhat different γ values due to the other PSD used by the authors. Here, fog microphysics is used to provide a theoretical validation of the γ-V models as well as to get an insight into the relationship between V and γ at different wavelengths, following the approach in [67]. We use a more extensive database of 54 PSDs of fog and haze, including recent measurements. Specifically, we take advantage of comprehensive observations of the PSD of radiation fogs in Paris by spectrometers in the particle range 0.2 to 50 μm [55]. These data highlight that fog is characterized by multi-modal PSDs modeled as many lognormal functions. An overall 20 multi-modal PSDs were reported [55], corresponding to different fog stages. The remaining 34 PSDs used in this work are taken from older studies and were usually modeled by modified gamma distributions [65][68][69][70].

Figure 3.2 presents the extinction coefficient as a function of the visibility

calculated at 0.785, 1.550, 3.7, and 10.6 μm, considering the above 54 PSD models. The 34 monomodal distributions are grouped by fog type. In the case of valley fog, the authors in [68][70] further distinguished into four evolutionary stages (i.e., growth, formation, mature, and dissipation fog), which are drawn with as many markers to highlight the dependence of γ-V on the life cycle of fog. Moreover, all the monomodal distributions were tabulated for nominal values of the particle number concentration. Therefore, as in [67], the number concentration is considered a parameter and allowed to range within realistic limits. Hence the corresponding PSDs are segments rather than points in the γ-V plane of Figure 3.2. The actual number concentration was provided in [55] for the multi-modal PSDs (filled circle markers). V is calculated from γ at 0.550 μm through (3-4), which is drawn in Figure 3.2 (a) to (d) as well as a reference. Finally, the Kim model (1.550 μm) and Nebuloni model (10.6 μm), taken from Table B.1, are plotted. Again, for consistency with original model formulations, we take $K = 17$. At 1.550 μm, γ is bounded by the Kim model and by (3-4). The markers are packed around $\gamma = 17/V$ as far as V is less than 1 km, whereas γ tends to decrease as the visibility increases. This trend is predicted by the Kim model even though it provides a lower bound of PSD data rather than a satisfactory fit. At 0.785 μm (Figure 3.2 (a)), there is no significant departure from (3-4) even at large visibility values.

To summarize, fog attenuation is roughly wavelength-independent from the visible range throughout the near-IR up to 1.550 μm as far as $V < 1$ km. Beyond this limit, 1.550 μm propagation seems better, as highlighted by seven of the multi-modal PSDs corresponding to Paris's early and late stages of radiation fog.

The picture changes moving into the mid-IR range. Data depart from $\gamma = 17/V$ at much lower visibility values than in the near-IR. Even though there is a huge scatter, the trend towards a significant decrease of γ concerning near-IR wavelengths is evident. The multi-modal radiation fog data highlight that $\gamma_{10.6}$ can be significantly smaller than in the near-IR even in the presence of dense fog, which is not as evident looking at the monomodal PSDs. If V grows beyond about 200 m, 10.6 μm transmission is always better than at shorter wavelengths, the ratio of the corresponding extinction coefficients being up to one order of magnitude and even higher.

Figure 3.3 provides a simple physical explanation of the above features by showing the extinction efficiency of water spheres as a function of the wavelength for different droplet radii. The efficiency is σ divided by the geometrical cross-section. The extinction of water droplets is wavelength-independent up to the near-IR range if $r \leq 4$ μm. However, if $r \leq 4$ μm,

the extinction efficiency in the 10.6 μm window decreases by a factor 3 at least concerning the near-IR, the decrease being as high as 10 for sub-micron particles. This is a simplified picture as real PSDs spread over a range of droplet sizes, which flattens the significant variations highlighted in Figure 3.3. What rules is the shape of the integrand function involved in the calculation of γ in (3-5), i.e., the $N\sigma$ product. However, the 4 μm threshold value is a relatively simple rule to bear in mind. For instance, the mode radius of the multi-modal PSDs is much smaller (0.4 - 0.6 μm) than the one of the monomodal PSDs of radiation fog (2 - 12 μm), which explains the different features in the γ-V plane.

There are two major conclusions from this discussion: first, in the near-IR, the departure from $\gamma = 17/V$ (or $\gamma = K/V$ if a different definition of visibility is used) is limited, and it should be considered only at 1.550 μm when $V > 1$ km; second, in the mid-IR, the existing models are not adequate to describe the spread of γ-V. Fog attenuation at 10.6 μm can be much smaller than in the near-IR, even in dense fog.

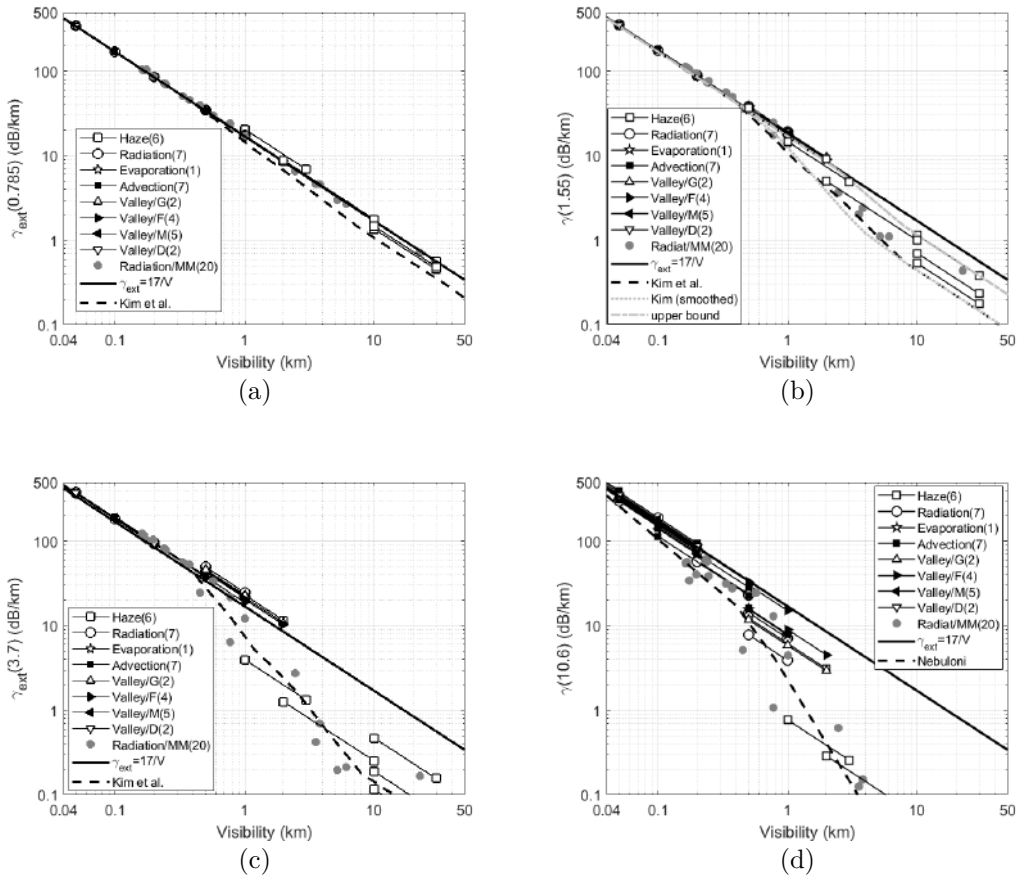

Figure 3.2: Extinction coefficient at different wavelengths against the visibility for 54 fog and haze types.

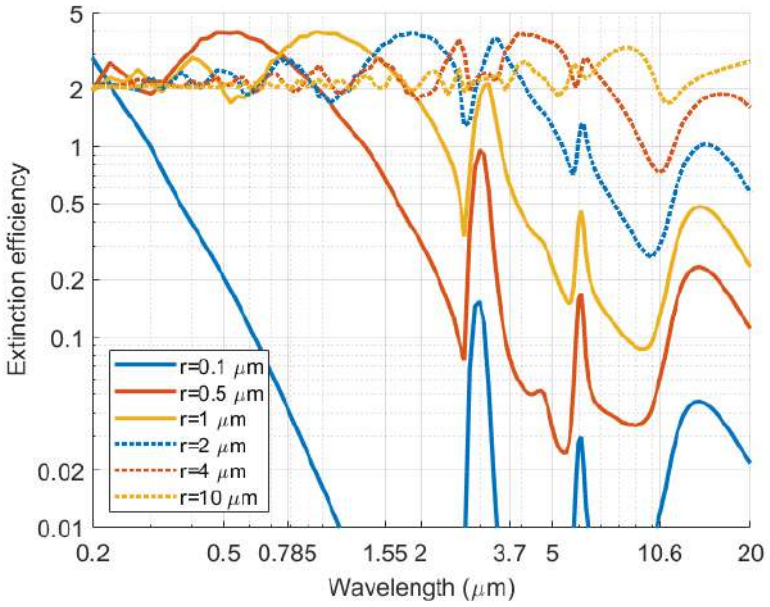

Figure 3.3: Extinction efficiency of water droplets in the optical spectrum for six different droplet radii.

3.3 Path length at Mid-IR

Using a method based on the knowledge of fog micro-physics (see Section 3.2), we estimate the path loss due to fog as well as the link range in the mid-IR (10.6 μm), comparing it with the near-IR (1.55 μm). We rely on new data from state-of-the-art particle sensors collected during radiation fogs at mid-latitude in a continental climate [71][72].

Specifically, to quantify the effect of fog on optical wave propagation, we need the PSD of fog at mid-IR wavelengths. Particle sensors usually bin the particles collected within the sampling volume of the instrument into a finite number of size intervals. A relatively simple continuous function subsequently fits the resulting histogram of the fog PSD.

3.3.1 Experimental data

The fog PSD data used here were collected during the ParisFog field experiment [71], aimed at characterizing the environment where fog occurs by monitoring surface conditions, radiation, precipitation, droplet, and aerosol microphysics and chemistry. The experiment was carried out in Paris during the winter season in 2010/2011 and 2011/2012. The droplet size distribution of fog was monitored by a Palas Welas-2000 particle counter installed 2 m above ground. The presence of fog and the visibility variation was recorded in a larger

200 x 200 km^2 area around Paris with a method proposed by Météo-France. The procedure is based on the combination of i) cloud type with precipitation information from radar data, ii) 2-m relative humidity, and iii) 10-m wind stamps. Finally, it produces an hourly analysis of fog probability [71]. The list of the instruments used to measure fog and aerosol micro-physics and their range and resolution are presented in Table 3.2 [72].

Table 3.2: Instruments used to measure fog and aerosol microphysics in ParisFog experiment [72].

Instrument	**Measured parameters**	**Range (µm)**	**Resolution (min)**
Palas Welas-2000 particle counter	Aerosol and fog PSD	0.4 – 10	5
TSI Scanning Mobility Particle Sizer (SMPS) particle counter	Aerosol PSD	0.01 – 0.4	10
GRIMM condensation particle counter (CPC)-5400 particle counter	Aerosol particle counter	0.01 – 0.4	1
Fog monitor (FM100) forward scattering spectrometer	Droplet particle counter	2 - 50	1

Taken from [72]

The fog events were defined as a sequence of at least 30 minutes of observations below a 1-km visibility threshold over a 50-min window; the near-fog events were in the 1 to 5 km range over the same time intervals as fog. The identified fog events occurred in weak to the moderate wind (wind speed < 5 m/s). Fog events were classified into the following five types through the algorithm proposed in [73]: radiation fog, advection fog, stratus lowering, precipitation fog, and morning transition fog. A 20% of the total time of the experiment was identified as one of the fog events, being 36 fog events and 89 near-fog events, distributed over 37 and 109 days, respectively. Radiation and stratus-lowering fog scenarios represent about 40% of all fog events. In the present work, we are considering the radiation fog measurements.
During fog events, the aerosol concentration ranges from 2.000 to 25.000 cm^{-3}, and 75% of the distribution ranges between 4.000 and 8.000 cm^{-3}. It is caused by the collision of aerosols with water aerosols and fog droplets.

Monomodal PSD

Deirmendjian [74] suggested that the modified gamma distribution can model fog and haze PSD. The number of particles per unit volume and unit increment of radius, $N(r)$, is represented by (3-6)

$$N(r) = ar^{\alpha}exp(-br^{\beta}) \tag{3-6}$$

r is the droplet radius, whereas a, b, α, and β are positive function parameters. If $\beta = 1$, (3-6) reduces to a simple gamma function. Deirmendjian and several other authors provided values for the above parameters for different types of fogs [65][68][70]. Figure 3.4 shows a set of 7 radiation patches of fog modeled by a modified gamma distribution, which will be used in the following for scattering calculations. As some models of the optical propagation channel are based on the above PSDs, they are used here as a benchmark for comparison with the ParisFog PSD models.

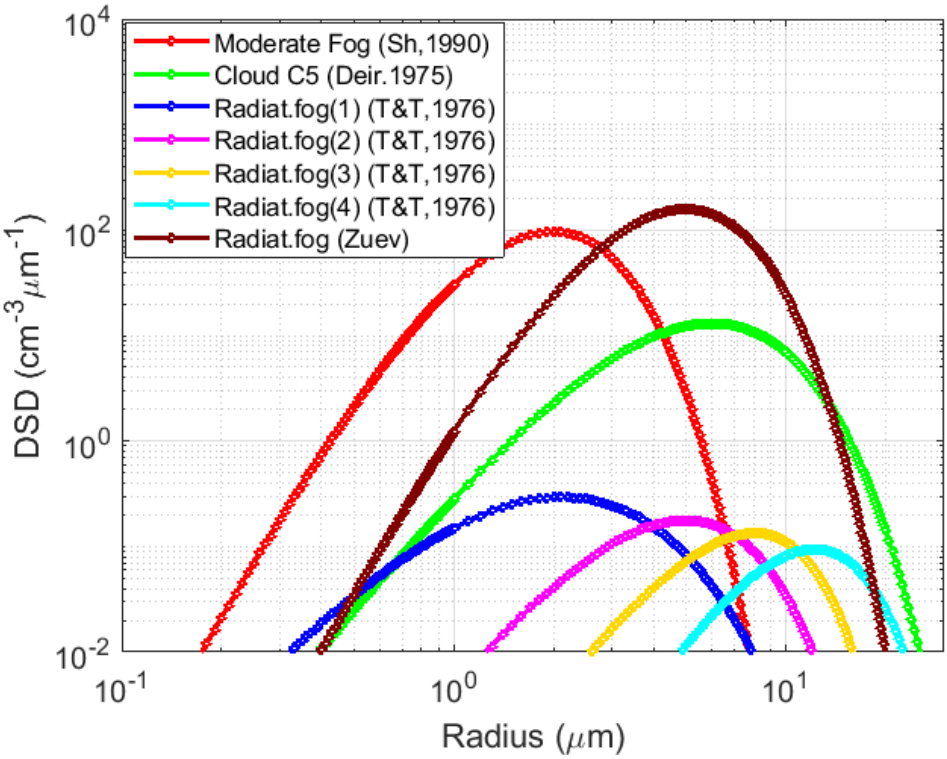

Figure 3.4: Modified Gamma PSDs for radiation fogs.

Multi-modal PSD

The recent ParisFog experiment described in Section 3.3.1, relied on state-of-the-art particle sensors to detect a wide range of particle sizes, includ-

ing the underlying aerosol distribution and droplets up to 50 μm (Table 3.2).

Data highlighted multimodal patterns, that were modelled using multiple log-normal functions:

$$n(r) = \frac{1}{\sqrt{2\pi r}} \sum_{k=1}^{M} \frac{N_k}{ln(\sigma_k)} exp\left[-\frac{1}{2ln^2(\sigma_k)} ln\left(\frac{r}{r_k}\right)^2\right] \tag{3-7}$$

r_k, σ_k and N_k are the modal radius, the width and the particle concentration of mode k, respectively. Here we analyze 20 multi-modal PSDs listed in [72] and corresponding to radiation fogs. Figure 3.5 shows four of the above PSDs for different evolutionary fog stages.

Please note the differences between Figure 3.4 and Figure 3.5. In the case of monomodal fogs, PSD peaks are between 2 and about 12 μm, whereas most of the particles in multi-modal fogs are submicron in size.

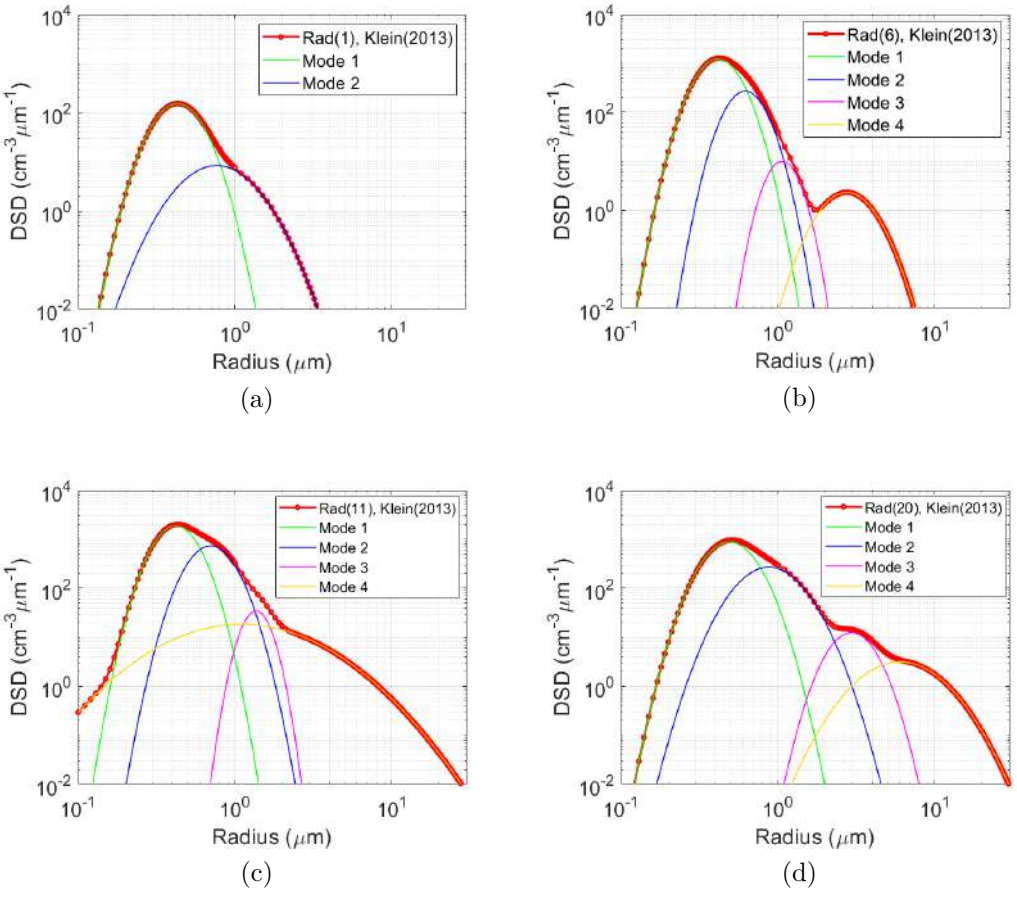

Figure 3.5: Example of multi-modal PSDs of radiation fogs observed during the ParisFog experiment.

3.3.2 Extinction coefficient calculation

Assuming multiple scattering effects are not relevant, the extinction coefficient γ, i.e., attenuation per unit path length, can be calculated through the well-known single-scattering integral presented in (3-5). Fog droplets are almost entirely made of water and are spherical. In multi-modal PSDs of radiation fog, there are several small-size modes, as presented in Figure 3.5 panel (b). However, their contribution in terms of extinction is small since the radius range is much smaller than the wavelength, indicating Rayleigh scattering. Moreover, their radius is the same order of magnitude as the FSO wavelengths involved. Hence, σ must be computed through full Mie theory.

Here, the extinction coefficient of fog is calculated by (3-5) at 10.6 μm for the multi-modal radiation fogs of the ParisFog experiment as well as for earlier measurements in Fig. 3.4. To characterize fog intensity, it is calculated here through its definition from the atmospheric visibility V [31], using as input the extinction coefficient calculated at 0.550 μm, as explained in section 3.2.

Figure 3.6 shows $\gamma(10.6\,\mu m)$ against V for the set of 27 considered radiation fogs. The circle markers represent multi-modal PSDs, whereas the star-shaped markers correspond to the monomodal PSDs. The thick black line corresponds to the extinction coefficient calculated with (3-8), while the dashed line has been obtained from the best fit of direct FSO measurements (not by PSD data) according to the γ-V model of Nebuloni [51] as presented in Table B.1. The wavelength dependence of fog attenuation is evident. The black line, which holds in the visible region of the spectrum, corresponds to larger attenuation values for every fog type, the difference increasing with visibility.

$$\gamma(0.55\,\mu m) = \frac{17}{V} \quad dB/km \tag{3-8}$$

Even though the model reasonably fits the data, they are quite scattered. Hence, predicting mid-IR optical attenuation from the visibility looks like a challenging task, even considering data collected in the same location. Besides, the dashed line looks like a lower bound at small visibility values (i.e., up to 500 m). Actual FSO technology operates in the near-IR windows, mainly at 1.550 μm. Therefore, it is interesting to compare fog attenuation in the near-IR and the mid-IR. Figure. 3.7 shows the scatter-plot of the extinction coefficient at 10.6 μm against the one at 1.55 μm. The 45° line highlights that mid-IR radiation propagates better than near-IR through all the considered fog models. Moreover, multi-modal fogs highlight a significant gain at 10.6 μm even at large values of the extinction coefficient, i.e., between 8 and 75 dB/km for $\lambda = 10.6\ \mu m$, which correspond to the 150-450 m visibility interval.

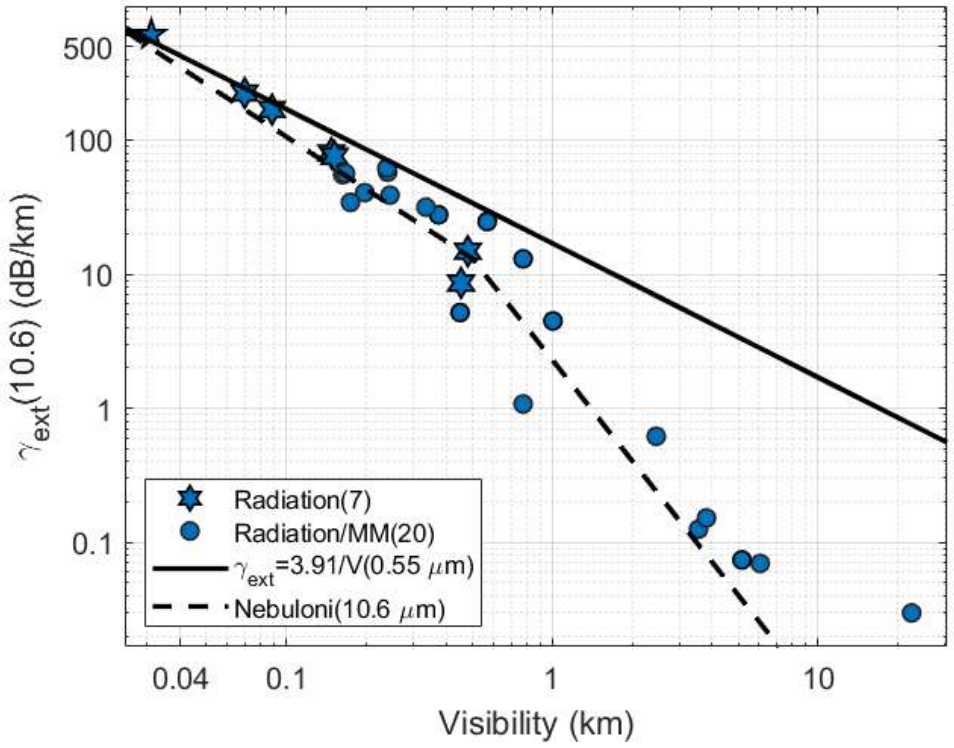

Figure 3.6: Extinction coefficient against the visibility for 27 radiation fog PSDs at 10.6 μm.

3.3.3 Path length estimation

As an application of the model of fog attenuation of Nebuloni [51], we estimate the link range as a function of the visibility conditions and the wavelength, assuming the component of optical attenuation due to fog is the dominant contribution. To this aim, we define the power budget equation as in (3-9), where the Friis transmission formula [90] gives the received power at the detector. The term *A(L)* on the left part of the expression represents the atmospheric attenuation as a function of the path length L. We assume the atmospheric attenuation *A(L)* can be caused by fog or rain occurrence for the present study.

$$A(L) - 10\log_{10}\frac{A_R}{\pi(\vartheta_T L)^2} + 60 = P_T - P_R - A_{sys} \tag{3-9}$$

The simplified FSO power budget equation [90] is reduced to (3-10) when it is assumed homogeneous propagation conditions across the path, as:

$$\gamma L - 10\log_{10}\frac{A_R}{\pi(\vartheta_T L)^2} + 60 = P_T - P_R - A_{sys} \tag{3-10}$$

P_T and P_R are the transmitted and received power (in dBm), A_{sys} are system losses (dB), A_R is the receiver area (m^2), ϑ_T is the beam divergence

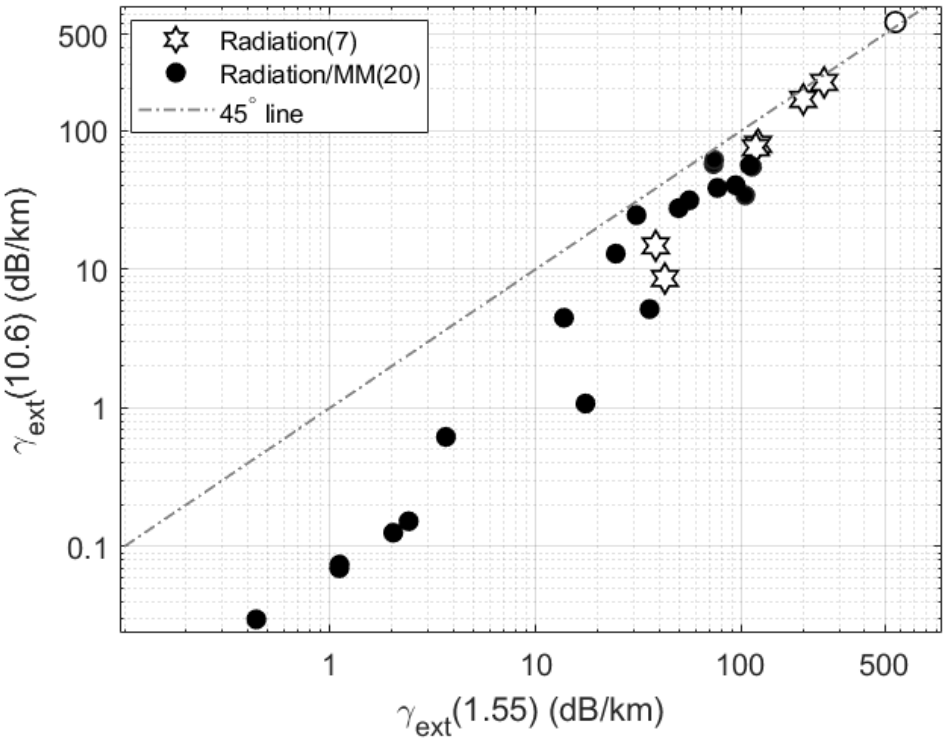

Figure 3.7: Corresponding Extinction coefficient for 27 radiation fog PSDs at two wavelengths.

(rad) and L is the path length (m). Other sources of path attenuation as gas absorption or clear-air scintillation, have been omitted, as their impact on FSO link availability is deemed not as relevant as the one of fog or rain (in statistical terms). The term on the right side of (3-10) depends on system characteristics.

It is assumed that fog is uniformly distributed along the propagation path. Hence, the corresponding attenuation over a path L is simply L times the extinction coefficient.

It is straightforward to infer L by substituting the link budget equation into (3-5) with the following (standard) values for the system parameters: $A_r = 0.01\ m^2$, $\vartheta_T = 0.5$ mrad, and $M = 50$ dB. Figure. 3.8 shows the calculated path length as a visibility function at 10.6 μm and 1.55 μm. As above, stars denote the mono-modal fogs and the circles multi-modal PSDs. Orange and blue markers correspond to $\lambda = 1.55$ μm and $\lambda = 10.6$ μm respectively. Best fits are obtained with power-law functions (i.e., straight line on log-log axes). At 1.55 μm, all fog models are well-fitted by the power-law model. The extinction coefficient is rather insensitive to the micro-physics and can be calculated from the visibility. The situation is not as simple in the mid-IR. Despite the fit being satisfactory for most points, a few multi-modal PSDs show significant departures from it. Comparing the best fits at the two wavelengths, 10.6 μm

transmission exhibits an advantage in path length. The ratio between the link distance in the mid-IR concerning the near-IR ranges from 2 to 3, depending on the visibility value. For instance, at 1 km visibility, the path length increases from 2 km at 1.55 μm to 4 km at 10.6 μm. However, this gain could be much higher in corresponding multi-modal fogs. For instance, if the visibility is 700 m, the path length can be as high as 10 km at $\lambda = 10.6$ μm, while being around 1.5 km for $\lambda = 1.55$ μm .

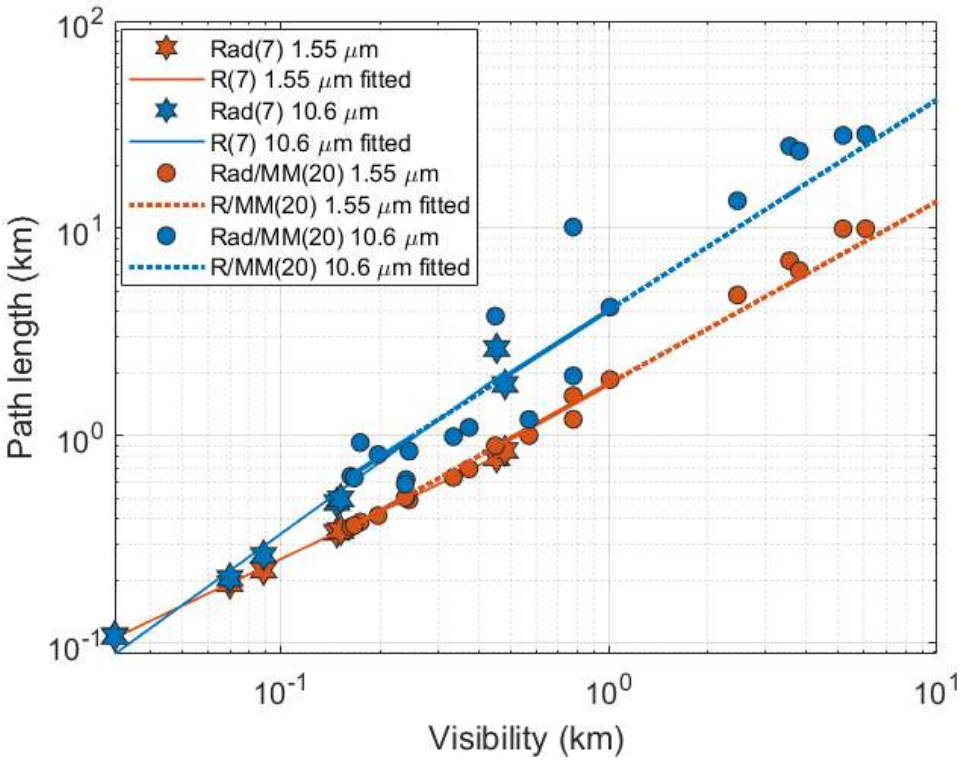

Figure 3.8: FSO path length as a function of the visibility conditions at two wavelengths.

Even though PSD data highlight the key optical properties of fog, these measurements are rare. Hence the PSD-based approach is not practical for modeling purposes. Models to predict the extinction coefficient, and therefore the path loss, over path lengths useful for 5G+ (i.e., around 1 km and above) should rely on extensive measurements of FSO transmission data over a statistically significant period.

3.4 Transmission Measurements in Reduced Visibility

Measurements of optical transmission in reduced visibility help to validate γ-V models when collocated visibility measurements are available. They unveil the wavelength dependence if multiple wavelengths are transmitted

across the same path and highlight effects as the spatial in-homogeneity across the propagation path.

A review of measurements carried out in the early days of FSO and empirical γ-V relationships based on these data are provided in [51]. As the available multi-wavelength transmission data usually included the visible radiation region, visibility was calculated from the transmission measurements. Therefore, in this case, the terms visibility and extinction coefficient in the visible spectrum are equivalent as $V = K/\gamma_{vis}$. Specifically, the data considered in [51] were collected at 0.53-0.63 μm, 1.2 μm, 3.5-4.01 μm and 10-10.6 μm, respectively. The major conclusions drawn from these data are:

– The ratio γ_{vis}/γ_{IR} has a median value of around 1 in both the near-IR and the 3.7 μm mid-IR window and a 90% quantile of 1.2 and 1.5, respectively, if γ_{vis} is less than about 34 dB/km (which means V<500 m if K = 17). In comparison, γ_{vis}/γ_{IR} is somewhat larger in the 10.6 μm window (median and 90% quantile equal to 1.6 and 3.7, respectively).

– IR transmission improves beyond the 500 m visibility threshold value. The effect is noticeable at the longer wavelengths. The largest transmission gain occurs at 10.6 μm, where the median value of γ_{vis}/γ_{IR} is about 9 if V > 500 m.

The above conclusions are consistent with the empirical relationships discussed in Section 3.1.1 and the micro-physical model in Section 3.2. In this work, more recent field data are considered. Specifically, Table C.1 summarizes several experiments carried out over the past 20 years. We focused on measurement campaigns with dual-or multi-wavelength transmission and collocated visibility data. Large mid-IR (8-9 μm) transmission gains over shorter wavelengths are reported by Corrigan et al. [44] and Colvero et al. [62].

Specifically, Corrigan et al. [44] studies the transmission of three wavelengths (1.345, 1.558 and 8 μm) during a moderate fog event with relatively large visibility values. From their Fig. 2, a minimum V of about 0.8 km can be deduced by the Kim model (lower-bound) [49] from 1.345 μm path loss data. The ratio $\gamma_{nIR}/\gamma_{mIR}$ consistently exceeds 2 and can be as high as 4. Two interesting features deserve a comment: first, the differences between the two near-IR windows though not negligible, are within 20%, 1.558 μm propagating better than 1.345 μm. Second, the onset of a light rain episode at the end of the event has a significant impact on path loss due to scavenging: the biggest suspended droplets are washed out by the falling raindrops, leading to a highly wavelength-selective behavior ($\gamma_{nIR}/\gamma_{mIR}$ values as high as 10).

The extensive measurement database in [62] includes more than 100 hours of coastal fog data spreading a visibility range from 20 m to 30 km. Visibility was measured by a CCD camera placed on one side of the link and pointing to a black and white target close to the other link terminal. The CCD camera measured the apparent contrast of the target gathering visibility with the 2% contrast reduction rule. Data highlight a mid-IR (9.11 μm) gain over shorter wavelengths (0.780 μm and 1.550 μm), which is large even at low visibility values. Due to the very short path length (75 m), the atmospheric path loss is very small, even with relatively small visibility values. For instance, it is less than 1 dB at the maximum visibility of 2 km shown in the above figure (that is, T$\geq$0.85).

The other works in Table C.1 include multi-wavelength measurements in the visible and near-IR spectrum [52][59][75][76]. For instance, 1.550 μm transmission through radiation fog is considered [75] and compared with the extinction coefficient predicted by the Kruse model from collocated visibility measurements. The γ-V best fit from data is $\gamma \approx 10/V$ for visibility down to about 50 m (the authors do not state the visibility range used to fit data) against an expected $\gamma = 17/V$, at least when visibility is less than 500 m. It makes a 70% decrease, observed in five of the six events in the database. This consistent difference can hardly be explained by fog in-homogeneity effects. On the other hand, the data at 1.550 μm and 0.532 μm through a moderate fog event (visibility down to 850 m according to the 2% rule) highlight very similar path attenuation values [59]. This time the longer wavelength performs marginally worse after a linear best fit. Measurements in dense advection fog [76], i.e., with larger droplets than in radiation fogs, highlight a very high correlation between visibility and 850 and 950 μm transmission data (over a short 28 m path) and a good agreement between the Kim model and data. Finally, the experiments at 850 μm and 1.550 μm discussed in [52] returned larger γ values than the ones predicted by the models in the 300 m – 1 km range on both wavelengths. Specifically, *K=20.6* at 850 μm and *K=18.2* at 1.550 μm, respectively (visibility calculated by the 2% rule). To the best of the authors' knowledge, this is the only reported example of path attenuation in the near-IR consistently exceeding the corresponding value in the visible region of the spectrum. The micro-physical model proposed by the same authors and based on a gamma PSD, which has been discussed in Section 3.2, explains, at least to a certain extent, the above results.

To conclude, there is no complete agreement among results from different measurement campaigns due to the differences in set-ups and path lengths, which add to the inherent variability of fog. The recent data confirm that mid-

IR propagates much better through haze and fog than the shorter wavelengths. However, it is unclear if this advantage is relevant even in dense fog (visibility of a few hundred meters). Differences between 0.550 μm and the near-IR windows are much less evident, which brings a problem in setting-up models that link visibility to near-IR attenuation, the former being basically inversely proportional to $\gamma_{0.550}$. Finally, the extinction coefficient gathered from transmission data is generally less than the one predicted by γ-V models. This could be due to issues related to visibility measurements or to effects of path in-homogeneity when visibility is measured in a single point.

3.5 Upper and lower bounds model

The simplified FSO power budget equation is presented in (3-11). The terms on the right: system losses (A_{sys}), the transmitted and received power (P_T and P_R) depend on system characteristics, in the present study, they are taken constant and hereafter named link margin M. On the right, we have the receiver area (A_R), the beam divergence (ϑ_T), and the path length (L).

$$\gamma L - 10\log_{10}\frac{A_R}{\pi(\vartheta_T L)^2} + 60 = P_T - P_R - A_{sys} \tag{3-11}$$

As presented above in the FSO power budget equation (see Section 6.1 for further explanation), the available link margin counteracts the sum of the path loss due to atmospheric attenuation (γL) and the one due to geometric beam-spreading. Differentiating the power budget equation in (3-11) leads to (3-12). The step-by-step differentiating process is in Appendix D.

$$\frac{dL}{L} = -\left[1 + \frac{20}{\ln 10}\frac{1}{\gamma L}\right]^{-1}\frac{d\gamma}{\gamma} \tag{3-12}$$

Last, we calculate the sensitivity of γ to V at 1.550 μm using lower and upper bounds for γ. As the Kim model has discontinuous derivatives at the edge points of each segment, we use third-order polynomials between the low visibility segment, i.e., $V \leq 0.5$ km (basically, wavelength-independent and approximated by $\gamma = K/V$) and the high-visibility range, $V \geq 6$ km, which fits well within the Rayleigh regime, where again the exponent q is constant. Hence we obtain (3-13)

$$\gamma = \frac{p_1}{V^3} + \frac{p_2}{V^2} + \frac{p_3}{V} + p_4 \tag{3-13}$$

and, imposing the continuity of the derivatives, we get $p_1 = -4.417$, $p_2 = 17.783$, $p_3 = -1.144$ and $p_4 = 0.453$. The new curve, which works as a

lower bound on γ, is plotted in Figure 3.9-(a) as an example for Rio de Janeiro. Another example is presented in Figure 3.2-(b) and labeled as the "Kim (smoothed)". Figure 3.9 (b) presents statistics of the γ-V conversion obtained for the measured visibility of Rio de Janeiro. The curve is labeled as the "Lower bound model".

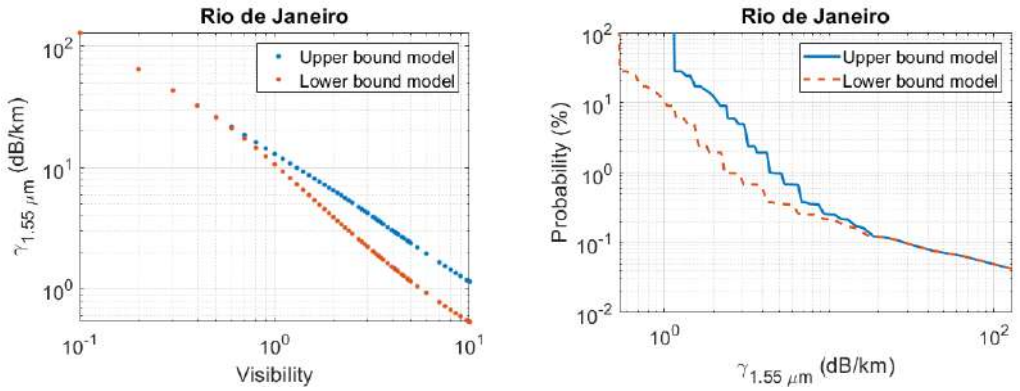

(a) (b)

Figure 3.9: Extinction coefficient at 1.55 μm (labeled as Specific attenuation due to fog) for the visibility measurements of Rio de Janeiro.

Similarly, we identify an "upper bound." This time we use different visibility thresholds as they look to better fit the micro-physical model's outcomes. Specifically, the wavelength-independent segment goes up to $V = 2$ km, whereas the Rayleigh regime is made to start from $V = 10$ km ($q = 1.3$). The polynomials are now constrained to pass through the PSD point of Figure 3.2-(b) with the maximum γ value at 10 km. The resulting coefficients are: $p_1 = -51.525$, $p_2 = 53.242$, $p_3 = 2.380$ and $p_4 = 0.429$. Figure 3.9 panel (a) presents the specific attenuation calculated for Rio de Janeiro using the proposed upper and lower bound models. Panel (b) presents the CCDF of the models applied to the visibility measurements of Rio de Janeiro.

3.6 Uncertainty in measurements

There are sources of uncertainty in the measurements of the physical properties of the environment. In particular, we spotted two significant sources of uncertainty in the conversion from visibility measurements to the extinction coefficient of fog. These are 1) the way visibility is measured and 2) the effect of fog micro-physics. Moreover, there are uncertainties due to fog characteristics, which is very much affected by micro-climate variations.

We follow the next procedure to study the uncertainties in the conversion from visibility measurements to the specific attenuation due to fog. First, We

get the relationships (3-14) between the differentials of λ and V, using the upper bound model:

$$\frac{d\gamma}{\gamma} = \begin{cases} -\dfrac{dV}{V}, & V < 2km, V > 10km \\ -\dfrac{3p_1 + 2p_2V + p_3V^2}{p_1 + p_2V + p_3V^2}\dfrac{dV}{V}, & 2km \leq V \leq 10km \end{cases} \tag{3-14}$$

Then, we can obtain the uncertainty on path length considering the fog effect by substituting (3-14) into (3-12), that is $\frac{d\gamma}{\gamma}$ into $\frac{dL}{L}$. Figure 3.10 shows the link distance at 1.550 μm as a function of the visibility across the link, according to the smoothed Kim model and the upper bound model presented in Section 3.5, respectively link distance comes out of (3-10), once the other system parameters are specified. We use standard values of state-of-the-art commercial FSO links, i.e., $\vartheta_T = 0.5$ mrad, $A = 0.01$ m^2 and $M = 50$ dB.

The shaded areas in Figure 3.10 represent the uncertainties due to the combined effect of the accuracy of visibility measurement and the γ-V model. The perimeters of the two shaded areas in gray correspond to 20% and 40% uncertainty bounds on V, respectively.

For instance, if $V = 1$ km, and $dV = 0$, the path length value obtained with the smoothed Kim model is about $2V$, whereas it is $1.6V$ with the upper bound model (i.e., a 25% smaller). As far as the slope of the γ-V curve is constant on log-log axes and, at the same time, atmospheric attenuation prevails over beam spreading loss, that is, if $V \leq 500$ m, then $\Delta L/L \cong \Delta V/V$ (replacing differentials by finite differences). Beyond this threshold, $\Delta L/L$ (in magnitude) slightly increases over $\Delta V/V$.

In the worst case ($\Delta V/V = 40\%$), the combined effect of micro-physics and visibility accuracy results in estimates of the path length, which differ by a factor close to three if V=1 km and close to four if V=2 km, respectively.

Another source of uncertainty for practical FSO design is that visibility measurements are unavailable in the FSO installation location. Indeed, fog is significantly affected by the micro-climate. As an example, Figure 3.11 highlights the difference between visibility records collected at Linate airport and the Politecnico di Milano campus (Italy). The airport is located in a rural area just outside the city borders, and it is only 5 km away from Politecnico, which is in the city area. There are notable differences between the two cumulative distribution functions if visibility is less than 1 km. The probability that $V < 0.5$, 1, and 2 km are three times, two times, and 25% higher at Linate than at Politecnico. Even though these numbers are indicative, as measurements in Linate have a much coarser resolution in time and space, the differences in visibility will reflect a corresponding decrease of the optical

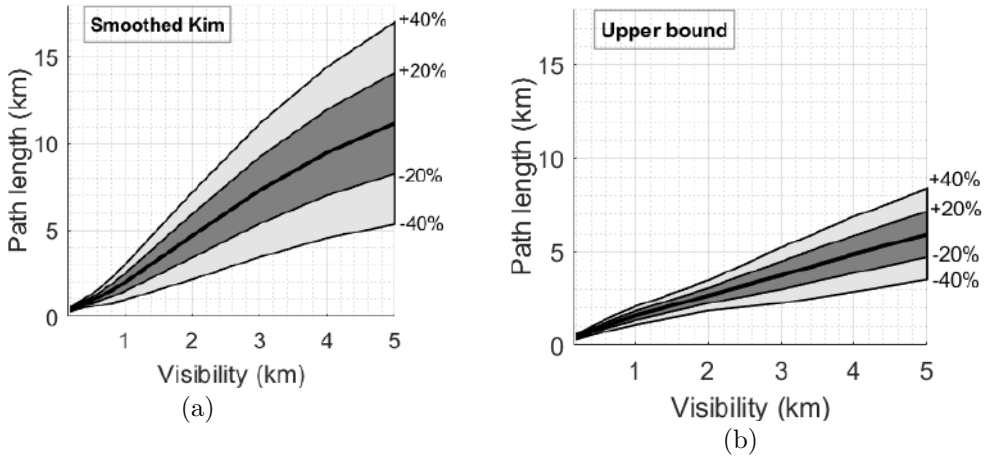

Figure 3.10: Path length as a function of the visibility across the path (thick black lines) according to the smoothed Kim model and to the upper bound curve studied in Section 3.5.

extinction coefficient in the urban area for the same percentage. We can also see the micro-climate effect in New York presented in Figure 2.2. One station is located in Central Park, an extensive green land around 3.4 km^2 situated in the urban area of New York. The second station is at John F. Kennedy Airport, 20 km from Central Park (see Figure 2.1) in a coastal area. The visibility at 99%, 99.9%, and 99.95% of the time are four times, more than five times, and three times higher at Central Park than at JFK Airport (see Table 2.2 for further details). Therefore, these visibility differences will also be evident in the specific attenuation due to fog in the coastal area for the same percentage of the time.

3.7 Discussion

Assuming that fog microphysics, i.e., the PSD and scattering theory, provide a rigorous method for predicting the path loss (per unit length) due to fog. We have that 1) the data-set used here does not cover the full range of possible fog PSDs, 2) the probability of occurrence of a certain PSD is unknown, and the micro-physical model does not have a practical application to FSO design. However, validating the simple γ-V models are a useful tool. Moreover, when the micro-physics has an impact, it makes sense to identify lower and upper bounds on γ, as visibility alone does not capture the complexity of the process. In the following, we discuss a few issues and limitations of the methodology proposed in Sections 3.1 and 3.2.

Equation (3-2) is based on the Bouguer-Lambert law of exponential decay, which holds when multiple scattering effects are negligible. Multiple-

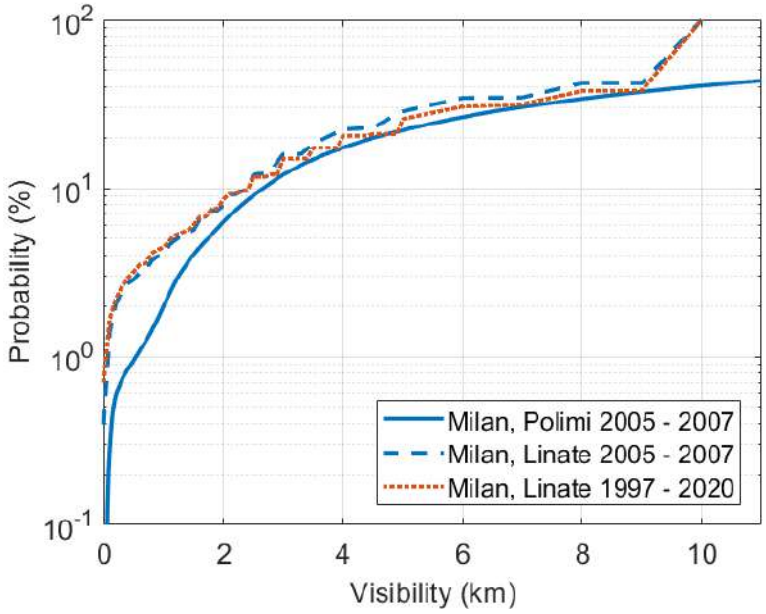

Figure 3.11: The cumulative distribution function of the visibility measured in Milan in two different locations: Politecnico di Milano (urban area) and Linate airport (rural area).

scattering actually increases the number of photons impinging on the receiver, hence the received power. Its impact depends, among others, on the path length, the wavelength, and the PSD. To quantify multiple-scattering effects through fog, we carried out simulations based on the approach used in [91]. Path attenuation decreases by less than 1% concerning the simple calculation in (3-5) when considering multi-modal radiation fogs (visibility values of about 180 m) across a path length of 500 m. In the presence of heavy advection fog (visibility values down to 50 m), path attenuation decreases by 5% after 200 m. However, extremely low visibility values would produce link outage as practical FSO path lengths are a few hundred meters at least. Multiple-scattering corrections do not significantly affect the propagation loss through fog.

The conversion into path attenuation across a path length L is a limitation of the micro-physical model and all models predicting the extinction coefficient. This is usually done by the simple scaling law γL. As a result of the inhomogeneous distribution of fog in space, path attenuation, on average, will be less than the one estimated from visibility or PSD data sampled at a single point. In this respect, visibility measurements collected by human observations of distant objects are better than automatic sensors, which usually carry out single-point measurements. However, to the authors, no available models include the above path reduction factor.

The best-fit curves of the path length of an FSO link as a function of

the atmospheric visibility in the mid-IR ($\lambda = 10.6$ μm) and in the near-IR ($\lambda = 1.550$ μm) window show that the ratio between the link range at mid-IR respect to the near-IR ranges from 2 to 3. The gain could actually be higher due to the scatter in the extinction coefficient data at 10.6 μm produced by different PSD shapes. Even though PSD data highlight the key optical properties of fog, these measurements are rare. Hence the PSD-based approach is not practical for modeling purposes.

A different approach to validate γ-V models and to evaluate the impact of the spatial distribution of fog relies on measurements of optical transmission and visibility. The latter can be measured by visibility sensors displaced along the link. Alternatively, path-averaged visibility values can be obtained from multi-wavelength transmission experiments featuring a laser in the visible range. A survey of older transmission measurements through fog is in [51]. Best fit curves and $\pm\sigma$ bounds were derived for the extinction coefficient at three different IR wavelengths (1.2, 3.7, and 10.6 μm) against the corresponding visibility values obtained from data in the visible range. The best fit line at 1.2 μm (not shown) is close to the Kim model. Data at 10.6 μm are scattered. However, most fogs considered here are within the $\pm\sigma$ bounds calculated in [51] or close to them (see Figure 3.2-(b)). Possible issues with the results of [51] are that: 1) the dataset includes very different path lengths (from 17 m to 2.6 km), and 2) best-fit lines at the three wavelengths are drawn from different datasets.

Recent measurements in the first optical window indicate that $\gamma = K/V$, with $K = 13$ or $K = 17$, depending on the visibility sensor, fits the data fairly well, regardless of the environment and the path length [76][77], even though there are exceptions. The results at 1.550 μm are different and sometimes disagree with each other. For instance, the authors in [75] compared 1.550 μm measurements through radiation fog across a 75 m path with visibility data. The best data fit is $\gamma = 10/V$ for V down to about 50 m (the authors did not state the visibility range used to fit data, though) against an expected $\gamma = 17/V$, at least when $V \leq 500$ m. The above trend was observed in five of the events in their database. On the other hand, transmission data at 1.550 μm and 0.532 μm during a moderate fog event (visibility down to 850 m according to the 2% rule) highlighted very similar path attenuation values [59]. Finally, the outcomes of experiments at 850 μm and 1.550 μm in [78] show larger γ values on both wavelengths than the ones predicted by the models if $0.3 \leq V \leq 1$ km. Specifically, $K = 20.6$ at 850 μm and $K = 18.2$ at 1.550 μm, respectively (visibility calculated by the 2% rule). There is a need for FSO field data featuring collocated visibility measurements and tests

carried out over a significant number of events.

4
Rain Attenuation on FSO

Although at mid-latitude continental climate, FSO availability is usually upper-bounded by fog occurrence, impairments such as rain could be statistically relevant in different environments. For instance, based on the global surface data repository available at the Wyoming University [33], we find that visibility reduction due to fog can be negligible in cities located in tropical regions with respect to the one due to rain. To illustrate that, in Guayaquil, Ecuador (i.e., a city with a humid tropical climate), the probability of low visibility (lower than 0.1% of the time for $V \leq 1$ km) is negligible. Moreover, in this city, rain is the main cause of visibility reduction for $V \leq 1$ km. It causes more than 90% of the decrease while fog is lower than 0.01%, as presented in Figure 2.13.

This chapter is devoted to the analysis of FSO path attenuation due to rain. The statistical characterization of rain attenuation moves from first-order statistics of the rainfall intensity. Hence, the first part of this chapter presents the global ITU model of the CCDF of rainfall rate and its application to three locations: Milan, in Italy; Rio de Janeiro, in Brazil and Guayaquil, in Ecuador. Then, we consider a few different rain attenuation prediction models applicable to terrestrial microwave links with the obtained rainfall statistics, specifically ITU-R P.530-18 model [46], Brazilian model [82], Lin model [83] and Moupfouma model [84]. The models are modified to be applicable at optical frequencies. We estimate rain attenuation for the three selected locations to compare the models. Moreover, rain attenuation is calculated by the definition of visibility considering the measured values of visibility during rain events from the Wyoming repository. Finally, we consider the multiple scattering effects when the optical beam interacts with several particles before arriving at the receiver. It traduces into a reduction of the path attenuation caused by rain occurrence. We quantify it through the multiple scattering gain, which is a function of the path length and the characteristics of the rain droplets.

4.1 Rainfall rate estimation by ITU-R P.837-7

Since reliable long-term local rainfall rate data is not available around the globe, Annex 1 of the ITU-R P.837-7 provides rainfall rate distribution maps to predict rainfall rate statistics with a 1-min integration time [85]. This prediction method calculates the rainfall rate exceeded for a desired average annual probability of exceedance at a given location on the surface of the Earth using digital maps of monthly total rainfall and monthly mean surface temperature.

4.1.1 Parameters

The input parameters are:

- p: Desired annual probability of exceedance (%).
- *Lat*: Latitude of the desired location (degrees, N).
- *Lon*: Longitude of the desired location (degrees, E).

The main output is the rainfall rate, R_p, exceeded for the desired probability of exceedance (mm/h).

4.1.2 Procedure

1. Definition of month number and number of days: For each month of the year, define the month number, i from 1 to 12, and the number of days in each month, N_i.

2. For each month number, i, determine the monthly mean surface temperatures, $T_i(K)$, at the desired location (Lat, Lon) from reliable long-term local data.
   If reliable long-term local data is not available, the monthly mean surface temperatures, $T_i(K)$, at the desired location (Lat, Lon) can be obtained from the digital maps of monthly mean surface temperature in Recommendation ITU-R P.1510 [86] applying a bi-interpolation procedure as described in Annex 1 Paragraph 1b of Recommendation ITU-R P.1144 [87].

3. For each month number i, determine the monthly mean total rainfall, MT_i (mm), at the desired location (Lat, Lon) from reliable long-term local data.
   If reliable long-term local data is not available, the monthly mean total

rainfall at the desired location (Lat, Lon) can be determined from the digital maps of monthly mean total rainfall, MT_i (mm).

4. For each month number, i, convert $T_i(K)$ to $t_i(^\circ C)$.

5. For each month number, i, calculate r_i in (mm/h) as follows:

$$\begin{cases} r_i = 0.5874e^{0.0883\times t_i} & for t_i \geq 0^\circ C \\ r_i = 0.5874 & for t_i < 0^\circ C \end{cases} \tag{4-1}$$

6. For each month number, i, the monthly probability of rain is:

$$P_{0_i} = 100\frac{MT_i}{24 \times N_i \times r_i}(\%) \tag{4-2}$$

7. For each month number, i: if $P_{0_i} > 70$ set:

   - $P_{0_i} = 70$
   - $r_i = \frac{100}{70} \times \frac{MT_i}{24N_i}$

8. The annual probability of rain $P_{0_{annual}} = P(R > 0)$ is calculated by:

$$P_{0_{annual}} = \frac{\sum_{i=1}^{12} N_i \times P_{0_i}}{365.25}(\%) \tag{4-3}$$

9. Validation: If $p \geq P_{0_{annual}}$, then $R_p = 0$ (mm/hr).
   if $p \leq P_{0_{annual}}$ adjust the obtained rainfall rate, named here ass R_{ref}, until the absolute value of the relative error between the annual rainfall rate probability of exceedance, $P(R > R_{ref})$, and the desired rainfall rate probability of exceedance, p, is less than 0.001%.

   At the end of the adjustment process, set $R_p = R_{ref}$

4.1.3 Application

We select three locations with different climatic characteristics to study the effects of rain on the FSO link. The list of the designated airports and their coordinates are presented in Table 4.1. Using the parameters in Table 4.1 as input, we calculate the climatological probability of rain at each location by applying the estimation explained in the previous section. The CCDF of climatological rainfall rate for the three sites is presented in Figure 4.1. Table 4.2 lists the rainfall rate exceeded for $p = 0.01\%$, since it is a required parameter for some of the propagation models available in the literature, and the probability of rain on an average basis for the three selected locations ($P_{0_{annual}}$).

Table 4.1: Selected locations list to study the effect of rain on FSO links.

Location	**ICAO code**	**Latitude**	**Longitude**
Milano, Linate	LIML	45.43	9.28
Rio de Janeiro, Galeão	SBGL	-22.82	-43.25
Guayaquil, Simon Bolivar	SEGU	-2.15	-79.88

Table 4.2: Rainfall rate, R_p, exceeded for $p = 0.01\%$ and probability of rain on log-term basis, $P_{0_{annual}}$ (%) estimated using ITU-R P.837-7 [85].

Location	**ICAO code**	R_p **(mm/hr)**	$P_{0_{annual}}$ **(%)**
Milano, Linate	LIML	34.54	7.21
Rio de Janeiro, Galeão	SBGL	67.37	3.02
Guayaquil, Simon Bolivar	SEGU	60.80	3.01

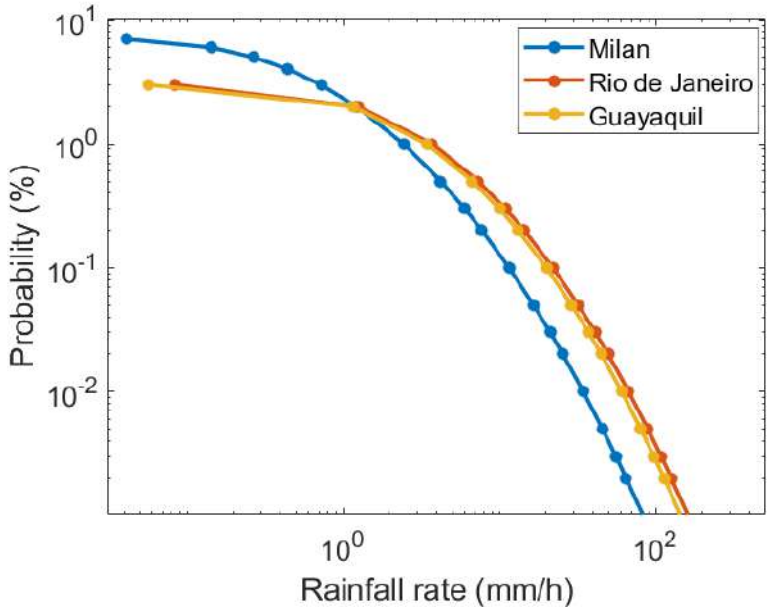

Figure 4.1: Climatological P(R) for three locations estimated using ITU-R P.837-7 [85].

Regarding the results,the rainfall rate exceeded for 0.01% of the time in Rio de Janeiro is the highest among the selected cities. Similarly, in Guayaquil it is almost 61 mm/h; those are typical figures of tropical climates. On the other side, in mid-latitude climates, as in Milan, the rainfall rate exceeded for $p = 0.01\%$ is lower, around 35 mm/h. However, the probability of rain in an average year is higher in the mid-latitude climate, whereas in cities with tropical climates is lower than 5%.

In the next section, we estimate the propagation through rain using the statistics of rain obtained above.

4.2 Propagation models through rain

We can use different methods available in the literature to estimate the rain attenuation at terrestrial links with the information about the rainfall rate statistics at the desired location. In the present work, the statistics are calculated using the Recommendation ITU-R P.837-7 [85]. The selected models consider as input:

1. The long-term rainfall rate probability distribution. In this case, it is the CCDF estimated using the Recommendation ITU-R P.837-7 [85] for the desired location.

2. The path length for the case of attenuation due to rain (in dB). For the scope of this study, we use two values: 1 km and 3 km.

3. The operation frequency.

4. The power-law coefficients k and α for the conversion of the rain rate, R, into specific attenuation γ, considering the micro-physics of the raindrops. The power-law is presented in (4-4). Alternatively, the coefficients can be calculated with the expressions in Recommendation ITU-R P.838 [88] or taken from the literature. In the present study, we use the micro-physics approach. The DSD gamma distribution is indicated in Table 4.3 [89], where the shape parameters are the input value for the gamma function. The coefficients in the table work in the optical transmission windows usually adopted by commercial FSO systems, which are the classical 0.780–0.850 and 1.520–1.600 μm bands.
   Figure 4.2 presents the specific attenuation due to rain estimated with (4-4) considering the coefficients in Table 4.3 calculated for 1.55 μm. For instance, if the rainfall rate is 100 mm/h, the specific attenuation due to rain varies from around 10 dB/km when $\mu = -3$, to more than 45 dB/km when $\mu = 7$. Thus, the specific attenuation due to rain is quite sensitive to the shape parameter we select, meaning it is susceptible to raindrop size distribution.

$$\gamma = kR^{\alpha} \tag{4-4}$$

Table 4.3: Coefficients α and k for multiple values of the DSD shape parameter (μ) [89].

Shape parameter μ	$\boldsymbol{k}$	α
-3	4.0684	0.2077
-2	2.2838	0.4050
-1	1.5921	0.5506
0	1.2924	0.6436
1	1.1394	0.7057
2	1.0505	0.7497
3	0.9938	0.7823
4	0.9551	0.8074
5	0.9273	0.8273
6	0.9065	0.8435
7	0.8905	0.8569
8	0.8779	0.8682

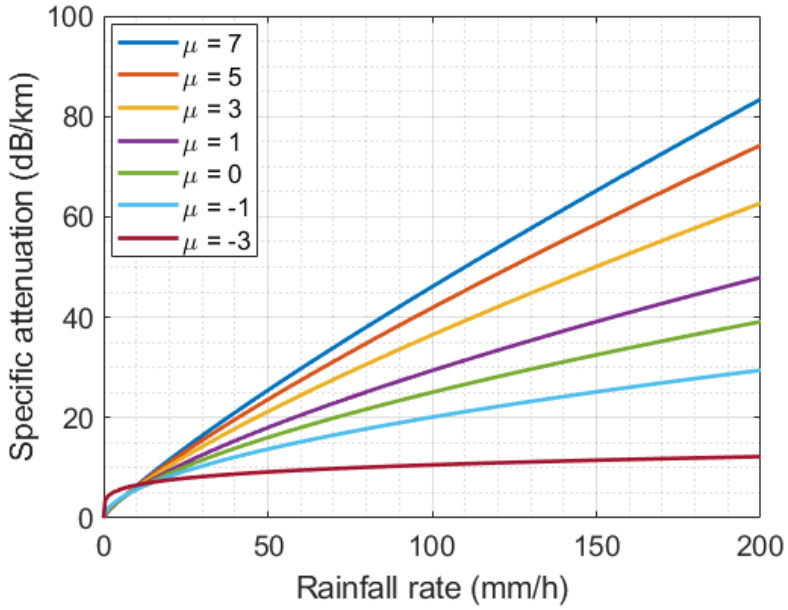

Figure 4.2: Specific attenuation due to rain against rainfall rate for different values of the shape parameter μ as indicated in Table 4.3.

4.2.1 ITU-R P.530-18 model

The Recommendation ITU-R P.530-18 presents propagation data for planning terrestrial line-of-sight radio systems. The rain prediction method presented in this recommendation is based on a simplified model for the temporal and spatial random variations of the rain field causing the attenuation. This recommendation provides a technique for estimating long-term rain attenuation statistics, assuming that an equivalent cell of uniform rainfall rate can

represent the effect of the non-uniform rainfall along the propagation path. The equivalent rain cell may intercept the path at any position with equal probability. The prediction procedure proposed by the recommendation is valid worldwide for frequencies up to 100 GHz and path lengths up to 60 km [46].

To obtain the attenuation due to rain, we follow the procedure:

1. Obtain the rain rate $R_{0.01}$ exceeded for 0.01% of the time (with an integration time of 1 min). Since this information is not available from local sources of long-term measurements, it was estimated from the information given in Recommendation ITU-R P.837-7 [85] as explained in Section 4.1.

2. Calculate of the specific attenuation, γ_R (dB/km) for the frequency, polarization, and rain rate of interest using Recommendation ITU-R P.838-3 [88]. That is the expression in (4-4) but using the coefficients for the DSDs in Table 4.3.

3. Calculate of the effective path length, L_{eff}, of the link by multiplying the actual path length L by a distance factor r. An estimate of this factor is in equation (4-5), f (GHz) is the frequency, and α is the exponent in the specific attenuation model from the previous step.

$$r = \frac{1}{0.477L^{0.663}R_{0.01}^{0.073\alpha}f^{0.123} - 10.579(1 - exp(-0.224L))} \tag{4-5}$$

4. Estimate of the path attenuation exceeded for 0.01% of the time is given in (4-6) in dB.

$$A_{0.01} = \gamma_R L_{eff} = \gamma_R Lr \tag{4-6}$$

5. The attenuation exceeded for $0.01\% \leq p \leq 1\%$ may be deduced from the power law in (4-7). Where C_1, C_2, and C_3 depend on the frequency [46].

$$A_p = A_{0.01}C_1 p^{-(C_2 + C_3 \log p)} \tag{4-7}$$

Extension to Optical Frequencies

The dependence of the ITU-R P.530-18 model with the frequency is mainly due to the distance factor in (4-5) up to a probability equal to 0.01%. We find that as the frequency reduces, the distance factor decreases.

Unlike other models, in which r is independent of the frequency, the distance factor calculated with with (4-5) in the ITU-R model is slightly greater than one at the maximum frequency value that the model works, that is $f = 100$ GHz [46]. For $0.01\% \leq p \leq 1\%$ of time, the recommendation considers the coefficients C_1, C_2, and C_3 depending on the frequency. Applying the current model to the optical frequency equivalent to $\lambda = 1.55$ μm, we find

a distance factor around 0.5 for $L = 1$ km. The estimated attenuation due to rain will be highly reduced compared to the actual path length. The effect of the frequency in the estimated attenuation is exhibited in Figure 4.3, for the power-law coefficients corresponding to $\mu = 1$ in Table 4.3 and the log-term statistics of rainfall rate in Milan. Therefore, to avoid an increased impact of the distance factor on the actual path length, we decide to arbitrary apply the ITU-R P.530-18 model for the maximum frequency allowed by the model (i.e., $f = 100$ GHz) when working at optical frequencies.

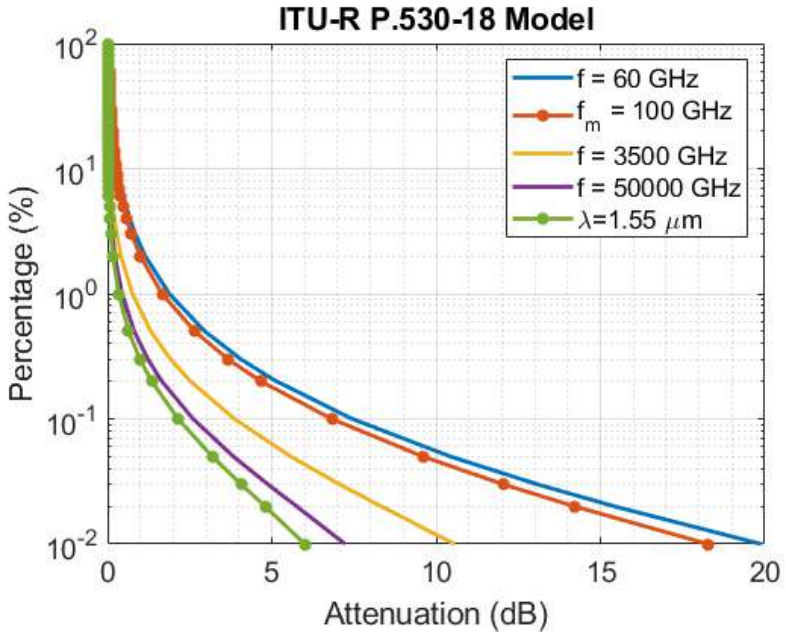

Figure 4.3: Normalized rain attenuation prediction for Milan for different frequencies and considering remaining constant as parameters.

4.2.2 Brazilian model

One limitation of the current ITU-R model is that the attenuation is predicted only considering the rainfall rate exceeded for 0.01% of the time. Then, an extrapolation function is used to obtain other percentages of time. Consequently, two different locations may present the same attenuation distributions if the local values of rainfall rate exceeded for 0.01% of the time are equal, not considering the behavior of the rainfall rate for other percentages of time.

The Brazilian model, proposed by Silva Mello et al. in [82], is a semi-empirical prediction method that uses the full rainfall rate distribution to predict the attenuation distribution. It also introduces the concept of effective rainfall rate to avoid inconsistencies and to retain the same general expression

for effective path length as in the ITU-R model. The effective rainfall rate relates to the contribution of a homogeneous rain with a length equal to the effective path length [106].

The steps to estimate the rain attenuation are:

1. Calculate the effective path length (equivalent path length with homogeneous rain) with (4-8), where L_0 is given in (4-9).

$$L_{eff} = \frac{1}{1 + \frac{L}{L_0}} L \tag{4-8}$$

$$L_0 = 119 R^{-0.244} \tag{4-9}$$

2. Obtain the effective rain rate as in (4-10).

$$R_{eff} = 1.763 R^{0.753 + \frac{0.197}{L}} \tag{4-10}$$

3. The rain attenuation exceeded for $P(\%)$ of time, *A(P)*, is obtained by (4-11).

$$A(P) = \gamma_R L_{eff} = k R_{eff}^{\alpha} L_{eff} \tag{4-11}$$

Extension to Optical Frequencies

The effective path length proposed in this model is independent of the frequency. As an example, Figure 4.4 presents the effective path length calculated with (4-8) and (4-9), against the estimated rainfall rate for Rio de Janeiro. The actual path length used for panel (a) is $L = 1$ km, whereas for panel (b) is $L = 3$ km. Panels (a) and (b) also include the curves of the effective rainfall rate calculated from the actual rainfall rate using (4-10). When $L = 1$ km, L_{eff} varies between 0.97 to 1 km depending on the rainfall rate, that is a maximum reduction of 3% compared to the actual path length. At the same time, the effective rainfall rate for the same path is higher than the actual value. For instance, when $R = 100$ mm/h, the effective value reaches 140 mm/h, which is 40% higher than the actual rainfall rate. On the contrary, when the path length equals 3 km, the effective rainfall rate reduces compared to the actual rainfall rate. As an example, when $R = 100$ mm/h, the effective value is 24% lower, that is $R_{eff} = 76$ mm/h. In terms of the path length, L_{eff} is between 2.75 and 3 km, which is up to 9% of path reduction compared with the actual path. The attenuation dependence on frequency, for this model, is entirely described by the parameters k and α, as it should be expected from the physical point of view. Therefore, for the case of optical frequencies, we decide to follow the model as proposed but consider the parameters k and α corresponding to optical wavelengths, as in Table 4.3.

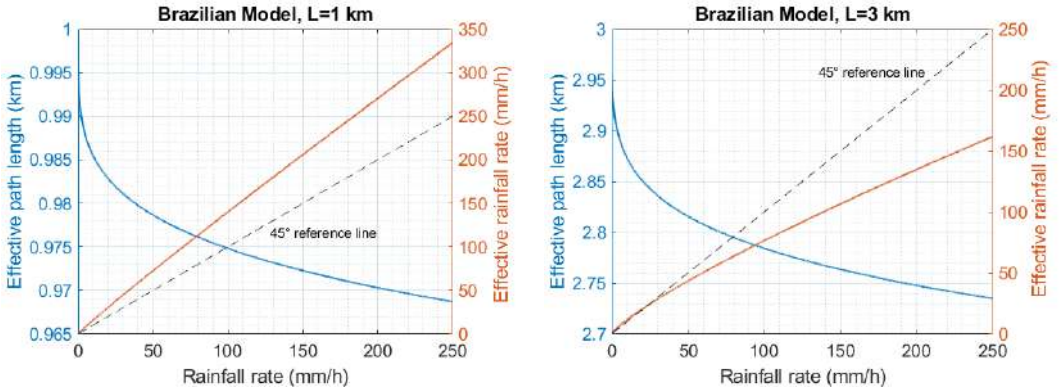

(a) (b)

Figure 4.4: Effective path length against the rainfall rate for Rio de Janeiro considering the Brazilian Model and two path lengths: 1 and 3 km.

4.2.3 Lin model

The Lin model also uses a path reduction factor to take into account the effect of rain variations along the propagation path [83]. Depending on the rainfall rate, a modification factor, $f(R)$, is estimated based on distribution measurement of 5-minute point rain rates from data published by the National Climatic Center for U.S. locations from August 1973-July 1974 with rain attenuation at 11 GHz on a 42.5km path. This model largely overestimates the measured values at higher rain rates [102].

The procedure is as follows:

1. Calculate the path reduction factor, r:

$$r = \frac{1}{1 + \frac{L}{f(R)}} \tag{4-12}$$

Where *f(R)* is:

$$f(R) = \frac{2623}{R - 6.2} \tag{4-13}$$

2. Calculate the rainfall attenuation exceeded for a percentage P using (4-14). Coefficients k and α to obtain the specific attenuation, can be either calculated with ITU-R P.838-3 [88] or from Table 4.3. Then, the effective path length is given by $L_{eff} = Lr$.

$$A(P) = kR^{\alpha}L_{eff} = kR^{\alpha}Lr \tag{4-14}$$

Extension to Optical Frequencies

In the Lin model, the path reduction factor, r, depends on a path length term, $L(R)$, which in turn is a function of the long-term statistics of rainfall rate as indicated in expressions (4-12) and (4-13). Finally, the effective path

length is the product between the path reduction factor r, and the actual path length, L. Figure 4.5 panel (a) indicates the obtained values of L_{eff} for Rio de Janeiro, assuming $L = 1$ km, and in panel (b) for $L = 3$ km. For this model and $L = 1$ km, L_{eff} varies between 0.94 to 1 depending on the rainfall rate, that is a maximum reduction of 6% compared to the actual path length; whereas for $L = 3$ km, it varies from 2.5 to 3km, that is up to a 16% of path reduction regards the actual path. For this model, the attenuation dependence on frequency is through the k and α parameters; then, we use the parameters k and α corresponding to optical wavelengths, as in Table 4.3.

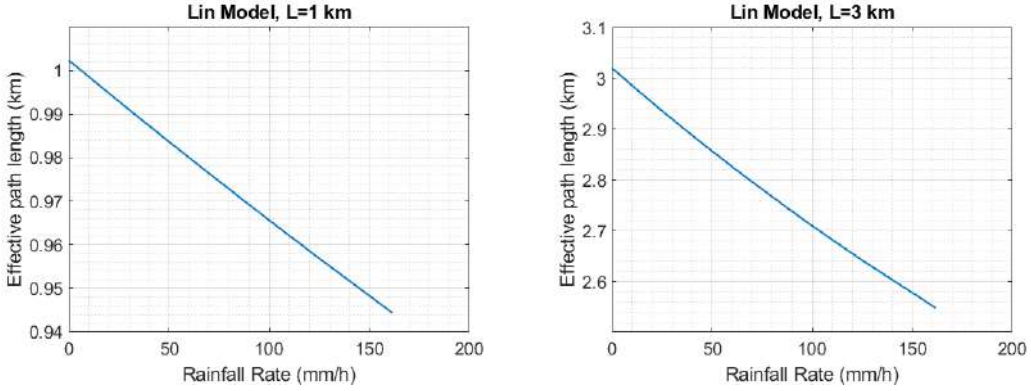

(a) (b)

Figure 4.5: Effective path length against the rainfall rate for Rio de Janeiro considering the Lin model and two path lengths: 1 and 3 km.

4.2.4 Moupfouma model

It considers experimental data of about 30 terrestrial links in Congo, Japan, the U.S., and Europe. The frequency ranges from 7 to 38 GHz, whereas the path length reaches up to 58 km [84].

The procedure is as follows:

1. Calculate the effective path length, L_{eff}, that is the product between the path length and a correction factor depending on the rainfall rate, *R(P)*, as presented in (4-15) for $L \leq 7$ km and, in (4-16) when $L > 7$ km.

$$L_{eff}(P, L) = L \times exp\left(-\frac{R}{1 - 100R}\right) \quad L \leq 7km \tag{4-15}$$

$$L_{eff}(P, L) = L \times exp\left(-\frac{R}{1 + \frac{44.2}{L}^{0.78} R}\right) \quad L > 7km \tag{4-16}$$

2. The attenuation prediction is calculated considering the full rainfall rate function R as in (4-17).

$$A(P) = kR^{\alpha}L_{eff}(P, L) \tag{4-17}$$

Extension to Optical Frequencies

Figure 4.6 presents curves of the effective path length, L_{eff}, against the rainfall rate for two values of the actual path length: $L = 1$ km and $L = 7$ km. For $L = 1$ km, L_{eff} is approximately equal to the actual path L. Whereas for the longest path example, we see a considerable decrease in the length. For instance, the effective path length is 25% lower than the actual path when the rainfall rate is 1 mm/h, and when $R \geq 25$ mm/h, the effective path length reaches its lowest value, 30% lower than the actual path. This behavior is due to the exponential term in (4-16). For FSO, the path length of interest is up to 3 km, then we consider only the blue curve Figure 4.6, with values of path reduction factor around 1. The final expression of attenuation depends on the frequency through the parameters k and α as indicated in (4-17). Therefore we use those corresponding coefficients from Table 4.3.

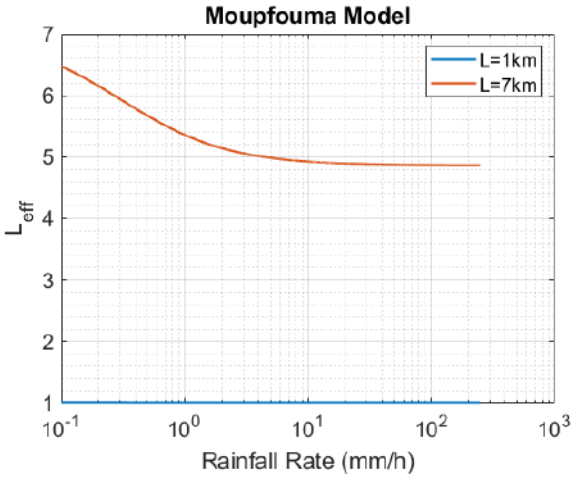

Figure 4.6: Effective path length against the rainfall rate considering the Moupfouma model.

4.3 Application of the Models and Discussion

We estimate the rain attenuation for the three selected locations (Table 4.1) considering as input the coefficients α and k for the shape parameter $\mu = 1$ in Table 4.3, and values of the path length that meet the requirement for backhauling in 5G and beyond systems (i.e., 1 km and 3 km). The respective CCDFs are presented in Figures 4.7, 4.8 and 4.9 for Milan, Rio de Janeiro, and Guayaquil. As a reference, the black dashed curve corresponds to the attenuation due to rain estimated using the effective path length equal to the actual path length, $L_{eff} = L$, that is, assuming the distance reduction factor

equals 1, $r = 1$. The specific attenuation for the reference curve is given by expression (4-4) with the same coefficients α and k.

Lin and Moupfouma's models provide the best agreement with the curve with a path reduction factor of 1; we can see the overlapping curve in the figures. Those two models also agree with measurements as found in [89]. Alternatively, the model proposed by the Recommendation ITU-R P.530-18 presents some drawbacks since it only considers the rainfall rate at 0.01% of the time and the dependence of the effective path length on the frequency. It reflects in underestimating the attenuation due to rain, especially when the size of the link increases, as seen in panels (b) of Figures 4.7, 4.8 and 4.9. In contrast, the Brazilian model clearly overestimates the attenuation values. This behavior may be due to the introduction of the effective rainfall rate concept together with the effective path length. The dependence of the effective rainfall rate in short paths (see Figure 4.4) on the actual rainfall rate traduces in overestimating the reference curve. When the path length is 3 km, this model still present higher attenuation values than the other models, but to a lower extent than in shorter links.

An important finding in this section is that the path reduction factor is approximately equal to 1 in all models. Therefore, for FSO as a back-hauling for 5G and beyond systems, the path reduction factor is a term we do not need to consider since the objective paths are up to 3 km.

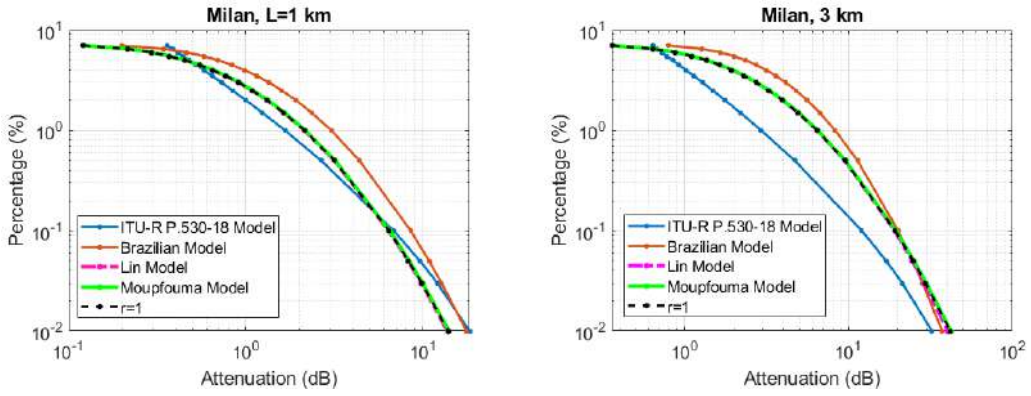

Figure 4.7: Rain attenuation prediction for Milan considering two path lengths and using the power-law coefficients corresponding to $\mu = 1$ in Table 4.3.

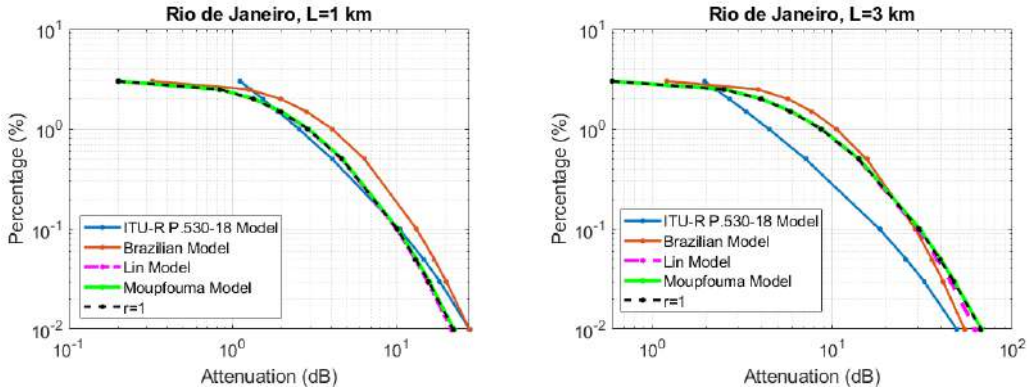

(a) (b)

Figure 4.8: Rain attenuation prediction for Rio de Janeiro considering two path lengths and using the power-law coefficients corresponding to $\mu = 1$ in Table 4.3.

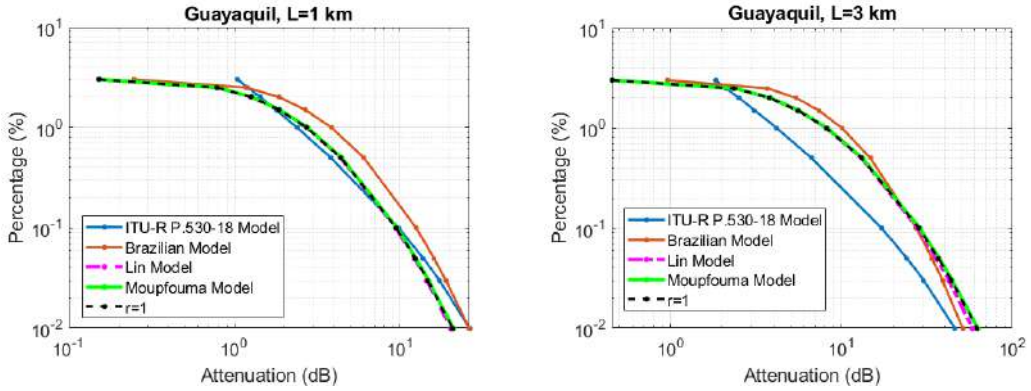

(a) (b)

Figure 4.9: Rain attenuation prediction for Guayaquil considering two path lengths and using the power-law coefficients corresponding to $\mu = 1$ in Table 4.3.

4.4 Rain attenuation from visibility measurements

Since rain occurrence directly affects visibility, and, in turn, low visibility impacts the optical signal, we estimate attenuation due to rain considering measurements of visibility during rain events. In the present study, we consider the visibility data from the Wyoming repository [33] that are tagged as rain and calculate the corresponding CCDF. After that, the visibility is converted into attenuation by the expression (3-2):

$$\gamma = K/V$$

K depends on the method used to measure visibility. In the present analysis, we take $K = 13$, which corresponds to instrumental measurements of the MOR,

and $K = 17$, referring to several proposed models in the literature, as explained in Section 3.1.1. Since the size of the raindrops is much bigger compared to the optical wavelengths, rain attenuation is wavelength independent for FSO. Hence, we are allowed to use the simple γ - V power law expression which holds in the visible range.

Figures 4.9, 4.10, and 4.11 show the estimation of the specific attenuation due to rain at three locations: Milan, Rio de Janeiro, and Guayaquil, respectively. γ is obtained by applying (4-4) to the rainfall rate estimated by the Recommendation ITU-R P.837-7 and considering the parameters k and α for DSD gamma with shape parameters: $\mu = 3$, $\mu = 1$, and $\mu = -2$. Those figures also present curves of the CCDF of rain attenuation obtained for $K = 13$ and $K = 17$ applying the definition of visibility (expression (3-2)).

In the case of Milan, the initial part of the curve of $\gamma = 13/V$ up to $\gamma = 3$ dB/km agrees with DSD gamma with $\mu = -2$ (see Figure 4.10). Then, the pattern changes, having differences in the specific attenuation of around 4 dB/km when the probability is 0.1%. For a probability lower than 0.05%, we find a better agreement between the curve $\gamma = 13/V$ and γ calculated for the shape parameter $\mu = 6$. However, there is an unexpected behavior in the lower part of V-based curves. It may be an effect of suspended particles different from rain, which are present during heavy rain, that is not described in the model of DSD gamma. Another cause for that behavior may be the quantization of visibility, since the final point of the curves is $V = 0.1$ km, which corresponds to the minimum level of visibility measurements.

On the other hand, in the data of Rio de Janeiro, we find that visibility measurements are not a good indicator of rain attenuation for low values of rainfall rate. It is reflected in the initial part of the V-based curves in Figure 4.11. Whereas, for the interval $\gamma = 3$ to $\gamma = 10$ dB/km, (i.e., a probability of 0.05%), the pattern of specific attenuation obtained for $K = 17$ fits with the one estimated by DSD gamma with a shape parameter $\mu = -2$, it is not easy to find a pattern related to another value of μ for the next part of the curve. Again, we see the behavior in the final part of the curve corresponding to the quantization of visibility, and, in turn, suggesting an effect of suspended particles different from rain.

In Guayaquil, the curves $\gamma = K/V$ do not follow a simple pattern, as see in Figure 4.9. Based on the curve shape, we can divide the $\gamma = 13/V$ curve into four parts: (i) the probability higher than 3% exhibits that for low values of rainfall rate, visibility is not a good indicator of rain attenuation; (ii) in the interval from $\gamma = 1.7$ to $\gamma = 8$ dB/km (i.e., a probability of 0.05%), we find a good agreement with DSD gamma with $\mu = -2$; (iii) the section

from probability between 0.005% and 0.1% is challenging to fit completely to a curve; (iv) when the specific attenuation is higher than 25 dB/km it can have a good agreement with DSD $\mu = 1$.

In an initial stage, we notice that the visibility based curves obtained with *K=13* and *K=17* present slight difference between them (i.e., it is about 30% on a dB/km scale). This uncertainty is small compared to the one with the difference between visibility-based model and DSD-based curves. Overall, there are four important comments about the CCDFs in this section. (i) the shape of the V-based CCDFs is not regular for the studied places, thus, it is difficult to associate to a given pattern. (ii) the distance between V-based and DSD-based curves at 99.99% level goes from 3 to around 6 dB/km, (Rio de Janeiro and Milan, respectively). Therefore, we have a considerable difference in the attenuation for the longest link we foresee, that is 3 km, corresponding to 9 and 18 dB for each case. (iii) at low values of rainfall rate, hence small values of specific attenuation, the V-based CCDFs suggest that the visibility measurements are not a good indicator of rain attenuation. Finally, (iv) the behavior at very large attenuation values in the V-based curves may be an effect of suspended particles different from rain, which are present during heavy precipitation, that is not described in the model of DSD gamma. Besides, the final point of the curves corresponding to the minimum level of visibility measurements, indicates that the resulting large values of specific attenuation may be due to the quantization of visibility. After analysing the models to estimate rain attenuation, we decide to use the one based on micro-physics of raindrops, that is the ITU-R power-law model but assuming the distance reduction factor equals 1; we consider the coefficients k and α for DSD gamma obtained for optical frequencies, i.e., the results in Table 4.3.

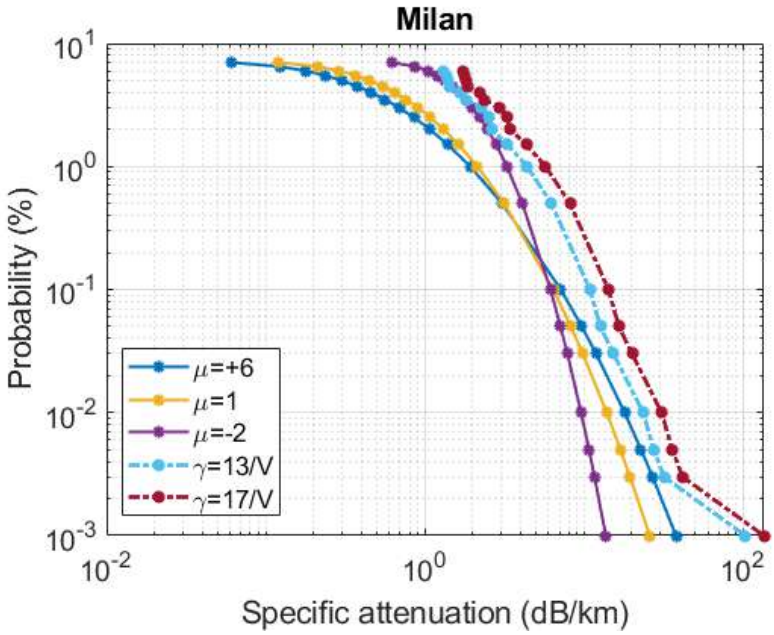

Figure 4.10: CCDF of the specific attenuation due to rain for Milan.

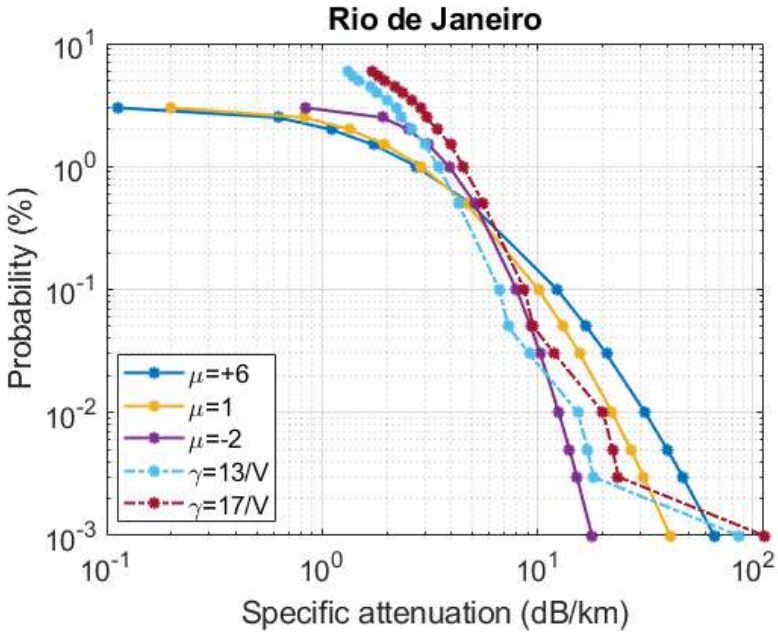

Figure 4.11: CCDF of the specific attenuation due to rain for Rio de Janeiro.

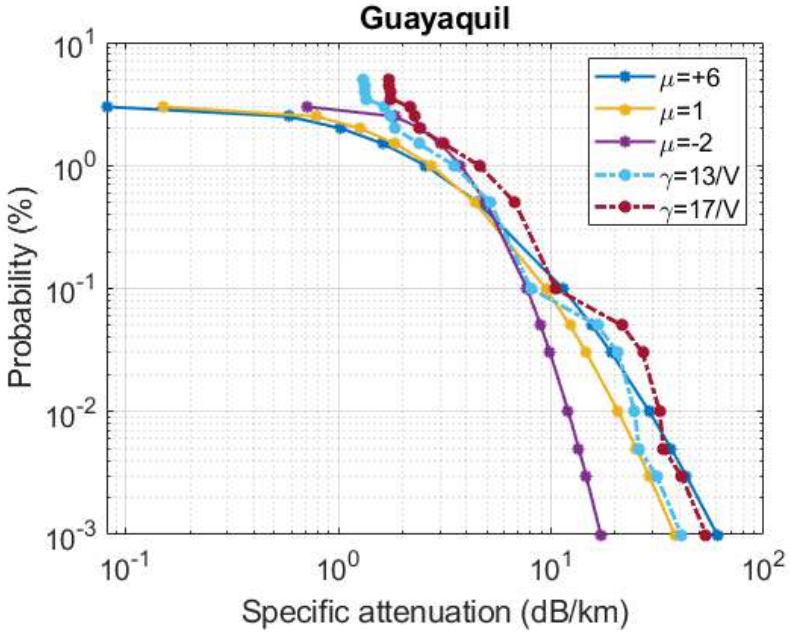

Figure 4.12: CCDF of the specific attenuation due to rain for Guayaquil.

4.5 Multiple scattering effects

The expressions of the extinction coefficient so far discussed are based on single scattering theory, which assumes that the incident energy intercepting a particle is lost; coefficients α and k in (4-4) have been derived using that theory. When an optical wave intercepts a raindrop, part of the radiation is absorbed and part is scattered. In the range of wavelengths used by current FSO systems (i.e. from 0.785 up to 1.55 μ), scattering is dominant. When the particle dimensions is orders of magnitude larger than the wavelength, scattering generates a narrow peak of radiation in the forward direction. Thus, particle scattering causes a significant portion of the transmitted radiation to be received when the optical signal crosses a layer of rain. Multiple scattering occurs when the optical beam interacts with several particles before arriving at the receiver. In terms of signal reduction, multiple scattering due to rain in optical frequencies reduces path attenuation [89]. Therefore, it is important to study it when a model to estimate the rain attenuation statistics is proposed for FSO links. The multiple scattering effects are usually quantified through the so-called multiple scattering gain, G_{ms} (in dB), which is a function of the path length and the DSD of rain, among others. It is defined as the ratio between the transmissivity when multiple scattering is accounted and the Beer-Lambert transmissivity, i.e.,

$$G_{ms} = 10 \log_{10} \left(\frac{\tau_{ms}}{\tau_{BL}} \right) \tag{4-18}$$

$$\tau_{BL} = e^{-\gamma L} \tag{4-19}$$

Thus, laser beam attenuation (in dB) over a rainy path of length L can be written as:

$$A_{ms}(L) = A_R(L, R) - G_{ms}(L, R) \tag{4-20}$$

A_R corresponds to the attenuation due to rain estimated using one of the models studied earlier in this chapter, while G_{ms} can be calculated, for instance, by a Monte Carlo photon propagation simulator [91][89].

In the Monte-Carlo simulation, the multiple scattering gain depends, besides the path length and the rainfall rate and the DSD shape, on the characteristics of both the transmitter and the receiver and the beam type. Specifically, it depends on: (i) the transmitted beam width, (ii) the aperture area of the receiver, and (iii) the receiver field of view (FOV). In [89] multiple simulations were carried out with the fixed parameters: (i) beamwidth = 2.5 mrad, (ii) Receiver aperture = 0.03 m^2 and, (iii) FOV = 90° (open detector). After finding the G_{ms} for different path lengths, rainfall rates, and DSDs, G_{ms} curves are fitted with a power-law expression with the coefficients a and b. Thus, the dependence on the rainfall rate for a given DSD is reflected in the coefficient a and b. The expression (4-21) indicates the relationship between the coefficients and the multiple scattering gain, the path length, L, is in meters.

$$G_{ms} = aL^b \tag{4-21}$$

The polynomial expressions (4-22) and (4-23) represent the best-fit of the measured coefficients [89]. The q_n coefficients are presented in Table 4.4.

$$a(R) = q_0 + q_1 ln(R) + q_2 [ln(R)]^2 \tag{4-22}$$

$$b(R) = q_0 + q_1 ln(R) + q_2 [ln(R)]^2 \tag{4-23}$$

Table 4.4: q_n coefficients for a and b polynomial best-fit [89].

	$\mu = 1$		$\mu = 2$		$\mu = 3$	
	a	b	a	b	a	b
q_0	0.0112	0.4965	0.0103	0.5194	0.0092	0.5504
q_1	0.0060	0.0390	0.0040	0.0389	0.0019	0.0372
q_2	0.0019	0.0053	0.0025	0.0052	0.0031	0.0047

We estimate the multiple-scattering gain for the three locations applying the q_n coefficients in Table 4.4 for $\mu = 1$ in (4-22) and (4-23), and in turn, in (4-21), with $L = 1$ km. The CCDF curves of attenuation due to rain, including

multiple-scattering and the single-scattering effects, are in Figures 4.13, 4.14, and 4.15 for Milan, Rio de Janeiro, and Guayaquil, respectively. In Milan, the multiple-scattering effect reduces the path attenuation by around 60% on dB scale when the attenuation considering single scattering only is around 25 dB (i.e., P=0.001%). Whereas in Rio de Janeiro and Guayaquil, it is in the order of 70% on dB scale when the attenuation considering single scattering only is about 40 dB (i.e., P=0.001%). The increased value of attenuation reduction is caused by the light beam propagation through the heavy rain conditions in these places. Those results are in good agreement with the findings in [89].

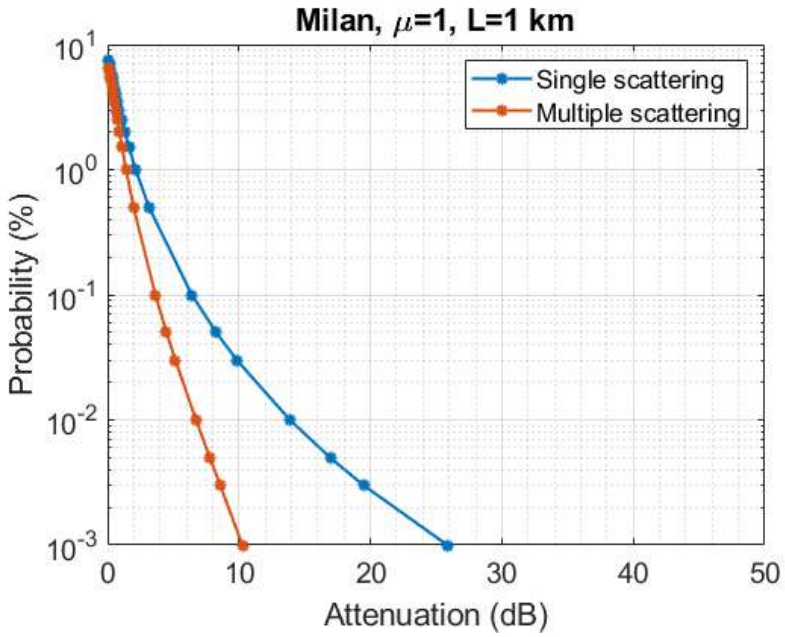

Figure 4.13: CCDF of rain attenuation over a 1 km path calculated assuming single scattering and including the effects of multiple scattering for Milan.

Since for high values of attenuation caused by rain, e.g., 25 dB in Milan when rainfall rate is around 100 mm/h, the reduction due to multiple-scattering by rain droplets is considerable, for the example of Milan it is approximately 60%, thus the multiple-scattering effects must be accounted in assessing FSO rain attenuation. Therefore, in the scope of this document, we will consider the estimation of rain attenuation given by expression (4-20), where $A_R(L, R)$ is obtained by ITU-R power-law with the coefficients k and α for DSD gamma obtained for optical frequencies, and the multiple scattering gain, G_{ms}, is calculated by (4-21) taking the corresponding coefficients from Table 4.4.

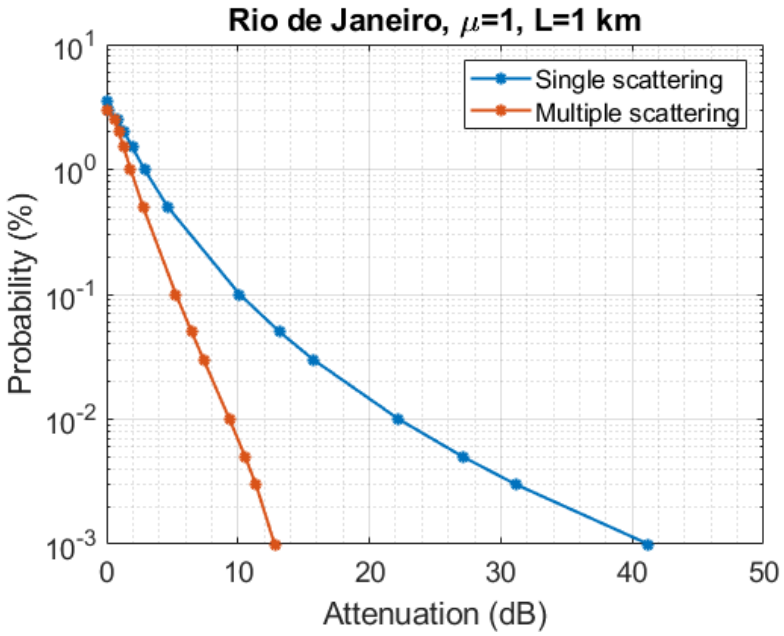

Figure 4.14: CCDF of rain attenuation over a 1 km path calculated assuming single scattering and including the effects of multiple scattering for Rio de Janeiro.

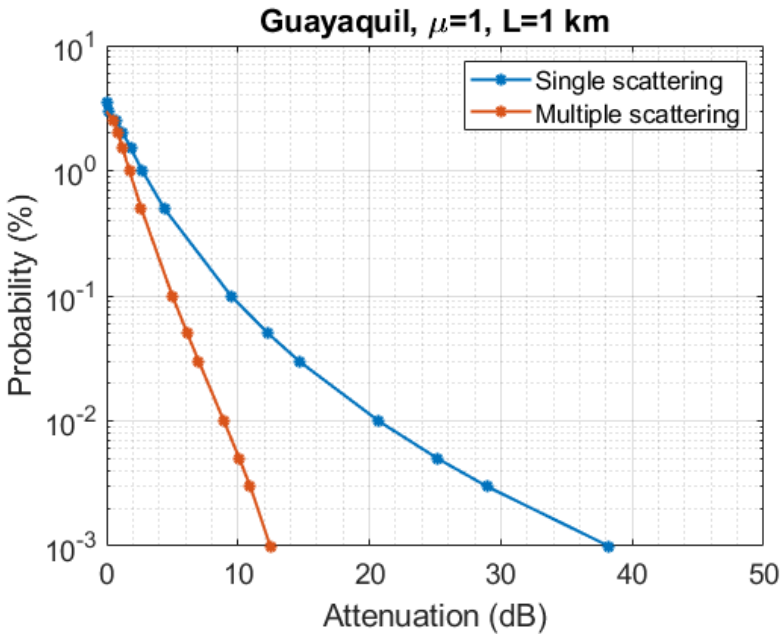

Figure 4.15: CCDF of rain attenuation over a 1 km path calculated assuming single scattering and including the effects of multiple scattering for Guayaquil.

5
Combined Attenuation on FSO

The occurrence of different weather conditions causes a reduction of visibility, and in turn, additional losses in the received optical signal. As studied in Chapter 3 and Chapter 4, fog and rain presence degrades the FSO signal strength through scattering and absorption. Thus, this chapter presents a method for statistically combining the attenuation on FSO due to four weather conditions: (i) rain, (ii) fog, (ii) other weather conditions different from fog or rain, and (iv) non-tagged conditions. Figures 5.1 and 5.2 present the block diagram of the procedure we propose. The main steps are:

1. Select the place of interest.
2. Collect meteorological statistics: Rainfall rate and visibility measurements.
3. Classify the weather conditions.
4. Filter visibility by condition and calculation of the statistics.
5. Select an attenuation model for each effect.
6. Calculate statistics of attenuation due to each effect.
7. Combine statistics of rain and fog attenuation.

In the following sections we go through each step to explain the procedure in more detail, taking as an example the meteorological statistics of Rio de Janeiro.

5.1
Selection of the place of interest

The first step is defining the place of interest, as indicated in the green block after *start*ing in Figure 5.1. It is then necessary to identify the nearest existing station in the database. After that, the surface data is downloaded from the Wyoming University repository [33].

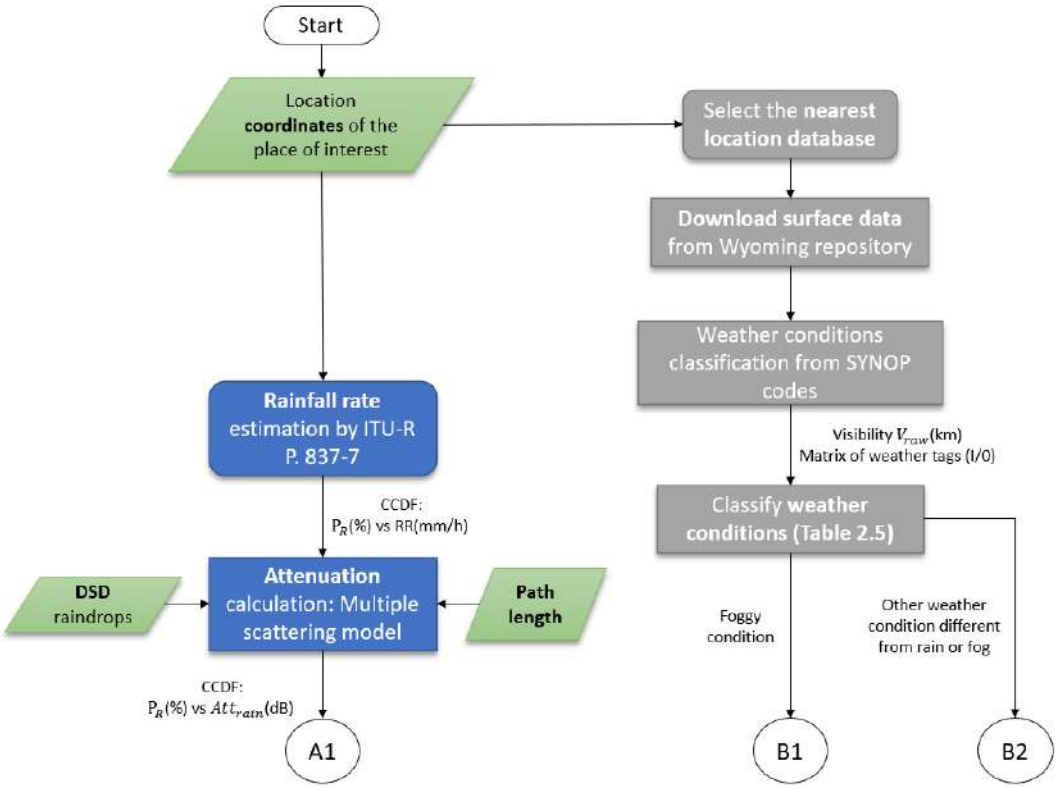

(a)

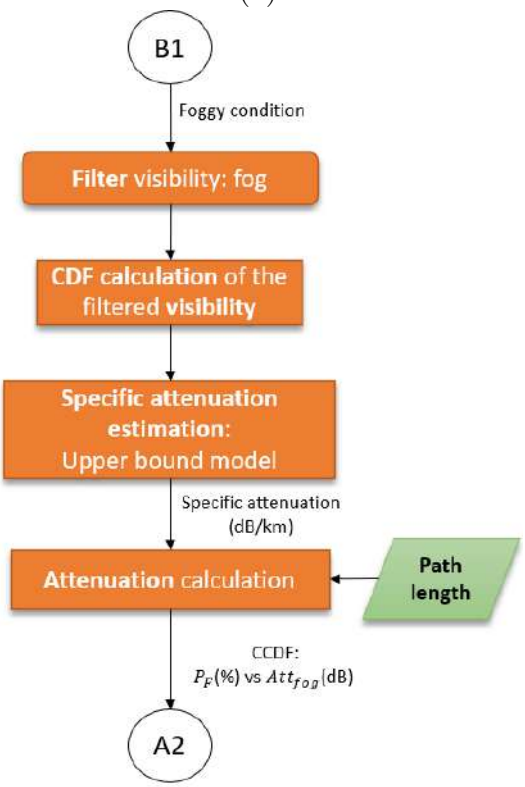

(b)

Figure 5.1: First part of the procedure to obtain the combined effect of the four weather conditions. (a) rain attenuation and classification of weather conditions, and (b) fog attenuation.

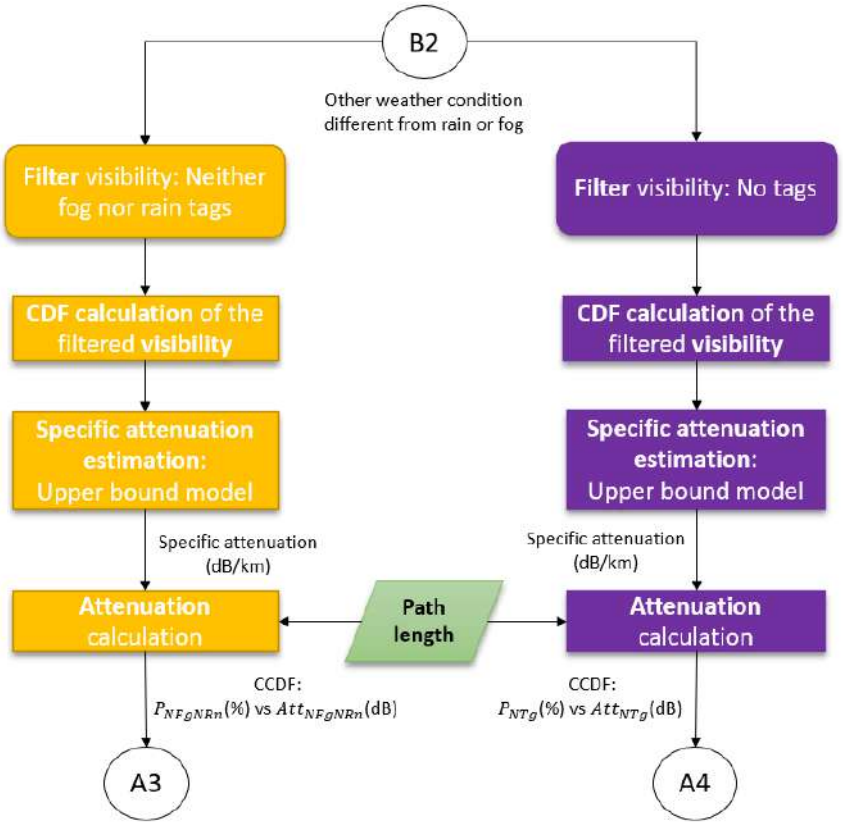

(c)

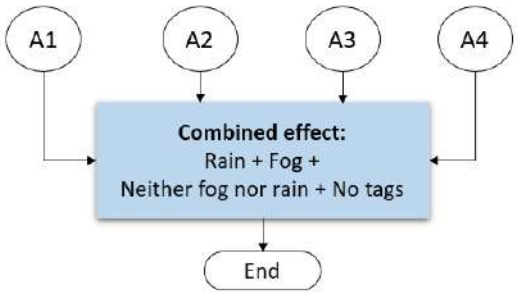

(d)

Figure 5.2: Second part of the procedure to the combined effect of the four weather conditions. (c) attenuation due to neither fog nor rain conditions and attenuation due to non-tagged conditions, and (d) total combined attenuation.

5.2 Collection of the meteorological statistics

The next step is the collection of meteorological statistics. On one side, rainfall rate statistics at a given location are most frequently estimated from reference maps of rain rate, shown in Recommendation ITU-R P.837-7, as we studied in Chapter 4. These maps provide rainfall rate statistics with a 1-min integration time [85]. For example, the CCDF of rainfall rate in Rio de Janeiro, estimated using the ITU recommendation, is in Panel (a) in Figure 5.3. We

illustrate the steps and the required inputs on the left branch in blue and green blocks in the diagram in Panel (a) in Figure 5.1.

On the other hand, an extensive database of surface measurements is obtained from the Wyoming university repository. In the present case, we use the measurements of visibility and the weather conditions tags based on the METAR Decoder Key [36], as we studied earlier in Section 2.5. Panel (b) in Figure 5.3 presents the CCDF of visibility, calculated from the complete set of visibility measurements in Rio de Janerio. The first pair of gray blocks on the right part of the diagram in Panel (a) in Figure 5.1 represents this step.

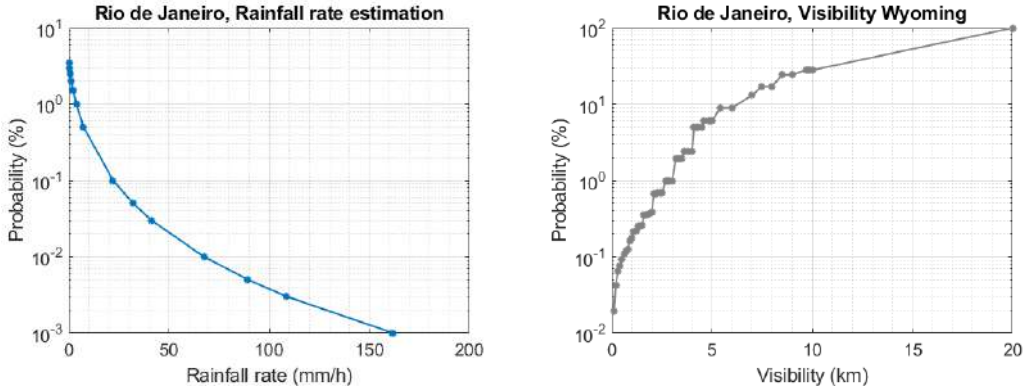

(a) (b)

Figure 5.3: Statistics of climatic parameters of Galeão Airport in Rio de Janeiro: (a) Rainfall rate estimated by ITU-R P.837-7 [85], (b) Measured visibility from the Wyoming database [33].

5.3 Classification of the weather conditions

The weather conditions from the surface measurements are classified according to the cases defined in Table 2.5, and we generate a binary matrix of weather conditions based on the METAR Decoder Key [36]. It contains a column for each weather case, and the rows correspond to the number of visibility samples. For the present study, we define four conditions to take into account: rainy, foggy, neither fog nor rain, and non-tagged condition:

1. Rain condition: Samples under the presence of labels belonging to *Case 5: only rain or drizzle or thunderstorm* in Table 2.5.

2. Fog condition: Samples under the presence of labels belonging to *Case 4: suspended particles that are water* in Table 2.5.

3. Neither fog nor rain condition: Samples under the presence of labels belonging to any of the following *Cases: 2,3,6,8,9,10,11,12,13* in Table 2.5.

4. Non-tagged condition: Samples that do not include any label.

The last gray block on the right in Panel (a) in Figure 5.1 indicates this process step. Case B1 corresponds to visibility samples shown as fog conditions, presented in orange in Panel (b) in the same figure. Case B2 corresponds to the visibility samples related to other weather conditions, i.e., neither fog nor rain, and non-tagged conditions, treated as indicated in the yellow and purple blocks in Panel (c) in Figure 5.2.

5.4 Filtering visibility and calculation of the statistics

The classified visibility measurements are filtered considering the desired condition: rain, fog, neither fog nor rain, and non-tagged conditions using the binary matrix explained before. Once the visibility is filtered, the respective CCDF is calculated. Figure 5.4 shows the CCDF of visibility for three different conditions in Rio de Janeiro. The curve corresponding to fog is the most relevant for the lowest visibility values, up to 6 km, followed by the CCDF of non-tagged conditions, which presents higher probability values than those caused by either fog or rain conditions when visibility is up to 2 km. In the interval V>2 km and V<6 km, the probability of neither fog nor rain exceeds the non-tagged condition. Finally, for higher visibility values (i.e., V>6 km), the non-tagged curve presents a higher probability, meaning that it includes more samples with high visibility than the other conditions. This step corresponds to the second block named *CDF Calculation of the filtered visibility* in Panel (b) in Figure 5.1, and on both branches in Panel (c) in Figure 5.2.

5.5 Selection of the attenuation models

The optical attenuation models for low visibility and rain available in the literature have been previously studied in Chapter 3 and Chapter 4, respectively. Table 5.1 lists the models for fog and rain attenuation studied in previous chapters.

In the case of rain attenuation in FSO, we consider the power-law model corrected by the gain of multiple scattering effects since it offers realistic predictions compared with experimental data [89]. The CCDF of rainfall intensity is derived from ITU-R. In general, the percentage of rainy time (i.e., the initial point of the ITU-R CCDF) might differ from the percentage time flagged as rainy by SYNOP codes (i.e., from the Wyoming data), as we can see in Figure 5.5. Although a linear fit of 1:1 presents good behavior (RMSE

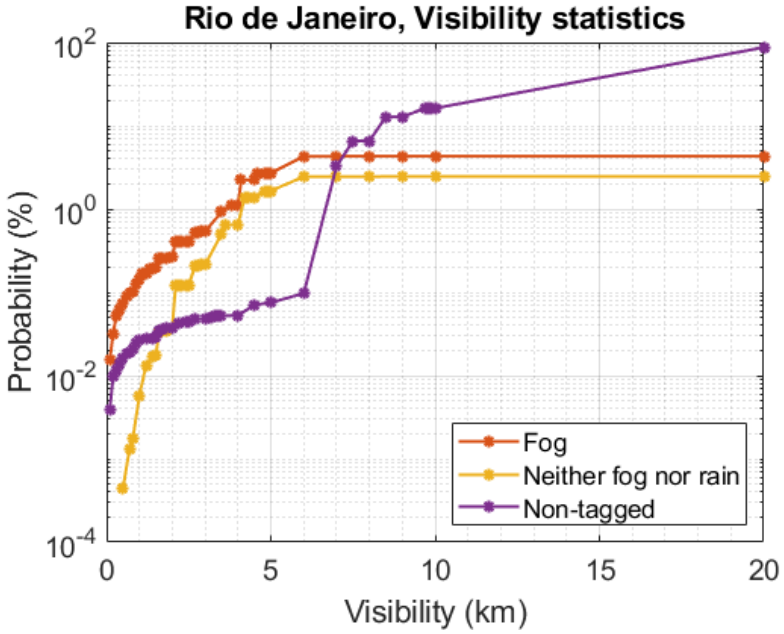

Figure 5.4: Statistics of visibility of Galeão Airport in Rio de Janeiro after filtering for three conditions: fog presence, neither fog nor rain occurrence, and non-tagged samples.

= 2.4), we also find a discrepancy between those two values for some stations. Hence, when adding the CCDF of rain attenuation to the CCDFs of the other components (e.g., fog), it is necessary to correct the data so that the resulting CCDF of total attenuation is exactly 100% at $A = 0$. The procedure followed to obtain a monotonically decreasing curve starting at 100% when $A = 0$ is presented in Appendix E.

For fog attenuation, although there are relevant models in the literature (see Table B.1 in Appendix B), we use the proposed upper bound model presented in Chapter 3 because it considers the sensitivity of γ to the visibility at 1.550 μm and the best fit to the outcomes of the micro-physical model. It also offers a conservative approach to estimate the extinction coefficient of fog, as presented in Figure 5.6.

The lack of a model to represent the attenuation due to neither fog nor rain conditions (i.e., smoke, snow, sand, haze, fog + snow) and also the unavailability of additional experimental data different from visibility or rainfall rate hampers a reliable estimation of the attenuation caused by those conditions. Regarding the attenuation caused by each effect, the attenuation due to snow is not negligible because it could vastly exceed the one caused by heavy rainstorms. Further, as in the case of rain events, using a visibility sensor is not appropriate to infer the correct fade levels experienced by the laser beam as studied in [37]. The authors showed that estimating snow attenuation from visibility data obtained through a sensor based on the scattering principle

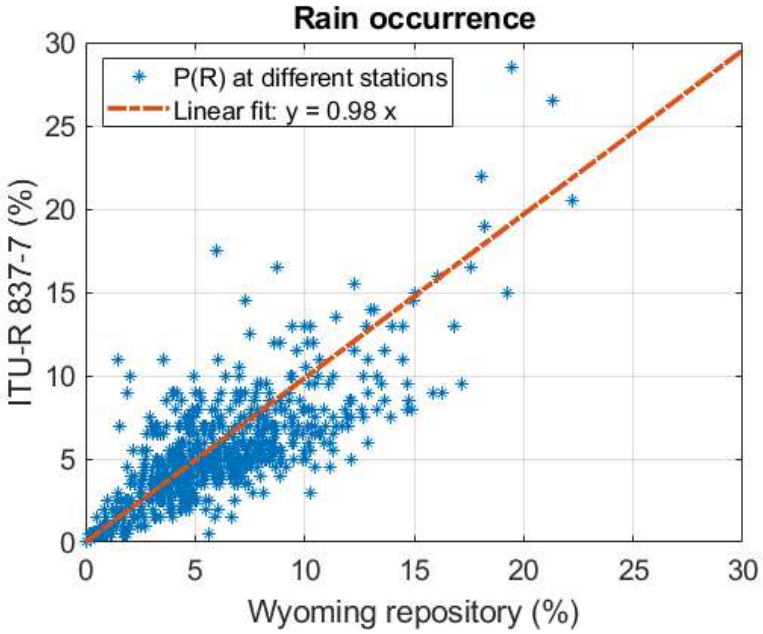

Figure 5.5: Probability of rain given by Recommendation ITU-R P.837-7 and the Wyoming repository.

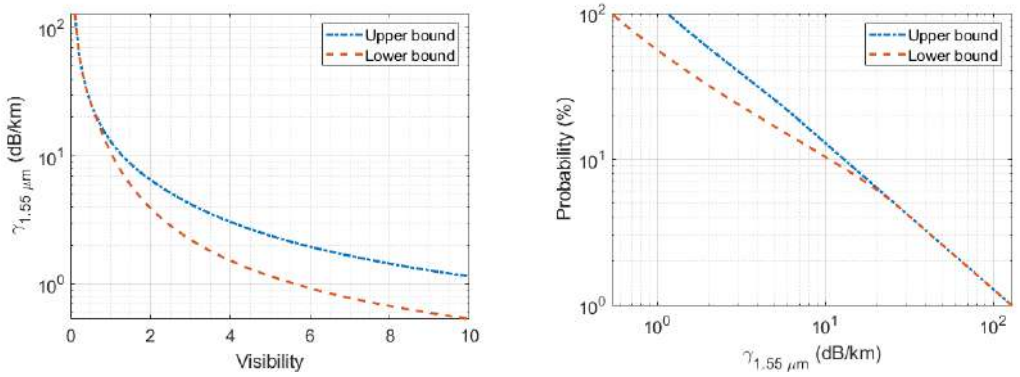

(a) (b)

Figure 5.6: Extinction coefficient at 1.55 μm.

underestimates the attenuation since the sample volume is usually too small. In fact, typical particle concentrations for rain and snow are orders of magnitude less than in the case of fog. Therefore, it is advised to obtain statistics of DSD of snow and snow occurrence when installing an optical link where the probability of snowfalls is non-negligible, as in the case of north Europe (as presented in Chapter 2). However, snow occurrence is not as relevant as fog or rain for the selected locations. Thus, we decided to estimate the attenuation due to other detected conditions (i.e., haze + water vapor particles) different from fog and rain with a fog attenuation model. Specifically, we use the upper bound model presented in Chapter 3.

Table 5.1: Examples of propagation models studied in this document.

Effect	Models	Ref.
Fog (Chapter 3)	Definition of visibility	[64]
	Kruse	[50]
	Kim	[49]
	Grabner	[52]
	Al Naboulsi	[53]
	Nebuloni	[51]
	Ijaz	[66]
	Smoothed Kim and Upper bound model	Section 3.5
Rain (Chapter 4)	Lin	[83]
	Moupfouma	[84]
	Brazilian model	[82]
	ITU-R P.530-18	[46]
	Multiple scattering effects	Section 4.5

5.6 Calculation of statistics of attenuation due to each effect

At this point, we generate the distributions of attenuation using the selected attenuation models with meteorological statistics as input. We consider the relevant input (e.g., rainfall rate or filtered visibility) as a random variable with a particular distribution and all other system parameters as constants. Besides, the probability of occurrence associated with a specific weather condition is also associated with the attenuation caused by that weather condition. Figure 5.7 presents the particular attenuation due to low visibility for three conditions: Fog, neither fog nor rain, and non-tagged samples for Rio de Janeiro. The attenuation distributions due to effects other than rain are estimated using the proposed upper bound model (see Section 5.1). The distribution of attenuation due to rainfall, also present in Figure 5.7, is calculated considering the correction of the multiple scattering effects, assuming a path length $L = 3$ km and a shape parameter $\mu = 1$, considering the coefficients in Table 4.3.

5.7 Combination of statistics of rain and fog attenuation

The calculation of statistics due to combined atmospheric effects requires assumptions about their dependence. An algorithm for deriving the composite attenuation from multiple effects for Earth-Space Paths working at *the Ka*-band (i.e., 30/20 GHz) is proposed in [92]. When combining the statistics of attenuation caused by each effect, the author makes two assumptions: i) total independence or ii) total dependence among effects. These assumptions

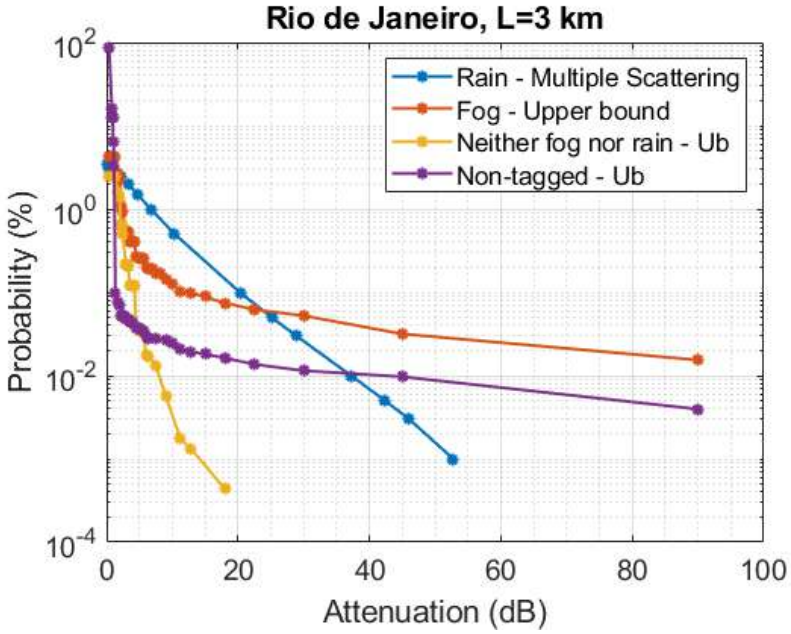

Figure 5.7: Attenuation distribution for each condition assuming path length equals 3 km for Rio de Janeiro.

create bounds on the predicted attenuation composed of all effects. The total dependence assumption is used in this work. It is incorporated into the final distribution of attenuation through equiprobable summation [92].

We define a vector of attenuation values to use as the x-axis for the distribution of the combined attenuation. Then, we find the probability values at a given attenuation (picked from the vector) from each curve presented in Figure 5.7. Finally, we sum the probability values to generate the curve corresponding to the combined attenuation. Figure 5.8 shows, in blue, the combined attenuation caused by fog and rain conditions; whereas the curve in red represents the combined attenuation caused by the four conditions (i.e., rain, fog, neither rain nor fog, and non-tagged conditions) for Rio de Janeiro assuming 3 km of path length.

5.8 Discussion

In general, the conditions different from rain and fog do not produce high attenuation compared to those generated by rain and fog as presented in Figure 5.7, as they correspond to relatively high visibility conditions. Rain is the most frequent cause of attenuation, up to around 25 dB. Moreover, beyond 25 dB, the effect of fog prevails. Finally, for small percentages of time (e.g., $P \leq 0.03\%$), there is a contribution of weather conditions other than rain or fog (see Figure 5.8). This contribution might be caused by the presence of haze particles together with water vapor or pollutants since haze particles

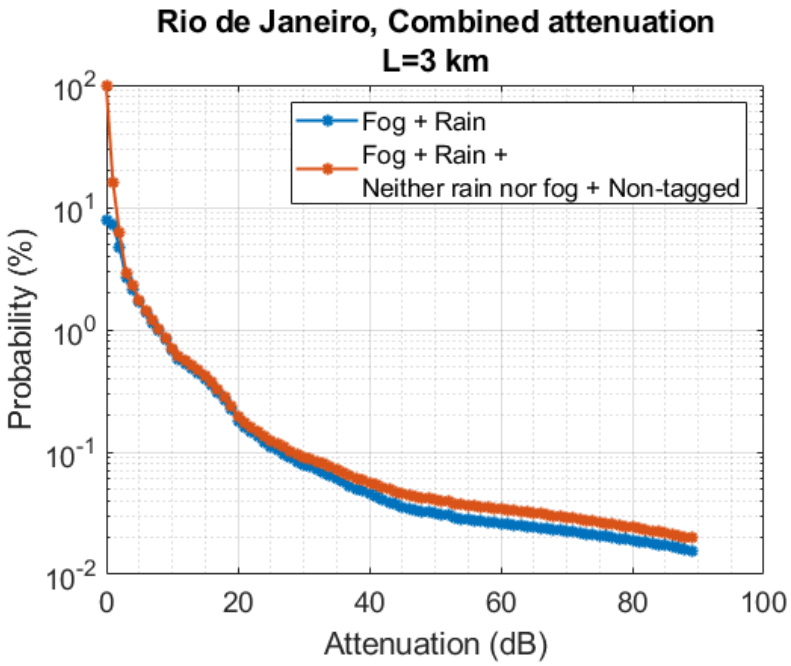

Figure 5.8: CCDF of combined attenuation assuming path length equals 3 km for Rio de Janeiro.

alone produce high values of visibility, as presented in Figure 3.2. Thus, for P$\leq$ 0.03%, those low visibility samples generate an increased attenuation for low probabilities, as indicated in Figures 5.7 and 5.8.

This chapter proposed a method to combine the attenuation due to four weather conditions: rain, fog, neither fog nor rain, and non-tagged. However, the method presents some limitations due to the assumptions and simplifications. To overcome this, the following will be required in the future: (i) A better understanding of what atmospheric conditions is causing low visibility to select an attenuation model properly (if available). And (ii) collect long-term measurements of atmospheric conditions different from fog, rain, or snow (e.g., haze, smoke, mist, or even sand) to develop empirical models relating visibility and extinction coefficient for these particles. It will depend on the micro-physics as for fog if the size of particles is comparable with the wavelength.

6
Performance of FSO links

One of the current challenges in designing FSO links is the lack of models to characterize the optical propagation channel. In this chapter, we build from the findings in the previous chapters and present FSO performance under fog and rain conditions. We apply the proposed upper bound model to estimate the attenuation of the optical signal under fog conditions, as studied in Chapter 3. Whereas, for rain, we consider the power-law model corrected by the gain of multiple scattering effects of raindrops since they generate a gain into the estimated attenuation, as presented in Chapter 4.

In the first instance, we use the power budget equation presented in Section 3.3.3 to relate the atmospheric attenuation with the attenuation due to geometric beam-spreading and system losses caused by the optical equipment parameters (e.g., receiver area and beam divergence). We present examples of potential optical links to illustrate the behavior of the power budget equation for parameters of beam divergence under different visibility values. Then, the performance of the optical link is presented in terms of link range against availability by solving the power budget expression and considering the state-of-the-art parameters of FSO. We find the maximum link distance under different conditions: (i) fog only; (ii) rain only; (iii) fog and rain; (iv) fog, rain, neither fog nor rain, and non-tagged conditions. Finally, we discuss the maximum link distance for each case.

6.1
FSO link budget: examples of potential links

Figure 6.1 illustrates the behavior of the received power under different conditions of visibility and multiples values of beam divergence, maintaining the remaining system parameters in the FSO link budget equation presented in (3-10) (repeated below for convenience) as constants, i.e., $P_T = 23.0$ dBm, $A_{sys} = 9$ dB, $A_R = 0.08$ m^2.

$$\gamma L - 10\log_{10}\frac{A_R}{\pi(\vartheta_T L)^2} + 60 = P_T - P_R - A_{sys}$$

Four visibility values have been considered (i.e., 0.25, 0.5, 1, and 10 km), representing the different curve colors in the figure. The proposed

Smoothed Kim model (see Section 3.5) is applied to convert V into the specific attenuation of fog, γ in (3-10). We also consider three-beam divergence values (i.e., 0.3, 1, and 3 mrad) denoted by dashed or solid lines in Figure 6.1. The dashed horizontal grey line corresponds to a typical value of the minimum detectable signal (MDS) of the FSO equipment.

One characteristic of the dependence of the link budget equation on the beam divergence is the slow decay of the received power in the initial part of the curves. This pattern is present in the curves of the narrowest beam, i.e., $\vartheta_T = 0.3$ mrad. When a wider beam is selected and the visibility is 1 km or lower, the curves drop faster.

Some examples of potential links based on Figure 6.1 considering MDS=-30 dBm are listed below:

- We can deploy a 700 m link under 500 m visibility conditions with a beam width of 1 mrad.
- If the beam divergence is reduced up to 0.3 mrad, we can deploy a link up to 1 km under the same visibility conditions (i.e., V=500 m). However, using a narrower optical beam causes high sensitivity to misalignment and requires higher transmission power.
- Visibility higher than 1 km is needed to deploy a longer link (at least 1.5 km) when the beam divergence is 1 mrad;
- An FSO equipment with a higher value of MDS, e.g., MDS=-10 dBm, restricts the maximum path length depending on (i) the visibility conditions we expect the link works in and (ii) the width of the beam. For instance, under $V = 500$ m, the device requires a narrow beam width, at around 0.3 mrad, to link up to 700 m;
- With $V = 1$ km and the same beam width (and MDS=-10 dBm), we can have a slightly longer path, up to 1 km. However, the designer needs to consider the drawbacks of a narrow beam.

Thus, the correct selection of the parameters of the optical equipment is crucial in the link design stage.

In this study, for the sake of simplicity, the right part of (3-10) is taken constant and hereafter named link margin M. The available link margin should be higher enough to counteract the sum of the path loss due to atmospheric attenuation and of the attenuation due to geometric beam-spreading. The following section presents the link range considering the atmospheric attenuation due to fog and rain independently, using the link budget equation and state-of-the-art parameters of commercial FSO links.

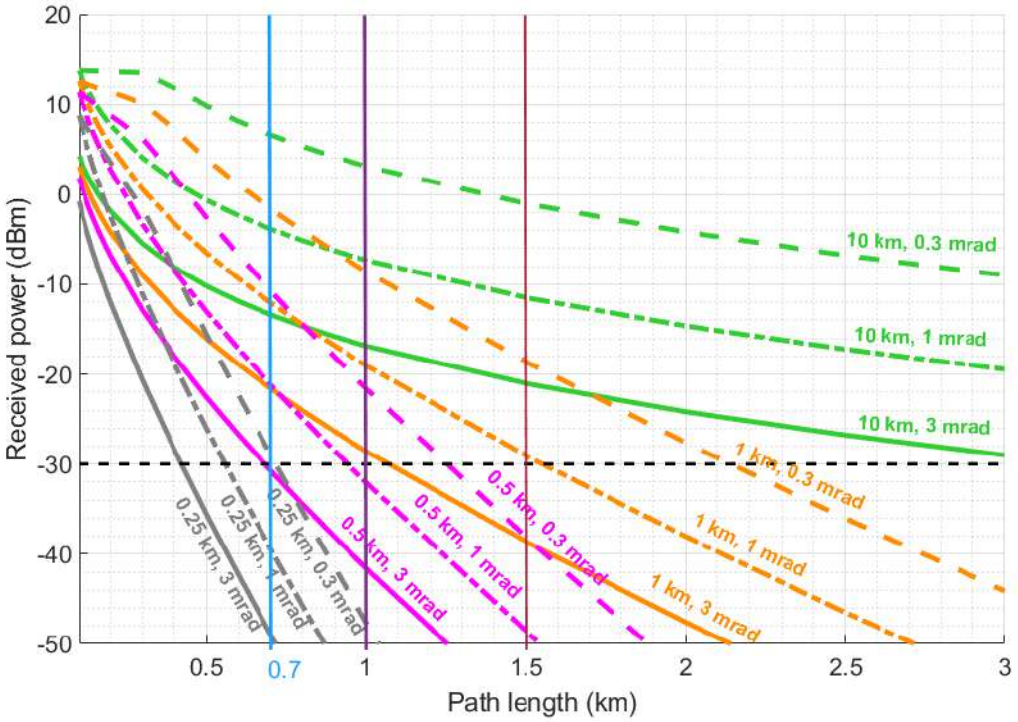

Figure 6.1: FSO link budget ($P_T = 23.0$ dBm, $A_{sys} = 9$ dB, $A_R = 0.08$ m^2).

6.2 Maximum link distance

The maximum path length is estimated in the above examples by a simple link budget formula. However, obtaining the maximum path length for a given availability (i.e., the percentage of time a target throughput is provided with a specific BER) of the link considering different weather conditions is essential.

Thus, to estimate the path length against the availability, we use: (i) the CDF of a given weather condition and (ii) the state-of-the-art parameters for the FSO equipment. The procedure to find the maximum link distance under each condition, principally rainy or foggy environment, is presented in the following subsections.

6.2.1 Fog effect

To calculate the maximum path length as a function of the availability of the link under foggy conditions, we consider the upper and lower γ-V models presented in Chapter 3 to find the extinction coefficient due to fog. The procedure is exemplified considering two locations, Milan and Rio de Janeiro.

1. We calculate the CDF of visibility obtained from the measurements corresponding to fog occurrences. Specifically, we use the data from the Wyoming University repository (see Chapter 2) after applying the filter

corresponding to *Case ID 4: Suspended particles that are water* (see Table 2.5). We use all available visibility samples. Timestamps labeled different from the fog are assumed to have maximum visibility (i.e., $V = 50$km). As an example, Figure 6.2 presents the CDF of visibility for Milan and Rio de Janeiro.

2. We obtain the visibility value at the desired availability from the CDF obtained in the previous step.

3. The specific attenuation due to fog is estimated at the visibility value found in the previous step applying the upper bound model (conservative approach).

4. We find the maximum path length, assuming a homogeneous path (i.e., $A(L) = \gamma L$), by solving the power budget expression in (3-9) and considering the state-of-the-art parameters of FSO, i.e., area of the receiver $A_R = 0.01$ m^2, beam divergence equals to 0.5 mrad, and link margin $M = 50$ dB.

5. Finally, we generate the curve of path length as a function of availability with the optimization results. The results for Milan and Rio de Janeiro are shown in Figure 6.3.

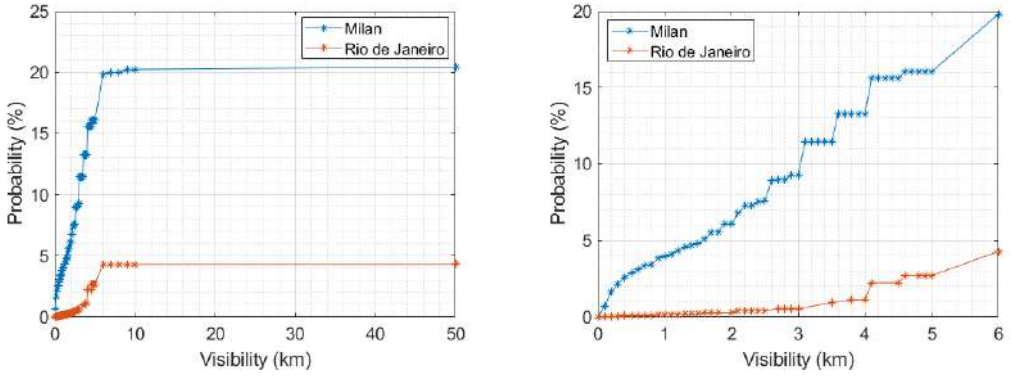

(a) (b)

Figure 6.2: Cumulative distribution function of the visibility measured at Linate airport in Milan, Italy, and at Galeão airport in Rio de Janeiro, Brazil, under foggy conditions.

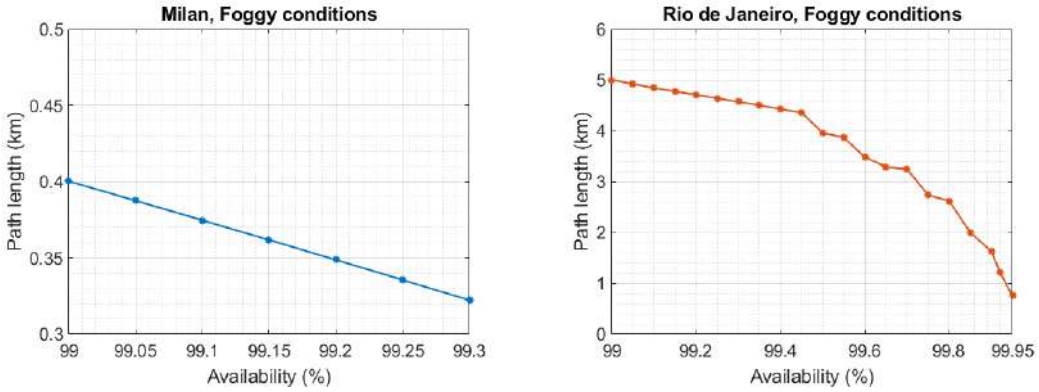

(a) (b)

Figure 6.3: Path length as a function of availability for (a) Milan and (b) Rio de Janeiro under foggy conditions.

6.2.2 Rain effect

In this section, we calculate the maximum path length as a function of the availability of the link under rainy conditions. We consider the model presented in Recommendation ITU-R P.530-18 with the path reduction factor equal 1 and attenuation reduction due to multiple scattering effects caused by raindrops, as discussed in Chapter 4. We exemplify the procedure considering two locations: Milan and Rio de Janeiro.

1. The CCDF of rainfall rate is obtained by the Recommendation ITU-R P.837-7 as explained in Section 4.1. The corresponding curves are presented in Figure 4.1.

2. The specific attenuation due to rain is calculated with the statistics of rain using the power-law coefficients corresponding to $\mu = 1$ in Table 4.3. Results of total attenuation due to rain are presented in Figures 4.13 and 4.14 for L=1 km.

3. For the case of single scattering rain, we obtain the specific attenuation at the desired availability from the CCDF obtained in the previous step. We assume a homogeneous path to calculate the total attenuation with the expression (4-4).

4. For the case of multiple scattering, as γ is a function of the path length, L, the total attenuation term ($A(L)$) is also a function of L as presented in (4-21). Thus, we include it as a dependent variable in the link budget expression. A value of attenuation is found at the desired availability from the CCDF of attenuation due to rain for each iteration.

5. We find the link range by solving the power budget expression in (3-9) and considering the state-of-the-art parameters of FSO: area of the receiver $A_R = 0.01$ m^2, beam divergence equals 0.5 mrad, and link margin $M = 50$ dB.

6. Finally, we generate the curve of path length as a function of availability for the given parameters. The results are in Panels (a) and (b) in Figure 6.4 for Milan and Rio de Janeiro, respectively.

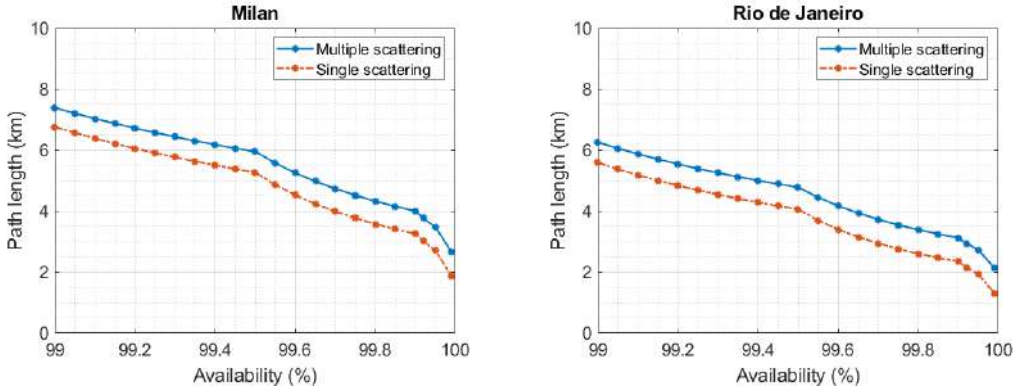

(a) (b)

Figure 6.4: Path length as a function of the availability under rainy conditions assuming single scattering and multiple scattering effects in (a) Milan and (b) Rio de Janeiro.

6.2.3 Combined effects

Here we use the method to calculate the combined attenuation presented in Chapter 5 to obtain the CCDF of the attenuation for two cases: (i) rain and fog conditions, and (ii) rain, fog, neither fog nor rain, and non-tagged conditions. The attenuation component due to rain is estimated by the model presented in Recommendation ITU-R P.530-18 assuming a path reduction factor equal to 1 and including multiple scattering effects. The attenuation component due to fog is obtained by applying the proposed lower bound model (i.e., the Smoothed Kim model). Finally, we estimate the path length as a function of the availability by solving the power budget expression in (3-9) and considering the state-of-the-art parameters of FSO: area of the receiver $A_R = 0.01$ m^2, beam divergence equals 0.5 mrad, and link margin $M = 50$ dB. The results are in Panels (a) and (b) in Figure 6.5 for Milan and Rio de Janeiro, respectively.

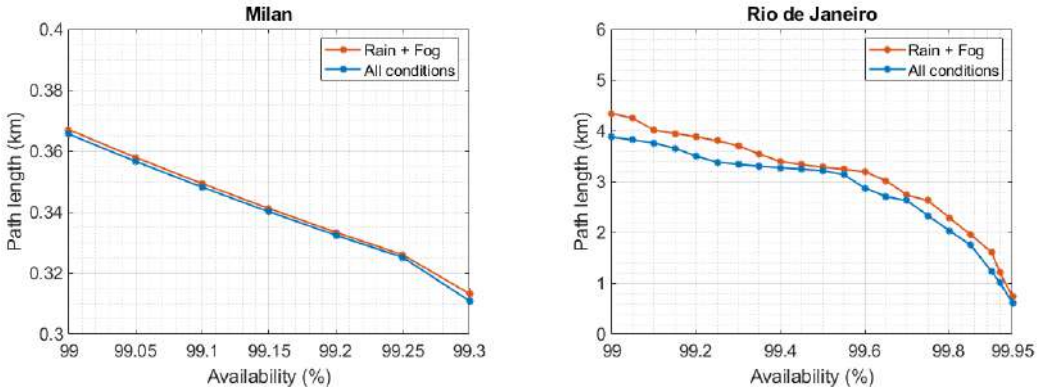

(a) (b)

Figure 6.5: Path length as a function of the availability under the combined effects for (a) Milan and (b) Rio de Janeiro.

6.3 Discussion

Considering only the fog effect in Milan, as presented in Panel (a) in Figure 6.3, a link of 400 m can be implemented with 99% availability, which means that the link could be in outage for around four days every year. If we want higher availability, the path length could be about 320 m for maximum availability of 99.3% of the time (approximately 2.5 days of outage). The maximum availability we can calculate from Milan data is 99.3%, as there is a limitation in the Wyoming repository database: it has a considerable number of visibility samples below 0.1 km, which increases the value of probability at high values of attenuation, that in turn, restricts the availability we can calculate under fog conditions as illustrated in Panel (a) in Figure 6.3.

In Rio de Janeiro, a link of 4.6 km can operate with around 99.3% availability under foggy conditions, as presented in Panel (b) in Figure 6.3. At the same time, a link of approximately 5 km can be deployed with 99% availability. Besides, we can deploy a link longer than 1.6 km with an availability of 99.9% of the time.

Under rainy conditions, the maximum link distance in Milan ranges from 3 to 4 km, considering the multiple scattering effects, for a link with 99.9% availability. It could also reach up to 7.3 km under rainy conditions with 99% availability as in Panel (a) in Figure 6.4.

For Rio de Janeiro, the rain effect causes an increased impact on the path length. It could be deployed a link ranging from 2.3 to 3 km with 99.9% availability. Moreover, it could reach up to 6.2 km under the rain, considering the multiple scattering effects with 99% availability as presented in Panel (b) in Figure 6.4.

Under the four conditions studied before (i.e., rain, fog, neither fog nor rain, and non-tagged), in Milan, a link around 370 m could be implemented with 99% availability, as illustrated in the blue curve in Panel (a) in Figure 6.5. Besides, we could deploy a link of around 310 m with 99.3% availability. Indeed, comparing those results with those obtained for the same place under fog conditions only (see Panel (a) in Figure 6.3), we see they are similar. Thus, in the case of Milan, the principal impairment against the deployment of FSO links up to 3 km with availability higher than 99% is the significant occurrence of fog (see Figure 6.2).

In Rio de Janeiro, a path length slightly shorter than 4 km could be achieved with 99% availability when considering the combined attenuation caused by the previously studied conditions, as presented in Panel (b) in Figure 6.5. Besides, a link of approximately 3.5 km, reaching 99.3% of availability, could be deployed when the combined attenuation is considered. Finally, we find that, for this location, the values of link range under a given availability are driven by both the occurrence of rain and fog. However, the probability of fog occurrence is the principal impairment against the deployment of FSO links longer than 1km with availability higher than 99% in Rio de Janeiro (see Figure 4.1).

Overall, the impact of the combined rain and fog attenuation on FSO is higher than that of the other two conditions as the link range for both cases is comparable. This is evident in both studied locations, as presented in Figure 6.5. Besides, in Milan, the highest impact on the deployment of FSO links for a short path length (L $<$ 500 m) under availability values higher than 99% is caused by the occurrence of fog. Moreover, although for Rio de Janeiro, the occurrence of low visibility (V $<$ 1km) is reduced (P$\leq$0.1%) as seen in Figure 4.1, fog occurrence also decreases the link range under availability higher than 99%. Thus, fog is one of the most detrimental conditions affecting FSO links.

7
Experimental Set-up: Parallel FSO-mmWave Links

An experimental set-up including an FSO link and a mmWave link has been deployed at the Politecnico di Milano campus to investigate the impact of different weather conditions on both terrestrial links. The set-up has been operational since late 2018 [21][20].

In this chapter, we describe the characteristics of the set-up located at the Leonardo campus, i.e., the FSO link, the mmWave link, and the ancillary equipment. After that, we present the selected atmospheric events between March 2019 and December 2020. The multiple study cases are classified into seven categories depending on the weather conditions: light rain, stratiform rain, convective rain, wind, fog, snow, and others. Data from both links (FSO and mmWave) are available for some events. Otherwise, we only consider data from the optical link and the ancillary equipment. Finally, we analyze case studies illustrating the effect of the different class events observed by the available links.

7.1
Location

The co-located mmWave and optical links transceivers are placed on the rooftop of two buildings, Building 14 (named B14) and Building 20 (B20), within the Leonardo Campus, located in Milan's urban area, Italy. Milan has a typical mid-latitude continental climate, with a maximum daily temperature of around 30°C in summer and a minimum of about 5°C in winter. Figure 7.1 shows the link position on the campus. The line-of-sight path is located at 65° NW, and it has an elevation of 2°. Figure 7.2 shows the link position seen from the rooftop on Building 14 (DEIB department).

The set-up includes two main parts: (i) commercial FSO equipment, operating at 0.785 and 1.550 μm, modified to carry out scientific experiments. (ii) mmWave transceivers operating at 148 GHz and 73 GHz in the frame of a joint research activity on EM wave propagation involving Politecnico di Milano, Milan, Italy, and the Huawei European Microwave Centre in Milan. It also includes ancillary equipment such as a sonic anemometer and a laser disdrometer.

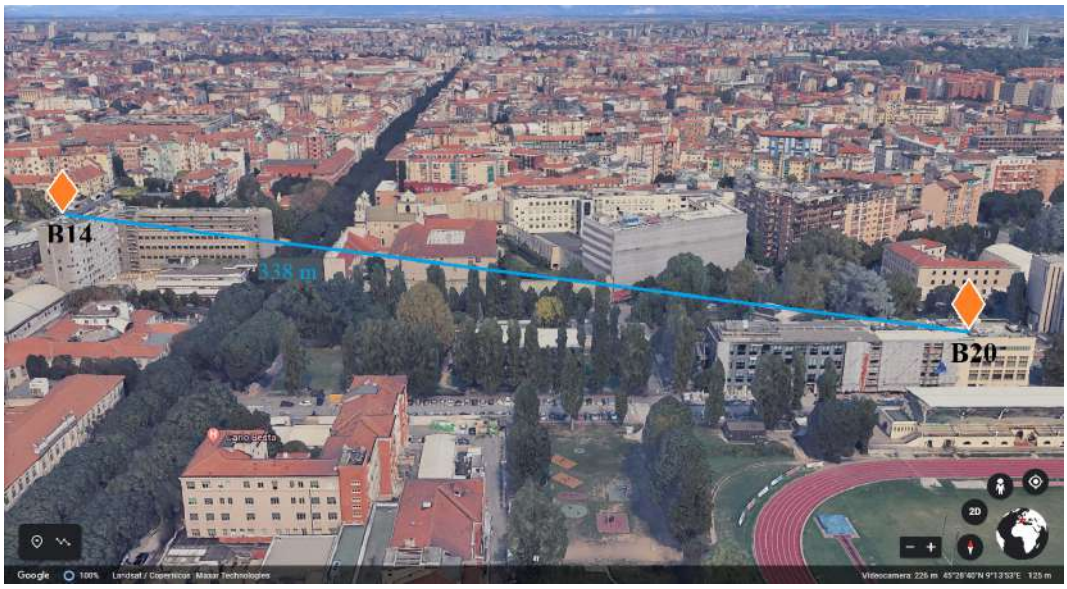

Figure 7.1: Location of the transceivers at the Leonardo Campus of Politecnico di Milano.

Figure 7.2: Location of the transceivers at the Leonardo Campus of Politecnico di Milano - frontal view.

7.2 FSO link: MOCKTOM equipment

The FSO link used in the experiments is commercial equipment developed by MOCKTOM-Artolink (model M1-GE-L) [96], featuring a duplex two-wave wireless optical communication channel at 0.785 and 1.550 μm. The service

Table 7.1: Characteristics of the FSO links [96].

Parameter	**Information Channel**	**Service Channel**
Wavelength	1550 nm	785 nm
Beamwidth	0.15 mrad	1.2 mrad
Field of view at the receiver	0.3 mrad	10 mrad
Transmitter power	2 mW – 200 mW (3 - 23 dBm)	3 mW – 42 mW (4.7 – 16.2 dBm)
Receiver area	64 cm^2	64 cm^2
Sampling time	50 ms	50 ms

channel, working at 0.785 μm, sends states and link parameters to control an auto-tracking system. The 1.550 μm channel, named the information channel, exchanges the data between the terminals.

Table 7.1 lists the main characteristics of the optical link. The beamwidth is the significant difference between the two channels. The service channel beamwidth is eight times larger than the information channel to increase link robustness against mispointing. Consequently, the geometrical loss is more significant. The receiver's field of view (FOV) of the service channel is larger as well, again to reduce the probability of link outage in the case of off-axis beam pointing.

The FSO equipment from Artolink is intended for use in computer networks, working in standard IEEE 802.3z (1 Gb Ethernet). This commercial equipment allows the creation of wireless optical "point-to-point" channels. The equipment set consists of two identical terminals, each of which comprises: an Optical Unit (OU), an Interface Unit (IU), and an Interface Cable (IC). The equipment M1-GE-T is manufactured applying the principle of Passive optics - Active tracking, meaning that the optical signal is transferred through the OU without any changes and, at the same time, the use of an active targeting system. The information signal from the user equipment is supplied to the IU. It converts the signal into an optical one (λ=1.550 μm) and transmits it to the OU through the IC. In addition, IU provides power to the OU and exchanges service information from the OU [96]. Figure 7.3 presents the scheme of the M1-GE-T Artolink equipment deployed at Polimi, indicating the interaction among the units at each terminal.

A close-up of the Optical Unit is shown in Figure 7.4. As presented in Panel (a), it comprises a fixed support and an optical interface. The latter is secured by a protective glass cover, as seen in Panel (b) in Figure 7.4 [96]. Photos of the Artolink optical units placed on the rooftops of Building 14 and Building 20 at Polimi are in Figure 7.5; here, we can also see how the supports

have been fixed to the surface.

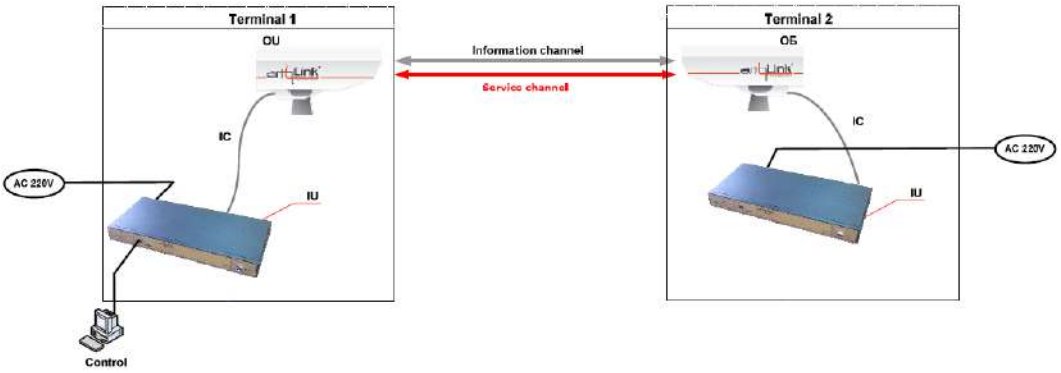

Figure 7.3: M1-GE-T Artolink equipment scheme. Source: [96].

(a) (b)

Figure 7.4: M1-GE-T Artolink equipment. Source: [96].

Data reduction

The raw-power data received by each optical terminal is recorded once every 50 ms. A moving average filter is applied with a 1-min window to reduce noise. The top and middle panels of Figure 7.6 show the time-series of transmitted and received power on 11 May 2019. The measured atmospheric attenuation is calculated by (7-1)

$$A_{measured} = -(P_{RX} - P_{REF}) \tag{7-1}$$

P_{REF} is a reference received power level (baseline), measured during an extremely clear day, i.e., with visibility higher than 10 km. In such conditions, the optical attenuation produced by atmospheric particulates is negligible across a 320 m link.

(a) (b)

Figure 7.5: M1-GE-T Artolink equipment placed on Leonardo Campus. (a) Building 14. (b) Building 20.

Therefore, attenuation due to atmospheric effects can be calculated as the excess contribution above the baseline level. The bottom Panel in Figure 7.6 shows the atmospheric attenuation calculated according to (7-1) on 11 May 2019. It is essential to highlight that not only particulates are responsible for signal loss. Strong wind and air turbulence deflect and disrupt the laser beam, resulting in signal fluctuations and extra attenuation. Therefore, the effect of rain should be carefully assessed in the presence of wind.

7.3 mmWave link: HUAWEI Technologies

Two co-located dual-band mmWave links provide similar D- and E-band experimental data. Table 7.2 lists the parameters of the link. The equipment at the D-band is a prototype designed in the Huawei Microwave Centre of Milan. It operates in the 140-160 GHz frequency range and is equipped with separated antennas for the transmitter and receiver. Two carrier frequencies at 148 and 156 GHz ("Low" and "High" bands, respectively) are used, with 250-MHz band channels. The E-band link is a commercial set-up that operates in the 71-86 GHz range over 250 MHz channels. The two carrier frequencies used are 73 ("Low" band) and 83 GHz ("High" band), respectively. A unique antenna is employed for the transmission and the receiver. Figure 7.7. shows

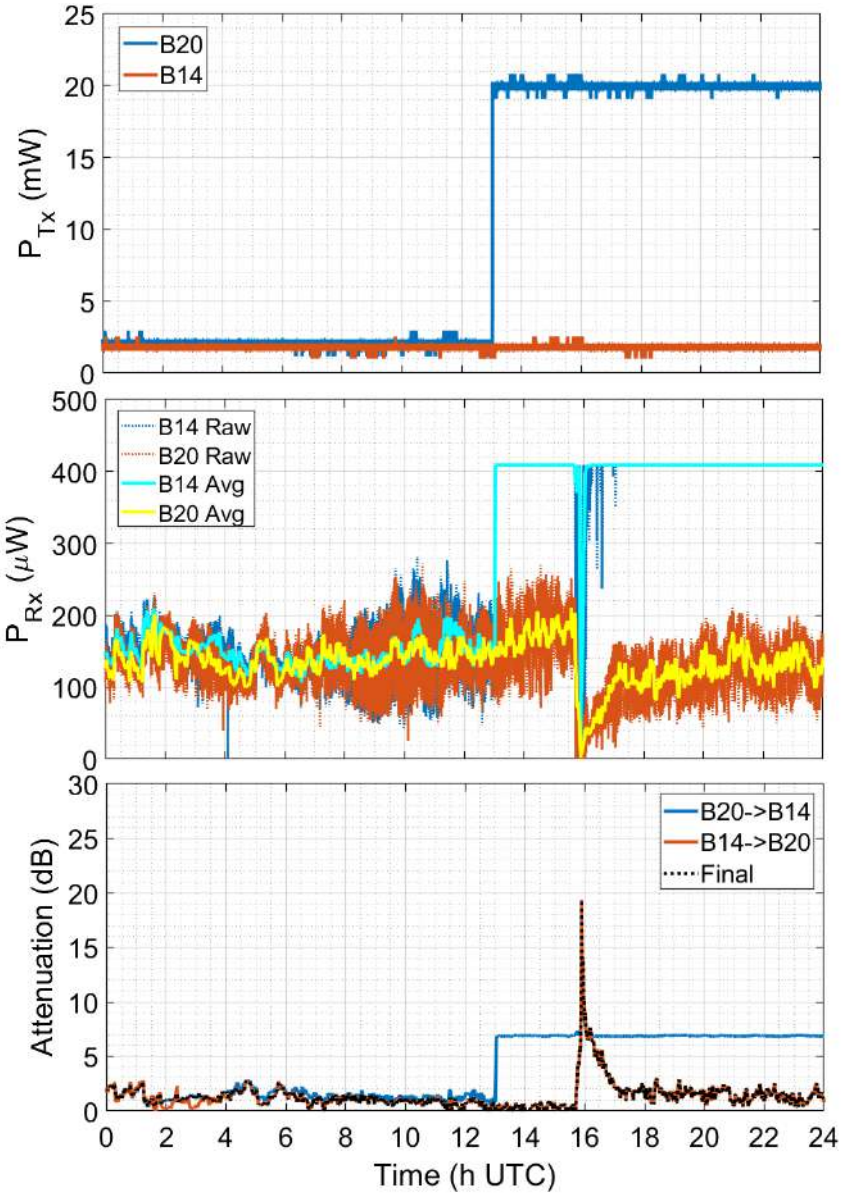

Figure 7.6: From top to bottom: time-series of transmitted power, received power (raw data and 1-min average), and 1-min attenuation (full-duplex channel) on 11 May 2019.

the transceivers installed on the rooftop of Building 20 of Politecnico di Milano. The bottom system corresponds to the E-band transceiver, while the D-band equipment is on the top.

Data reduction

The first step to derive the atmospheric attenuation from the received power, P_{RX}, for the mmWave links is to process jointly the time series of received power (from the link) and the rainfall rate (from the disdrometer) to identify and isolate rain events. After that, the received power samples are 1-

Figure 7.7: mmWave link transceivers. Bottom: E-band, top: D-band [20].

min averaged to obtain the same temporal resolution as the rainfall rate. Since the path is short, and as verified by visual inspection of the collected data, rain affects both the link and the disdrometer simultaneously; thus, the latter is used to identify the samples of the received power corresponding to rain [21]. Starting from the identified P_{RX} samples, rain attenuation is calculated as:

$$A_R = -(P_{RX} - P_{REF}) \tag{7-2}$$

P_{REF} takes into account the reference baseline value of the received power level (baseline) before and after the rain event. Equation (7-2) represents a simple yet effective way to derive rain attenuation.

7.4 Ancillary equipment

The atmospheric parameters are monitored by ancillary equipment. Surface measurements retrieved from the Wyoming University repository [33] are also available; they were taken at Linate airport, about 5 km from the link. A deeper description of this repository is presented in Chapter 2. The 30-min resolution measurements include visibility, wind speed, relative humidity temperature, and weather tags.

Table 7.2: Characteristics of the mmWave links [20].

Parameter	**D-Band**	**E-band**
Carrier frequencies	148 GHz 156 GHz	73 GHz 83 GHz
Bandwidth	250 MHz	250 MHz
Receiver sensitivity	- 67 dBm with QPSK	- 71 dBm with QPSK
Antenna gain	34 dBi	40 dBi
System gain	140 dB	161 dB
Transmitter power	+ 5 dBm (3.16 mW)	+ 10 dBm (10 mW)
Wave polarization	Linear vertical	Linear vertical
Fading margin over 350 m	15 dB	36 dB
Sampling time	50 ms	50 ms

7.4.1 Disdrometer

A disdrometer based on the laser transmission principles (Laser Precipitation Monitor), manufactured by Thies Clima, is located on the rooftop of Building 20, as indicated in Panel (a) in Figure 7.8. It is well-suited for measuring and detecting different types of precipitation such as drizzle, rain, hail, snow, and mixed precipitation. The acquisition comprises the types of precipitation, intensity, and spectrum. Specifically, this sensor returns a 1-min rainfall intensity estimation and a matrix with the count of collected particles across the sensor area classified into 22 size bins (from 0.025 to 8 mm) and 20 velocity bins (from 0.2 to 10 m/s).

The mode of operation is as follows. A laser-optical beaming source (laser diode and optics) produces a parallel light beam (infrared, 0.750 μm, not visible). A photodiode with a lens is situated on the receiver side to measure the optical intensity by transforming it into an electrical signal. The receiving signal is reduced when a precipitation particle falls through the light beam (measurement area S=4560 mm^2). The particle diameter is calculated from the amplitude of the reduction. Moreover, the fall speed of the particle is determined by the duration of the reduced signal. Figure 7.8 Panel (b) shows the particles falling through the light beam [101].

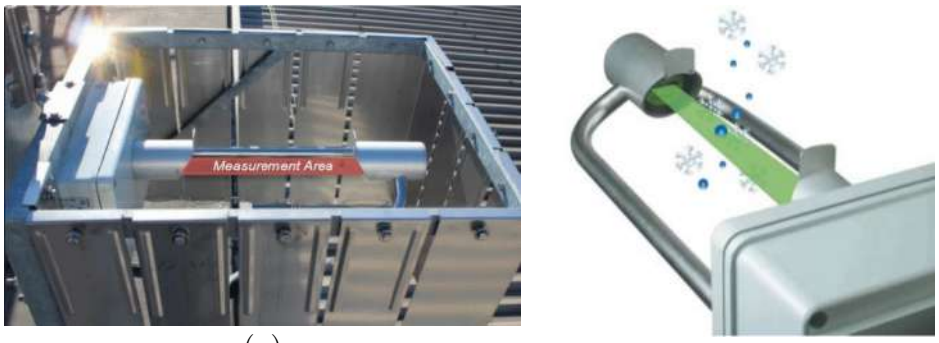

(a) (b)

Figure 7.8: Thies Clima Disdrometer [101].

Attenuation calculation from disdrometer measured data

The attenuation induced by rain on EM waves is a function of the precipitation intensity, and the shape and size of the rain drops [85]. This information is typically provided in terms of the DSD, which indicates the number of raindrops per unit volume with a diameter between D and $D + dD$. It is calculated from the available disdrometric data as follows:

$$N(D_i) = \frac{10^6 n_i}{Sv(D_i)T\Delta D_i} \tag{7-3}$$

n_i is the number of raindrops whose diameter falls in the ith class (with the mean diameter D_i). D_i(mm) represents the width of each drop-size class, S(mm^2) is the disdrometer sampling area, T(s) is the instrument integration time, and $v(D_i)$(m/s) is the terminal velocity of rain drops obtained from the Gunn and Kinzer formula [97].

The specific attenuation, considering the measured DSD, γ_R in dB/km due to rain can be calculated as:

$$\gamma_R = 4.343 \times 10^{-3} \int_{D_1}^{D_2} C_{ext_R}(\lambda, D) N(D) dD \tag{7-4}$$

C_{ext_R} represents the extinction cross-section, quantifying the energy subtracted from the wavefront by a particle. Assuming, for the sake of simplicity, spherical raindrops, the rigorous calculation through Mie theory shows that, at 1.55 μm, the optical approximation is accurate to calculate C_{ext_R} in the particle size range sampled by the disdrometer. Therefore, the extinction cross-section is calculated as:

$$C_{ext_R} \approx \frac{\pi D^2}{2} \tag{7-5}$$

Finally, since the FSO is relatively short, around 300 m, we assume uniform atmospheric conditions along the propagation path, the attenuation due to rain (in dB) over a length L(km) is calculated as:

$$A_R = \gamma_R L \tag{7-6}$$

As studied in Chapter 4, at optical frequencies, the multiple scattering effects caused by rain droplets reduce rain attenuation related to the one predicted by (7-6). Therefore, laser beam attenuation (in dB) over a rainy path of length L is calculated as in the expression (4-20) (repeated below for a better understanding):

$$A_{ms}(L) = A_R(L, R) - G_{ms}(L, R)$$

In this chapter, the term G_{ms} is calculated from the 1-min estimated DSDs by using the Monte-Carlo approach in [91] and considering the length of the path.

7.4.2 Sonic anemometer

A sonic anemometer located on one side of the link (B20 – see Figure 7.1 and Figure 7.2) provides measurements of the three spatial components of wind speed and the virtual temperature, i.e., the temperature at which dry air would have the same density as moist air at a given pressure. The air temperature can be retrieved from the virtual temperature and the specific humidity, as shown in [103]. Wind data measured with the sonic anemometer, with a sampling time of one second, are available until July 2020. We consider the wind measurements collected at Linate airport for periods during which wind speed data from the anemometer are unavailable. Figure 7.9 presents a photo of the anemometer located in Building 20.

7.4.3 ARPA repository

A 10-min accumulated rainfall time series are gathered from two weather stations owned by ARPA Lombardia (The Environmental Regional Protection Agency of Lombardy) to corroborate the disdrometer measurements and the evolution of the precipitation cells. The rain gauges are located at about 1.1 km SW (Via Juvara) and 2.5 km NE (Lambrate) from the link.

7.5 Study cases: Attenuation on mmWave and FSO

Key atmospheric events that occurred in the period March 2019 – December 2020 at the Politecnico di Milano, Italy, are presented in Table 7.3. They are classified into seven categories:

Figure 7.9: Sonic Anemometer.

1. Rain, further subdivided into
   (a) Light rain
   (b) Stratiform rain
   (c) Convective rain
2. Wind
3. Fog
4. Snow
5. Others

Cells marked in green indicate concurrent data for the mmWave and the FSO link. Cells in yellow show that only the optical link measurements are available. The following subsections summarize the main conclusions on the atmospheric effects impairing the links for the categorized events. Further examples and descriptions for each category are presented in Appendix F. Additional events are in Appendix G.

Table 7.3: Selected atmospheric events detected by the links installed within the Politecnico di Milano campus from March 2019 to December 2020. Green: data available for both links. Yellow: data available only for FSO link.

ID	**Date**	**Str. rain**	**Con. rain**	**L. rain**	**Wind**	**H. fog**	**Snow**	**Othr.**
1	04/03/19							
2	17 – 18/03/19							
3	04/04/19							
4	07/04/19							
5	17/11/19							
6	13/12/19							
7	02/02/20							
8	03/02/20							
9	05/02/20							
10	10/02/20							
11	20/04/20							
12	28 – 29/04/20							
13	11/05/20							
14	14 – 15/05/20							
15	02/06/20							
16	04/06/20							
17	07/06/20							
18	08/06/20							
19	13/06/20							
20	14/06/20							
21	03/07/20							
22	15/07/20							
23	03/08/20							
24	28/08/20							
25	29/08/20							
26	07/09/20							
27	22/09/20							
28	02/10/20							
29	03/10/20							
30	22/10/20							
31	02/12/20							

7.5.1 Light rain

Light rain refers to long episodes featuring a few (up to 2 – 3) mm/h drizzle [105]. Strong wind has sometimes been detected during light rain episodes. We introduced this class of events because FSO attenuation can be significant during light rain, conflicting with theoretical models that predict much smaller attenuation values due to light rain. On optical links, the attenuation is not only caused by rain: low visibility and wind occurring during light rain events typically lead to additional attenuation.

As an example, a light rain event occurred on 10 February 2020 with a rain rate lower than 1 mm/h, maximum attenuation in FSO is 14 dB. As the values of the expected attenuation do not exceed 1 dB, the FSO link attenuation is not only caused by the detected drops. In mmWave links, the magnitude of the attenuation is considerably lower than the FSO, at around 1.7 dB. Further explanation is available in Appendix F.

7.5.2 Stratiform precipitation

Stratiform precipitation is characterized by statistically small vertical velocities (lower than one m/s), low rain rates (<10 mm/h), and extensive (approx. 100-km horizontal dimension), horizontally homogeneous radar echo. It is typical of wintertime [104].

Large values of measured attenuation at the optical channels might be explained by the effect of very tiny suspended particles that significantly reduce the visibility but are not detected by the disdrometer. Besides, if the sealing of the optical unit is not sufficient, some condensation might appear on the inner side of the protective glasses. Wet glasses might contribute to explain as well the long transient of attenuation after the end of the event. The maximum attenuation found is 7.6 dB for FSO and 3.5 dB for mmWave links.

7.5.3 Convective precipitation

Convective precipitation regions are generally identified with intermittently strong vertical velocities (higher than one m/s), high rain rates (>50 mm/h), and small (approx. 1–10-km horizontal dimension), intense, horizontally in-homogeneous radar echo. It is typical of summertime [104]. However, this type of rain is encountered even in late autumn and early spring due to climate change.

As an example, panel (a) in Figure 7.10 shows the atmospheric attenuation obtained at the optical channel during a short convective rain occurred on 22 September 2020. As shown in panel (b), the heavy rain episode lasts about one hour with a peak intensity higher than 250 mm/h. The rainfall rate presented is given by the disdrometer. The estimation of rain attenuation considers the multiple scattering effects using the drop size distribution measured by the disdrometer. The FSO attenuation is in good agreement with the main peak of the estimation considering the experimental DSD. Panel (c) presents the attenuation in the mmWave path, the peaks of signal reduction at FSO and mmWave are comparable (around 8 dB).

The lowest peaks of attenuation were obtained with FSO link (service channel) if compared to mmWave links for the study cases (see Appendix F and G). This is expected from the theory and, if compared to the results given by the information channel, the lower attenuation shown on the service channel is likely due to the broader field of view and the wider laser beam of the latter. Considering the studied cases, the maximum attenuation found is 25 dB for FSO and 20 dB for mmWave links.

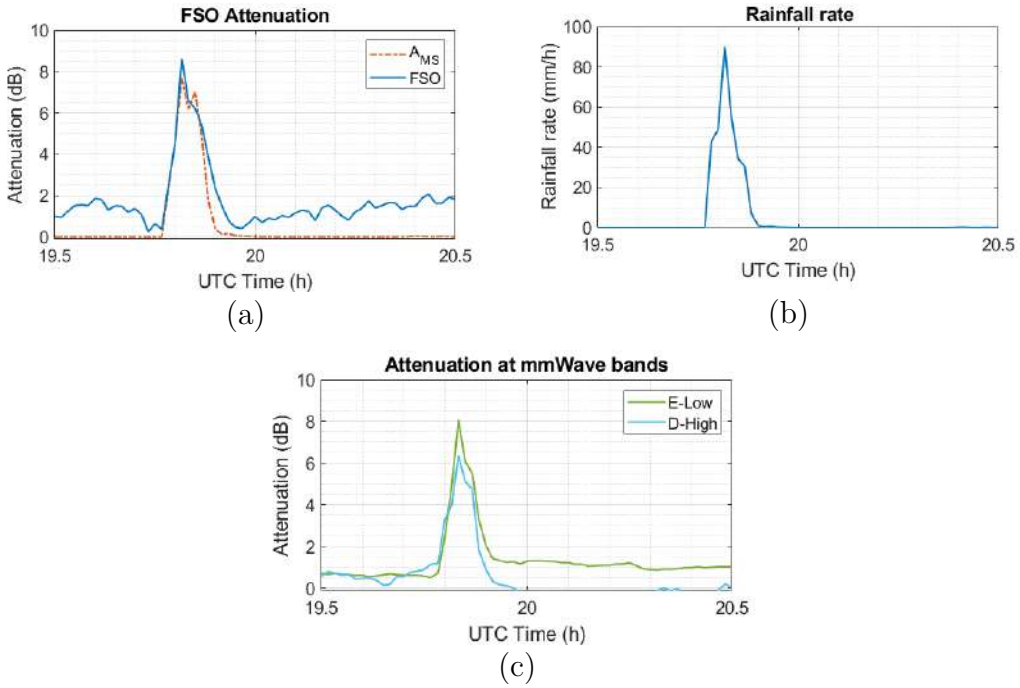

Figure 7.10: Short convective rain event

7.5.4 Wind

In this category, we mean atmospheric conditions with instantaneous wind gusts over 15 m/s (54 km/h) [105], affecting the optical link. An example

of the measured attenuation at FSO during a wind event is presented in panel (a) in Figure 7.11. The measurements during the clear and windy day show attenuation values as high as 10-15 dB (1-min avg.) when wind was blowing (14 m/s). There is a clear correspondence between the measured attenuation and the sonic anemometer's wind speed (in panel (b)). The strong wind deflects and disrupts the laser beam, leading to large fluctuations of the beam as indicated in panel (c) with the beam pointing in pixels. The wind presence produces an effect called *beam wander*, which is the displacement of the received optical beam off the receiver center. The image on the left in Panel (d) indicates the aligned beam pointing in the center of the receiver area, that is the state during calm air; on the right, the received optical beam is off the receiver center. In these terms, the signal reduction due to beam wander is the fraction of the beam wave that falls within the receiver area. An estimation of the signal reduction can be calculated by a simple geometric approach considering the receiver area and the area of the beam pointing, further explanation is in Appendix F.

Commercial FSO links, even though they are usually equipped with an auto-tracking system, can be affected by a significant signal loss during heavy wind events. Moreover, if very narrow beams are transmitted, the phenomenon is observed even over relatively short paths.

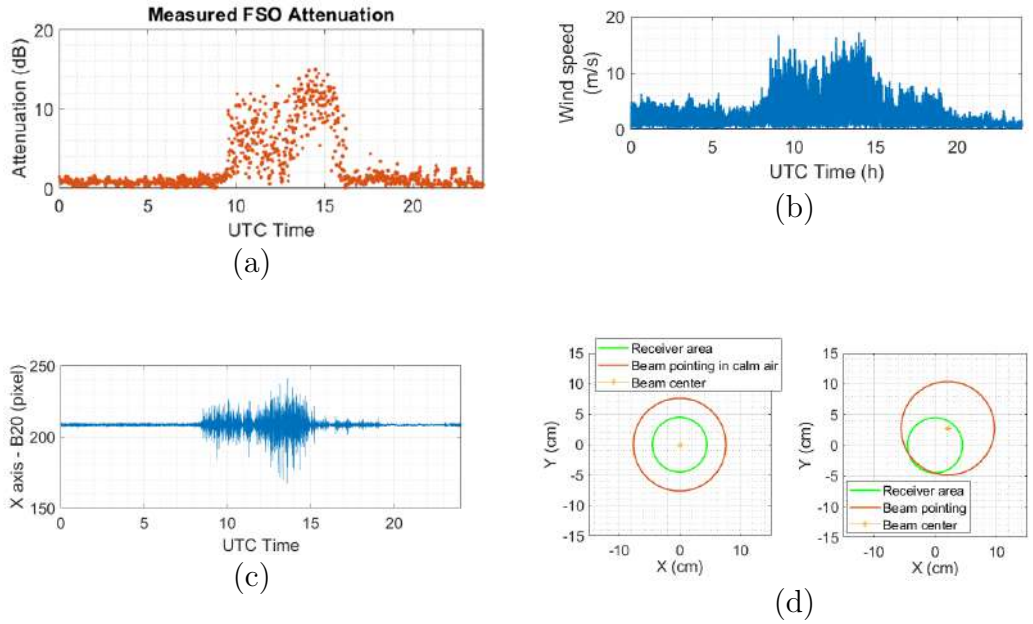

Figure 7.11: Wind event

7.5.5 Fog

Following the meteorological definition, fog occurs when visibility drops below 1 km [64]. We consider the visibility measured at Linate airport available from the Wyoming University repository [33] and the measurements of signal reduction in the FSO link to classify the events in this category.

An event of attenuation on the FSO link due to fog is presented in panel (a) in Figure 7.12. The attenuation pattern agrees with the low visibility registered at Linate airport (5 km apart) as indicated in top of panel (b). The outliers in the measured attenuation occurred when it exceeds 40 dB since that value corresponds to the limit of the dynamic range of the commercial equipment. There are missing values of attenuation corresponding to the 10% of the samples, since values at the received power are zeros or in-saturation. Finally, as the wind speed increases, the visibility raises simultaneously; therefore, the attenuation reduces.

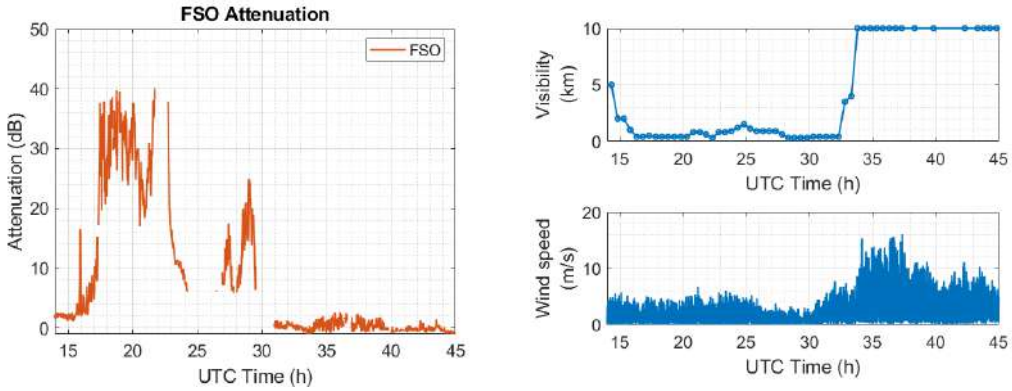

(a) (b)

Figure 7.12: Heavy fog event

7.5.6 Snow

In temperate regions, except in the mountainous areas, snow is usually constituted by aggregates of ice crystals. This process occurs when temperature and crystal shape conditions happen within clouds. Snowflakes are larger than raindrops, though their number concentration is lower. They are predicted to significantly affect the path loss across an optical link while having a minor impact on mmWave links.

The theoretical calculation of snow attenuation from the disdrometer data is not straightforward because of the physical characteristics of the snowflakes. Then, the absence of a reference does not allow to state whether

the attenuation peaks are caused by snow or by the receiver sensor. Statistics of snow occurrence are essential to install an optical link in locations where the probability of snowfall is non-negligible. The maximum attenuation measured by the FSO link during snow events is comparable to the one of heavy rain, while for the mmWave link is much lower and similar as the stratiform rain. Further explanation of study cases of snow events are in Appendix F.

7.5.7 Others

The category named others includes episodes of significant path attenuation that could be explained by the presence of any of the above atmospheric effects, study cases in this category are presented in Appendix G.

8
Conclusions

This thesis deals with the development of models for predicting the attenuation due to fog and rain for designing FSO links in 5G and beyond technologies. The current lack of a global path loss model motivates the study of the behavior of the optical link under different atmospheric conditions. Specifically, we study the fog and rain weather conditions using as a benchmark available surface meteorological data in a global context. Regarding fog attenuation in FSO, we consider models based on measurements and micro-physics of the fog particles. We propose an upper and lower bound model to convert visibility into the extinction coefficient of fog. Existing models for attenuation due to rain, valid for microwave links, have been studied and adapted to be applied to FSO links. We also propose a method to calculate the combined attenuation caused by different weather conditions. The link's performance is evaluated by predicting the link range as a function of the desired availability. Finally, experimental data collected by a 300-m FSO link located at the Leonardo Campus within the Politecnico di Milano have been analyzed, together with concurrent measurements from a mmWave link installed parallel to the optical path. The case studies have been classified into seven categories depending on the weather condition: stratiform rain, convective rain, light rain, wind, heavy fog, snow, and others.

Databases of surface meteorological parameters from four sources have been considered. We assess the databases regarding the number of valid samples and available locations. We select the Wyoming University repository as a benchmark for developing global path loss models. We analyze the weather occurrence in more than 600 stations worldwide. Almost 70% of the stations present at least 3% of fog occurrence. Besides, nearly 70% of the studied stations present at least 3.3% of rain occurrence. Concerning snow, only 30% of the locations showed an occurrence higher than 2% of the time. Thus, we select fog and rain as the focus of this study because: (i) the highest impact on visibility in the studied locations is caused by fog and rain; (ii) the difficulty in assessing snow effects on FSO links due to the lack of experimental data.

We find that, for visibility $V < 1$ km, the attenuation due to fog in FSO

is almost wavelength-independent from the visible range throughout the near-IR, up to 1.550 μm. Beyond this limit, the picture changes as one moves into the mid-IR range, reducing the attenuation. Data depart from the $\gamma = 17/V$ law at much lower visibility values than near-IR. Even though there is a huge scatter, the trend towards a significant decrease of γ at near-IR wavelengths is evident. Comparing the near-IR and the mid-IR, we find that multimodal radiation fog data indicate that $\gamma_{10.6}$ can be significantly smaller than in the near-IR even in dense fog. It is not evident if only the monomodal PSDs are considered. If $V > 200$ m, 10.6 μm transmission is better than at shorter wavelengths, the corresponding extinction coefficients' ratio is up to one order of magnitude and even higher.

Regarding measurements, there is not a complete agreement among results of fog attenuation from different campaigns. It is due to the differences in set-ups, adding to the inherent variability of fog. Recent data confirm that mid-IR propagates much better through haze and fog than shorter wavelengths. However, it is unclear if this advantage is relevant in dense fog. Besides, the extinction coefficient derived from transmission data is generally less than that predicted by γ-V models. It could be related to the accuracy of visibility measurements or to the effects of path in-homogeneity when visibility is measured at a single point. We propose an upper and lower bounds model, which considers uncertainties in the sensitivity of γ to visibility at 1.550 μm and micro-physics of fog.

Considering rain attenuation, when applying prediction models valid for microwave links to FSO, we find that Lin and Moupfouma's models agree with the power-law model predictions with a path reduction factor of 1 and measurements found in the literature. The model proposed in ITU-R Rec. P., 530-18 underestimates the attenuation due to rain as the path length increases. On the other hand, the Brazilian model tends to overestimate the attenuation values. An important finding is that, for all models, the path reduction factor is approximately 1 for path lengths within the range for back-hauling links.

For high rainfall rates, the models considered predict high values of rain attenuation (e.g., 25 dB in Milan when the rainfall rate is around 100 mm/h). At optical frequencies, the attenuation reduction due to multiple-scattering by rain droplets is considerable (e.g., it is approximately 60% in Milan for 100 m/h). Thus, the multiple-scattering must be accounted for assessing FSO rain attenuation. Therefore, in this work, we consider the estimation of rain attenuation based on the micro-physics of raindrops, that is, the power-law model assuming the coefficients k and α for DSD gamma obtained for optical frequencies, and include the gain due to the multiple scattering effects.

The occurrence of weather conditions other than fog and rain also causes a reduction in visibility, generating small additional losses in the received optical signal. Hence, we propose a method to combine the attenuation on FSO caused by four weather conditions: (i) rain, (ii) fog, (iii) identified weather conditions different from fog or rain, and (iv) non-identified conditions (non-tagged in the database). We use as input (i) the coordinates of the place of interest, (ii) the DSD of the raindrops, and (iii) the path length. From the coordinates, we estimate the rainfall intensity statistics using Recommendation ITU-R P. 837-7 and download the visibility measurements of the nearest location in the database from the Wyoming University repository. The lack of a model to represent the attenuation due to neither fog nor rain conditions (i.e., smoke, snow, sand, fog + snow) and the unavailability of additional experimental data hampers a reliable estimation of the attenuation caused by other conditions. However, as the major impact on the optical signal is due to reduced visibility between the terminals, we estimate the attenuation due to these other conditions with the fog attenuation model. Overall, from the estimation of the combined attenuation in two cases: (i) rain and fog and (ii) all four conditions, we find that the conditions different from rain and fog do not produce significantly higher attenuation when compared to that generated by rain and fog only.

We obtain the maximum link distance against availability to assess the performance of optical links. We apply the proposed upper bound fog model to estimate the attenuation of the optical signal. We consider the power-law model corrected by the gain of multiple scattering for the rain effect. By solving the power budget expression with state-of-the-art parameters of FSO equipment, we find the maximum link distance under different conditions: (i) fog only; (ii) rain only; (iii) rain and fog, and (iv) non-tagged conditions.

We find that, in Milan, a link around 370 m could be implemented with 99% availability considering the four conditions. Indeed, comparing these results with those obtained for the exact location under fog conditions only, we see they are similar. Thus, for this location, the main impairment in deploying FSO links is the occurrence of fog. In Rio de Janeiro, a path length slightly shorter than 4 km could be achieved with 99% availability when considering the combined attenuation effects. For this location, the performance is limited by the occurrence of both rain and fog. Overall, the impact of the combined rain and fog attenuation on FSO is higher than that of the other two conditions.

Considering experimental data, we infer that the mmWave links present lower attenuation than the optical links. However, it is worth pointing out that the FSO link employs commercial equipment, so the link operation software

had to be adapted to collect the data necessary to calculate signal attenuation. Consequently, the attenuation measurements are not as accurate as those gathered using specially designed equipment. Significant differences in attenuation values are observed in the information channel (1.550 μm) and the service channel (0.785 μm). It is probably due to system characteristics, as electromagnetic theory does not predict relevant differences between propagation at 0.785 μm and 1.550 μm.

Under heavy rain peaks above 50 mm/h, attenuation in the information channel of the optical link is much larger than that in the mmWave links, even considering the multiple scattering gain. As for the service channel of the optical link, rain attenuation is closer to (and sometimes lower than) observed in the mmWave measurements. During light rain, the information channel measured large attenuation values, which are not due to rainfall. This effect is probably produced by the interaction between rainfall and the sensor. Wet glasses and vapor humidity penetrating the protective cover of the optical transceiver might explain this additional attenuation.

The models developed in this work assume that the FSO propagation channel is characterized by visibility, at least for path loss modeling. Moreover, a comprehensive channel model should include other sources of attenuation as clear-air scintillation and address the channel's temporal correlation. As for signal loss in clear air, note that turbulence and fog are, with good approximation, mutually exclusive. Hence, the total system margin against atmospheric losses is usually available to mitigate scintillation. Moreover, the existing FSO technology featuring direct detection significantly reduces scintillation by aperture averaging. For instance, clear-air turbulence is not expected to affect FSO link availability unless long links are employed [79]. Finally, the effect of the coherence time of the optical channel during fog or turbulent air motions is addressed in [80] and [81], respectively.

In conclusion, FSO links can be used to increase connectivity, offering high data rates with availability higher than 99% of the time over short links (L<1 km). FSO might have substantial advantages compared to RF links. However, environmental and atmospheric effects limit the link range, particularly in heavy fog conditions. One solution to overcome this limitation might be using hybrid FSO/mmWave links, as mmWaves are less affected by conditions of reduced visibility.

8.1 Novel contributions

These are the novel contributions provided in this thesis:

– Analysis of global surface meteorological data.
– Development of upper-lower bound models for path loss of FSO due to fog valid on a global scale, considering the microphysics of fog, including multimodal PSDs.
– Proposal of a method, valid on a global scale, to statistically combine the attenuation effects on FSO links caused by different weather conditions.
– Analysis of attenuation events on the FSO and mmWave links implemented at Politecnico di Milano classified depending on the occurring atmospheric effect.

8.2 Future work

This is a list of suggestions for works that can be developed as a continuation of this thesis:

1. Reach a better understanding of what atmospheric conditions are causing low visibility in the surface measurements to select an attenuation model properly. Collect long-term measurements of atmospheric conditions different from fog, rain, or snow (e.g., haze, smoke, mist, or even sand) to develop empirical models relating visibility and extinction coefficient for these particles.

2. Propose a model for visibility using atmospheric input measurements such as relative humidity, pressure, and temperature. In this case, artificial intelligence algorithms might be used to predict the visibility using a percentage of the available data as the training set and the remaining to evaluate the model. Additional considerations such as the weather classification of the local and the probability of rain occurrence should also be taken into account.

3. Produce curves of the maximum link distance of FSO links depending on a comprehensive study of the weather classification of each place or region.

4. Study the atmospheric effects on experimental FSO links working at mid-IR (10.6 μm) as an alternative to near-IR (1.55 μm) to reduce the fog effect on the signal reduction.

5. Study the long-term behavior of an experimental hybrid FSO/mmWave link for a considerable period (years) to obtain reliable statistics on the availability of the hybrid link.

6. Analyse the cost-effective deployment of hybrid FSO/mmWave terrestrial links for back-hauling solutions in the context of 5G and beyond networks.

7. In the development of this thesis, we focused on a path loss model analysis, basically a narrow-band channel model. Thus, to provide a more general performance evaluation of FSO in the future, it is required to develop a wide-band model.

Bibliography

[1] UNITED NATIONS, DEPARTMENT OF ECONOMIC AND SOCIAL AFFAIRS. **World population prospects 2019. population facts 2019/6: How certain are the united nations global population projections?**, 2019.

[2] BUHR, WALTER. **What is infrastructure?** Technical report, Volkswirtschaftliche Diskussionsbeiträge, 2003.

[3] MITGANG, ELIZABETH A AND BLAYA, JOAQUIN A AND CHOPRA, MICKEY. **Digital health in response to covid-19 in low-and middle-income countries: Opportunities and challenges**. Global Policy, 12:107–109, 2021.

[4] CHAOUB, ABDELAALI AND GIORDANI, MARCO AND LALL, BREJESH AND BHATIA, VIMAL AND KLIKS, ADRIAN AND MENDES, LUCIANO AND RABIE, KHALED AND SAARNISAARI, HARRI AND SINGHAL, AMIT AND ZHANG, NAN AND OTHERS. **6g for bridging the digital divide: Wireless connectivity to remote areas**. IEEE Wireless Communications, 2021.

[5] ALZENAD, MOHAMED AND SHAKIR, MUHAMMAD Z AND YANIKOMEROGLU, HALIM AND ALOUINI, MOHAMED-SLIM. **Fso-based vertical backhaul/fronthaul framework for 5g+ wireless networks**. IEEE Communications Magazine, 56(1):218–224, 2018.

[6] SLALMI, AHMED AND CHAIBI, HASNA AND CHEHRI, ABDELLAH AND SAADANE, RACHID AND JEON, GWANGGIL. **Toward 6g: Understanding network requirements and key performance indicators**. Transactions on Emerging Telecommunications Technologies, 32(3):e4201, 2021.

[7] PARKASH, SOORAJ AND SHARMA, ANURAG AND SINGH, HARSUKHPREET AND SINGH, HARJIT PAL. **Performance investigation of 40 gb/s dwdm over free space optical communication system using rz modulation format.** Advances in Optical Technologies, 2016.

[8] YAACOUB, ELIAS AND ALOUINI, MOHAMED-SLIM. **A key 6g challenge and opportunity—connecting the base of the pyramid: A survey on rural connectivity**. Proceedings of the IEEE, 108(4):533–582, 2020.

[9] KAUSHAL, HEMANI AND KADDOUM, GEORGES. **Optical communication in space: Challenges and mitigation techniques**. IEEE communications surveys & tutorials, 19(1):57–96, 2016.

[10] AHMAD, ISHTIAQ AND NGUYEN, KHOA D AND LETZEPIS, NICK. **Performance analysis of high throughput satellite systems with optical feeder links**. In: GLOBECOM 2017-2017 IEEE GLOBAL COMMUNICATIONS CONFERENCE, p. 1–7. IEEE, 2017.

[11] GU, ZHIQUN AND ZHANG, JIAWEI AND JI, YUEFENG AND BAI, LIN AND SUN, XIANG. **Network topology reconfiguration for fso-based fronthaul/backhaul in 5g+ wireless networks**. IEEE Access, 6:69426–69437, 2018.

[12] KHALIGHI, MOHAMMAD ALI AND UYSAL, MURAT. **Survey on free space optical communication: A communication theory perspective**. IEEE communications surveys & tutorials, 16(4):2231–2258, 2014.

[13] ALI, SARDAR H. **Advantages and limits of free space optics**. International Journal of Advanced Smart Sensor Network Systems (IJASSN), 9(1/2/3), 2019.

[14] GLOBAL MARKET INSIGHTS, INC. **Free space optics (fso) communication market**, 2020. Access on: January 2022.

[15] 3GPP. **3rd generation partnership project; technical specification group radio access network; study on requirements for n.r. beyond 52.6 ghz (release 16)**, 2021. Access on: October 2021.

[16] BOGALE, TADILO ENDESHAW AND LE, LONG BAO. **Massive mimo and mmwave for 5g wireless hetnet: Potential benefits and challenges**. IEEE Vehicular Technology Magazine, 11(1):64–75, 2016.

[17] DAHLMAN, ERIK AND MILDH, GUNNAR AND PARKVALL, STEFAN AND PEISA, JANNE AND SACHS, JOACHIM AND SELÉN, YNGVE AND SKÖLD, JOHAN. **5g wireless access: requirements and realization**. IEEE Communications Magazine, 52(12):42–47, 2014.

[18] GE, XIAOHU AND CHENG, HUI AND GUIZANI, MOHSEN AND HAN, TAO. **5g wireless backhaul networks: challenges and research advances**. IEEE network, 28(6):6–11, 2014.

[19] ANDREWS, JEFFREY G AND BUZZI, STEFANO AND CHOI, WAN AND HANLY, STEPHEN V AND LOZANO, ANGEL AND SOONG, ANTHONY CK AND ZHANG, JIANZHONG CHARLIE. **What will 5g be?** IEEE Journal on selected areas in communications, 32(6):1065–1082, 2014.

[20] LUINI, L AND ROVEDA, G AND ZAFFARONI, M AND COSTA, M AND RIVA, C. **Em wave propagation experiment at e band and d band for 5g wireless systems: Preliminary results**. In: 12TH EUROPEAN CONFERENCE ON ANTENNAS AND PROPAGATION (EUCAP 2018). IET, 2018.

[21] LUINI, LORENZO AND ROVEDA, GIUSEPPE AND ZAFFARONI, MAURIZIO AND COSTA, MARIO AND RIVA, CARLO G. **The impact of rain on short e-band radio links for 5g mobile systems: Experimental results and prediction models**. IEEE Transactions on Antennas and Propagation, 68(4):3124–3134, 2019.

[22] LUINI, LORENZO AND ROVEDA, GIUSEPPE AND ZAFFARONI, MAURIZIO AND COSTA, MARIO AND RIVA, CARLO G.. **The impact of rain on short e-band radio links for 5g mobile systems: Experimental results and prediction models**. IEEE Transactions on Antennas and Propagation, 68(4):3124–3134, 2020.

[23] DOUIK, AHMED AND DAHROUJ, HAYSSAM AND AL-NAFFOURI, TAREQ Y AND ALOUINI, MOHAMED-SLIM. **Hybrid radio/free-space optical design for next generation backhaul systems**. IEEE Transactions on Communications, 64(6):2563–2577, 2016.

[24] AKBULUT, AHMET AND EFE, MURAT AND CEYLAN, A MURAT AND ARI, FIKRET AND TELATAR, ZIYA AND ILK, H GOKHAN AND TUGAC, SERDAR. **An experimental hybrid FSO/RF communication system**. In: PROCEEDING (393) COMMUNICATION SYSTEMS AND NETWORKS, 2003.

[25] KAMALAKIS, THOMAS AND NEOKOSMIDIS, IOANNIS AND TSIPOURAS, A AND SPHICOPOULOS, T AND PANTAZIS, S AND ANDRIKOPOULOS, I. **Hybrid free space optical/millimeter wave outdoor links for broadband wireless access networks**. In: 2007

IEEE 18TH INTERNATIONAL SYMPOSIUM ON PERSONAL, INDOOR AND MOBILE RADIO COMMUNICATIONS, p. 1–5. IEEE, 2007.

[26] NADEEM, FARUKH AND KVICERA, VACLAV AND AWAN, MUHAMMAD SALEEM AND LEITGEB, ERICH AND MUHAMMAD, SAJID SHEIKH AND KANDUS, GORAZD. **Weather effects on hybrid FSO/RF communication link**. IEEE journal on selected areas in communications, 27(9):1687–1697, 2009.

[27] ZHANG, YANG AND PARK, YOUNGIL AND KIM, BYUNGYEON AND KIM, KIDOO. **Performance analysis of hybrid FSO/RF system**. In: 2011 THIRD INTERNATIONAL CONFERENCE ON UBIQUITOUS AND FUTURE NETWORKS (ICUFN), p. 279–283. IEEE, 2011.

[28] KOLKA, ZDENĚK AND KINCL, ZDENĚK AND BIOLKOVA, VIERA AND BIOLEK, DALIBOR. **Hybrid FSO/RF test link**. In: 2012 IV INTERNATIONAL CONGRESS ON ULTRA MODERN TELECOMMUNICATIONS AND CONTROL SYSTEMS, p. 502–505. IEEE, 2012.

[29] TOUATI, ABIR AND ABDAOUI, ABDERRAZAK AND TOUATI, FARID AND UYSAL, MURAT AND BOUALLEGUE, AMMAR. **On the effects of combined atmospheric fading and misalignment on the hybrid FSO/RF transmission**. Journal of Optical Communications and Networking, 8(10):715–725, 2016.

[30] BAG, BANIBRATA AND DAS, AKINCHAN AND ANSARI, IMRAN SHAFIQUE AND PROKEŠ, ALEŠ AND BOSE, CHAYANIKA AND CHANDRA, ANIRUDDHA. **Performance analysis of hybrid FSO systems using FSO/RF-FSO link adaptation**. IEEE Photonics Journal, 10(3):1–17, 2018.

[31] WORLD METEOROLOGICAL ORGANIZATION (WMO). **Guide to meteorological instruments and methods of observation**, 2018. Access on: October 2021.

[32] THE DEPARTMENT OF AIRSPACE CONTROL (DECEA). **DECEA archive**, 2021. Access on: October 2021.

[33] UNIVERSITY OF WYOMING. **University of wyoming repository**, 2021. Access on: October 2021.

[34] NATIONAL OCEANIC AND ATMOSPHERIC ADMINISTRATION. **national oceanic and atmospheric administration (NOAA)**, 2021. Access on: October 2021.

[35] CENTRE FOR ENVIRONMENTAL DATA ANALYSIS. **CEDA archive**, 2021. Access on: October 2021.

[36] INTERNATIONAL CIVIL AVIATION ORGANIZATION. **Metar/taf list of abbreviations and acronyms**, 2021. Access on: October 2021.

[37] NEBULONI, R AND CAPSONI, CARLO. **Laser attenuation by falling snow**. In: 2008 6TH INTERNATIONAL SYMPOSIUM ON COMMUNICATION SYSTEMS, NETWORKS AND DIGITAL SIGNAL PROCESSING, p. 265–269. IEEE, 2008.

[38] AWAN, MUHAMMAD SALEEM AND CSURGAI-HORVÁTH, LÁSZLÓ AND MUHAMMAD, SAJID SHEIKH AND LEITGEB, ERICH AND NADEEM, FARUKH AND KHAN, MUHAMMAD SAEED. **Characterization of fog and snow attenuations for free-space optical propagation.** J. Commun., 4(8):533–545, 2009.

[39] CHIMELIS, VINCENT. **Extinction of co2 laser radiation by fog and rain**. Applied optics, 21(18):3367–3372, 1982.

[40] BORAH, D. K.; VOELZ, D. G.. **Pointing error effects on free-space optical communication links in the presence of atmospheric turbulence**. Journal of Lightwave Technology, 27(18):3965–3973, 2009.

[41] NEBULONI, ROBERTO AND CAPSONI, CARLO. **Effects of adverse weather on free space optics**. In: OPTICAL WIRELESS COMMUNICATIONS, p. 47–68. Springer, 2016.

[42] IEC STANDARD 60825-1. **Iec 60825-1:2014 safety of laser products - part 1: Equipment classification and requirements**, 2014. Access on: October 2021.

[43] FAIST, JEROME AND CAPASSO, FEDERICO AND SIVCO, DEBORAH L AND SIRTORI, CARLO AND HUTCHINSON, ALBERT L AND CHO, ALFRED Y. **Quantum cascade laser**. Science, 264(5158):553–556, 1994.

[44] CORRIGAN, PAUL AND MARTINI, RAINER AND WHITTAKER, EDWARD A AND BETHEA, CLYDE. **Quantum cascade lasers and the kruse model in free space optical communication**. Optics Express, 17(6):4355–4359, 2009.

[45] LEITGEB, ERICH AND PLANK, THOMAS AND AWAN, MUHAMMAD SALEEM AND BRANDL, PAUL AND POPOOLA, WASIU AND GHASSEMLOOY, ZABIH AND OZEK, FARUK AND WITTIG, MANFRED. **Analysis and evaluation of optimum wavelengths for free-space optical transceivers**. In: 2010 12TH INTERNATIONAL CONFERENCE ON TRANSPARENT OPTICAL NETWORKS, p. 1–7. IEEE, 2010.

[46] INTERNATIONAL TELECOMMUNICATION UNION. **Propagation data and prediction methods required for the design of terrestrial line-of-sight systems**, 2021. Access on: October 2021.

[47] INTERNATIONAL TELECOMMUNICATION UNION. **Propagation data required for the design of terrestrial free-space optical links**, 2012. Access on: October 2021.

[48] HULST, HENDRIK CHRISTOFFEL AND VAN DE HULST, HENDRIK C. **Light scattering by small particles**. Courier Corporation, 1981.

[49] KIM, ISAAC I AND MCARTHUR, BRUCE AND KOREVAAR, ERIC J. **Comparison of laser beam propagation at 785 nm and 1550 nm in fog and haze for optical wireless communications**. In: OPTICAL WIRELESS COMMUNICATIONS III, volumen 4214, p. 26–37. International Society for Optics and Photonics, 2001.

[50] KRUSE, PAUL W AND MCGLAUCHLIN, LAURENCE D AND MCQUISTAN, RICHMOND B. **Elements of infrared technology: Generation, transmission and detection**. New York: Wiley, 1962.

[51] NEBULONI, ROBERTO. **Empirical relationships between extinction coefficient and visibility in fog**. Applied optics, 44(18):3795–3804, 2005.

[52] GRABNER, MARTIN AND KVICERA, VACLAV. **The wavelength dependent model of extinction in fog and haze for free space optical communication**. Optics express, 19(4):3379–3386, 2011.

[53] AL NABOULSI, MAHER C AND SIZUN, HERVE AND DE FORNEL, FREDERIQUE. **Fog attenuation prediction for optical and infrared waves**. Optical Engineering, 43(2):319–329, 2004.

[54] CHYLEK, PETER. **Extinction and liquid water content of fogs and clouds**. Journal of Atmospheric Sciences, 35(2):296–300, 1978.

[55] KLEIN, C AND DABAS, A. **Relationship between optical extinction and liquid water content in fogs**. Atmospheric Measurement Techniques, 7(5):1277–1287, 2014.

[56] MAYERHÖFER, THOMAS G AND PAHLOW, SUSANNE AND POPP, JÜRGEN. **The bouguer-beer-lambert law: Shining light on the obscure**. ChemPhysChem, 21(18):2029, 2020.

[57] BEER, AUGUST. **Bestimmung der absorption des rothen lichts in farbigen flussigkeiten**. Ann. Physik, 162:78–88, 1852.

[58] KOSCHMIEDER, HARALD. **Theory of horizontal visibility**. Contribut. Phys. Free Atmos, 12:33–53, 1924.

[59] PIERCE, ROBERT MICHAEL AND RAMAPRASAD, JAYA AND EISENBERG, ERIC C. **Optical attenuation in fog and clouds**. In: OPTICAL WIRELESS COMMUNICATIONS IV, volumen 4530, p. 58–71. International Society for Optics and Photonics, 2001.

[60] WAUBEN, WIEL AND ROTH, MARTIN. **Exploration of fog detection and visibility estimation from camera images**. In: WMO TECHNICAL CONFERENCE ON METEOROLOGICAL AND ENVIRONMENTAL INSTRUMENTS AND METHODS OF OBSERVATION, CIMO TECO, p. 1–14, 2016.

[61] BABARI, RAOUF AND HAUTIERE, NICOLAS AND DUMONT, ERIC AND BRÉMOND, ROLAND AND PAPARODITIS, NICOLAS. **A model-driven approach to estimate atmospheric visibility with ordinary cameras**. Atmospheric Environment, 45(30):5316–5324, 2011.

[62] COLVERO, CP AND CORDEIRO, MCR AND DE FARIA, GV AND VON DER WEID, JP. **Experimental comparison between far-and near-infrared wavelengths in free-space optical systems**. Microwave and optical technology letters, 46(4):319–323, 2005.

[63] CROSBY, JOHN D. **Visibility sensor accuracy: what's realistic**. In: 12TH SYMPOSIUM ON METEOROLOGICAL OBSERVATIONS AND INSTRUMENTATION, p. 1–5. Citeseer, 2003.

[64] WORLD METEOROLOGICAL ORGANIZATION (WMO). **Manual on codes - international codes**, 2021. Access on: October 2021.

[65] SHETTLE, ERIC P. **Models of aerosols, clouds, and precipitation for atmospheric propagation studies**. In AGARD, 1990.

[66] IJAZ, MUHAMMAD AND GHASSEMLOOY, ZABIH AND PESEK, JIRI AND FISER, ONDREJ AND LE MINH, HOA AND BENTLEY, EDWARD. **Modeling of fog and smoke attenuation in free space optical communications link under controlled laboratory conditions**. Journal of Lightwave Technology, 31(11):1720–1726, 2013.

[67] KOTAMRAJU, SARAT KUMAR AND KORADA, CH SRI KAVYA. **Precipitation and other propagation impairments effects at microwave and millimeter wave bands: a mini survey**. Acta Geophysica, 67(2):703–719, 2019.

[68] TAMPIERI, FRANCESCO AND TOMASI, CLAUDIO. **Size distribution models of fog and cloud droplets in terms of the modified gamma function**. Tellus, 28(4):333–347, 1976.

[69] DEIRMENDJIAN, D. **Far-infrared and submillimeter wave attenuation by clouds and rain**. Journal of Applied Meteorology and Climatology, 14(8):1584–1593, 1975.

[70] ZUEV, VLADIMIR EVSEEVICH. **Atmospheric Transparency in the Visible and the Infrared**. Israel Program for Scientific Translations;[available from the US Department . . . , 1970.

[71] GUIDARD, VINCENT AND TZANOS, DIANE. **Analysis of fog probability from a combination of satellite and ground observation data**. Pure and Applied Geophysics, 164(6):1207–1220, 2007.

[72] HAEFFELIN, M AND BERGOT, T AND ELIAS, T AND TARDIF, R AND CARRER, D AND CHAZETTE, P AND COLOMB, M AND DROBINSKI, P AND DUPONT, E AND DUPONT, J-C AND OTHERS. **Parisfog: Shedding new light on fog physical processes**. Bulletin of the American Meteorological Society, 91(6):767–783, 2010.

[73] TARDIF, ROBERT AND RASMUSSEN, ROY M. **Event-based climatology and typology of fog in the new york city region**. Journal of applied meteorology and climatology, 46(8):1141–1168, 2007.

[74] DEIRMENDJIAN, DIRAN. **Electromagnetic scattering on spherical polydispersions**. Technical report, Rand Corp Santa Monica CA, 1969.

[75] FISCHER, KW AND WITIW, MR AND EISENBERG, E. **Optical attenuation in fog at a wavelength of 1.55 micrometers**. Atmospheric Research, 87(3-4):252–258, 2008.

[76] GEBHART, MICHAEL AND LEITGEB, ERICH AND MUHAMMAD, S SHEIKH AND FLECKER, BENNO AND CHLESTIL, CHRISTOPH AND AL NABOULSI, MAHER AND DE FORNEL, F AND SIZUN, H. **Measurement of light attenuation in dense fog conditions for fso applications**. In: ATMOSPHERIC OPTICAL MODELING, MEASUREMENT, AND SIMULATION, volumen 5891, p. 58910K. International Society for Optics and Photonics, 2005.

[77] DEV, KAPAL AND NEBULONI, ROBERTO AND CAPSONI, CARLO AND FISER, ONDREJ AND BRAZDA, VLADIMIR. **Estimation of optical attenuation in reduced visibility conditions in different environments across free space optics link**. IET Microwaves, Antennas & Propagation, 11(12):1708–1713, 2017.

[78] GRABNER, MARTIN AND KVICERA, VACLAV. **Physical and statistical modeling of attenuation due to atmospheric hydrometeors on free-space optical links at 850 and 1550 nm**. In: LASER COMMUNICATION AND PROPAGATION THROUGH THE ATMOSPHERE AND OCEANS, volumen 8517, p. 851716. International Society for Optics and Photonics, 2012.

[79] KHALIGHI, MOHAMMAD-ALI AND SCHWARTZ, NOAH AND AITAMER, NAZIHA AND BOURENNANE, SALAH. **Fading reduction by aperture averaging and spatial diversity in optical wireless systems**. Journal of optical communications and networking, 1(6):580–593, 2009.

[80] STRICKLAND, BRIAN R AND LAVAN, MICHAEL J AND WOODBRIDGE, ERIC AND CHAN, VICTOR. **Effects of fog on the bit-error rate of a free-space laser communication system**. Applied optics, 38(3):424–431, 1999.

[81] ANGUITA, JAIME A AND NEIFELD, MARK A AND HILDNER, BJÖRN AND VASIC, BANE. **Rateless coding on experimental temporally correlated fso channels**. Journal of Lightwave Technology, 28(7):990–1002, 2010.

[82] MELLO, LAR DA SILVA AND PONTES, MS AND DE SOUZA, RM AND GARCIA, NA PEREZ. **Prediction of rain attenuation in terrestrial links using full rainfall rate distribution**. Electronics Letters, 43(25):1442–1443, 2007.

[83] LIN, SH. **11-ghz radio: nationwide long-term rain rate statistics and empirical calculation of 11-ghz microwave rain attenuation**. Bell System Technical Journal, 56(9):1581–1604, 1977.

[84] MOUPFOUMA, FIDÈLE. **Electromagnetic waves attenuation due to rain: A prediction model for terrestrial or los shf and ehf radio communication links**. Journal of Infrared, Millimeter, and Terahertz Waves, 30(6):622–632, 2009.

[85] INTERNATIONAL TELECOMMUNICATION UNION. **Characteristics of precipitation for propagation modelling**, 2017. Access on: October 2021.

[86] INTERNATIONAL TELECOMMUNICATION UNION. **Mean surface temperature**, 2017. Access on: October 2021.

[87] INTERNATIONAL TELECOMMUNICATION UNION. **Guide to the application of the propagation methods of radiocommunication**, 2021. Access on: March 2022.

[88] INTERNATIONAL TELECOMMUNICATION UNION. **Specific attenuation model for rain for use in prediction methods**, 2005. Access on: March 2022.

[89] KORAI, UMAIR AHMED AND LUINI, LORENZO AND NEBULONI, ROBERTO. **Model for the prediction of rain attenuation affecting free space optical links**. Electronics, 7(12):407, 2018.

[90] MANOR, HAIM AND ARNON, SHLOMI. **Performance of an optical wireless communication system as a function of wavelength**. Applied optics, 42(21):4285–4294, 2003.

[91] GRABNER, MARTIN AND KVICERA, VACLAV. **Multiple scattering in rain and fog on free-space optical links**. Journal of lightwave technology, 32(3):513–520, 2013.

[92] FELDHAKE, GLENN. **Estimating the attenuation due to combined atmospheric effects on modern earth-space paths**. IEEE Antennas and Propagation Magazine, 39(4):26–34, 1997.

[96] MOSTCOM. **Artolink FSO equipement MI-GE/MI-GE-L: User's manual**. Access on: October 2021.

[97] GUNN, ROSS AND KINZER, GILBERT D. **The terminal velocity of fall for water droplets in stagnant air**. Journal of Atmospheric Sciences, 6(4):243–248, 1949.

[98] GROISMAN, PAVEL YA AND LEGATES, DAVID R. **The accuracy of united states precipitation data**. Bulletin of the American Meteorological Society, 75(2):215–228, 1994.

[99] DUCHON, CLAUDE E AND ESSENBERG, GAVIN R. **Comparative rainfall observations from pit and aboveground rain gauges with and without wind shields**. Water Resources Research, 37(12):3253–3263, 2001.

[100] ANDREWS, L. C.. **Laser beam propagation through random media**. SPIE-International Society for Optical Engineering, 2005.

[101] ADOLF THIES GMBH CO KG . **Laser precipitation monitor: Instructions for use**, 2021. Access on: October 2021.

[102] SURIZA, AZ AND RAFIQUL, ISLAM MD AND WAJDI, AK AND NAJI, AW. **Effects of rain intensity variation on rain attenuation prediction for free space optics (fso) links**. In: 2012 INTERNATIONAL CONFERENCE ON COMPUTER AND COMMUNICATION ENGINEERING (ICCCE), p. 680–685. IEEE, 2012.

[103] KAIMAL, J.; GAYNOR, J.. **Another look at sonic thermometry**. Boundary-layer meteorology, 56(4):401–410, 1991.

[104] HOUZE JR, ROBERT A. **Cloud dynamics**. Academic press, 2014.

[105] METEOROLOGICAL SERVICE OF CANADA. **Manual of surface weather observations**, 2013. Access on: March 2022.

[106] PONTES, MS AND DA SILVA MELLO, LAR AND DE SOUZA, RSL. **Modeling of effective rainfall rate and rain attenuation in terrestrial links in the tropics**. In: 2007 6TH INTERNATIONAL CONFERENCE ON INFORMATION, COMMUNICATIONS & SIGNAL PROCESSING, p. 1–4. IEEE, 2007.

A
Conditions to Evaluate Wyoming repository

A.0.1
Conditions to discard a station

1. Since to find a statistically valid value of the visibility exceeded 99.99% of the time, we require at least 100.000 samples. Then, we define the first condition as: A station is discarded if the quantity of valid samples is equal or lower than 100.000.

2. In total, we examine data for 25 years. To avoid the use of stations with very low available data in terms of years, we define the second condition as: If the quantity of *valid years* is lower than seven, then the station is discarded. The requirements to classify a full year as *invalid* are presented below.

A.0.2
Conditions to consider a year as *invalid*

To classify a year as valid or invalid, we define the *expected sampling time* of each station. It is the most frequent sampling time obtained from the histogram of the differences in the multiple timestamps. For instance, Figure A.1 presents the distribution of sampling time of the available measurements from the stations in Linate airport in Milan, Italy, and Galeão airport in Rio de Janeiro, Brazil. In the case of Milan, only a few samples ($< 1\%$) present a 1-hour interval between each two of them, and the vast majority (97%) are within 30-mins sampling time. Then, the expected sampling time for Milan is 30 mins. Similarly, for Rio de Janeiro, 84% of the samples present a sampling time of one hour, whereas 14% are within a 30-mins interval. Thus, the expected sampling time for this location is one hour. Figure A.2 panel (a) draws the distribution of expected sampling time considering all the sites; we estimate that almost 70% of the stations present a sampling time of 30 minutes, while about 30% of them may have a sampling time of one hour.

A.0.3
Expected number of samples

Another significant figure is the *expected number of samples per year*; it is estimated by multiplying the number of days in the year (leap-years are considered) by the number of samples in the day regarding the expected sampling rate obtained before. The expected number of samples per year ranges from 8.760 to 17.568 (considering a regular year with 1-hour sampling time and a leap year with 30-mins sampling time).

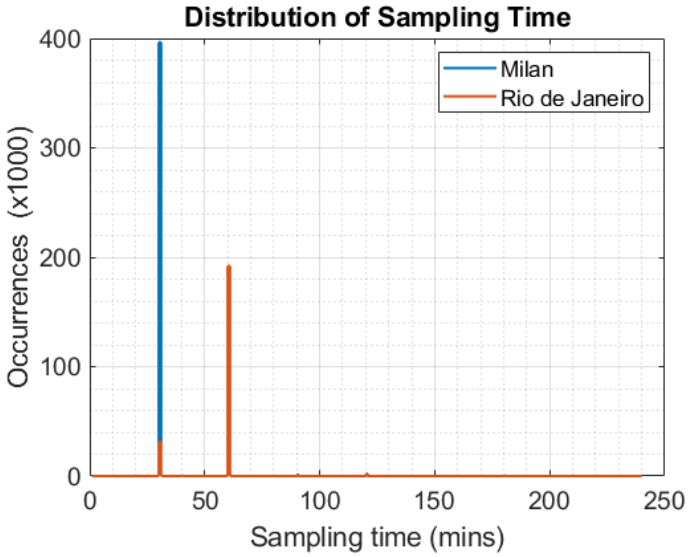

Figure A.1: Histogram of differences in the timestamps.

- A year is invalid if the percentage of valid samples to the available samples is lower than the 80%.
- A year is invalid if the percentage of available samples is lower than 50% of the total expected samples in that year.
- A year is invalid if the percentage of samples with a sampling rate equal to the expected one is lower than the 30%.

Figure A.2 panel (b) exhibits the distribution of the percentage of years classified as invalid per station.

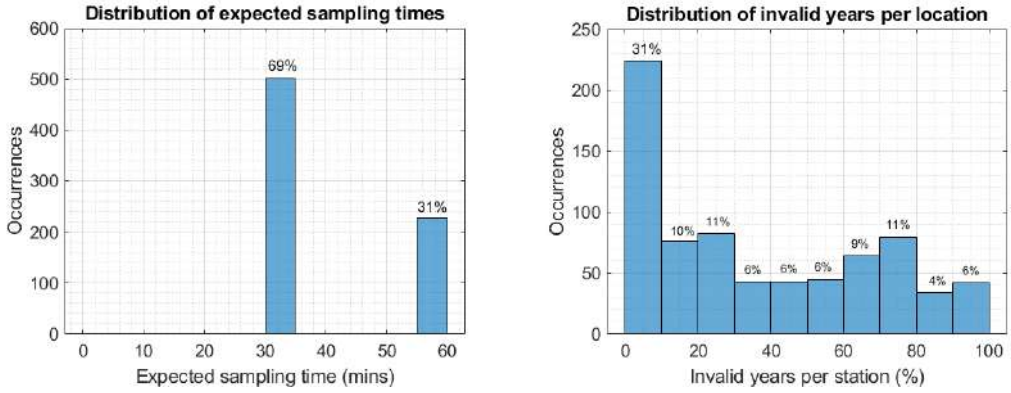

(a) (b)

Figure A.2: Distribution of the calculated expected sampling time and the percentage of invalid years per station for the locations from the Wyoming University repository.

B
List of $\gamma - V$ models

Table B.1: List of γ-V models. V is in km, γ is in dB/km, λ is the wavelength in μm.

ID	Model name	Model	Comment
1	Definition of visibility	$\gamma = \frac{K}{V}$	If $K = 13$, V equals the meteorological optical range (MOR). [31]
2	Kruse [50]	$\gamma = \frac{17}{V}(\frac{0.550}{\lambda})^q$, $q = \begin{cases} 1.6 & V > 50km \\ 1.3 & 6km < V \leq 50km \\ 0.585V^{\frac{1}{3}} & V < 6km \end{cases}$	
3	Kim [49]	$\gamma = \frac{17}{V}(\frac{0.550}{\lambda})^q$, $q = \begin{cases} 1.6 & V > 50km \\ 1.3 & 6km < V \leq 50km \\ 0.16V + 0.34 & 1km \leq V \leq 6km \\ V - 0.5 & 0.5km \leq V < 1km \\ 0 & V < 0.5km \end{cases}$ $0.4\mu m \leq \lambda \leq 1.55\mu m$	Kruse model upgrade for fog conditions.

<table>
<tr>
<td>4</td>
<td>Grabner [52]</td>
<td>$\gamma = \frac{17}{V}(\frac{0.550}{\lambda})^q$,
$q = -2(\tanh(p_1(w+p_4)) - 1) + p_2 \exp(-p_3(w+p_5)^2)$,
$w = \log_{10} r_e, \quad r_e = 10\sqrt{\frac{0.05}{V}}$,
<table>
<tr><th>Coef.</th><th>$0.2 < \lambda < 0.55\mu m$</th><th>$0.55 \leq \lambda < 2\mu m$</th></tr>
<tr><td>p_1</td><td>2.21888</td><td>1.94311</td></tr>
<tr><td>p_2</td><td>0.67214</td><td>0.59076</td></tr>
<tr><td>p_3</td><td>8.04794</td><td>6.36656</td></tr>
<tr><td>p_4</td><td>0.8</td><td>0.45</td></tr>
<tr><td>p_5</td><td>0.3</td><td>-0.15</td></tr>
</table>
$0.2\mu m < \lambda < 2\mu m, \qquad V \leq 10km$</td>
<td>Microphysical model. Based on fog PSD modelling by the gamma function.</td>
</tr>
<tr>
<td>5</td>
<td>Al Naboulsi [53]</td>
<td>$\gamma_{Adv} = \frac{0.49488\lambda + 16.66258}{V}$,
$\gamma_{Rad} = \frac{0.78720\lambda^2 + 0.59537\lambda + 16.28691}{V}$,
$0.690\mu m \leq \lambda \leq 1.55\mu m$,
$0.05km \leq V \leq 1km$</td>
<td>Microphysical model advection and radiation fog.</td>
</tr>
<tr>
<td>6</td>
<td>Nebuloni [51]</td>
<td>$\gamma = aV^b$
<table>
<tr><th>Center</th><th>Center-band (μm)</th><th>Visibility (km)</th><th>a</th><th>b</th></tr>
<tr><td>Visible</td><td>0.55</td><td>$V > 0$</td><td>16.98</td><td>-1.00</td></tr>
<tr><td>Near IR</td><td>1.20</td><td>$0.06 \leq V < 0.5$</td><td>15.85</td><td>-1.02</td></tr>
<tr><td></td><td></td><td>$0.5 \leq V < 2$</td><td>12.38</td><td>-1.38</td></tr>
<tr><td>Mid IR</td><td>3.70</td><td>$0.06 \leq V < 0.5$</td><td>13.07</td><td>-1.11</td></tr>
<tr><td></td><td></td><td>$0.5 \leq V < 10$</td><td>10.42</td><td>-1.43</td></tr>
<tr><td>Far IR</td><td>10.6</td><td>$0.06 \leq V < 0.5$</td><td>5.30</td><td>-1.30</td></tr>
<tr><td></td><td></td><td>$0.5 \leq V < 3$</td><td>2.30</td><td>-2.51</td></tr>
</table></td>
<td>The best fit of measurements carried out by several authors.</td>
</tr>
<tr>
<td>7</td>
<td>Ijaz [66]</td>
<td>$\gamma = \frac{17}{V}(\frac{0.550}{\lambda})^q$,
$q = 0.1428\lambda - 0.0947$
$0.6\mu m \leq \lambda \leq 1.6\mu m$,
$0.015km < V < 1km$</td>
<td>Based on the best fit of measurements using a 5.5-m chamber simulating the foggy channel.</td>
</tr>
</table>

C
Recent Measurements of Optical Transmission

Table C.1: Summary of Recent Measurements of Optical Transmission.

Reference	**Site, Data**	**λ (μ m)**	**L (m)**	**V**	**Results**
Colvero et al. 2005 [62]	800 m mountain top in Rio de Janeiro (BR). 116 h dataset basically in coastal upslope fog.	0.785 1.550 9.1	75	30 m – 20 km	"When the visual range became comparable to the link length, the transmission of the far IR was at least an order of magnitude better than the other two".

Corrigan et al. 2009 [44]	2 km from mid-town Manhattan on the bank of the Hudson River (U.S.A). 6 h fog on 19/10/2006 (rain in the end). Visibility estimated by Kruse model.	1.3345 1.558 8.1	550	1.05 - 12 km	"8.1 μm source provides 2x to 3x greater transmission over near-IR wavelengths during fog formation and up to 10x after a short scavenging rain event where fog developed and visibility reduced to 1 km".
Fischer et al. [75]	Redmond, WA (USA), semi-rural area. 6 fog events during fall 2002.	1.55	85	Down to 48 m	Kruse model is pessimistic if V$<$ 650 m. $\cong 10/V$ fits 1.55 μm measurements.
Pierce et al. [59]	Seattle, WA (USA). Downtown area. 2 fog events on 12/2000.	0.532 1.55	N.A.	N.A.	1.55 μm exceeds 0.53 μm attenuation by 6% (their Fig. 4 - left panel).

Grabner and Kvicera [52]	Prague (Czech Republic). 35 foggy days over two years (2008-09).	0.830 1.550	100 100	60 m to 2 km	$\cong 20.5/V$ and $\cong 18.2/V$ over the short link at both wavelengths if $0.3 \leq V \leq 1km$ From their Figure 2b: 200m/100/90 400m/70/60-70 600m/50-60/40-50 800m/30-40/30 1000m/20-30/20
Gebhart et al. [76]	La tête de chien Hill, La Turbie (France). Event of 28/06/2004 (dense maritime fog).	0.850 0.950	28	30 m-1 km	Very good correlation between visibility and attenuation (their Fig. 6).
Dev et al. [77]	Milan city area (Italy). 31 events (radiation fog).	0.785	319	0.2- 2 km	Good correlation between visibility (13/V) and attenuation in Milan (their Fig. 4).
Dev et al. [77]	Top of Milesowka mount at 837 m amsl (Czech Rep.). 25 fog events. Slant path + 2 visibility sensors.	0.850	80	50 m – 2 km	Challenging environment, fog and cloud occurrence, fair correlation only if fog is homogeneous.

D
Differentiating process to find expression (3-12)

Differentiating power budget expression (3-10), assuming $P_T - P_R - A_{sys} = M$ and M is constant.

$$\gamma L - 10\log_{10}\frac{A_R}{\pi(\vartheta_T L)^2} + 60 = P_T - P_R - A_{sys}$$

$$\frac{d}{d\gamma}(\gamma L) - \frac{d}{d\gamma}\left[10\log_{10}\frac{A_R}{\pi(\vartheta_T L)^2}\right] + \frac{d}{d\gamma}60 = 0$$

The path length, L, is not a constant.

$$L\frac{d}{d\gamma}(\gamma) + \gamma\frac{d}{d\gamma}(L) = 10\frac{d}{d\gamma}\left(\log_{10} A_R\right) - 10\frac{d}{d\gamma}\left(\log_{10}\pi(\vartheta_T L)^2\right)$$

Since A_R is a constant, then $10\frac{d}{d\gamma}\left(\log_{10} A_R\right) = 0$

$$L\frac{d}{d\gamma}(\gamma) + \gamma\frac{d}{d\gamma}(L) = -20\frac{d}{d\gamma}\left(\log_{10}\pi^{-2}\right) - 20\frac{d}{d\gamma}\log_{10}(\vartheta_T L)$$

Again, $-20\frac{d}{d\gamma}\left(\log_{10}\pi^{-2}\right) = 0$

$$L\frac{d}{d\gamma}(\gamma) + \gamma\frac{d}{d\gamma}(L) = -20\left(\frac{d}{d\gamma}\left(\log_{10}\vartheta_T\right) + \frac{d}{d\gamma}\log_{10}(L)\right)$$

Since ϑ_T is a constant, then $\frac{d}{d\gamma}\left(\log_{10}\vartheta_T\right) = 0$

$$L\frac{d}{d\gamma}(\gamma) + \gamma\frac{d}{d\gamma}(L) = -20\left(\frac{d}{d\gamma}\log_{10}(L)\right)$$

Calculating the derivation of the logarithm we have:

$$L\frac{d}{d\gamma}(\gamma) + \gamma\frac{d}{d\gamma}(L) = -20\left(\frac{1}{\ln 10}\frac{1}{L}\frac{d}{d\gamma}(L)\right)$$

Multiplying by $d\gamma$:

$$L(d\gamma) + \gamma(dL) = -\frac{20}{\ln 10}\frac{1}{L}(dL)$$

Dividing by L:

$$d\gamma + \gamma\frac{dL}{L} = -\frac{20}{\ln 10}\frac{1}{L}\frac{dL}{L}$$

Dividing by γ:

$$\frac{d\gamma}{\gamma} + \frac{dL}{L} = -\frac{20}{\ln 10}\frac{1}{\gamma L}\frac{dL}{L}$$

$$\frac{dL}{L} + \frac{20}{\ln 10}\frac{1}{\gamma L}\frac{dL}{L} = -\frac{d\gamma}{\gamma}$$

Grouping:

$$\frac{dL}{L}\left[1 + \frac{20}{\ln 10}\frac{1}{\gamma L}\right] = -\frac{d\gamma}{\gamma}$$

And the expression (3-12) is the one inside the box:

$$\boxed{\frac{dL}{L} = -\left[1 + \frac{20}{\ln 10}\frac{1}{\gamma L}\right]^{-1}\frac{d\gamma}{\gamma}}$$

E
Process to correct the CCDF of total attenuation

Once different classes of weather conditions have been identified according to SYNOP codes, a propagation model is selected to extract the corresponding CCDF of specific attenuation. Then, the curves are added together in probability. In the case of rainfall, we use the power-law model:

$$\gamma_{rain} = kR^{\alpha} \tag{E-1}$$

corrected by the multiple scattering effects:

$$A_{rain} = \gamma_{rain} G_{ms}(R, L) = kR^{\alpha} G_{ms}(R, L) \tag{E-2}$$

The CCDF of rainfall intensity is derived from ITU-R. In general, the percentage of rainy time (i.e., initial point of the ITU-R CCDF) might differ from the percentage time flagged as rainy by SYNOP codes (i.e., from the Wyoming data). Hence, when adding the CCDF of rain attenuation to the CCDFs of the other components (e.g., fog), it is necessary to correct the data in order that the resulting CCDF of total attenuation is exactly 100% at $A = 0$.

$$P(A) = P_r(A) + P_{nor}(A) \tag{E-3}$$

where, $P_r(A)$ is estimated by the ITU-R, and, for sake of simplicity, we reduce the weather conditions to rainy and other than rainy, i.e., $P_{nor}(A)$. The corrected CCDF is:

$$\hat{P}(A) = P_r(A) + \hat{P}_{nor}(A) = P_r(A) + P_{nor}(A) + \Delta(A) \tag{E-4}$$

where $\Delta(A)$ is to be determined. Moreover, $P^{itur}(0)$ and $P^{syn}(0)$ are the probability of rain (i.e., probability that $A_r > 0$) according to ITU-R and SYNOP codes, respectively. Finally, $P(0)$ is the probability that total attenuation is larger than 0. There are two cases:

1. if $P^{itur}(0) < P^{syn}(0)$, then $P(0) < 100\%$.
2. if $P^{itur}(0) > P^{syn}(0)$, then $P(0) > 100\%$.

In the first case, we assume that the missing time, which is rainy according to SYNOP codes, corresponds to the first bin, i.e., $A = 0$ hence, in (E-4) we have:

$$\Delta(A) = \begin{cases} 100 - (P_r(0) - P_{nor}(0)), & \text{if } A = 0 \\ 0, & \text{if } A > 0 \end{cases} \tag{E-5}$$

The second case is more complex as we cannot rule out that $P(A) > 100\%$ for $A > 0$. Here, we have to delete some time from one flagged as not rainy by SYNOP codes. For the initial bin, $P(A = 0)$, it is reasonable to proceed as in the first case. For the k_r bins such that $P(R) > 0$, we proceed as follows:

$$\hat{P}(k) = xP_{nor}(k) + P_r(k), \text{where } k = 0, 1, 2, ...k_r \tag{E-6}$$

where the ratio, x, to scale the rainy bins is given by:

$$x = \frac{\hat{P}_{nor}(0)}{P_{nor}(0)} = \frac{100 - P_r(0)}{P_{nor}(0)} \tag{E-7}$$

In this way, we spill the same fraction of time from $P_{nor}(A)$ whatever the attenuation bin and we get a monotonically decreasing curve, as it should be, as $\hat{P}_{nor}(k) < \hat{P}_{nor}(k-1)$.

F
Relevant study cases

F.1
Stratiform rain

Event 5: 17/11/2019

Stratiform precipitation is characterized by low-intensity intermittent rain throughout the day [105]. The selected event allowing to study of the effects on the mmWave and FSO links is the one that occurred on 17 November 2019. Panel (a) of Figure F.1 presents the measured attenuation data. Two main episodes (1:00 to 6:00 and 6:30 to 14:00) are separated by a short dry period. The rain intensity in the first episode does not exceed 3 mm/h, while the maximum in the second one is about 6 mm/h.

Figure F.1 Panel (c) presents the optical attenuation detected by the information channel and the predictions calculated considering the multiple scattering effects (A_{MS}) and without the multiple scattering effects (A_R). The two episodes are detectable when considering the time series of measured attenuation in the information channel (Figure F.1 (c)). However, the oscillations of rain rate and attenuation are not well correlated. Moreover, the magnitude of the measured attenuation is much higher than the one predicted by the theory. For instance, the measured attenuation peak at 8:30 is 7.6 dB, whereas, at the same time, the expected attenuation is less than 2 dB (Panel (c)). On the other side, the maximum predicted attenuation, which occurs at noon (around 2 dB), is still much less than the measurements (slightly less than 6 dB). Finally, note that the maximum of predicted attenuation does not always correspond to the rain rate peak.

The attenuation detected by the service channel correlates well with the two main rain episodes. However, there is a small peak at 20:00 due to lower visibility (Panel (b)). In general, the attenuation time series derived from the service channel is slightly lower and more stable than those associated with the information channel. The broader field of view might explain this effect at the receiver of the service channel. Panel (d) shows the atmospheric parameters during the rainy event. Visibility variations are quite significant during the

day (from 2 to 10 km) and are not always correlated with rain occurrence. During the two principal episodes, the wind velocity profile highlights four distinct periods with velocity peaks above four m/s (15 km/h) correlated with the attenuation pattern.

The large values of measured attenuation might be explained by the effect of tiny suspended particles that significantly reduce the visibility but are not detected by the disdrometer; therefore, they cannot be included in the computation of predicted attenuation. Wind and turbulence might increase signal fluctuations, hence attenuation. Moreover, the wind might be the reason for an effect strictly not related to propagation: wind might deviate the falling raindrops from the vertical direction. As a result, raindrops might hit the glass cover placed in front of the optical transceivers, producing an effect equivalent to the wet-antenna attenuation observed in mmWave links. Besides, the sealing of the optical unit is probably not sufficient. In that case, some condensation might appear on the inner side of the protective glasses (see Figure 7.4 showing an optical unit and its cover). The wet glass might also explain the long transient attenuation after the end of the event [96].

The total atmospheric attenuation measured by the dual-band mmWave link on this day is shown in Figure F.1 Panel (b). Attenuation values are usually below 4 dB, hence well below the ones of the optical link. The rain attenuation can be predicted using the same procedure for optical wavelengths, with two critical differences. First, the raindrops are in the same order of magnitude as the wavelength. Hence Mie theory (in the spherical approximation) or numerical methods (e.g., the T-matrix method) should be used to calculate the extinction cross-section. Second, multiple scattering does not significantly affect attenuation calculation. The predicted attenuation calculated considering recommendation ITU-R P.838-3 [88], presented in Panel (b) in Figure F.1, correlates reasonably well with measurements, though the latter also includes the attenuation contributions associated with gases. While the E-band recorded attenuation agrees with the rain intensity, the D-band signal unusual variations are mainly due to the hardware stability.

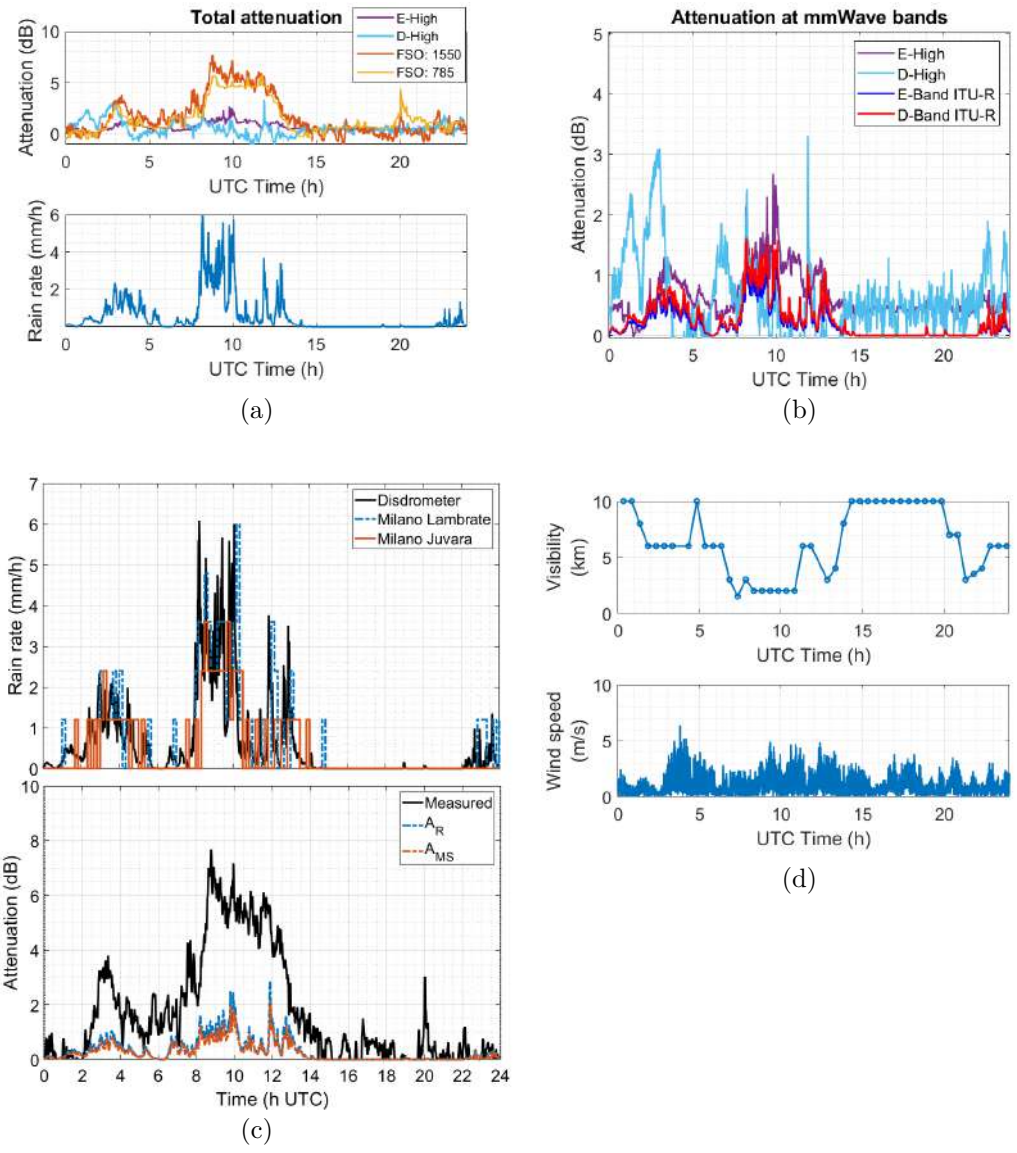

Figure F.1: Event 5: 17th Nov 2019, stratiform rain.

F.2
Convective rain

Event 14: 14 – 15/05/2020

The convective rain typically exhibits a temporal pattern of short rainfall episodes with high intensity. Figure F.2 presents the measurements for the nightly heavy rain event that occurred on 14 May 2020. Two significant episodes lasting about two hours, each with a peak intensity of 50 and 150 mm/h, respectively. The latter features a 100 mm/h peak as well. The patterns of attenuation and rainfall rate around the peaks are well correlated. As for the laser attenuation, presented in Figure F.2 Panel (a), the maximum measured value across the link is around 25 dB for the information channel and 19 dB for the service channel.

The predicted value of rain attenuation from the DSD provided by the disdrometer, without considering multiple scattering effects, is about 30 dB for the information channel. When multiple scattering gain is calculated using the DSD estimated by the disdrometer and subtracted, the predicted attenuation at the information channel drops to about 25 dB (Panel (b)). In the service channel, it is approximately 17 dB which is 2 dB lower than the measurement at the peak. The agreement is not that good when the rainfall intensity decreases. The measured attenuation exhibits a slowly decreasing trend between the two peaks in the second episode, with path attenuation still significant.

Panel (c) presents the predicted rain attenuation for the mmWave links provided by recommendation ITU-R P.838-3 [88] and the attenuation at the mmWave frequency bands. The experimental values agree with the values predicted by the ITU-R model.

Other atmospheric effects such as visibility and wind speed are presented in Panel (d): visibility was higher than 4 km during the rain periods, and the wind speed was not considered high. To validate the disdrometer rain rate, Panel (e) shows data from rain gauges near the link. Measurements of temperature and relative humidity are presented in Panel (f).

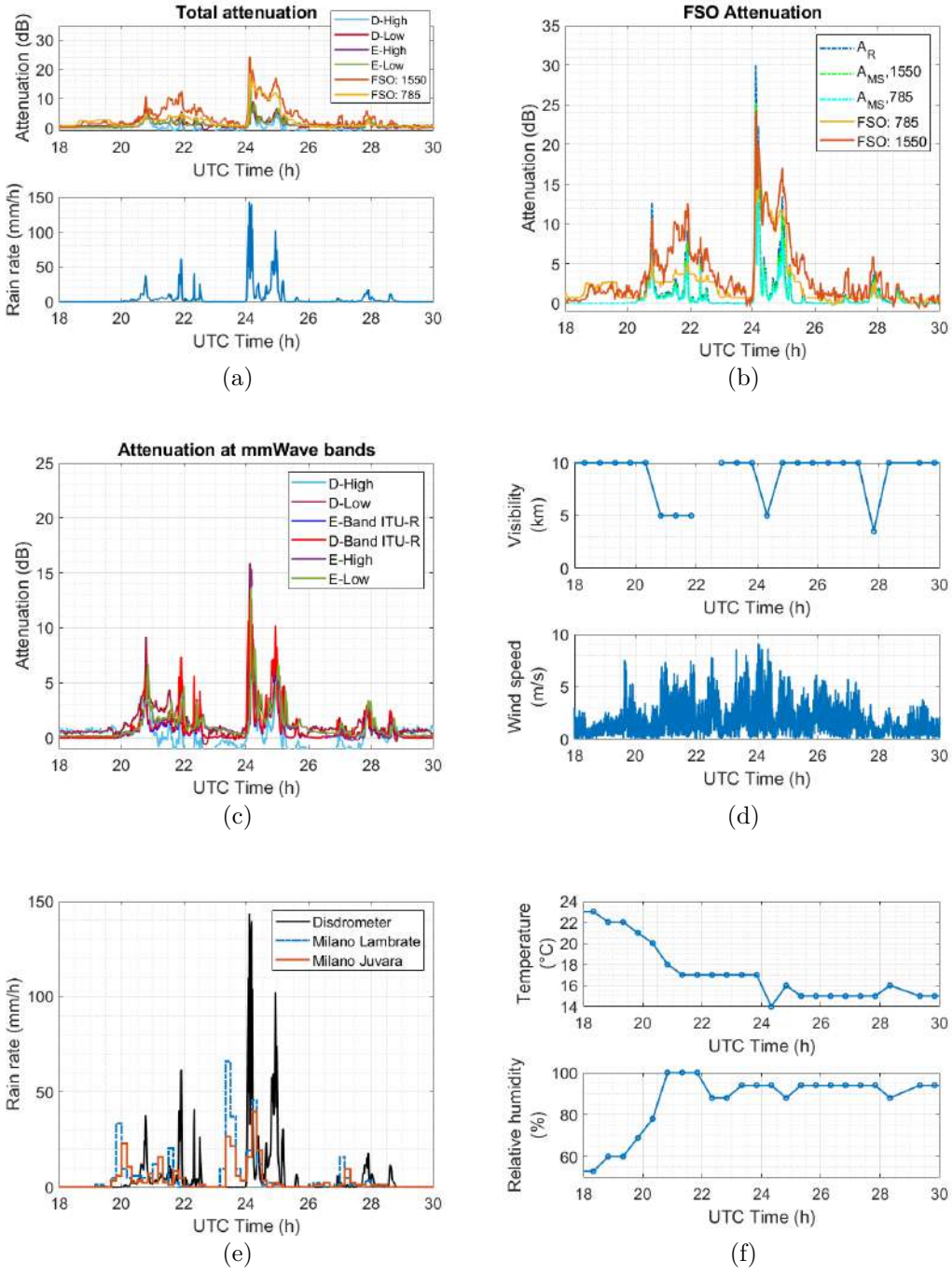

Figure F.2: Event 14: 14th – 15 May 2020, convective rain.

Event 20: 14/06/2020: Short convective rain

A short convective rain episode that occurred on 14 June 2020 at night is presented in Figure F.3. During the 15-min event, mmWave and optical attenuation (Panel (a)) are well correlated with the trend of the rain intensity in the bottom part of the Panel. The lowest attenuation value is found for the optical link service channel; this might be due to the broader field of view at the receiver and high visibility during the short episode (Panel (d)).

Panel (b) presents the measured time-series at both optical channels and the attenuation predicted without considering multiple scattering (A_R), as well as the one considering multiple scattering at both channels ($A_{(MS,1550)}$) and ($A_{(MS,785)}$). At the service channel, attenuation up to 6.3 dB is predicted considering the multiple scattering effects, whereas at the information channel, the attenuation reaches 7.7 dB. The multiple-scattering simulator receives as input, besides the wavelength, the field of view at the receiver, which explains the lower attenuation predicted in the case of the service channel.

For this event, the attenuation data collected by the mmWave links agree with the predictions obtained with the ITU recommendation, as shown in Panel (c). The strong peak shown by the disdrometer and the absence of rain on the rain gauges presented in Panel (e) can be explained by the very localized nature of extreme events. Besides, the rain gauges in Juvara and Lambrate collect 10-min average rainfall while the disdrometer measures 1-min rain rate enabling more accurate detection of rain bursts. Finally, rain gauges underestimate the actual precipitation under heavy rain conditions [98][99].

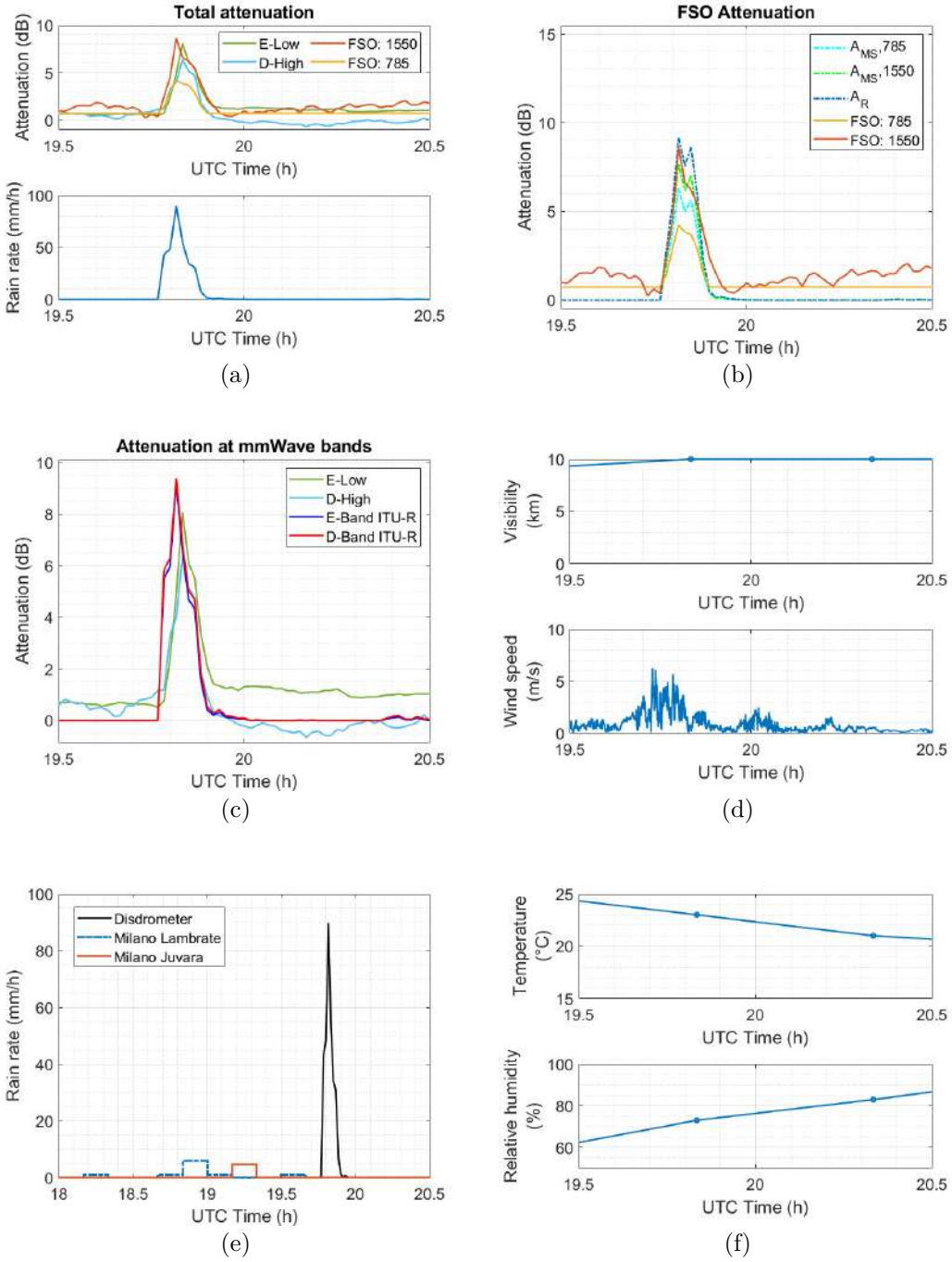

Figure F.3: Event 20: 14 June 2020, Short convective rain.

Event 27: 22/09/2020: Heavy convective rain

Another selected convective rain is the one on 22 September 2020. Panel (a) in Figure F.4, shows the atmospheric attenuation obtained at the optical channels, measured by the mmWave links and, on the bottom, the concurrent rainfall rate measurements. As shown in the bottom part of the Panel, the heavy rain episode lasts about one hour with a peak intensity higher than 250 mm/h.

A clear peak of attenuation due to rain is detected by all the links. Similar to previous convective rain events, the service channel obtains lower attenuation than the attenuation affecting the information channel. The lowest attenuation peak is associated with the service channel FSO link and is around 12 dB, while the mmWave link reaches 16 dB (Panel (c)). That behavior in the service channel depends on the high visibility during the rain episode (see Panel (d)), the broader field of view, and the wider laser beam of the service channel link.

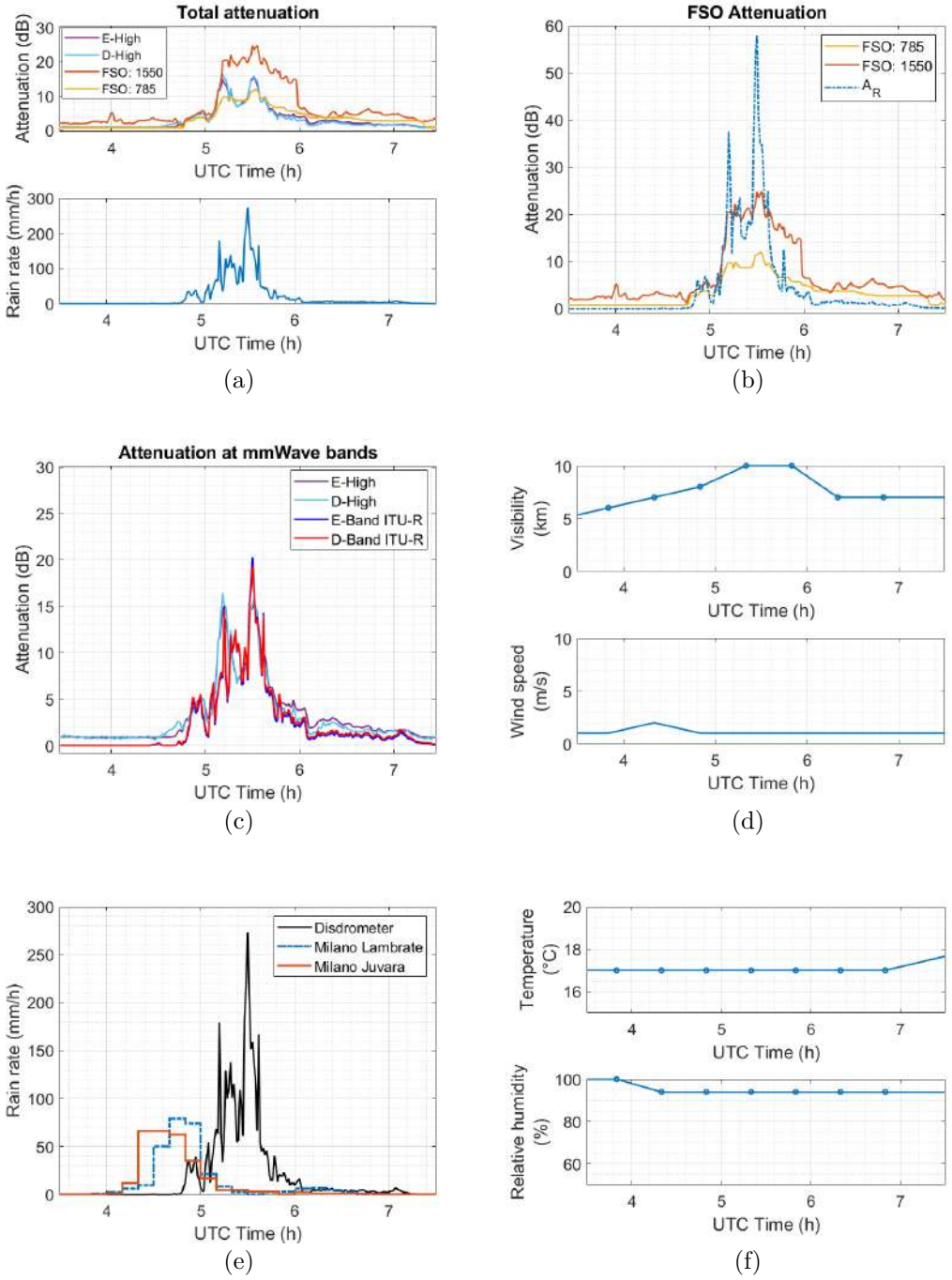

Figure F.4: Event 27: 22 September 2020, Convective rain.

F.3
Light rain

Event 10: 10/02/2020: light rain

The selected light rain event occurred on 10 February 2020 with a rain rate lower than 1 mm/h. Figure F.5 presents the experimental data. Three episodes within one hour between them are shown in the rainfall rate provided by the disdrometer (Panel (a)). The central episode starts at 04:00, and it lasts around four hours. Correspondingly, a strong peak of attenuation is shown by the optical links. The episode's duration corresponds to the central one exhibited by the disdrometer. Still, it starts two hours after the first one registered by the disdrometer, but it fits with the rain gauge measured in Juvara station (Panel (e)).

There is another peak at optical wavelengths one hour later; it corresponds to the smallest peak of rain rate and a higher wind speed, as shown in Panel (d). Visibility was low during the whole period, with values lower or equal to 3 km. The light rain rate episode at 02.00 is not well correlated with the attenuation measured by the optical links. The predicted attenuation is calculated using the DSD data recorded by the disdrometer; it is in Panel (b). As values of the expected attenuation do not exceed 1 dB, the FSO link attenuation is not only caused by the detected drops. Indeed, the attenuation peaks are likely due to a sudden further drop in the visibility, which is missed by the sensor at Linate airport (coarse sampling time and 5 km from the site where the FSO link is installed).

In mmWave links, only data of D-High link are available, which are presented in Panel (c). The pattern does not correspond to the disdrometer measurements. The magnitude of the attenuation predicted by ITU-R is lower than that obtained experimentally; however, neither exceeds 2 dB.

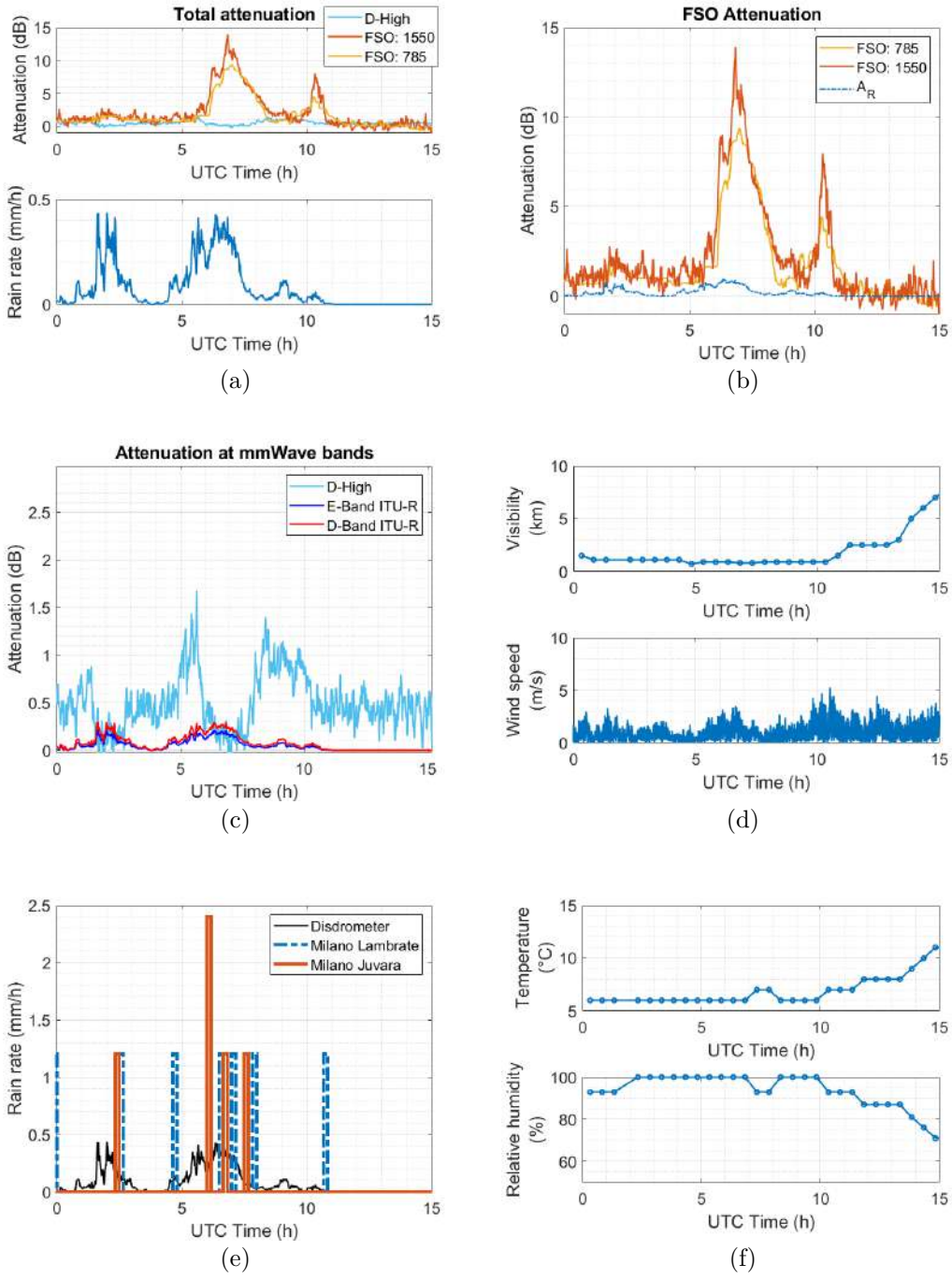

Figure F.5: Event 10: 10 February 2020, Light rain + low visibility.

F.4
Wind

Event 9: 05/02/2020: Windy event

We observed significant attenuation values on the FSO link during clear sky days and under strong wind conditions. Therefore, we decided to investigate the reason for this behavior on the FSO link only since the wind occurrence did not significantly affect the received signal of the mmWave links.

An intense windy episode of some hours occurred on 5 February 2020. The 1-min average attenuation is presented for both channels of the optical link in Panel (a) in Figure F.6. Panel (b) shows the atmospheric conditions. There is a clear correspondence between the measured attenuation at both channels and the sonic anemometer's wind speed.

The bottom part of Panel (b) highlights horizontal wind speed values up to 16 m/s (about 57 km/h). The strong wind deflects and disrupts the laser beam, leading to large fluctuations and extra attenuation. The beam pointing is critical at optical frequencies because the laser beam is relatively narrow. It is 0.3 mrad for the information channel and 1.2 mrad for the service channel: the latter is more stable. There is a clear correlation between the off-axis of the laser beam caused by the wind speed normal to the link and the measured attenuation at the information channel, as presented in Panel (c).

A displacement of the received optical beam off the receiver center is called beam wander. This phenomenon can be characterized by an offset in the average position of the beam center and by oscillations around the above position [100]. The signal reduction due to beam wander can be quantified by calculating the fraction of the beam wave that falls within the receiver area. The latter is a circle with an area equal to 64 cm^2. We assume that the transmitted beam has a Gaussian shape with a beamwidth of 0.3 mrad, as from MOSTCOM specifications (see Table 7.1). A simple geometrical calculation was carried out to explain the observed attenuation, and a linear fit was obtained for the relation between both magnitudes, as shown in Panel (d). Panel (e) shows the variation and the transmitted beam's X and Y coordinates (in pixels), showing an evident correlation with the wind-speed peaks. In all plots of panels (c), (d), and (e), σ is the standard deviation. The attenuation is much lower on the service channel than on the information channel. The broader field of view and the wider laser beam might explain this behavior against the wind-speed effect.

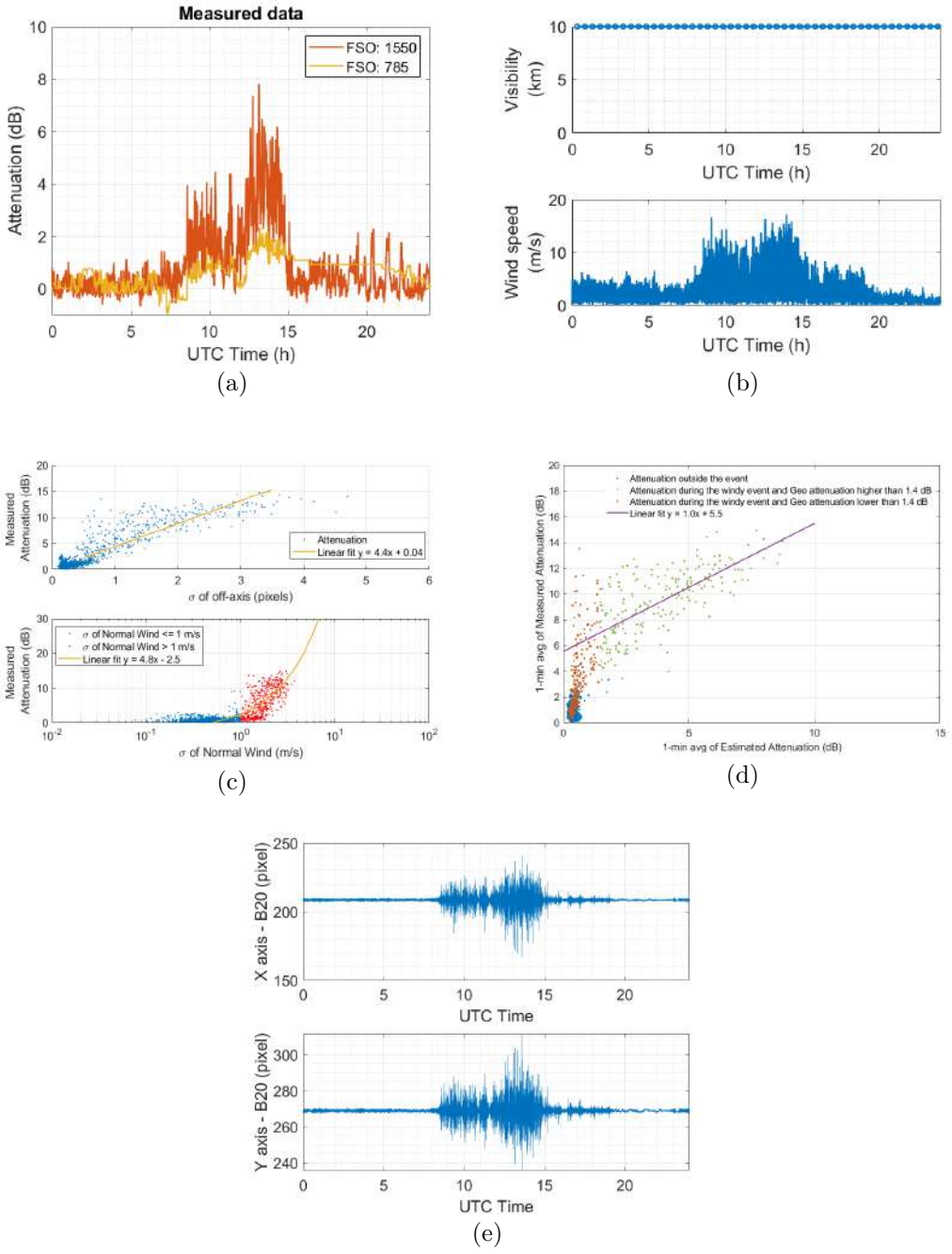

Figure F.6: Event 9: 5th February 2020, windy event.

F.5
Heavy Fog

Event 8: 03/02/2020: Heavy fog event

On 3 February 2020, the optical channels registered a heavy fog event, starting around 15:00 and crossing over to 4 February. Figure F.7 presents the attenuation for service and information channels and the atmospheric parameters. The attenuation patterns at both wavelengths agree with the low visibility registered at Linate airport (Panel (b)). Some outliers occurred in both channels at 1-min average attenuation when it exceeds 40 dB; it means that more than 10% of the samples at the received power are zeros and in-saturation values. The y-axis is limited to 40 dB due to the limits in the dynamic range of the commercial equipment used.

The atmospheric parameters are presented in panels (b) and (c), the visibility is minimum, with values around 0 km. It corresponds to the attenuation interval measured by the equipment. From hour 35:00 onward (relative to the beginning of the 3 February), the wind speed increases, raising the visibility simultaneously; therefore, the attenuation at both channels reduces almost to zero.

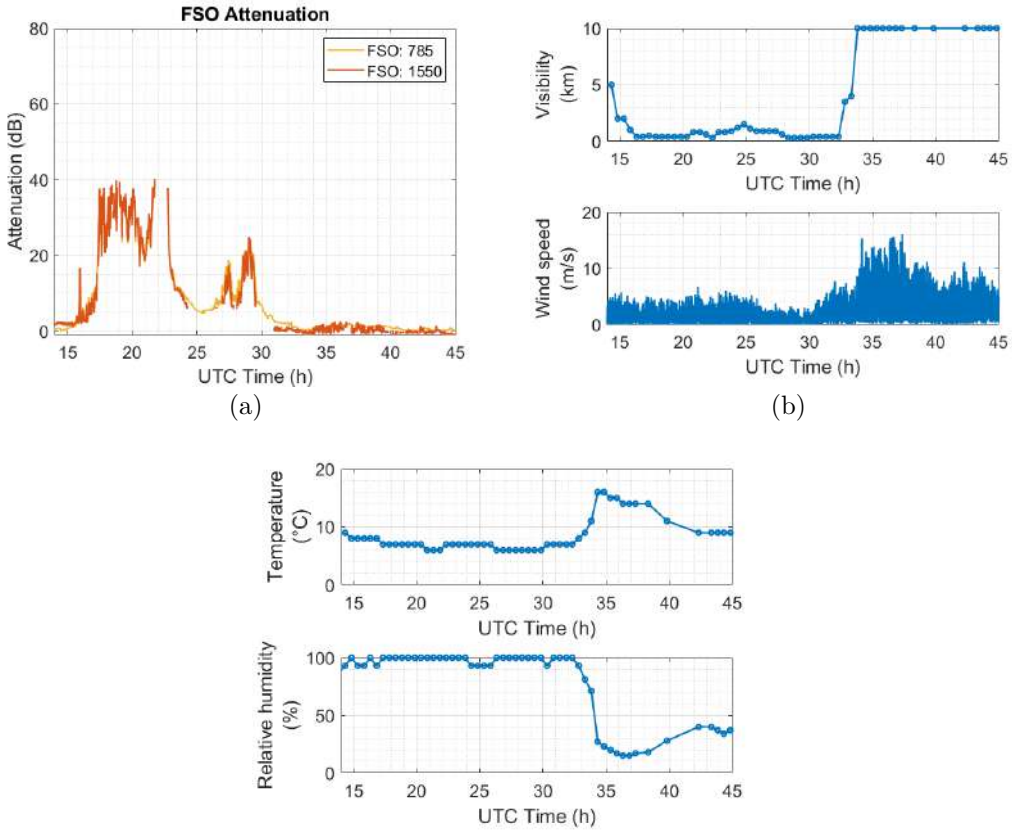

Figure F.7: Event 8: 3rd February 2020, Fog event.

F.6 Snow

Event 6: 13/12/2019

Measurements corresponding to the snow episode that occurred on 13 December 2019 are presented in Figure F.8 for the available mmWave links and the FSO channels. The bottom part of the same Panel offers the corresponding snow rate provided by the disdrometer.

At the information channel, the maximum path attenuation during the snowfall was around 14 dB at about 10:00; it correlates with the snow rate peak measured by the disdrometer. At approximately 07:00, the snow rate reaches the second peak at around 3 mm/h. The laser attenuation is less than 10 dB at the information channel and less than 5 dB at the service channel. However, the second peak of laser attenuation at both channels is around 09:00. At the same time, the snow rate is lower than before: the snow rate given by the disdrometer is not always in good agreement with the attenuation detected by the optical equipment.

The predicted attenuation, calculated by assuming spherical particles and considering the particle counts distribution provided by the disdrometer, is presented in Panel (b). Overall, the values of predicted attenuation are significantly lower than those measured by the information channel, but, on the contrary, they correlate well with attenuation affecting the service channel.

The attenuation registered by the mmWave links is shown in Panel (c). In general, the measured attenuation correlates with the snow rate. All links show the main peak at around 10:00. The discrepancy between the measured attenuation at optical and at mmWave frequencies might be due to the decay in visibility during the event: indeed, as shown in Panel (d), after 05:00, the visibility decreases significantly, thus leading to a marked increase in attenuation at optical wavelengths.

The rain gauge data are also considered to corroborate the disdrometer measurements. Panel (e) presents the 10-min accumulated snowfall time series obtained from two weather stations of ARPA. The snow rate pattern is not entirely correlated with the rain gauge data. That might be due to the difference between the instruments since the disdrometer considers particles crossing a given area, and the rain gauge quantifies liquid precipitation over an area.

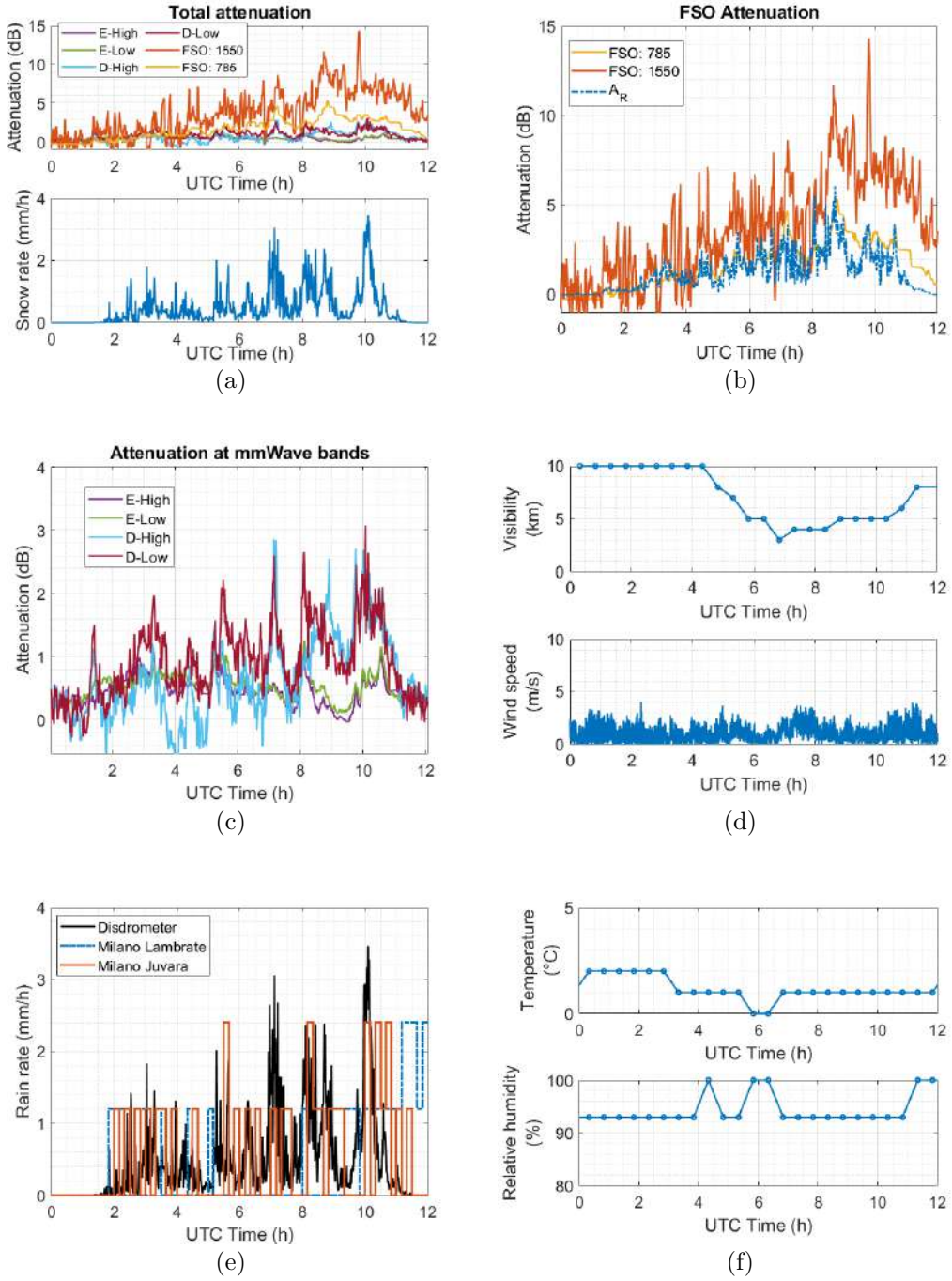

Figure F.8: Event 6: 13 December 2019, snow event.

F.7
Others type of events

Event 26: 07/09/2020: Stratiform rain + convective peak

Panel (a) of Figure F.9 highlights a major convective rain peak between 2:00 and 4:00, with light stratiform rain occurring after it. In this case, optical and mmWave attenuations correlate well with the rain rate (bottom side of Panel (a)). Measurements of rain attenuation at the mmWave frequencies agree with those predicted using recommendation ITU-R P.838-3 (see Panel (c)).

The laser attenuation affecting the information channel shows the main peak of 8 dB. The service channel attenuation is up to 5 dB; the mm-wave attenuation is lower than for the information channel (up to 7 dB) but in the same order of magnitude as the service channel. The estimated rain attenuation (without considering multiple scattering) is reported in Panel (b). As for convective rain events, the attenuation considering multiple scattering drops to around half of A_R (Panel (b)), enhancing the agreement with the service channel attenuation.

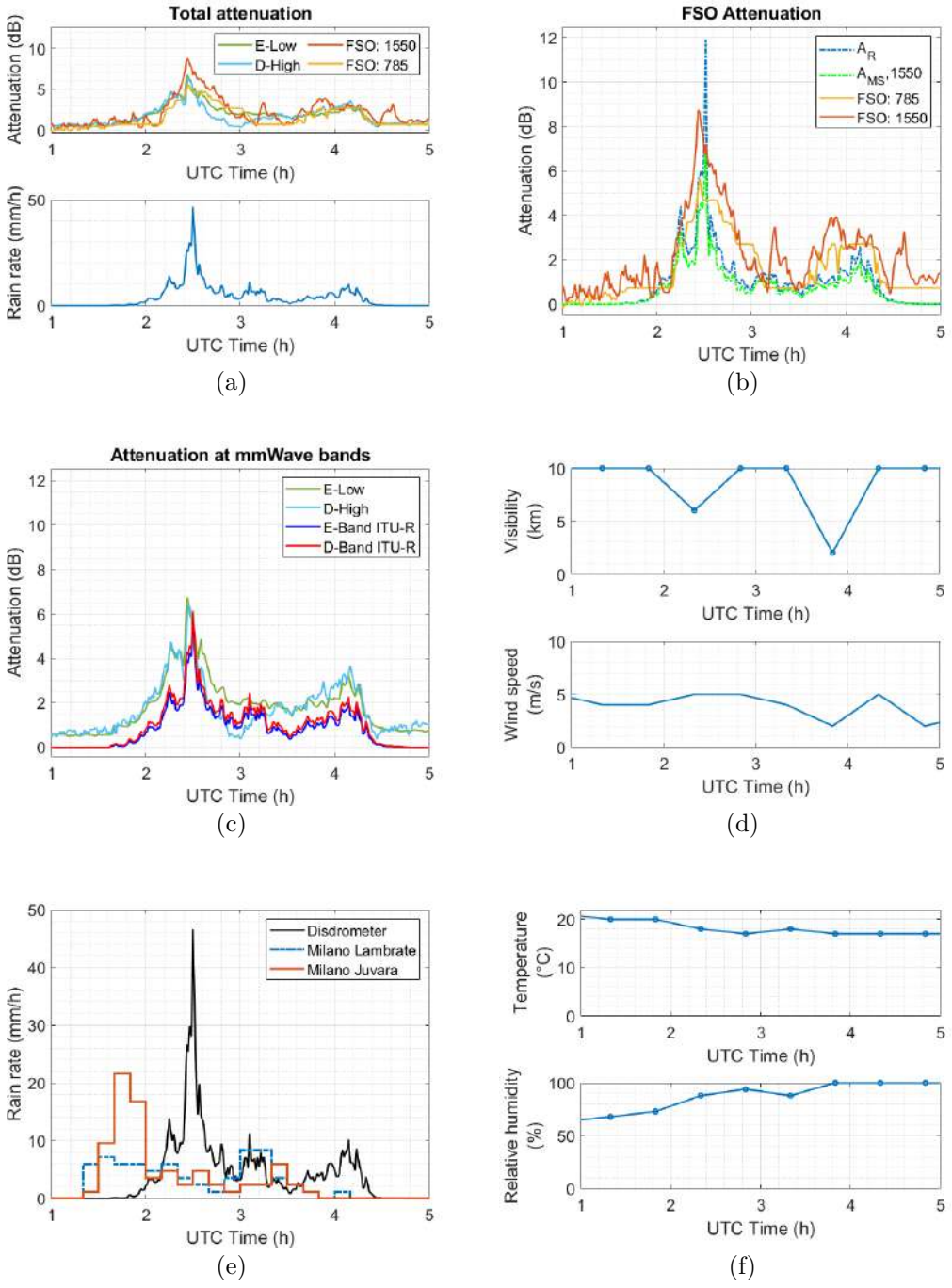

Figure F.9: Event 26: 7 September 2020, Stratiform rain and a convective rain peak.

G
Additional events

Appendix F presented relevant study cases for each event category. This section presents figures corresponding to the remaining events listed in Table 7.3. Sometimes, the attenuation measured by the service channel (785 nm) exhibits a flat pattern during the observation window. This behavior is due to the system settings, which are not optimized to observe the entire dynamics of the event. For instance, one reason for the flat pattern is the saturation of the sensor which measures received power level.

G.0.1
Event 7: 02/02/2020: Heavy fog

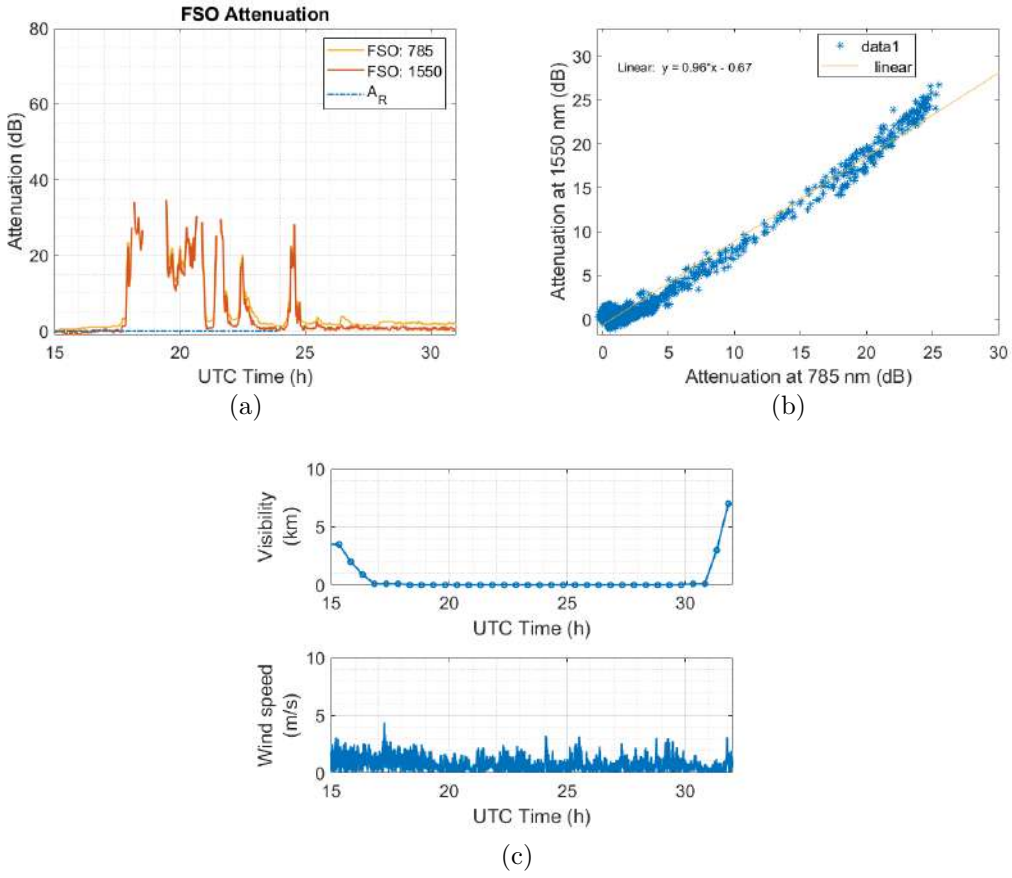

Figure G.1: Event 7: 2nd February 2020, Heavy fog event.

G.0.2
Event 11: 20/04/2020: Light rain

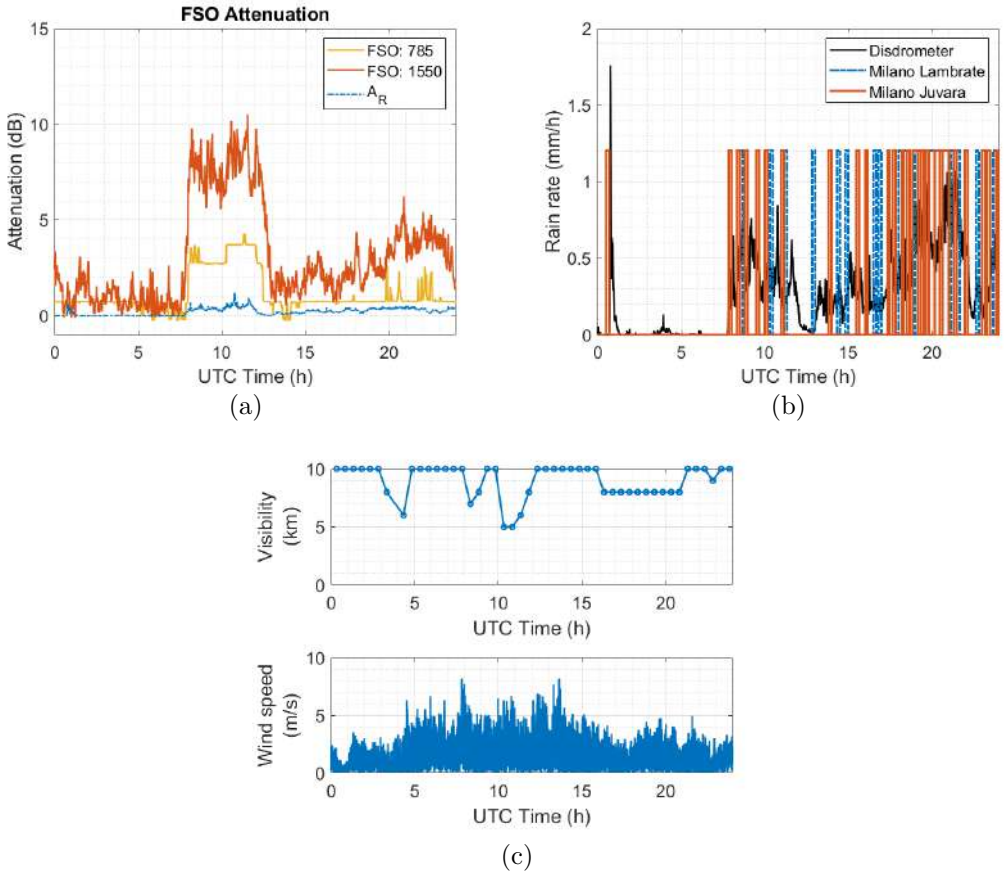

(a) (b) (c)

Figure G.2: Event 11: 20th April 2020, Light rain.

G.0.3
Event 12: 28-29/04/2020: Stratiform rain

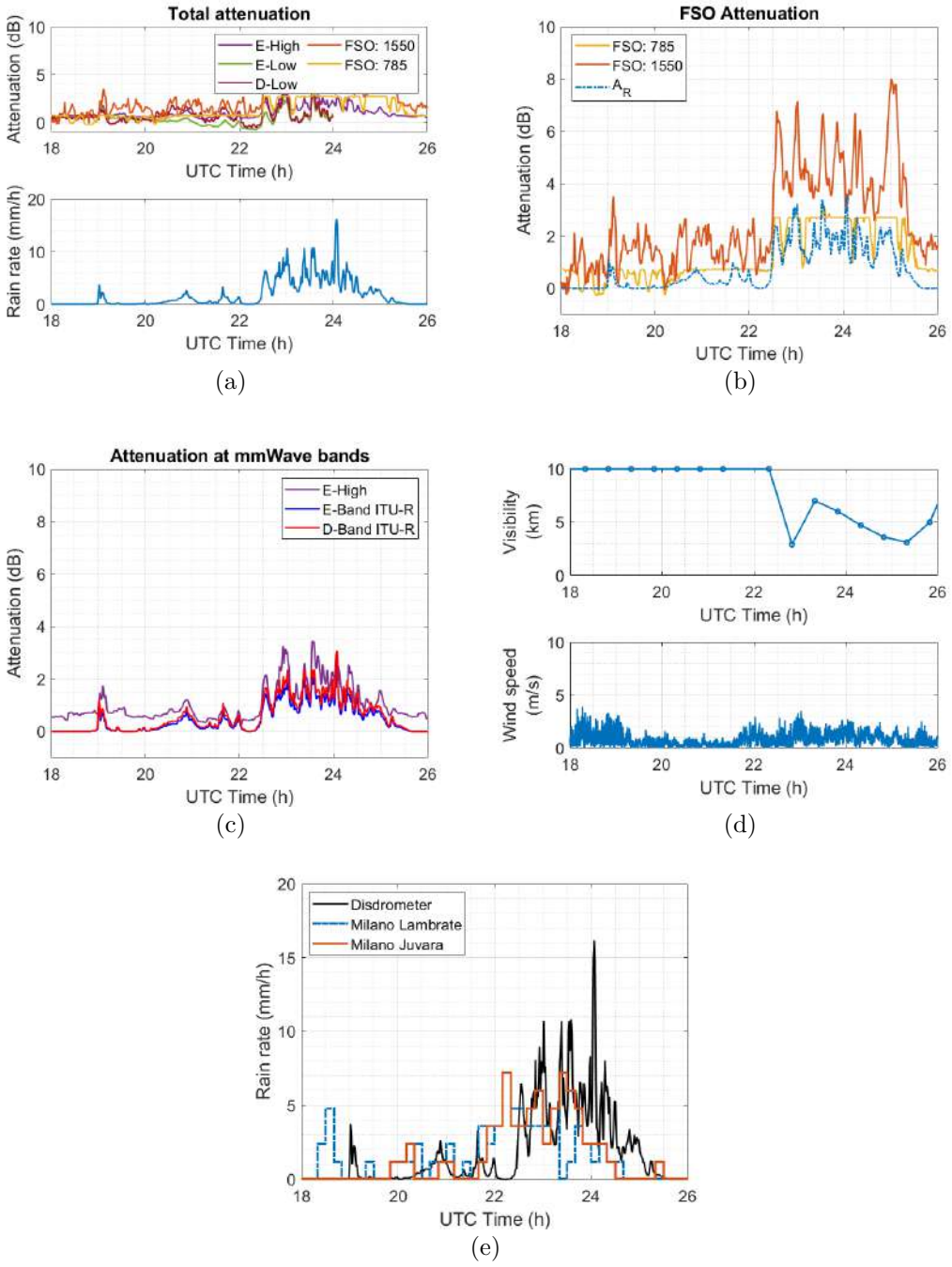

Figure G.3: Event 12: 28th April 2020, Rain.

G.0.4
Event 13: 11/05/2020: Stratiform rain + Convective rain

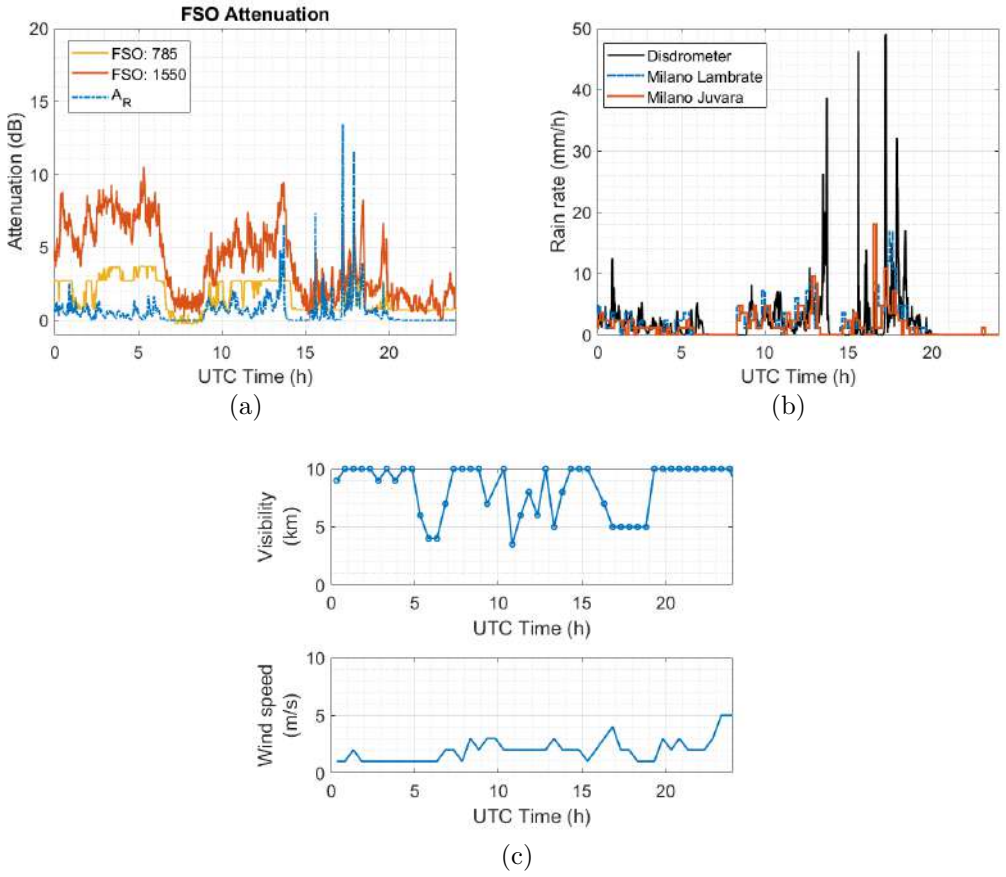

Figure G.4: Event 13: 11th May 2020, Rain.

G.0.5
Event 15: 02/06/2020: Convective rain + Wind

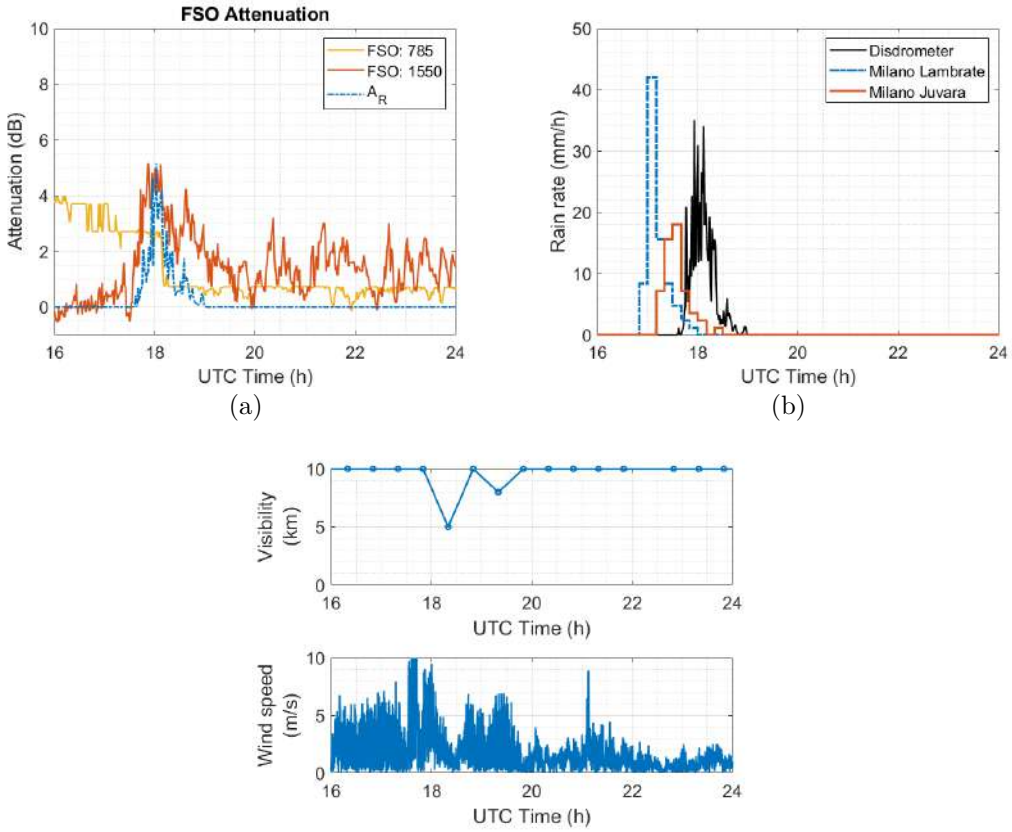

(a) (b) (c)

Figure G.5: Event 15: 2nd June 2020, Rain.

G.0.6
Event 16: 04/06/2020: Stratiform rain

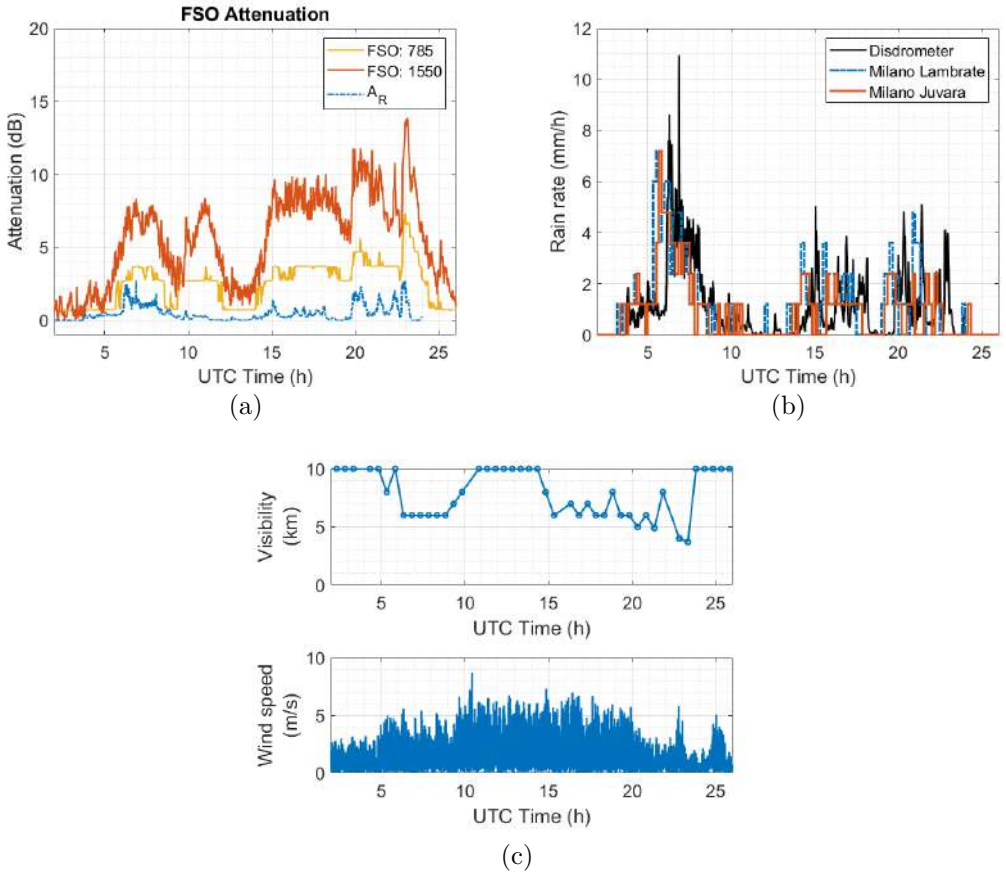

(a) (b) (c)

Figure G.6: Event 16: 4th June 2020, Rain.

G.0.7
Event 17: 07/06/2020: Stratiform rain + Convective rain

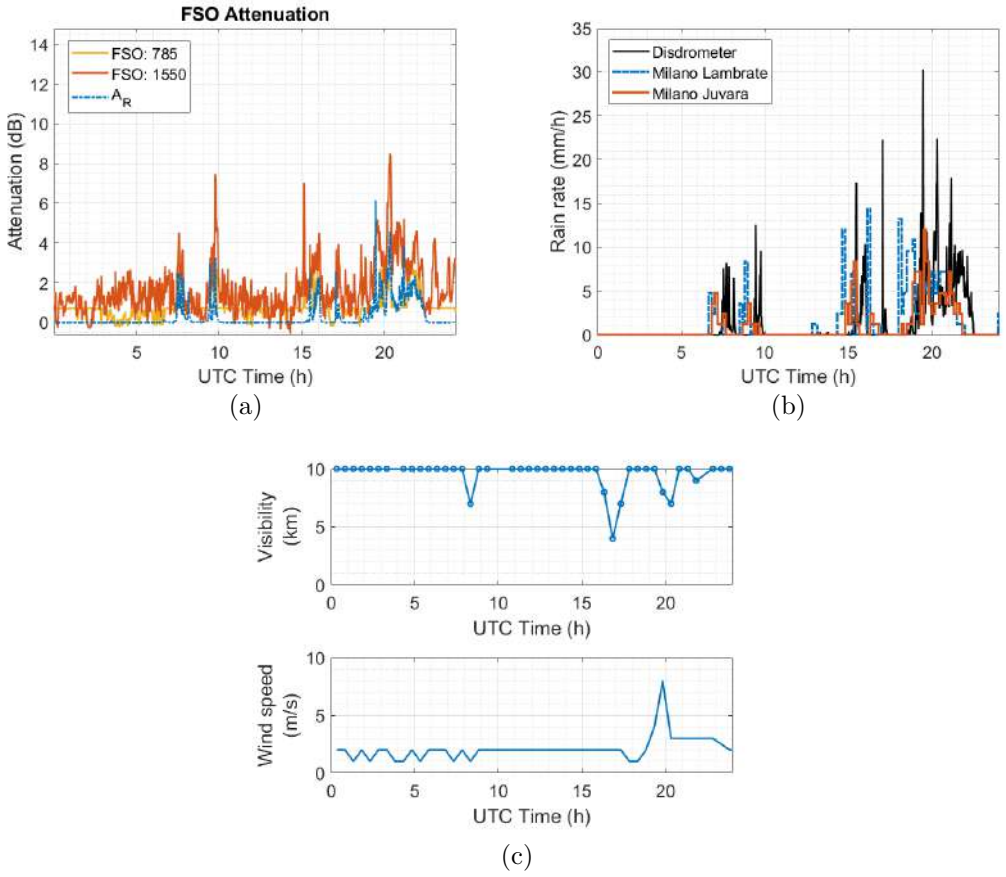

Figure G.7: Event 17: 7th June 2020, Rain.

G.0.8
Event 18: 08/06/2020: Convective rain

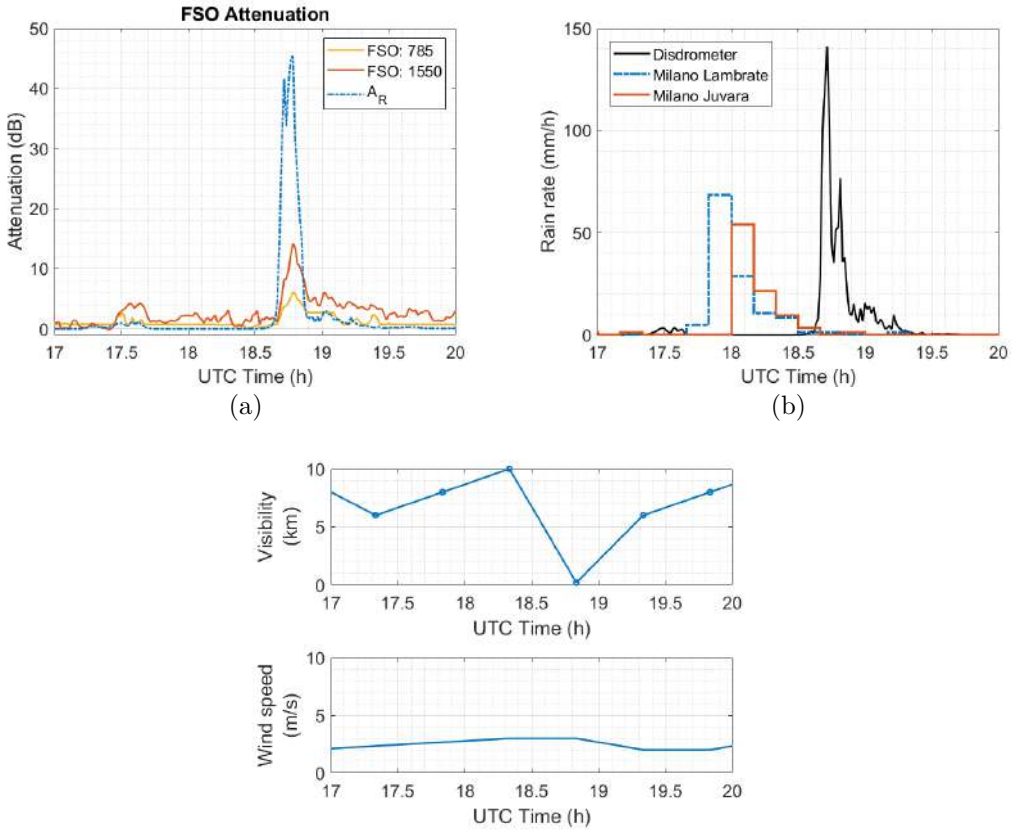

Figure G.8: Event 18: 8th June 2020, Convective rain.

G.0.9
Event 19: 13/06/2020: Light rain + Wind

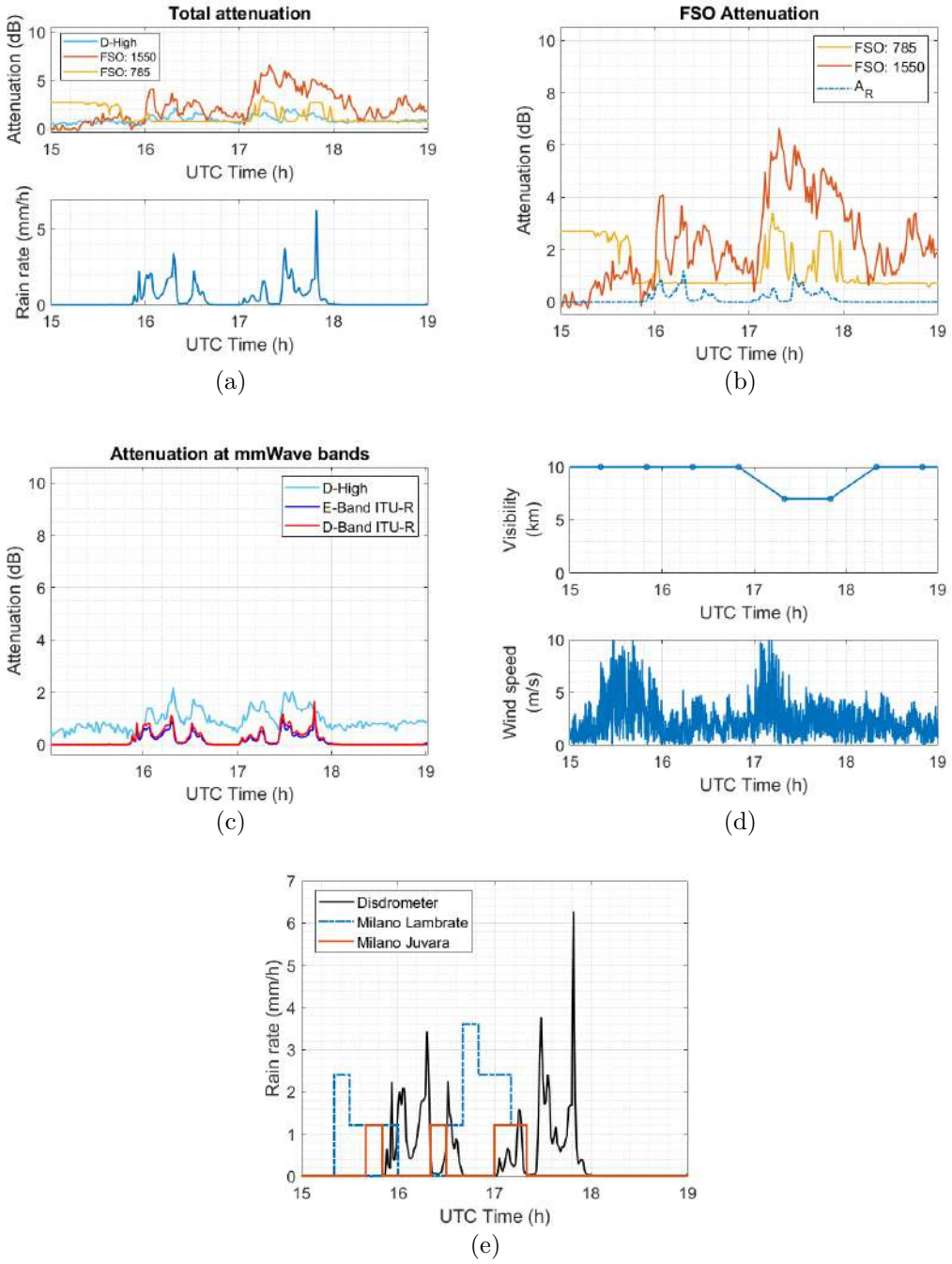

Figure G.9: Event 19: 13th June 2020, Light rain + wind.

G.0.10
Event 21: 03/07/2020: Others (FSO peaks)

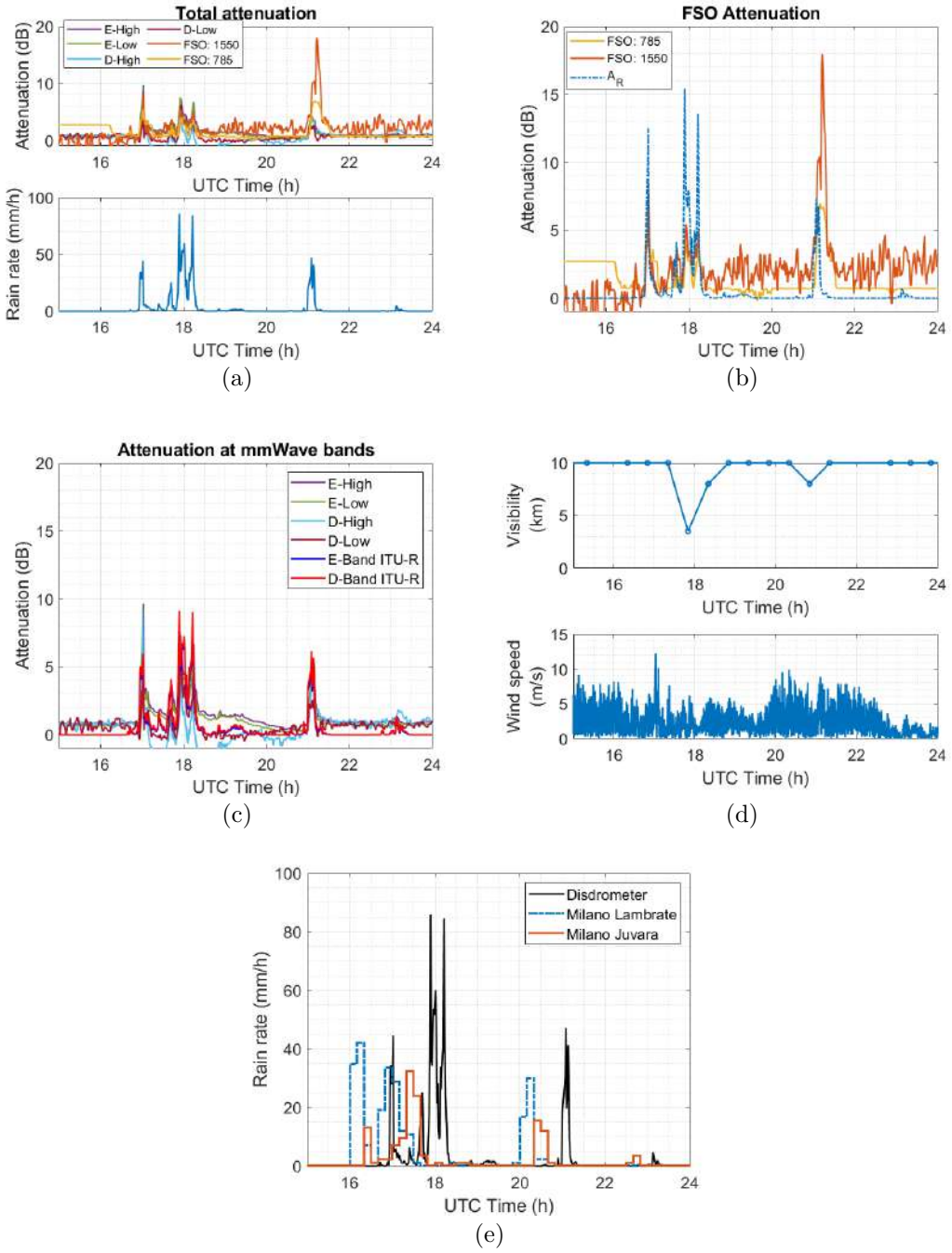

Figure G.10: Event 21: 3rd July 2020, Others: FSO peaks.

G.0.11
Event 22: 15/07/2020: Convective rain

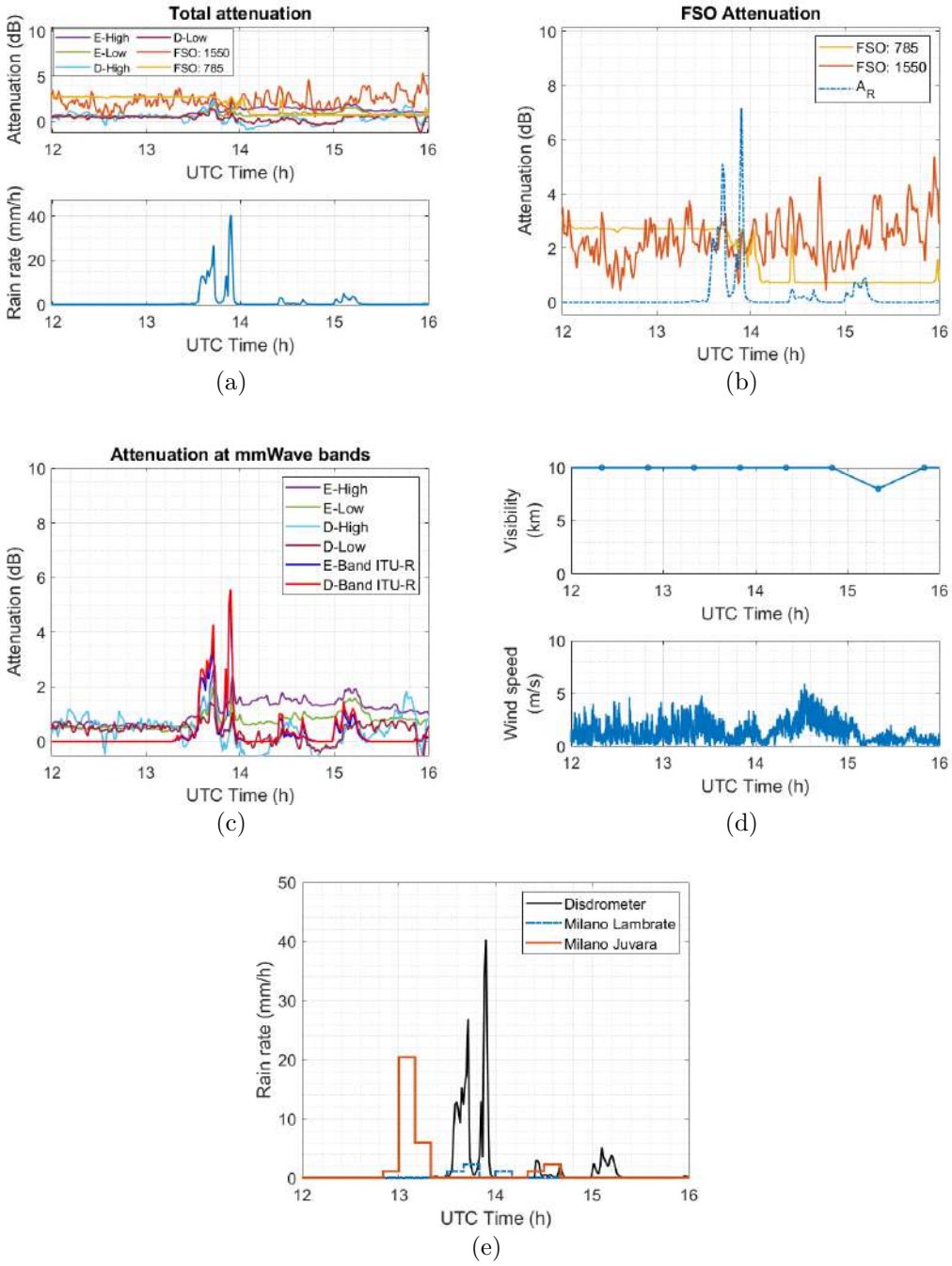

Figure G.11: Event 22: 15th July 2020, Convective rain.

G.0.12
Event 23: 03/08/2020: Convective rain

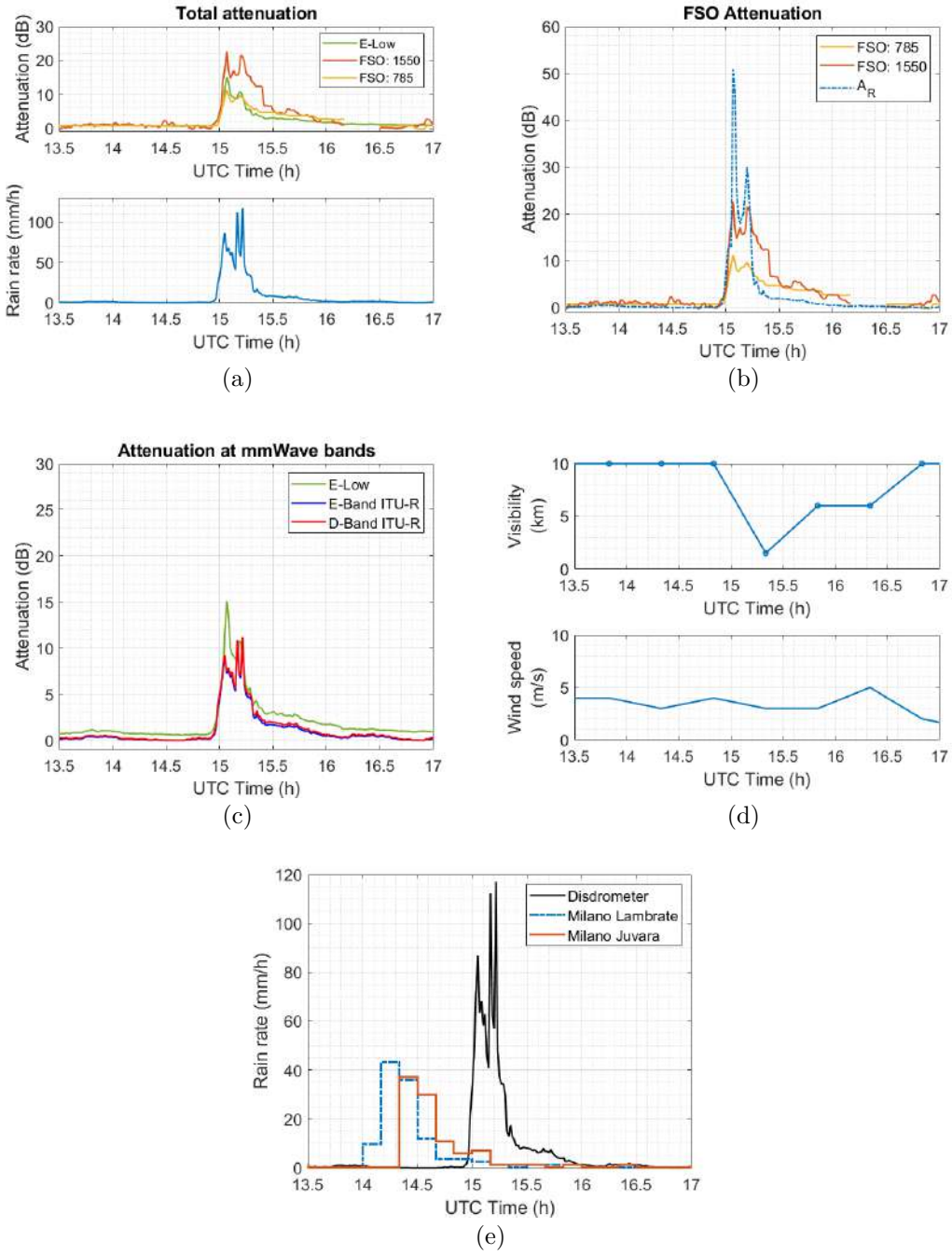

Figure G.12: Event 23: 3rd August 2020, Convective rain.

G.0.13
Event 24: 28/08/2020: Convective rain

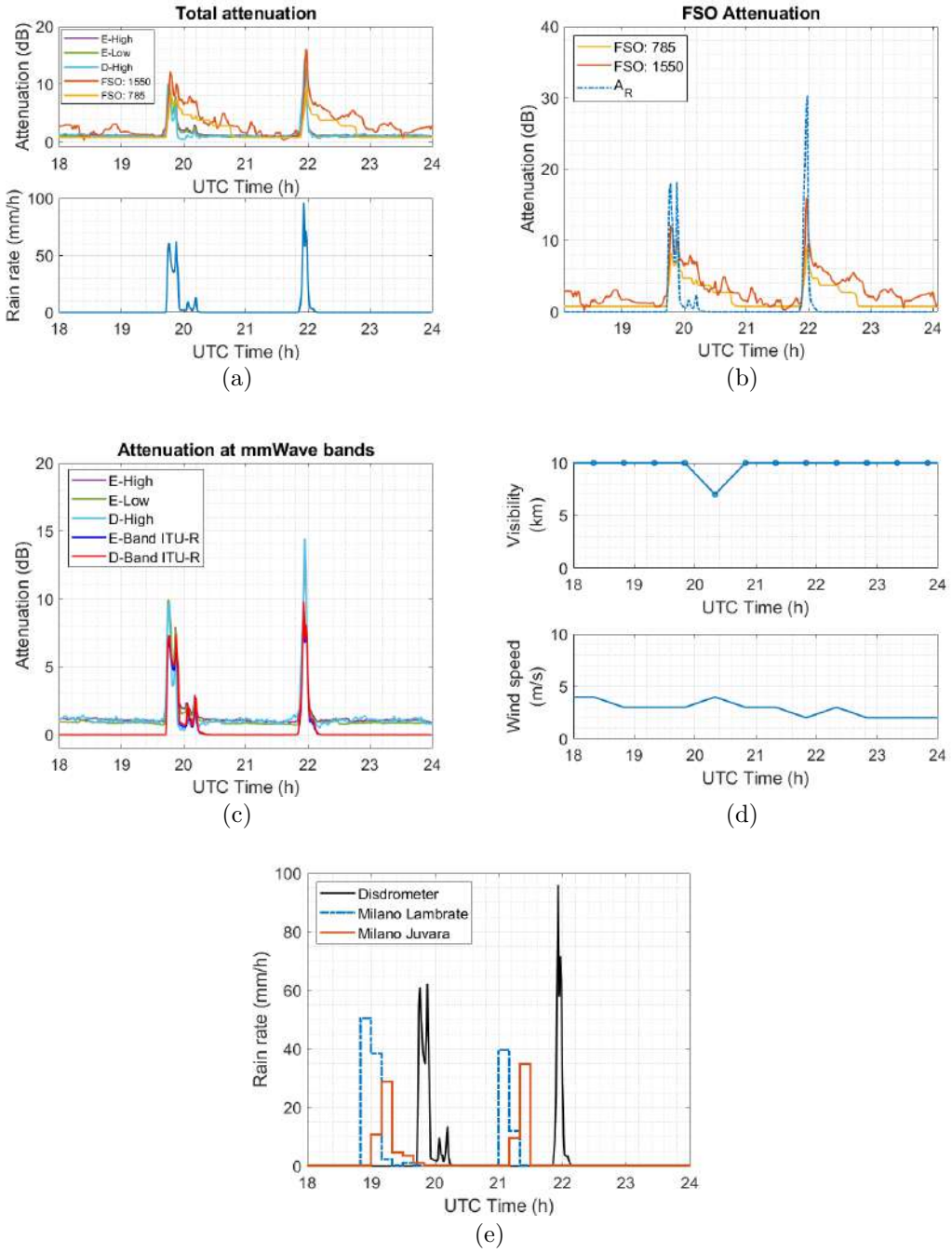

Figure G.13: Event 24: 28th August 2020, Rain.

G.0.14
Event 25: 29/08/2020: Light rain

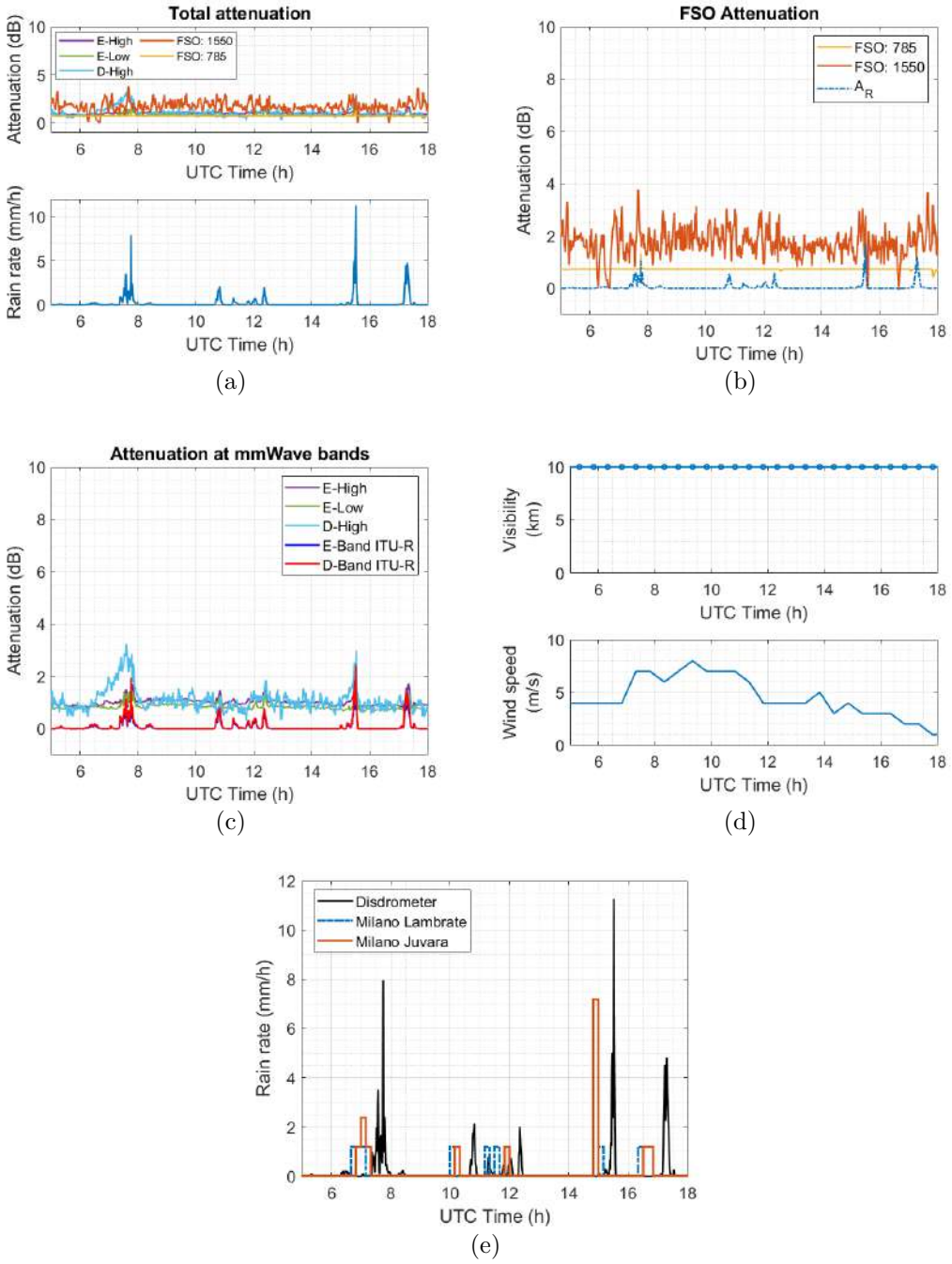

Figure G.14: Event 25: 29th August 2020, Rain.

G.0.15
Event 28: 02/10/2020: Stratiform Rain

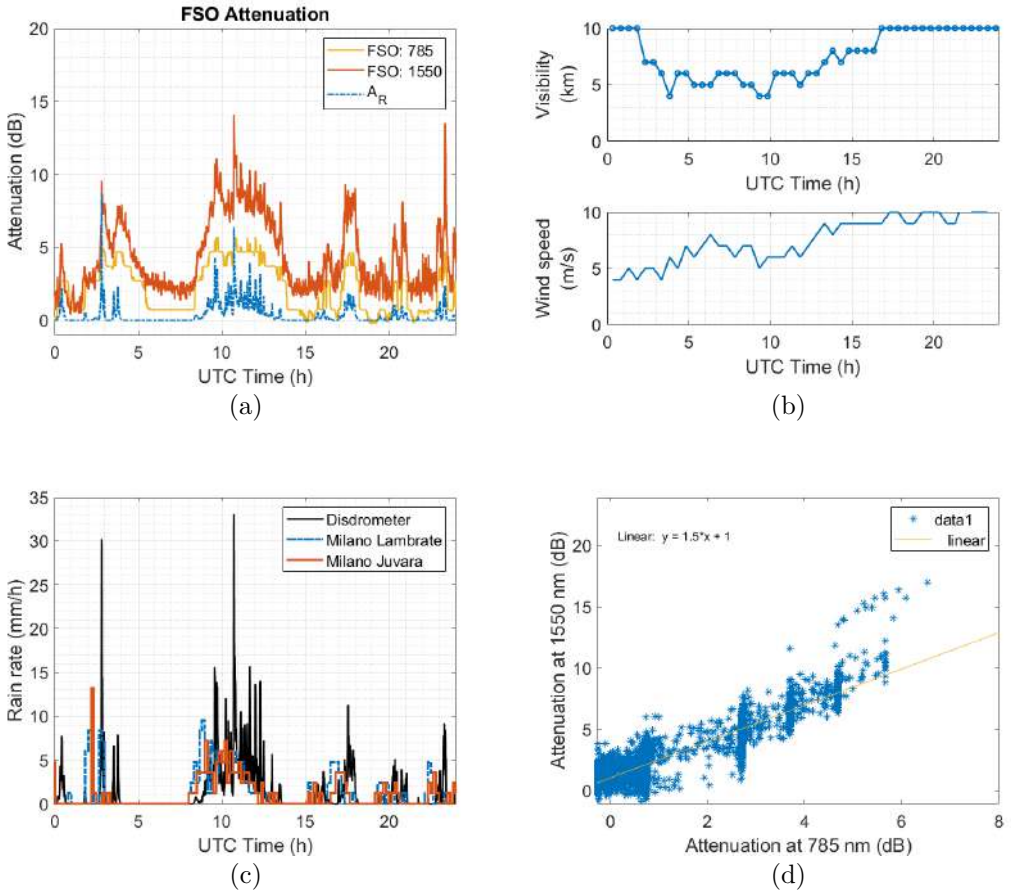

Figure G.15: Event 28: 2nd October 2020, Rain.

G.0.16
Event 29: 03/10/2020: Stratiform Rain

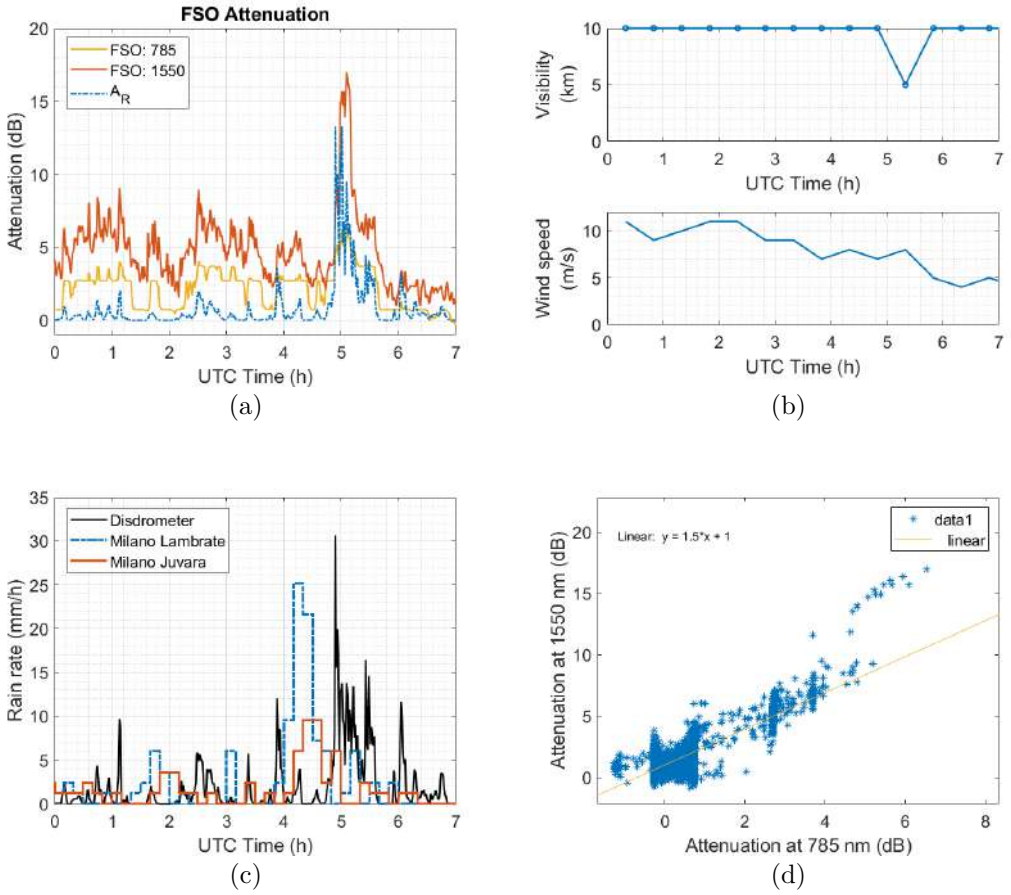

Figure G.16: Event 29: 3rd October 2020, Rain.

G.0.17
Event 30: 22/10/2020: Light rain

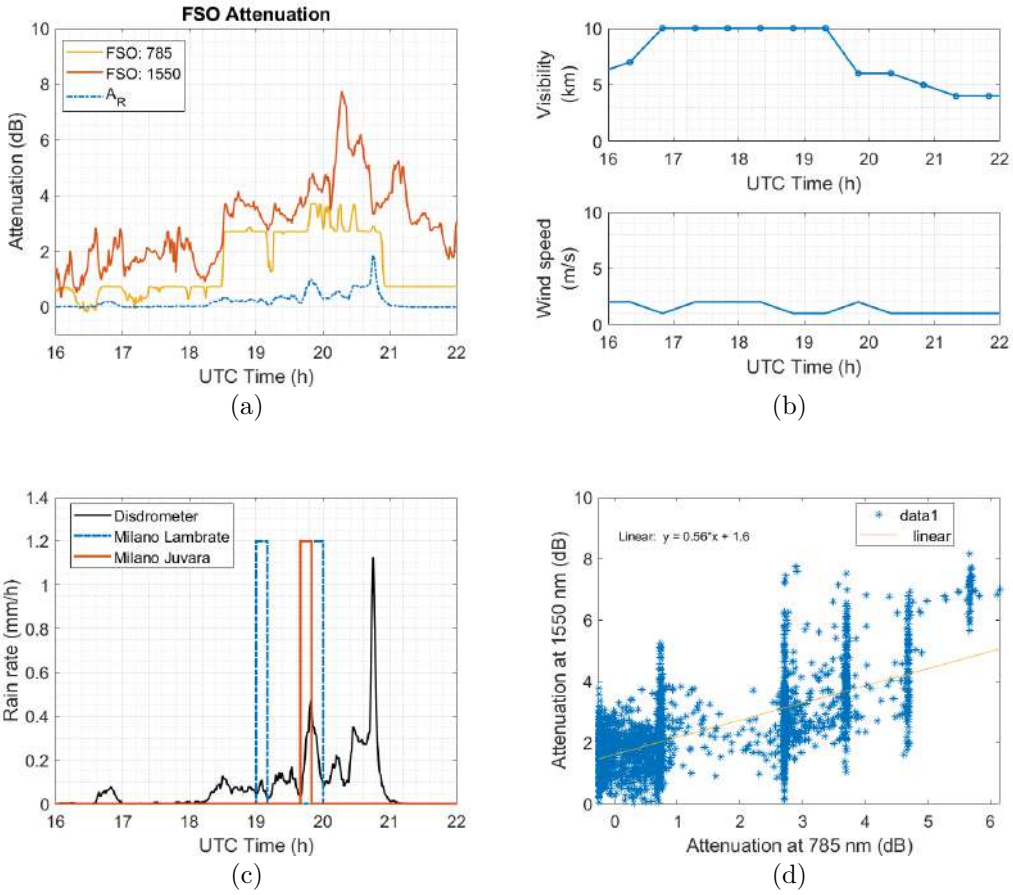

Figure G.17: Event 30: 22nd October 2020, light rain.

G.0.18
Event 31: 02/12/2020: Snow

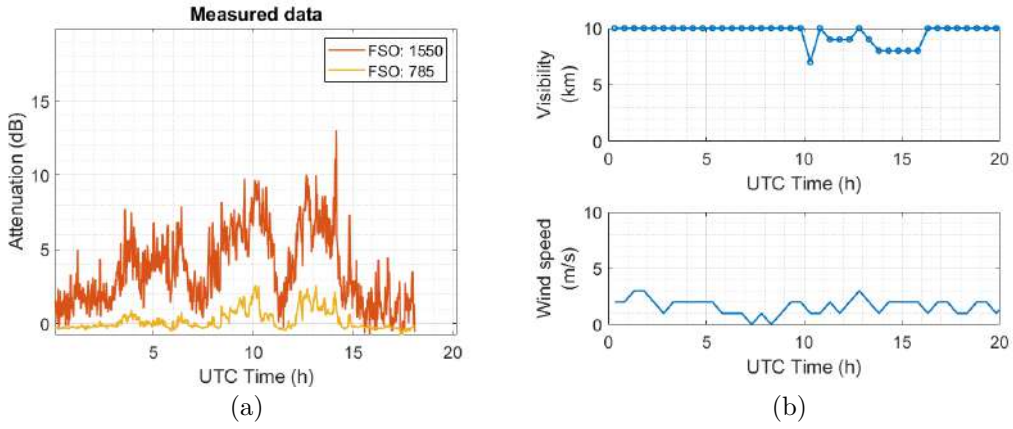

Figure G.18: Event 31: 2nd December 2020, Snow.

H
Published papers

The following papers have been published during the development of this thesis.

1. R.Nebuloni, and **E. Verdugo**, "FSO Path Loss Modelling Based on Visibility". IEEE Photonics Journal 14.2 (2022): 1-9. https://ieeexplore.ieee.org/abstract/document/9718170

2. **Verdugo, E.**, Mello, L. D. S., Riva, C., Luini, L., and Nebuloni, R. (2022, March). Estimation of FSO Path Length at Mid-IR Wavelength. In 2022 16th European Conference on Antennas and Propagation (EuCAP) (pp. 1-4). IEEE. https://ieeexplore.ieee.org/abstract/document/9768987

3. **E. Verdugo**, R. Nebuloni, L. da Silva Mello, and C. Riva, "Effect of Wind in a Clear-day on Beam Wander of a Terrestrial Free Space Optical link", (MOMAG 2020), Niteroi, Brazil, 8-12 November 2020.

4. **E. Verdugo**, R. Nebuloni, L. Luini, C. Riva, L. d. S. Mello and G. Roveda, "Rain Effects on FSO and mmWave Links: Preliminary Results from an Experimental Study," 2020 29th Wireless and Optical Communications Conference (WOCC), Newark, NJ, USA, 1-2 May 2020. https://ieeexplore.ieee.org/document/9114936